Reactivity of Metals Tethered to Metal-Organic Frameworks

Rosemary J. Young

School of Physical Sciences, The University of Adelaide

and

School of Chemistry, University of Nottingham

A Thesis Presented to The University of Adelaide and the University of Nottingham

in fulfilment of the requirements for the Degree of Doctor of Philosophy

May 2021

Declaration

I certify that this work contains no material which has been accepted for the award of any other degree or diploma in my name, in any university or other tertiary institution and, to the best of my knowledge and belief, contains no material previously published or written by another person, except where due reference has been made in the text.

In addition, I certify that no part of this work will, in the future, be used in a submission in my name, for any other degree or diploma in any university or other tertiary institution without the prior approval of the University of Adelaide and the University of Nottingham.

I acknowledge that copyright of published works contained within this thesis resides with the copyright holder(s) of those works. I also give permission for the digital version of my thesis to be made available on the web, via the Universities' digital research repository, the Library Search and also through web search engines, unless permission has been granted by the University to restrict access for a period of time.

I acknowledge the support I have received for my research through the provision of an Australian Government Research Training Program Scholarship.

Rosemary Young

20/05/2021

Acknowledgements

Completing this PhD would not have been possible without the support of many people. It has been a privilege to work under the guidance of Prof. Chris Sumby and Prof. Neil Champness, and I thank them for their constant aid and encouragement. I had the great honour to be a member of two fantastic research groups and benefit from the advice of many excellent researchers, in particular Em. Prof. Richard Keene, Prof. Christian Doonan and Dr. Witold Bloch.

I am very grateful for collaborations with Prof. Chris McDevitt and Dr. Steph Begg for the microbiological experiments, Prof. Mike George, Dr. Ashley Love and Dr. Katie Reynolds for the matrix-isolated IR experiments and A. Prof. James O'Shea and Jack Hart for the XPS experiments. I would also like to thank the staff at Adelaide Microscopy, particularly Aoife McFadden, Sarah Gilbert and Ken Neubauer, and at the Nanoscale and Microscale Research Centre, especially Beth Steer, for their assistance.

This PhD has fostered my love for X-ray crystallography, and I am incredibly grateful for the crystallographers who have helped me, namely Dr. Stephen Argent, the MX Beamline Scientists at the Australian Synchrotron, especially Dr. Jason Price and Dr. Alan Riboldi-Tunnicliffe, and the i19 Beamline Scientists at Diamond Light Source, Dr. Sarah Barnett, Dr. Dave Allan, Dr. Mark Warren and Dr. Lucy Saunders.

I would not have reached this far without the guidance of some incredible post-doctoral researchers, especially Dr. Cam Coghlan, Dr. Alex Burgun, Dr. Nic Pearce, Dr. Michael Huxley, Dr. Sarah Griffin and Dr. Georgia Orton.

To the Sumby-Doonan group and the occupants of Labs 9 and 10, especially Jesse, Pat, Oliver, Tash, Kate, Harley, Tom, Chris, Tania, Ricardo, and Natasha, thank you for help in the lab and many cakes over the years. To the Champness Group, especially Arjun, Joe, Olukayode, Mark, Alex, Marysia, Nathan, Asia, Eleanor, Zoe, Claire and Jen, thank you for the great times pre- and mid-pandemic.

Participation in the Nottingham/Adelaide Joint PhD program not only allowed for many research opportunities but gave me the chance to meet some incredible people, so I thank all the other students in the program for their friendship and assistance.

Finally, I wish to acknowledge the unwavering support and encouragement of my family, especially my Mum, over these last 4 years.

Table of Contents

Abbreviations

CO	Carbon Monoxide
CP	Coordination Polymer
DMF	Dimethylformamide
DUT	Dresden University of Technology
EDX/EDS	Electron Dispersive X-ray Spectroscopy
EtOH	Ethanol
IR	Infrared
MeCN	Acetonitrile
MeOH	Methanol
MnMOF	Manganese MOF
MnOx	Manganese oxide
MOF	Metal-Organic Framework
MS	Mass Spectroscopy
NMR	Nuclear Magnetic Resonance
PSM	Post-synthetic Modification
PSMet	Post-synthetic Metalation
PXRD	Powder X-ray Diffraction
SCSC	Single Crystal-to-Single Crystal
SCXRD	Single Crystal X-ray Diffraction
SEM	Scanning Electron Microscopy
THF	Tetrahydrofuran
TRIR	Time-Resolved Infrared
UiO	Universitetet i Oslo
UV-Vis	Ultraviolet-Visible
XPS	X-ray photoelectron Spectroscopy

Abstract

The reactivity of solid-state materials differs from those in solution or gaseous states due to structure, surface and transport effects.[1] While the reactivity of metal complexes in solution have been well explored,[2,3] the study of well-defined solid-state metal complexes has been stymied by difficulties in characterisation and poor stability. Metal-organic frameworks (MOFs) provide a promising platform for the site-isolation, characterisation and reaction of such complexes.

The controlled delivery of CO gas from photoactivated Mn(I) carbonyl complexes is desired for medical and chemical synthesis applications. A *fac*-tricarbonyl Mn(I) complex was tethered to the bis-pyrazole coordination site of L′ in MnMOF, [Mn_3L_2L'] (H_2L = 4,4'-{methylenebis(3,5-dimethyl-1H-pyrazole-1,4-diyl)}dibenzoic acid), and found to undergo a series of solvent-induced isomerisations. The photoactivated decarbonylation pathway for MnMOF[$Mn(CO)_3X$]Y (X,Y = Br^- or solvent) was studied, involving the stepwise loss of the carbonyl ligands, with di- and mono-carbonyl intermediates observed by IR spectroscopy and photocrystallography. Exposure to environmental oxidising agents resulted in a proposed final Mn(II) decarbonylation product, which formed a Mn(II) carbonyl species when exposed to CO gas.

MnMOF[$Mn(CO)_3X$]Y was used as an *ex-situ* light-triggered source of CO gas for aminocarbonylation reactions, achieving high yields with low excesses of CO. Two other Mn(I) carbonyl metalated MOFs, UiO-67-bpy and DUT-5-bpy, were likewise tested, and achieved high yields, although with different efficiencies. This demonstrated the influence of structure, topology and particle size on the effectiveness of these CO sources. To examine the former, MnMOF was structuralised from sacrificial sol-gel-derived manganese oxide templates. The template structure was found to influence the kinetics of formation and macrostructural properties of the MOF crystals.

Inorganic azides may react photochemically through a range of mechanisms, including the formation of highly reactive nitrene intermediates. As such, they are useful synthetic or catalytic intermediates.[4] An azidocarbonyl Mn(I) molecular complex dissolved in tetrahydrofuran or dichloromethane was found to form a bridging isocyanate complex upon irradiation with light, while the same complex isolated within MnMOF showed different reactivities at different temperatures in the presence of a coordinating solvent. Isocyanate was formed at room temperature for bulk, matrix

isolated samples, and at 190 K in a single crystal. At lower temperatures, decarbonylation occurred without formation of a nitrene.

The site-isolation of palladium catalysts in MOFs has allowed for improved reactivities and selectivities, but few of these complexes have been structurally characterised through single-crystal X-ray diffraction techniques.[5] Palladium halide complexes were tethered to MnMOF by post-synthetic metalation, but further investigations were hindered by the lability of the complexes and their propensity to form of pore-bound species, in addition to ligand-bound species, resulting in unpredictable metalation efficiencies.

Finally, silver coordination polymers have demonstrated antibacterial behaviour, but the properties controlling their activity are not well understood.[6] The dissolution behaviour of a sub-set of four silver coordination polymers, chosen to probe the relative impacts of coordination chemistry and topology, revealed that metal-ligand bond strength has the greatest impact on controlling silver ion release. The formation of composite materials with organic polymers attenuated the release of silver ions in water, with the more water permeable polymer, polycaprolactone, allowing for greater silver release than polyethylene. All four coordination polymers showed antibacterial activity, albeit to different extents.

For the reactions of metal complexes tethered to MOFs to be studied, the retention of long-range order and complex stabilities are the major barriers to characterisation. Judicious choice of a MOF host which permits changes in the coordination sphere of the metal, without loss of crystallinity, and site-isolation mitigates some of these challenges. In this work, it has been observed that environmental parameters such as temperature, light and exposure to air and moisture, all affect the reactions of metals tethered to MOFs. In addition, structural parameters of topology, morphology and structuralisation affect the utility of these materials.

Chapter One: Introduction

1.1 Reactions of metal complexes in the solid-state

The chemistry of solid-state materials has been instrumental in the societal development of the human race, from the formation of alloys leading to the bronze and iron ages, to the development of semiconductors and polymers used in the modern era.[7,8] Understanding the atomic structure and the fundamental chemical properties and behaviour of these materials, was not well explored until the 20th century where advancements in characterisation techniques, namely X-ray diffraction, allowed for the great developments in this field.[9] In 1947 Cohn wrote a review on the known reactions of inorganic compounds in the solid-state and proposed that the properties of solids can be divided into structure sensitive and structure insensitive categories.[1] Chemical reactivity, he stated, is very rarely structure insensitive. Thus, chemical reactions performed in the solid-state are not only influenced by the elemental composition, bonding, and chemical environment but also by the material properties such as particle size and shape, surface properties and diffusion. Chemical reactions in the solid-state are therefore controlled by a complex interplay between internal and external factors, as well as the mechanism through which the reaction takes place (Figure 1.1).[10]

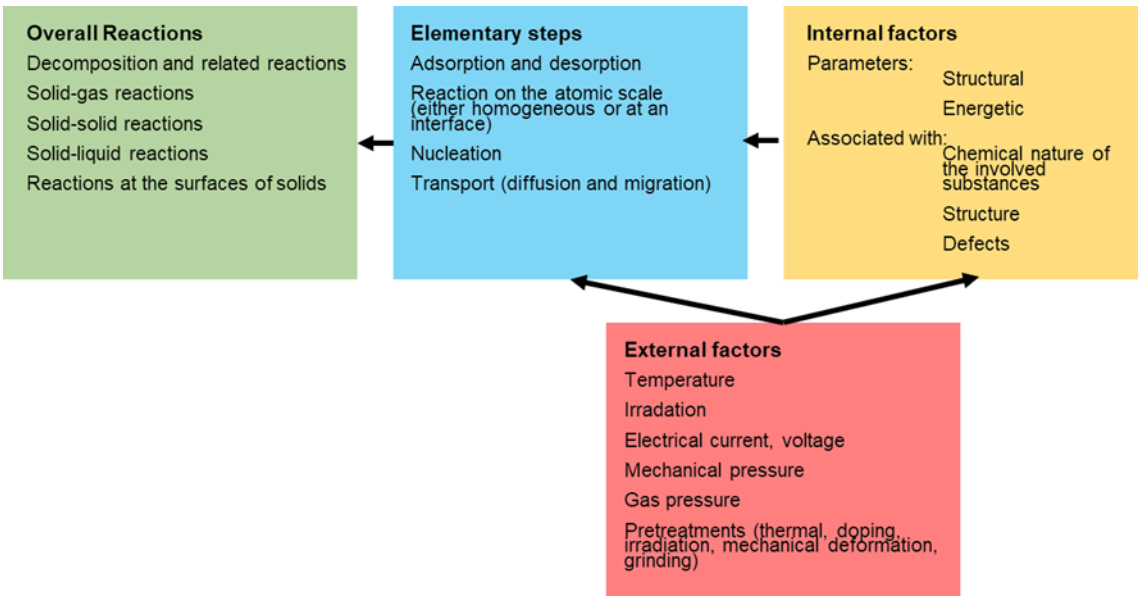

Figure 1.1. General scheme showing the relationships between factors influencing the reactivity of solid-state materials. Figure adapted from Gomes and Dekeyser.[10]

Metals and metal complexes in the solid-state can react in several ways, by reacting with other solid, liquid or gaseous reagents, through decomposition or through polymerization, where a solid starting material is turned into one or more products.[1] While the reactivity and kinetics of simple metal salts have been investigated extensively, those of more complicated coordination complexes and organometallic compounds have not. The solution-state behaviour and activity of these complexes has been well developed over the last century; whereas reactions of well-defined metal complexes and "matrix isolation" of reactive species in the solid-state have received more limited attention,[11] due to the great difficulties involved in both performing the reactions and characterising the reaction process. If these challenges may be overcome, solid-state chemistry provides unique opportunities to study highly reactive species and garner insight into reaction mechanisms. This can lead to improved selectivities, higher yields and access to reactions which are not feasible to study in solution.[12,13] This exploration also extends to mixed-phase reactions, wherein a solid reacts with a liquid or gas phase, such as in heterogeneous catalysis.

The challenges involved in the reactions of solid-state metal complexes can be classified in terms of characterisation, stability, and diffusion. To study these reactions, the limitations of the characterisation techniques must be understood. Single-crystal X-ray diffraction (SCXRD) is the "gold standard" technique for the structural determination of a solid-state material; however, for this to be used for solid-state reactions, several criteria must be met. Crystallinity must be retained, conversion levels should be high, and the complex(es) must be stable over the lifetime of the experiment. In recent years stability has become a lesser concern due to the rapid collection times afforded by synchrotron facilities and modern diffractometers. For retention of crystallinity and single crystal-to-single crystal (SCSC) conversions to occur, long range order must be preserved after the rearrangement of atoms that takes place during a reaction. For molecular crystals, typically only small structural reorganisations are accepted without loss of crystallinity, unless the sites in which the reaction occurs do not affect the integrity of the crystal structure. It has been suggested that, in general, volume changes of *ca.* 15% are the maximum tolerated in transformations of molecular organometallic crystals.[12,14] Although other characterisation methods are available, including spectroscopy (solid-state NMR, IR etc.), microscopy (AFM, TEM, SEM etc.) and diffraction (PXRD, electron and neutron diffraction) techniques, the use of these methods are also

hampered by the general problem of diffusion, as incomplete reactions, and complex reaction pathways resulting in a multitude of different reaction products are generally challenging to characterise. It is, therefore, still advantageous to strive for crystalline materials that can be analysed by SCXRD.

Due to solid-state reactions being largely diffusion dependent, reaction kinetics at the surface of a particle may be vastly different to those at the interior, obfuscating reaction rate analysis.[10] In addition, the particle surface may become passivated by a layer of product, slowing the progress of the reaction, and inhibiting the diffusion of reagents to the interior of the particle. On the other hand, the confined environment of a solid-state structure may aid the stability of reactive metal species, by preventing the loss of weakly bound species, impeding the attack of competing coordinating species (including solvent) and inhibiting the formation of dimers or clusters.[12,13]

Despite these challenges, reactions of well-defined metal complexes in the solid-state have been successfully achieved in a select series of cases. The reversible and controllable addition of gaseous sulfur dioxide to crystalline platinum complexes was demonstrated by van Koten *et al.*[14,15] The tridentate pincer ligands forced the coordination of SO_2 into an unusual conformation, with the crystal structure stabilised by the presence of a β-type bonding network and exhibiting an expansion of *ca.* 15% of the unit cell volume (Figure 1.2a).[14] Although the crystal shape was retained, the single crystal starting material was converted to a multi-crystal composite during the reaction, a process which could be observed to travel inwards from the surface of the crystal.

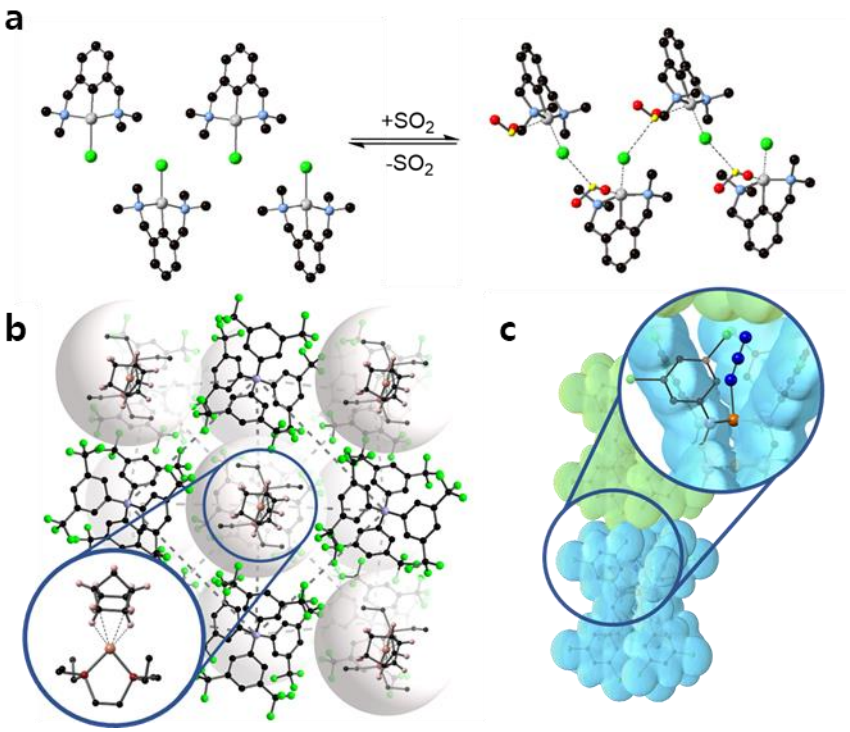

Figure 1.2. Metal based species have been isolated in the solid-state through the use of **a)** conformationally constraining ligands demonstrated by van Koten's platinum pincer complexes coordinating to SO_2 and stabilised by a β-type bonding network;[15] **b)** bulky anions forming a stable structure with cavities in which the cation is confined and preventing the departure of the coordinating alkane;[16] and **c)** sterically bulky ligands forming a reaction pocket in which an azide photo-cleavage can occur without disrupting the crystal lattice.[17,18]

One approach to retaining crystallinity through a solid-state reaction is to use bulky ligands or anions which dominate the packing to create a rigid pseudo-framework within which small movements around the metal centre can be tolerated. This method was used to report, for the first time, the synthesis and isolation of a σ-bonded alkane-rhodium complex in the solid-state (Figure 1.2b).[16] In addition, this complex was shown to be comparatively stable at room-temperature, with a lifetime of several minutes. This was achieved using the bulky tetrakis[3,5-bis(trifluoromethyl)phenyl]borate ($[BAr^F_4]^-$) anion, which forms a stable crystal structure with rhodium cations confined within pockets linked by small channels. These channels were used to introduced gaseous reagents into the crystal but were too small for the alkane products to escape, trapping and stabilising the σ-bound complex such that it could be characterised by SCXRD. This system was used to great effect by Weller *et al.* to explore the consequences of modifying the ligands coordinated to the cation[19–21] and changing rhodium for iridium,[22] as well as demonstrating selective C-H activation[23] and light hydrocarbon catalysis.[24] This method, utilising $BAr^F_4{}^-$ anions, allows highly unstable complexes to be sterically trapped within a crystal structure, thus allowing the characterisation of the resulting

species. The overall robustness of the crystal structure is created by the rigid packing of the bulky anions, allowing for changes in the coordination environment of the metal centre without loss of crystallinity.

A similar approach was taken by Brookhart *et al*, who utilised a bulky, electron-deficient pincer ligand to coordinate to iridium cations, which formed a reaction pocket in which the selective hydrogenation of ethylene (relative to propylene) was catalysed.[13] The crystalline packing of the complexes resulted in the formation of channels running along the *a* and *b* axes, which were filled with crystallographically disordered solvent molecules. These channels were instrumental in allowing the diffusion of gaseous reagents to the catalytic centres. The steric constraints of the reaction pocket prevented the reaction of longer chain alkenes as this was only effective for sites in the interior of the crystal. The surface was intentionally passivated with CO to prevent unselective reactions at catalytic sites on the crystal surface.

Another tactic for retaining crystallinity is to design reactions which require minimal changes in the overall molecular shape, such as those based around photo-initiated rearrangements[25,26] or ligand cleavage.[18] An elegant demonstration of the latter was reported by Powers *et al*, where a ruthenium nitride complex was observed crystallographically from the photo-excitation and subsequent cleavage of an azide ligand to liberate N_2.[18] This process occurred through a single crystal to single crystal (SCSC) transformation which was achieved by the formation of a binding pocket between bulky chloro-substituted phenyl pendent groups on the ancillary ligands, resulting in minimal changes to geometry or coordination environment when the photo-cleavage occurred (Figure 1.2c).

These examples show that to facilitate solid-state reactions of metal complexes or to isolate and characterise interesting reactive species crystallographically, it is important to design crystalline systems with several key features. Primarily, reagents must be able to access the reactive sites. This is most readily achieved by a porous network; however, it has been demonstrated by gas diffusion experiments that small molecules can diffuse through ostensibly non-porous materials.[9] Nevertheless, it has been shown that porosity is crucially important for reaction kinetics, but this must be weighed against some level of confined environment to allow for selectivities that are not available in solution.[19] Therefore a balance needs to be achieved between providing open networks with ready access to the reaction centre and constraining the

environment around said reaction centre to stabilise the species and direct reactivity. This can be compared to the behaviour of enzymes, which provide selective and confined binding sites without sacrificing fast reaction rates.[27]

Secondly, reactions in the solid-state should occur with the least degree of molecular movement, particularly avoiding changes that lead to large modifications of the crystal packing. Lastly, complete conversion must occur to facilitate characterisation, as the solid-state does not allow for traditional isolation and purification processes. Complete conversion, combined with minimised molecular motion, during and after the reaction process, can aid in maintaining crystallinity, thereby allowing investigation by SCXRD.

With open pore networks and tailorable pore chemistry metal-organic frameworks (MOFs) readily meet many of these criteria. Molecular level control of their structural chemistry instilled by a building-block synthetic approach[28] allows for both the tailoring of the pore network to anchor inorganic or organometallic compounds, and controllable access to these reactive sites without significant disruptions to the structure. A number of MOFs have inherent flexibility[29] and can tolerate significant structural changes, particularly when this does not involve the framework components. Furthermore, these design features are, generally, coupled with a high degree of crystallinity that allows for SCXRD to be used to characterise intermediates and products.[30,31] Compared to molecular crystals, MOFs also provide a high degree of chemical and thermal stability[32] allowing for reactions, which might not be tolerated in a molecular crystal, to be stabilised by intermolecular, covalent and coordination bonding and occur without host decomposition.

1.2 Metal-Organic Frameworks

Metal-organic frameworks (MOFs) are a class of materials formed from the coordination of organic linkers with metal nodes to form an extended repeating framework (Figure 1.3). Hoskins and Robson in 1989 were generally accepted as the first to recognise these structures and their potential to form an extensive new category of synthetic materials.[33] These first materials were formed from simple, rigid, uncharged ligands coordinated to lone metal centres and were shown to contain remarkably large

cavities, resulting in crystals which were approximately, by volume, two-thirds liquid (Figure 1.4a).[34] The authors also noted that, with careful selection of reactants, these "infinite", ordered frameworks will form spontaneously in the right conditions and that these new materials had the potential to show unusual properties with many uses.[34]

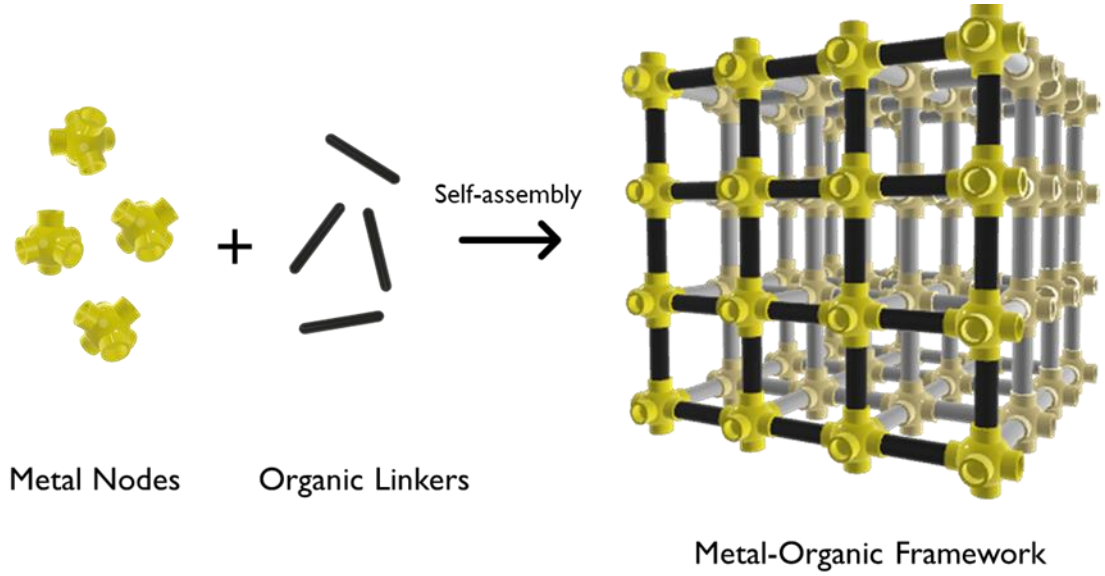

Figure 1.3. Pictorial representation of the formation of metal-organic frameworks from metal node and organic linkers.

The term "metal-organic framework" was first used by Yaghi *et al.* in 1995 when describing a framework material synthesised from cobalt and 1,3,5-benzenetricarboxylic acid (btc) which displayed the ability to selectively host aromatic guest molecules.[35] This material was thermally stable up to 350 °C and was able to undergo several cycles of guest uptake and removal. It was found that anionic ligands such as carboxylates, imidazolates, and pyrazolates were key to forming strong frameworks without counterions taking up space in the pores.[36] The permanent porosity of MOFs was demonstrated by gas absorption analysis of a sample of $[Zn_2(bdc)_2]$ (bdc = 1,4-benzenedicarboxylate) (Figure 1.4b) where all guest molecules had been removed by heating under vacuum.[37] Since then, the field of MOFs has grown exponentially, with a recent (2020) survey of the Cambridge Structural Database showing an incredible 99,075 crystal structures of MOFs deposited in the database, comprising of elements from across the periodic table.[38,39] This tsunami of research interest has been due to not only the almost infinite range of structures which can be synthesised, nor to the many potential applications, but to the way in which previous perceptions of solid-state chemistry have been transformed by MOFs.[36]

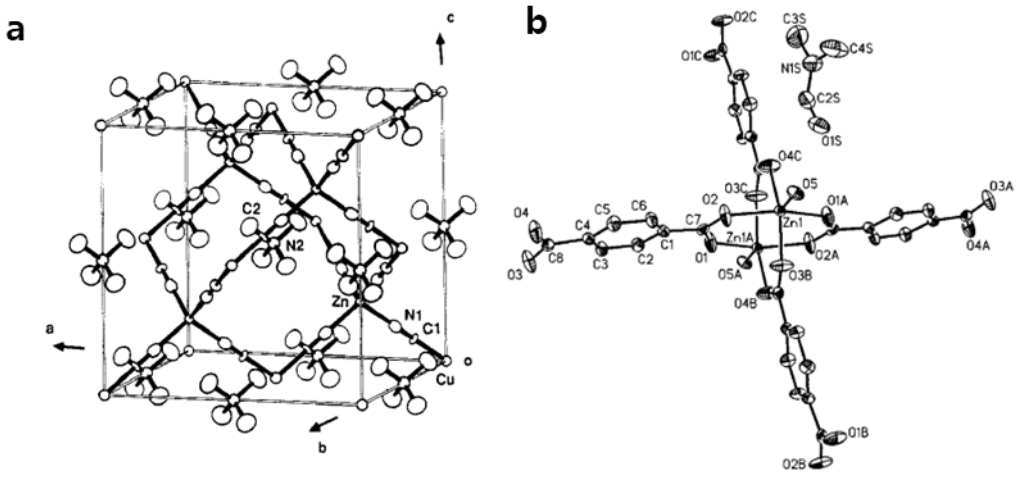

Figure 1.4. Structures of **a)** $[N(CH_3)_4][CuZn(CN)_4]$ reported by Hoskins and Robson in 1990[34] and **b)** $[Zn_2(bdc)_2(H_2O)]\cdot DMF$ used to show gas adsorption in MOFs in 1998.[37]

MOFs may show high permanent porosity and, as a result, have been extensively investigated for applications in gas adsorption and separation, catalysis, and drug delivery.[40,41] However, their open pore networks also offer excellent opportunities as solid-state matrices for the isolation, stabilisation, and structural characterisation of reactive species. This is due to the molecular level control of their structural chemistry that is facilitated by a building-block synthetic approach. For example, the size, shape and chemical functionality of their pore cavities can be tailored to anchor inorganic or organometallic compounds to their framework,[30,31] isolate guests via supramolecular forces or confine molecules through steric effects.[32] The periodic nature of the host framework isolates reactive metal sites, thereby negating the need to use sterically demanding ligands to prevent ligand disproportionation, decomposition and nanoparticle formation; thus, similar to matrix isolation methods the reactive entity is predominantly stabilised through kinetic factors. These design features are, generally, coupled with a high degree of crystallinity that allows for X-ray diffraction methods to be employed as a technique for the structural elucidation of guests.[33–36]

In short, MOFs are synthesised via the self-assembly of metal salts or clusters with organic ligands in solution or under solvothermal, hydrothermal, microwave assisted, solvent assisted, mechanochemical or electrochemical synthetic conditions. They have potential porosity and are highly modifiable and often crystalline making them ideal candidates for the study of reactive inorganic or organometallic complexes in the solid-state.

1.3 Nomenclature and terminology

Naming conventions for MOFs and the broader category of coordination polymers are not well adhered to in the literature. Recommendations to IUPAC in 2013 stated that a coordination polymer is "a coordination compound with repeating coordination entities extending in 1, 2, or 3 dimensions" while a MOF is a "coordination network with organic ligands containing potential voids".[42] Thus, in this work, the term "MOF" shall be used for coordination polymers with potential porosity (also called porous coordination polymers or PCPs in the literature), while coordination polymer or CP shall be used for those without potential porosity. Many MOFs in the literature are referred to by a three- or four-letter code and number referencing the institute where the MOF was first made (e.g., UiO-66 (Universitetet i Oslo),[43] MIL-53 (Materiaux de l'Institut Lavoisier)[44] etc.). Herein, these names shall be used where applicable or, if not named as such, described by its metal and ligand components with the coordination entity in square brackets with anions after the brackets and any solvent or guest molecules after the brackets and anions and separated by a middle dot "·". For example, MnMOF[$Mn(CO)_3Br$]·THF, indicates that the metal-organic framework known as MnMOF contains the [$Mn(CO)_3Br$] complex, and the compound is solvated with THF. Post-synthetic modification (PSM) is the direct chemical modification of a solid MOF, without decomposition and reformation of the MOF crystals.[45] The term "metalation" refers to a PSM process in which a metal ion is introduced to chemically bond to the MOF framework and may also be abbreviated to PSMet. Though widely used, the terms "reactive" and "stable" are not well defined. In general, a reactive species might react vigorously or release substantial energy upon reaction; however, this definition will be broadened to include species which are difficult to isolate and characterise using routine methods as discrete entities due to short lifespans, propensity for dimerization, or readiness to undergo isomerisation or ligand exchange. In contrast the term "stable" will be used to refer to those species which can be characterised as discrete entities using routine methods.

1.4 Isolating reactive species in MOFs

Examining the structures of reactive molecular species can provide invaluable insights into the mechanisms of bond activation and formation which are essential to fields of fundamental scientific and commercial interest, such as chemical synthesis and catalysis.[46–49] Characterising, *in situ*, the reactive intermediates which form from ligand dissociation processes, which are the active forms of many homogeneous catalysts, is a difficult proposition due to their short lifetimes in solution.[50,51] This has been achieved by extending the lifetimes of the reactive species by kinetic trapping in low-temperature matrix isolation[52,53] or by interrogating the compounds at ultra-fast time scales (nano-, pico- and femto-seconds) using laser-pulsed time-resolved spectroscopic techniques.[54–57] Another method for enhancing the stabilities of these species, in order to structurally characterise them, is through encapsulation within the cavity of a host.[58–60] The earliest example of this was by Cram *et al* in 1991, who utilised a hemicarcerand as a host to isolate cyclobutadiene.[61] This was achieved by the photochemical transformation of α-pyrone inside the cavity of the carcerand, which produced a constrained environment in which cyclobutadiene was formed and stable at room temperature. In later years, discrete molecular cages[62] were shown to also contain the confined microenvironment conducive for stabilising reactive organic (Figure 1.5),[63] inorganic,[64] and organometallic species.[5,65]

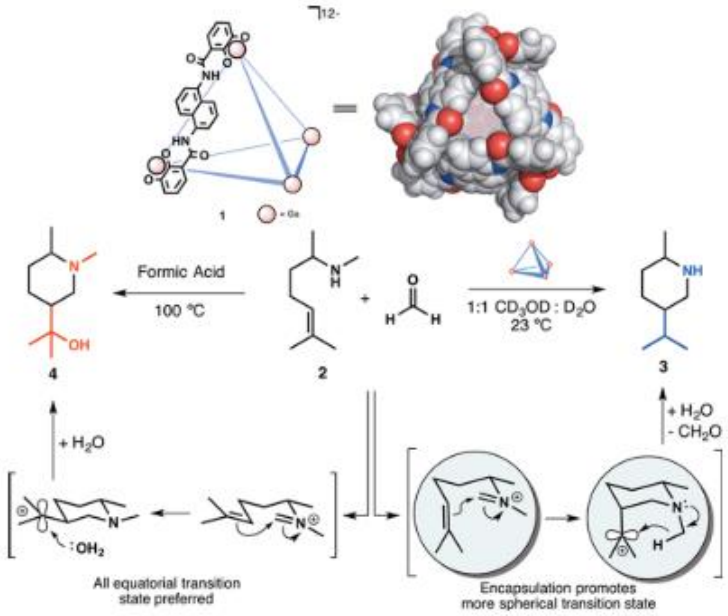

Figure 1.5. Metal-organic cage $[Ga_4(L)_6]^{12-}$ {H_4L = N,N'-(naphthalene-1,5-diyl)bis(2,3-dihydroxybenzamide)} in which selective organic transformations may occur.[63]

Research in this field has strived to comprehend and control the supramolecular interactions that are behind the specific kinetic and thermodynamic factors that result in guest stabilisation. Such studies have led to the synthesis of new catalysts which mimic the selectivity and efficiency of enzymes.[63,66–68]

As discussed earlier, MOFs are ideal candidates to act as isolation matrices for the study of metal complexes that are unstable in solution. The size, shape and chemical functionality of their pores can be tuned to confine guests via steric effects, intermolecular forces, or chemical bonding.[69–71] The periodic nature of the host framework negates the need for sterically demanding ligands to prevent disproportionation, decomposition, and aggregation by isolating the reactive sites. Therefore, MOFs behave in a similar manner to matrix isolation methods in that they trap the reactive species predominantly through kinetic control. These features, combined with their generally highly crystalline structures, allow for X-ray diffraction methods to be used to structurally interrogate guests.[31,72–74] Single crystal X-ray diffraction experiments have been used to show in MOFs the initial stages of gas adsorption,[75] binding sites of substrates,[76] and the structures of molecules adsorbed from solution.[30,72,74,77]

Unlike the molecular solid-state materials discussed in Section 1.1, in which porosity has yet to be reliably controlled or predicted, the well explored porosity of MOFs allows for control over guest diffusion, allowing for the solid-state environment to be fully exploited. The means by which reactive complexes have been isolated in MOF pores have broadly fallen into four categories (Figure 1.6), namely:

a) Modification of the metal node, for example PSMet of the node to attach a metal complex or cation metathesis to replace a node metal ion with one of desirable reactivity.

b) Growth or encapsulation of metal nanoparticles, clusters, or complexes within the pores.

c) Post-synthetic metalation at a pre-installed vacant linker binding site, or a binding site which is exposed post-synthetically.

d) Pre-metalation of the organic linker before construction of the MOF framework. This approach often requires subsequent chemistry to activate the metal.

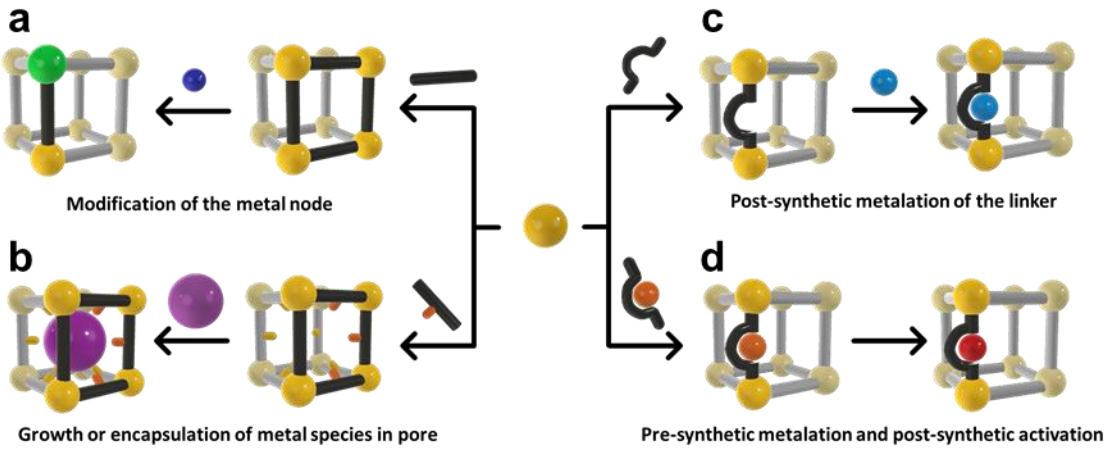

Figure 1.6. Matrix isolation of metal compounds in MOFs can be achieved via; **a)** node related PSM to facilitate attachment of a species, or complete cation metathesis/PSM; **b)** utilising the pore chemistry to stabilise molecular complexes or subnanometre metal clusters; **c)** PSMet at preinstalled linkers or those exposed in the MOF post-synthetically; and **d)** installation of a pre-metalated linker and subsequent chemistry to reveal reactivity.[17]

1.4.2 Isolation at MOF nodes and within MOF pores

Although the isolation of reactive metals at MOF nodes and pores is not the focus of this thesis, examples of these methods will be briefly outlined to give context for the research directions undertaken in this work. These methods (a and b above) are distinct to those which utilise binding sites on MOF ligands (methods c and d), and hence will be discussed separately. The metal nodes of MOFs have been shown to act as sites for anchoring unusual species through substitution of the metal cations[78,79] or through binding of molecules to the existing nodes (Figure 1.7a and b). [80] The MOF nodes have also been used as tethering sites for appending metal complexes to the existing node (Figure 1.7c).[81] Although structures have been achieved that were unable to be accessed in solution, obtaining structural insights into these species is difficult due to the metal nodes often occupying high symmetry sites within crystals. This results in crystallographic disorder where the position of species of interest overlaps with the atoms of the original node. In many cases, a combination of spectroscopic and scattering techniques was used to gain structural insight instead of SCXRD.

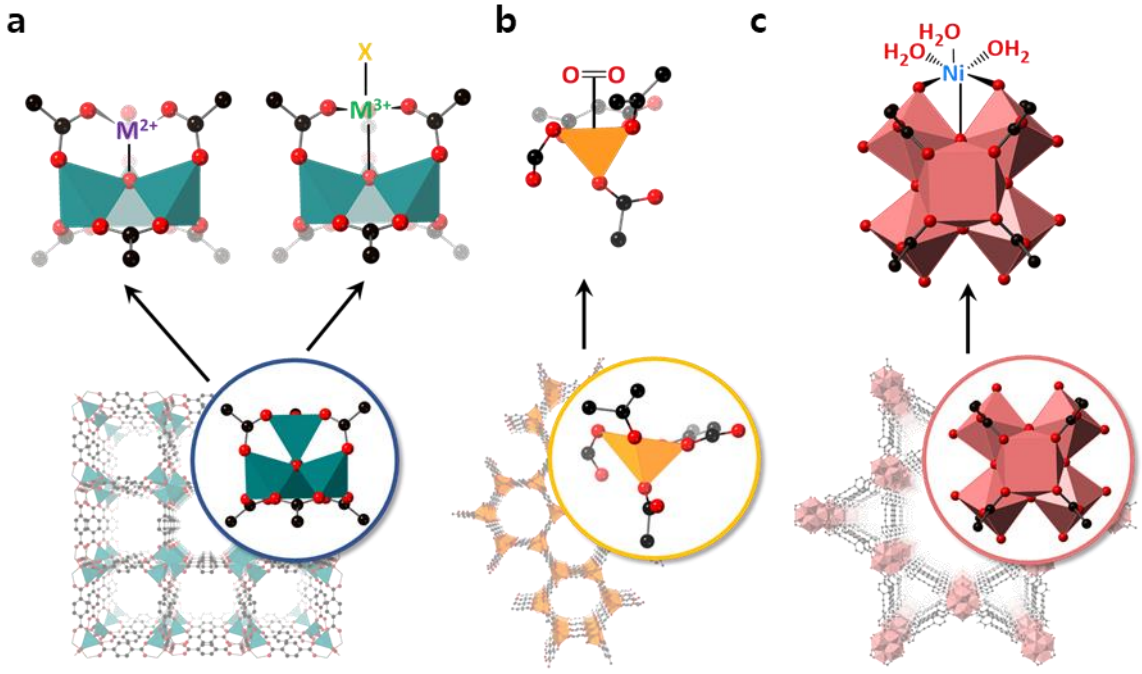

Figure 1.7. Simplified representations of matrix isolation at the MOF nodes including: **a)** selective cation exchange of the Zn_4O nodes of MOF-5 with a range of transition metals in the +2 and +3 oxidation states, allowing the formation of unusual coordination environments (Zn – teal; O – red; C – black);[82] **b)** the formation of coordinatively unsaturated nodes in MOF-74 allowing oxygen binding at low temperatures (Fe – yellow; O – red; C – black);[80] **c)** and the introduction of nickel atoms at the zirconium nodes of NU-1000 by atomic layer deposition. (Zr – pink; O – red; C – black)[17,83]

MOF pores have been used to a great extent to host a vast array of guests, from gases, drug molecules, polymers and metal clusters and complexes, to proteins and enzymes. Structural characterisation of those guests has been investigated to a lesser extent but still with great impact, most notably through the "crystalline sponge" method. This method employs the pores of MOFs to hold and order the guest molecules, and has enabled the structural characterisation of a range of organic molecules, including those susceptible to decomposition, without the need for growing single crystals of these compounds.[30,72,74,84–99] In this method, the pore size, shape, and chemical functionality can be modified to better stabilise the guest molecule, although structural determination by SCXRD is still non-trivial due to the degrees of freedom for the guest within the pore. Metal complexes and clusters have also been studied within MOF pores using direct impregnation, "cartridge" or "ship-in-a-bottle" approaches. The cartridge method involves attaching the complex of interest to a "cartridge" which directs the binding in the pore,[5] while the ship-in-a-bottle approach relies on the assembly of the active species in the MOF pore.[100] For the structural characterisation of pore bound species to be effective, the design of both the host and guest must be considered to achieve the stabilisation, high loadings and positioning effects needed to achieve the long range order necessary for characterisation by SCXRD.

1.4.3 Isolation at MOF linkers

The metalation of MOF linkers (methods c and d) to append reactive inorganic or organometallic complexes has been explored extensively through a variety of approaches. Most of these approaches either employ nitrogen-containing heterocycles, carbenes or phosphines to bind the metal of interest. Nitrogen-containing heterocycles coordinated to catalytically active metals are the most numerous in the MOF literature, with the most prevalent ligands being those based around 2,2′-bipyridine. 2,2′-Bipyridine (2,2′-bipy) is a neutral, chelating ligand widely used in coordination chemistry, and has been identified as the most widely used ligand.[101] The chelating ability of 2,2′-bipy provides strong coordination to metals of a range of sizes and coordination environments, whilst still allowing for redox activity. As a result of these versatile properties, 2,2′-bipy complexes of transition metals are widely used as catalysts,

for example in the electrochemical reduction of CO_2 (Mn, Rh, Re)[102] and cross-coupling reactions (Pd),[103] amongst others.[104,105]

Given that 2,2′-bipy is such an effective and extensively studied ligand it is, therefore, unsurprising that this moiety has been widely used to tether metal complexes to MOFs. Importantly, such metalated MOFs can be used to illustrate both the pre-synthetic metalation and post-synthetic metalation pathways to appending metal complexes to MOFs. The pre-synthetic metalation approach entails preparing a metal complex that is suitably functionalised with groups that are capable of binding further metals in an *exo*-dentate fashion, such that when combined with an appropriate metal source a MOF is formed. Post-synthetic metalation involves the initial synthesis of a MOF, which contains vacant binding sites that can be subsequently metalated with a suitable species, introduced via diffusion into the MOF. Each approach has its advantages and disadvantages.[17]

Pre-synthetic metalation requires the metalated ligand to exhibit sufficient stability so that it survives the MOF forming reaction but, when successful, this approach typically leads to high occupancy of the appended complex. In addition, this approach requires the ligand to retain *exo*-binding sites available for the subsequent MOF forming reaction. Common examples include using 2,2′-bipyridine-5,5′-dicarboxylic acid or 2,2′-bipyridine-4,4′-dicarboxylic acid, both of which allow the tethering of the metal complex at the chelating bipyridine site while leaving the carboxylates free to serve as ligands in MOF formation. A range of 2,2′-bipy metal complexes have been successfully incorporated into MOFs by this method, including [M(2,2′-bipy)$_3$] {M = Ru(II), Os(II)},[106] [M(2,2′-bipy)$_2$(CN)$_2$] {M = Ru(II), Os(II)},[107,108] [Ir(2,2′-bipy)(Cp*)Cl],[109] [Ir(2,2′-bipy)Cl$_3$(THF)],[110] or 2-phenylpyridine (ppy) complexes, such as [Ir(ppy)$_2$(bpy)]$^{+}$[111] and [Ir(Cp*)(ppy)].[112,113] This approach was also used to study the photochemical behaviour of [M(2,2′-bipy)(CO)$_3$X] complexes (M= Mn(I) or Rh(I), X = Br$^-$or Cl$^-$) in Mn(II), Li(I) or Cu(II) MOFs, which will be discussed further in Chapter 2.[26,114–116]

The group of Lin have exploited this metalation strategy[106–111,113] but have also used post-synthetic metalation methods with great success in the UiO family of MOFs. The UiO (Universitetet i Oslo) family of MOFs exhibit highly thermal and chemical stability and are based on [($Zr_6(OH)_4O_4)^{12+}$] nodes connected by linear dicarboxylate linkers including biphenyl-4,4′-dicarboxylate (UiO-67) and terphenyl-4,4′′′′-dicarboxylate (UiO-68) (Figure 1.8).[109,110,113,117,118] 2,2′-bipy moieties can be incorporated into linkers of

varying lengths and then used to prepare UiO-type MOFs. These MOFs can then be post-synthetically metalated to bind isolated iridium and palladium catalysts. For example, [Ir(III)$(Cl)_3$(THF)] was bound to the chelating 2,2′-bipy site in a UiO-67 analogue containing a mixture of 2,2′-bipyridine-5,5′-dicarboxylate and biphenyl-4,4′-dicarboxylate ligands. A combination of ligands with *endo*-dentate binding sites (2,2′-bipyridine-5,5′-dicarboxylate) and only *exo*-dentate binding sites (biphenyl-4,4′-dicarboxylate) was employed to prevent steric crowding of the MOF pores and hence catalyst loadings were deliberately lowered to 2.4-3.8 wt %, which enhanced catalytic efficiency by maintaining diffusion to the active sites. These MOFs were used to catalyse the hydrogenation of CO_2 and afforded turnover numbers (TONs) as high as 6149 in 15 hrs and turnover frequency (TOF) of up to 410 h^{-1}, much higher than the analogous homogeneous catalyst which displayed a TOF <1 hr^{-1}.[110]

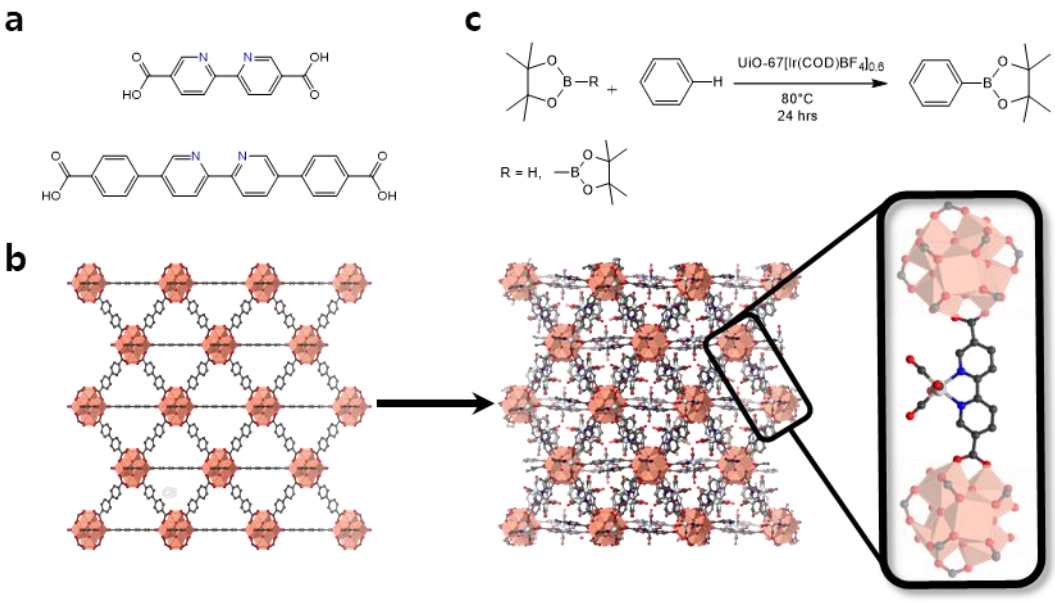

Figure 1.8. Analogues of UiO-67 that incorporate a 2,2'-bipy binding site have been post-synthetically metalated with a variety of metals (Co, Cu, Fe, Ir or Cr) to afford MOFs with site-isolated metal complexes, some of which perform C-H borylation catalysis.[119] **a)** Examples of 2,2'-bipy containing ligands, **b)** post-synthetic metalation with $Cr(CO)_6$ and **c)** C-H borylation reactions catalysed by UiO-67[Ir(cod])$BF_4]_{0.6}$ (Zr, pink; Cr, light grey; C- grey; O, red; N-blue).

Extending the 2,2′-bipyridine core with terminal benzoic acid or alkanoic acid groups produced similar, isotopological, MOFs which were demonstrated to catalyse the C-H activation of aryl ketones, aldehydes and arenes after post-synthetic metalation with iridium complexes.[109] For these systems, however, although the metal catalysts were isolated and stabilised by the MOF, the characterisation of the catalytic metal centres was challenging due to small crystal sizes, high symmetry space groups, low

occupancies of the bipyridine sites and crystallographic disorder preventing analysis by SCXRD. Instead, the catalysts were characterised by a combination of methods including powder X-ray diffraction (PXRD), which demonstrated that the bipyridine MOFs were isostructural to their biphenyl counterparts, energy-dispersive X-ray scanning electron microscopy (EDX-SEM) and transmission electron microscopy (TEM) to determine the elemental ratios and spatial distribution of elements within the crystallites and extended X-ray absorption fine structure (EXAFS)/X-ray absorption near edge structure (XANES) to probe the coordination environments of the metals.

In a few select cases, characterisation of metal catalysts in UiO-type MOFs by SCXRD has been reported. Long and co-workers introduced Co, Cu, Fe, Ir and Cr to UiO-67[2,2′-bipy] by post-synthetic metalation techniques to give near quantitative loadings (Figure 1.8b).[119] SCXRD studies revealed that the metalation process caused a slight distortion of the zirconium nodes, leading to a lowering of crystallographic symmetry. The structures also exhibited rotational disorder in addition to disordered anions and solvent molecules. These factors, coupled with weak scattering, meant that the authors could not fully model the coordination environment of the tethered complex. The extended coordination sphere of the catalytic metals was also challenging to resolve but soaking the crystals in different solvents, leading to different occupancy of the MOF pores, was found to resolve the disorder in some cases, probably due to steric restrictions of rotational freedom due to solvent packing effects. The catalytic activity of a tethered Ir complex in facilitating arene C-H borylation reactions was investigated (Figure 1.8c). To prevent steric crowding inhibiting transport of reagents to the catalytic centres, a sample with only 10% metalation was used, and a modest TOF of 860 h^{-1} was recorded. Importantly the catalyst could be recycled over 5 catalytic cycles without noticeable loss of activity.[119]

Another seminal example of utilising the 2,2′-bipyridine-5,5′-dicarboxylate ($bipydc^{2-}$) moiety to isolate homogeneous catalysts was demonstrated in MOF-253 ([Al(OH)(bipydc)]).[120] This MOF contains uncoordinated bipyridine sites, open channels and high porosity and can be post-synthetically metalated. Palladium chloride ($PdCl_2$) was introduced to the 2,2′-bipy sites with an overall 83% loading, and the coordination environment studied by PXRD and EXAFS. These investigations confirmed that the appended complex was structurally analogous to the molecular analogue, [Pd(2,2′-bipy)Cl_2]. Subsequently, MOF-253 was used by myriad researchers to isolate metal

complexes for catalysis, and as such only a few examples will be described. Li and co-workers incorporated copper iodide (CuI) into MOF-253 and demonstrated the catalytic coupling of alcohols and phenols with aryl halides without the need for phosphine ligands.[121] Copper(I) loadings of 50% were used to achieve high yields, with low leaching and little loss of activity after 3 cycles. Characterisation was achieved by a combination of PXRD and X-ray photoelectron spectroscopy (XPS), where a shift in the binding energy of the N 1s peak, by approx. +1.2 eV in MOF-253[CuI], was observed. This indicated a decrease in the electron density on the 2,2′-bipy nitrogen atoms due to strong coordination to copper.

Post-synthetic metalation in flexible, lower symmetry MOFs has been demonstrated to be an effective approach to study the coordination environment of the reaction intermediates of tethered metal complexes. MnMOF ($[Mn_3(L)_2L']$) is one such material, where L = bis(4-carboxyphenyl-3,5-dimethyl-pyrazol-1-yl)methane) and L′ contains a vacant chelating bis-pyrazole site linked by a flexible methylene bridge (Figure 1.9).[122] A range of transition metals including Co, Fe, Rh, Mn and Cu have been installed into the L′ site by post-synthetic metalation procedures.[122–125] The catalytic carbonylation reaction of MeX (X = I, Br) by MnMOF[$Rh(CO)_2$] was followed by SCXRD, with the coordination environment of key reaction intermediates isolated and characterised.[125] While the catalytic performance was poorer, in this case, than molecular equivalents, the study demonstrates the ability for a MOF to not only site-isolate metal complexes, but to enhance our chemical understanding of catalytic processes by direct observation of the coordination environments of active catalysts and intermediates. A similar approach was taken using the same MnMOF metalated with [$Mn(CO)_3(N_3)$] to demonstrate a site selective triazole formation from dialkynes (Figure 1.9b and c).[126] The spatial distribution of the metal centres along the pores of the MOF prevented a second cyclization reaction occurring for short chain dialkynes, while longer chain reactants could bridge the distance between adjacent metal centres. This study will be discussed further in Chapter 4.

Distribution of reactive metal centres, fixed in specific positions uniformly throughout a MOF, is an underutilised and yet powerful tool for increasing reaction efficiency and for accessing selectivities and binding modes not available in analogous solution or molecular solid-state materials.

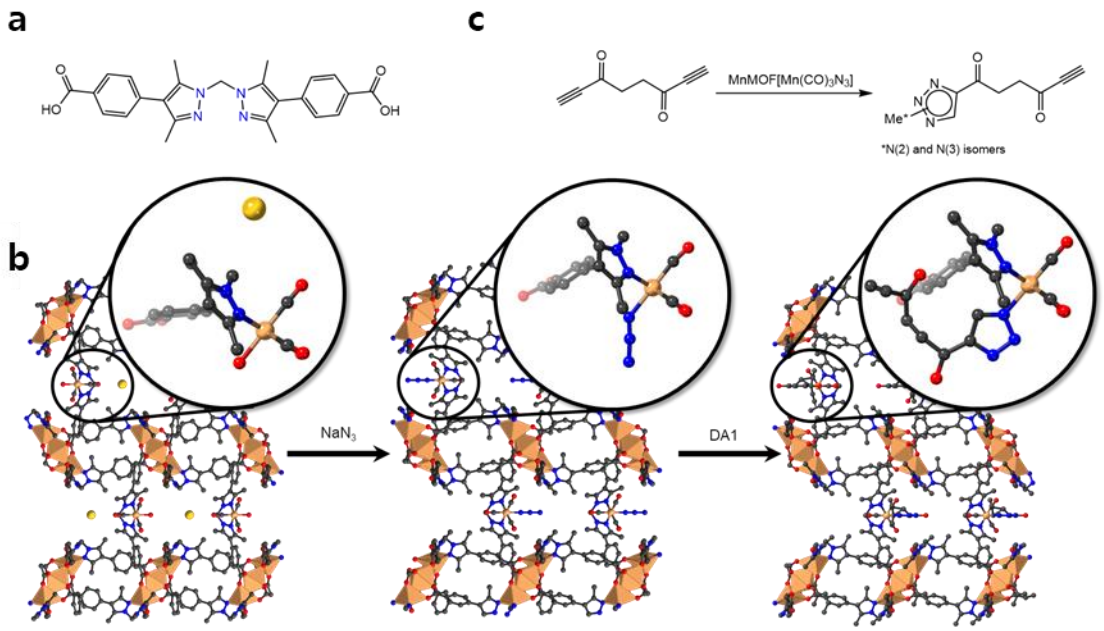

Figure 1.9. a) Bridging dicarboxylate ligand bearing a bis-pyrazole coordination site; **b**) MnMOF binding a $[Mn(CO)_3(OH_2)]^+$group which can be transformed a SCSC manner to prepare $[Mn(CO)_3(N_3)]$. This can be reacted with an activated alkyne (DA1 = 1,7-octadiyne-3,6-dione) within the MOF, forming a bound triazole species; **c)** the cycloaddition reaction performed by the tethered Mn complex.[126] (Mn, beige; Br, yellow; C, grey; O, red; N, blue)

A one-pot MOF formation and metalation reaction was demonstrated by Dincă *et al.* who produced copper(I) scorpionate-like complexes appended to a zirconium framework.[127] The combination of 1,1′,1′′-methanetriyltris-(3,5-dimethyl-1H-pyrazole-4-carboxylate) ligands with zirconium oxychloride and copper(I) iodide under solvothermal conditions produced a porous 3D MOF, based around $[Zr_6O_4(OH)_4]$ clusters. The flexibility of the ligand prevented the formation of the MOF without the presence of the CuI, which coordinated to the tridentate pyrazole binding sites of the ligand. This 'locked' the flexible ligand to create a rigid linker, allowing the formation of the desired MOF. The lability of copper(I) then enabled the MOF to be readily de-metalated post-synthetically, and re-metalated with other metals of interest. Although the crystals were too small for SCXRD, the structure was determined by Rietveld analysis of PXRD data which revealed an accessible pore diameter of 8.3 Å. The Cu(I)-containing MOF was used to catalyse the cyclopropanation of olefins and the insertion of carbene into C-H bonds in cyclohexane. The latter reaction achieved yields of 67%, greater than the 30% achieved by the equivalent homogeneous catalyst under comparable conditions and recyclability testing revealed no appreciable loss of activity after 5 cycles.

The discussion of N-heterocyclic ligands for site-isolating metals in MOFs would not be complete without mention of porphyrins. Their behaviour, however, is notably different to the other examples discussed, due to their extensive delocalised network of π electrons. A range of MOFs have been synthesised to incorporate porphyrin components, which can bind to metals and demonstrate an extensive range of catalytic and biomimetic functions.[128] One study of note involves PCN-224, a zirconium-based MOF with a tetracarboxyphenylporphyrin bridging ligand.[129] This ligand underwent post-synthetic metalation with $FeBr_2$ to give a metalloporphyrin, analogous to heme-proteins contained in biological systems (Figure 1.10a). This study reported the first example of a coordinatively unsaturated heme in a MOF. Interestingly, this species could subsequently bind to O_2, giving a 5-coordinate complex which was observable by SCXRD (Figure 1.10b). The structural characterisation of this complex was of great interest, as previously, in solution, this species had only been observed transiently. Once again, a MOF allowed the trapping and stabilisation of an intermediate unable to be achieved in solution phase.

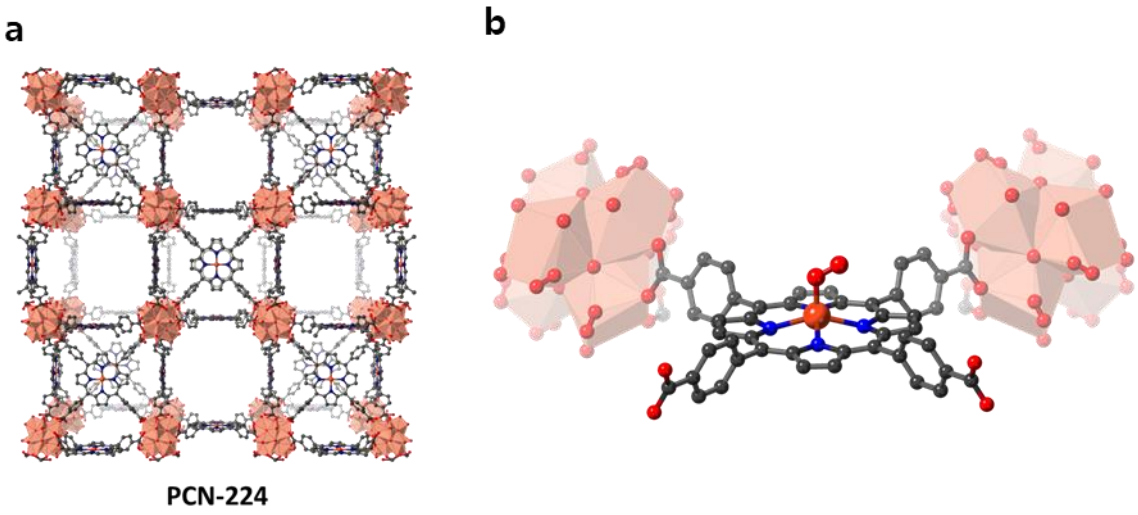

Figure 1.10. View of **a)** PCN-224, containing the tetracarboxyphenylporphyrin bridging ligand; **b)** Post-synthetic metalation with $FeBr_2$ yielded a coordinatively unsaturated heme-like group within the MOF which subsequently bound O_2 to form a 5-coordinate species.[129] (Zr, pink; Fe, orange; C, grey; O, red; N, blue)**.**

Post-synthetic metalation of MOF linkers is a powerful tool for incorporating site-isolated metal complexes into MOFs; however, there are some stipulations. Post-synthetic metalation requires a metal precursor to diffuse through the MOF to the binding sites, therefore requiring an open and interconnected pore network and, although the parent MOF can often be more readily prepared, it can be challenging to achieve post-synthetic metalation with high occupancies. The types of binding sites can

also be limiting, as the success of this method relies on vacant sites being available after the MOF is synthesised. Despite these challenges, when a MOF with available binding sites and the ability to achieve high post-synthetic metalation can be prepared, great successes have been achieved in studying reactive intermediates and accessing unusual structures.

1.5 Advantages and challenges of using MOFs for isolating reactive species

Reactive metal species have been isolated and characterised in a range of MOFs, utilising the metal nodes, pore space or organic linkers to stabilise complexes or clusters and allow for the exploration and exploitation of unusual compounds. Significant scope, however, remains to develop MOFs as stabilising matrices. In the numerous examples presented in Section 1.4, MOF crystallinity was shown to be a key feature to allow precise structural determination of species that have been otherwise challenging to interpret through spectroscopic methods. In many of those cases, the impetus behind the generation of the reactive moieties was to enhance the performance of a specific characteristic such as catalysis or gas adsorption, but the fundamental insights that these systems may offer should not be ignored. Metal-based reaction mechanisms are essential in heterogeneous catalysis, and the confined environment within a MOF pore allows for all aspects of such a reaction to be highly controlled.

Using MOFs to isolate reactive species is still highly challenging. For this strategy to be most effective, crystallinity must be retained. Thus, structural flexibility is needed to allow for changes in bond lengths and coordination geometries of metal atoms. The MOF must also be adequately stable under the reaction conditions and finding this combination of stability and flexibility is not trivial, despite the large library of MOFs available. The number of MOFs available for these studies is limited further by a preference for low crystallographic symmetry (to permit structural elucidation by SCXRD) and a low density of guest sites to mitigate steric crowding.

In assessing the four methods of isolating metal complexes in MOFs described in Sections 1.4.2 and 1.4.3, pre- and post-synthetic metalation of MOF linkers stand out as the most successful for structural characterisation by SCXRD. Reactions at metal nodes were effective at installing a wide variety of species, with extensive opportunities

for subsequent ligand coordination and substitution; however, the nature of these sites is that they often occupy high symmetry crystallographic positions and substitutions are rarely homogeneous across the sample. These factors result in the characterisation of these materials by SCXRD to be difficult. Isolating guests within MOF pores has been comprehensively explored in the literature but has only just begun to be developed for metal-based species. In these systems the pore environment must be carefully considered to enable to SCXRD to be used without prohibitive amounts of disorder. While this is difficult to design experimentally, the use of MOF databases[130] and theoretical calculations[131] as well as the development of new computational methods to screen MOFs[132] may soon allow this technique to be more universally applicable; however, current methods rely on trial-and-error.

For linker-bound metal species the density of the sites in the MOF is a key consideration and one in which the answer differs based on the intended application. For successful structural characterisation, long-range order is necessary, meaning that all available sites should be occupied to gain the best data. This can be disadvantageous if full occupancy causes steric crowding and inhibition of diffusion within the crystal. Some studies using low loadings of guest metal have achieved high catalytic efficiencies, but in turn, structural interrogations were hindered. MnMOF, discussed in Section 1.4.3, enables post-synthetic metalation at high loadings without steric impediments due to the availability of only 1 in 3 of the linkers in the MOF as metalation sites. Conversely, this may be a disadvantage if the intention is to have a high loading of guests in the MOF, which will be explored in Chapter 3 in the utilisation of MOFs as reservoirs of gases for chemical synthesis. The flexibility of the MnMOF linkers also allows for the binding of a range of guests of different van der Waals radii and coordination environments, making it an ideal platform for the site isolation and structural characterisation of active metal complexes.

The incorporation of reactive metal species into solid, porous supports such as MOFs offer many advantages over their soluble, solution-based counterparts. Several strategies may be employed to achieve this goal; however, some fundamental requirements are common among them, namely that the MOF must be stable to the reaction conditions, and the binding site(s) must be accessible for the species of interest.

Clearly, it is rare for a single characterisation technique to be sufficient to fully appreciate a system. As MOFs are generally crystalline materials, SCXRD remains a 'gold-

standard' for their characterisation. Where possible SCXRD can give unprecedented insight into reaction processes, but this is not always viable. Even when SCXRD is possible, the use of other techniques, for example spectroscopic analysis, can give into insight into the bulk material and to processes which occur on other timescales than those typically used for diffraction analysis. It is evident that to fully appreciate a reaction process within a MOF it is often necessary to employ multiple characterisation techniques.

Ultimately there are clear advantages in anchoring reactive metal complexes, and particularly those capable of catalysing reactions, to the interior of MOF pores. MOF tethered metal complexes and clusters can provide insight into reaction processes or simply deliver enhanced performance, thereby providing significant advantages over alternative approaches. Returning to the challenges of characterisation, diffusion and stability, examined in Section 1.1, for performing reactions on inorganic or organometallic species in the solid-state, the use of MOFs addresses all said challenges. MOFs with open pore networks allow for diffusion through the crystal, while the size of these channels can be modified to allow for selectivity. The presence of long-range order makes many MOFs suitable to be studied by diffraction techniques including SCXRD and PXRD, and the use of multiple complementary techniques has been demonstrated to provide deep levels of structural insights. Finally, the ability to tune the chemical and physical properties of pore environments in MOFs has allowed for the stabilisation of reactive species that have not been able to be trapped in solution.

1.6 MOFs as reservoirs for the controlled release of active compounds

While the stability of MOFs and their guests was cited in Section 1.5 as key to successful site isolation and characterisation, stability is not always advantageous. Many MOFs have low chemical and aqueous stability due to the labile nature of the coordination bonds between their metal nodes and organic linkers.[133] While this has been seen as a drawback in certain industrial applications, this behaviour can also be a desirable trait when considering MOFs as solid-state reservoirs of useful organic and inorganic components. This approach had led MOFs to be considered for innovative applications in drug delivery,[134] gas storage and release,[135] food and perfume

industries[136,137] and agrichemicals.[138] Three main methods have been used to pursue these results; namely where the desired compound is a structural component of the MOF, which is released upon decomposition of the framework (Figure 1.11a),[139] the compound is encapsulated within the MOF pores and released through diffusion or as a result of external stimuli (Figure 1.11b),[140,141] or the compound is chemically bound to the MOF (either to the ligand or node) and is released in response to a physical or chemical trigger (Figure 1.11c).[142–144]

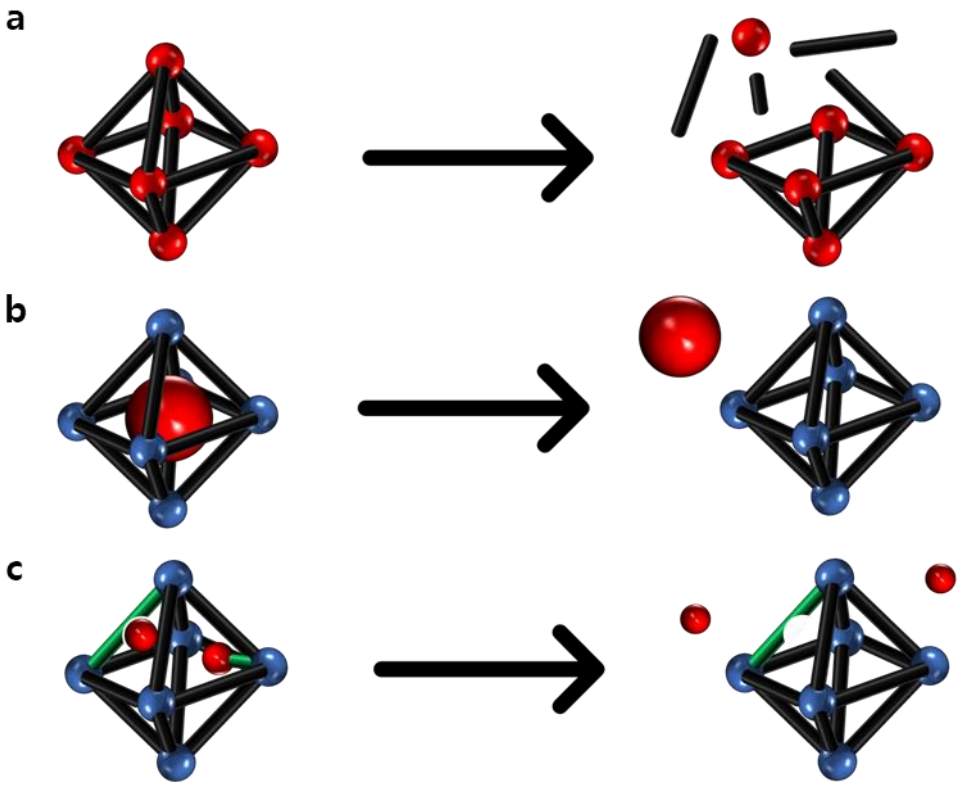

Figure 1.11. General methods by which MOFs can be used as reservoirs for the release of useful compounds **a)** when the desired compound is an integral component of the MOF and is released by framework decomposition, **b)** the compound is encapsulated within the MOF pores and is released through diffusion of external stimuli and **c)** the desired compound is chemically bound to the MOF and is released through the application of a physical or chemical trigger.

These approaches have been the most developed in the field of drug delivery, where MOFs have been employed to store and release anticancer, antibacterial, analgesic and chelating drugs, among others.[134,145] Synergistic therapeutic effects can also be accessed through the incorporation of multiple active components into or with the MOF, either as structural or guest components.[146] Selected examples are outlined below.

The controlled release of nitric oxide (NO) gas from the MOF HKUST-1, $[Cu_3(btc)_2]$ (btc = benzene-1,3,5-tricarboxylate), incorporated into a polycaprolactone/gelatine matrix was demonstrated by Chen et al to promote the regeneration of injured tendon fibres both *in vitro* and *in vivo*.[147] In this system the gaseous NO was encapsulated within the MOF pores, which had been post-synthetically modified to contain secondary amino groups to aid in the binding of the guest (Figure 12a). The loaded MOF was then incorporated with the polymer/gelatine scaffold and electrospun into fibres (Figure 1.12b), to aid in the healing of the tendon by mimicking the organisation of natural collagen fibres (Figure 1.12c). The release of NO from the MOF was then studied, and demonstrated slow and stable release rates, without any burst release stage, due to controlled diffusion of the gas out of the MOF pores. This was a promising demonstration of fully taking advantage of MOF properties to load the pores with therapeutically active compound, tune the MOF pore chemistry to obtain better release rates and add macrostructural elements to achieve optimal results.

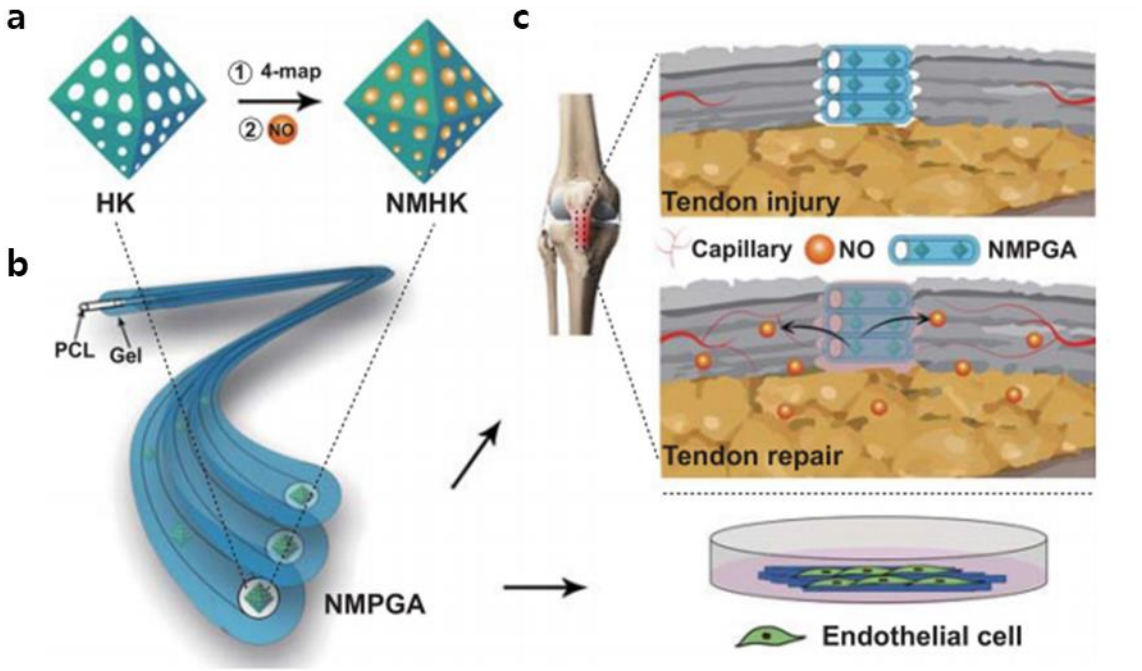

Figure 1.12. Example of drug delivery from a MOF with **a)** pore modification and loading of HKUST-1 with NO, **b)** incorporation in a PCL/gelatine matrix and electrospinning into fibres before **c)** in vitro and in vivo studies into the promoting of tendon tissue repair.[147]

Another example of nitric oxide release from a MOF was reported by Kim *et al*, this time using an active release mechanism in the form of irradiation.[144] Titanium and aluminium MOFs containing the MeNH-bdc (bdc = benzene dicarboxylate) linker were post-synthetically modified to incorporate nitroso moieties bound to the ligands (Figure

1.13). Subsequent irradiation of the MOF resulted in release of NO, which showed much higher release kinetics than the equivalent nitroso compound not incorporated into a MOF.

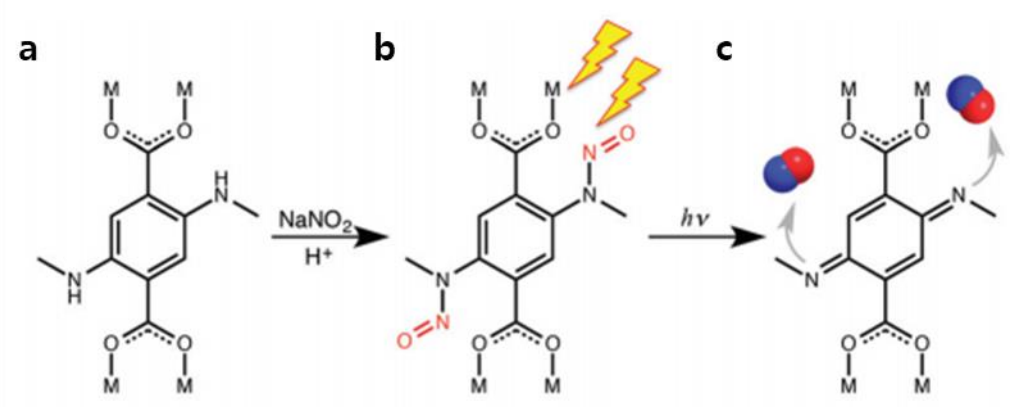

Figure 1.13. Light controlled release of nitric oxide from titanium or aluminium MOFs containing **a)** MeNH-bdc linker (M = $Ti^{4+,}$ Al^{3+}) post-synthetically modified to contain **b)** light sensitive nitroso moieties which **c)** release NO upon irradiation.[144]

Using MOFs as a delivery system has great potential as the release can be highly controlled through passive or active mechanisms. Passive mechanisms rely on internal factors of the material (bonding, lattice, defects etc) while active mechanisms depend on external factors (temperature, irradiation, pressure etc), both of which can be exploited in MOFs. For solid-state reactivity, the fundamental factors controlling such release in MOFs, as opposed to solution-state analogues, has not been well explored. The relative importance of internal and external factors, as well as particle effects such as crystal size, shape, and macrostructural formation, are subjects with much scope for exploration and great significance for future applications.

1.7 Research Directions

This thesis focuses on exploring the properties of solid-state materials with two main research directions, namely the site isolation and characterisation of reactive metal species in MOFs and the exploring the factors controlling the release of small molecules and metal ions from MOFs. The latter aspects were investigated in order to consider them as reservoirs for chemical synthesis and drug delivery applications.

Chapter 2 centres on studying the photochemistry of a manganese carbonyl complex post-synthetically metalated into MnMOF. The effects of site isolation on this complex within a MOF matrix was explored before, during and after irradiation with light, with emphasis on the effects of solvent. Complementary techniques including matrix isolated infrared spectroscopy, photocrystallography and X-ray photoelectron spectroscopy were used to build a picture of the reaction pathway.

Chapter 3 concentrates on using the MOF-bound complex discussed in Chapter 2 as a photo-activated source of carbon monoxide for chemical synthesis. Improving loading efficiency using alternative MOF supports and controlling crystal size and macrostructural morphology through sol-gel derived structuralisation were explored.

Chapter 4 develops on the themes investigated in Chapter 2 by examining the photochemical behaviour of a manganese azidocarbonyl complex in MnMOF. The effects of temperature on the ability to access different reaction pathways were explored through matrix isolated infrared spectroscopy and photocrystallography. Tethering complexes of potentially catalytically active metals, namely palladium, to MnMOF was also investigated.

Chapter 5 is directed at examining the effects of MOF structural properties on the stability of the MOFs and hence their effectiveness as sources of silver ions for antibacterial applications. Particular attention was directed at considering the nature of the metal-ligand bond and the porosity of the frameworks. This work was then extended to incorporating these MOFs into polymer matrices and the effects of this on the release of silver ions.

Chapter 6 will conclude this body of work, summarise the findings and propose future directions of study to extend the outcomes discovered in these investigations.

1.8 References

1 G. Cohn, *Chem. Rev*, 1948, **42**, 527–579.

2 R. H. Crabtree, *The Organometallic Chemistry of the Transition Metals*, John Wiley & Sons, Inc., Hoboken, NJ, USA, 2014, vol. 9781118138076.

3 J. House, *Inorganic Chemistry - 3rd Edition*, 3rd edn., 2019.

4 W. K. Seok and T. M. Klapötke, *Bull. Korean Chem. Soc.*, 2010, **31**, 781–788.

5 K. Ikemoto, Y. Inokuma, K. Rissanen and M. Fujita, *J. Am. Chem. Soc.*, 2014, **136**, 6892–6895.

6 K. M. Fromm, *Appl. Organomet. Chem.*, 2013, **27**, 683–687.

7 B. D. Fahlman, *Materials Chemistry*, Springer, Dordrecht, 2007.

8 J. R. Chamorro and T. M. McQueen, *Acc. Chem. Res.*, 2018, **51**, 2918–2925.

9 C. N. R. Rao and J. Gopalakrishnan, *New Directions in Solid State Chemistry*, Cambridge University Press, 2nd edn., 1997.

10 W. P. Gomes and W. Dekeyser, in *Treatise on Solid State Chemistry*, Springer US, 1976, pp. 61–113.

11 W. A. Herrmann and B. Cornils, *Angew. Chem. Int. Ed. English*, 1997, **36**, 1048–1067.

12 S. D. Pike and A. S. Weller, *Philos. Trans. R. Soc. A Math. Phys. Eng. Sci.,* 2015, **373**: 20140187

13 Z. Huang, P. S. White and M. Brookhart, *Nature*, 2010, **465**, 598–601.

14 M. Albrecht, M. Lutz, A. L. Spek and G. Van Koten, *Nature*, 2000, **406**, 970–974.

15 M. Albrecht, M. Lutz, A. M. M. Schreurs, E. T. H. Lutz, A. L. Spek and G. Van Koten, *J. Chem. Soc. Dalton Trans.*, 2000, 3797–3804.

16 S. D. Pike, A. L. Thompson, A. G. Algarra, D. C. Apperley, S. A. Macgregor and A. S. Weller, *Science*, 2012, **337**, 1648–1651.

17 R. J. Young, M. T. Huxley, E. Pardo, N. R. Champness, C. J. Sumby and C. J. Doonan, *Chem. Sci.*, 2020, 4031–4050.

18 A. Das, J. H. Reibenspies, Y.-S. Chen and D. C. Powers, *J. Am. Chem. Soc.*, 2017, **139**, 2912–2915.

19 S. D. Pike, F. M. Chadwick, N. H. Rees, M. P. Scott, A. S. Weller, T. Krämer and S. A. Macgregor, *J. Am. Chem. Soc.*, 2015, **137**, 820–833.

20 A. I. McKay, T. Krämer, N. H. Rees, A. L. Thompson, K. E. Christensen, S. A. Macgregor and A. S. Weller, *Organometallics*, 2017, **36**, 22–25.

21 A. J. Martínez-Martínez, B. E. Tegner, A. I. McKay, A. J. Bukvic, N. H. Rees, G. J. Tizzard, S. J. Coles, M. R. Warren, S. A. Macgregor and A. S. Weller, *J. Am. Chem. Soc.*, 2018, **140**, 14958–14970.

22 F. M. Chadwick, N. Olliff and A. S. Weller, *J. Organomet. Chem.*, 2016, **812**, 268–271.

23 F. M. Chadwick, T. Krämer, T. Gutmann, N. H. Rees, A. L. Thompson, A. J. Edwards, G. Buntkowsky, S. A. Macgregor and A. S. Weller, *J. Am. Chem. Soc.*, 2016, **138**, 13369–13378.

24 F. M. Chadwick, A. I. McKay, A. J. Martinez-Martinez, N. H. Rees, T. Krämer, S. A. Macgregor and A. S. Weller, *Chem. Sci.*, 2017, **8**, 6014–6029.

25 L. E. Hatcher, J. M. Skelton, M. R. Warren and P. R. Raithby, *Acc. Chem. Res.*, 2019, **52**, 1079–1088.

26 A. J. Blake, N. R. Champness, T. L. Easun, D. R. Allan, H. Nowell, M. W. George, J. Jia and X. Z. Sun, *Nat. Chem.*, 2010, **2**, 688–694.

27 N. S. Punekar, *ENZYMES: Catalysis, Kinetics and Mechanisms*, Springer Nature Singapore Pte Ltd, 2018.

28 O. M. Yaghi, M. O'Keeffe, N. W. Ockwig, H. K. Chae, M. Eddaoudi and J. Kim, *Nature*, 2003, **423**, 705–714.

29 A. Schneemann, V. Bon, I. Schwedler, I. Senkovska, S. Kaskel and R. A. Fischer, *Chem. Soc. Rev.*, 2014, **43**, 6062–6096.

30 Y. Inokuma, S. Yoshioka, J. Ariyoshi, T. Arai, Y. Hitora, K. Takada, S. Matsunaga, K. Rissanen and M. Fujita, *Nature*, 2013, **495**, 461–466.
31 W. M. Bloch, N. R. Champness and C. J. Doonan, *Angew. Chem. Int. Ed.*, 2015, **54**, 12860–12867.
32 H. L. Wang, H. Yeh, Y. C. Chen, Y. C. Lai, C. Y. Lin, K. Y. Lu, R. M. Ho, B. H. Li, C. H. Lin and D. H. Tsai, *ACS Appl. Mater. Interfaces*, 2018, **10**, 9332–9341.
33 B. F. Hoskins and R. Robson, *J. Am. Chem. Soc*, 1989, **111**, 5962–5964.
34 B. F. Hoskins and R. Robson, *J. Am. Chem. Soc*, 1990, **112**, 1546–1554.
35 O. M. Yaghi, G. Li and H. Li, *Nature*, 1995, **378**, 703–706.
36 L. Öhrström, F. M. Amombo Noa, R. Bender and O. M. Yaghi, *Metal-Organic Frameworks*, American Chemical Society, Washington, DC, USA, 2021.
37 H. Li, M. Eddaoudi, T. L. Groy and O. M. Yaghi, *J. Am. Chem. Soc.*, 1998, **120**, 8571–8572.
38 P. Z. Moghadam, A. Li, X. W. Liu, R. Bueno-Perez, S. D. Wang, S. B. Wiggin, P. A. Wood and D. Fairen-Jimenez, *Chem. Sci.*, 2020, **11**, 8373–8387.
39 S. L. Griffin and N. R. Champness, *Coord. Chem. Rev.*, 2020, **414**, 213295.
40 H. Furukawa, K. E. Cordova, M. O'Keeffe and O. M. Yaghi, *Science*, 2013, **341**, 1–12.
41 O. M. Yaghi, M. J. Kalmutzki and C. S. Diercks, *Introduction to Reticular Chemistry: Metal-Organic Frameworks and Covalent Organic Frameworks*, Wiley-VCH Verlag GmbH & Co. KGaA, Weinheim, Germany, 2019.
42 S. R. Batten, N. R. Champness, X.-M. Chen, J. Garcia-Martinez, S. Kitagawa, L. Öhrström, M. O'keeffe, M. P. Suh and J. Reedijk, *Pure Appl. Chem*, 2013, **85**, 1715–1724.
43 J. H. Cavka, S. Jakobsen, U. Olsbye, N. Guillou, C. Lamberti, S. Bordiga and K. P. Lillerud, *J. Am. Chem. Soc.*, 2008, **130**, 13850–13851.
44 C. Serre, F. Millange, C. Thouvenot, M. Noguès, G. Marsolier, D. Louër and G. Férey, *J. Am. Chem. Soc.*, 2002, **124**, 13519–13526.
45 S. M. Cohen, *Chem. Sci.*, 2010, **1**, 32–36.
46 A. A. Thomas and S. E. Denmark, *Science*, 2016, **352**, 329–332.
47 T. Stahl, P. Hrobárik, C. D. F. Königs, Y. Ohki, K. Tatsumi, S. Kemper, M. Kaupp, H. F. T. Klare and M. Oestreich, *Chem. Sci.*, 2015, **6**, 4324–4334.
48 D. Zell, M. Bursch, V. Müller, S. Grimme and L. Ackermann, *Angew. Chem. Int. Ed.*, 2017, **56**, 10378–10382.
49 J. Hu, Y. Zhao, J. Liu, Y. Zhang and Z. Shi, *Angew. Chem. Int. Ed.*, 2016, **55**, 8718–8722.
50 R. H. Crabtree, *Chem. Rev.*, 2016, **116**, 8750–8769.
51 A. S. Weller, F. M. Chadwick and A. I. McKay, in *Advances in Organometallic Chemistry*, Academic Press Inc., 2016, vol. 66, pp. 223–276.
52 L. Andrews, *Chem. Soc. Rev.*, 2004, **33**, 123–132.
53 J. K. Burdett, *Coord. Chem. Rev.*, 1978, **27**, 1–58.
54 S. A. Bartlett, N. A. Besley, A. J. Dent, S. Diaz-Moreno, J. Evans, M. L. Hamilton, M. W. D. Hanson-Heine, R. Horvath, V. Manici, X.-Z. Sun, M. Towrie, L. Wu, X. Zhang and M. W. George, *J. Am. Chem. Soc*, 2019, **141,** 11471–11480.
55 M. K. Kuimova, W. Z. Alsindi, J. Dyer, D. C. Grills, O. S. Jina, P. Matousek, A. W. Parker, P. Portius, X. Z. Sun, M. Towrie, C. Wilson, J. Yang and M. W. George, *J. Chem. Soc. Dalton Trans.*, 2003, **21**, 3996–4006.
56 P. M. Kraus, M. Zürch, S. K. Cushing, D. M. Neumark and S. R. Leone, *Nat. Rev. Chem.*, 2018, **2**, 82–94.
57 M. Di Donato, E. Ragnoni, A. Lapini, P. Foggi, R. G. Hiller and R. Righini, *J. Chem. Phys.*, 2015, **142**,

212409.
58 D. J. Cram and J. M. Cram, *Acc. Chem. Res.*, 1978, **11**, 8–14.
59 Y. Inokuma, T. Ukegawa, M. Hoshino and M. Fujita, *Chem. Sci.*, 2016, **7**, 3910–3913.
60 S. Zarra, D. M. Wood, D. A. Roberts and J. R. Nitschke, *Chem. Soc. Rev.*, 2015, **44**, 419–432.
61 D. J. Cram, M. E. Tanner and R. Thomas, *Angew. Chem. Int. Ed. Eng.*, 1991, **30**, 1024–1027.
62 F. J. Rizzuto, L. K. S. von Krbek and J. R. Nitschke, *Nat. Rev. Chem.*, 2019, **3**, 204–222.
63 D. M. Kaphan, F. D. Toste, R. G. Bergman and K. N. Raymond, *J. Am. Chem. Soc.*, 2015, **137**, 9202–9205.
64 P. Mal, B. Breiner, K. Rissanen and J. R. Nitschke, *Science*, 2009, **324**, 1697–1699.
65 D. M. Kaphan, M. D. Levin, R. G. Bergman, K. N. Raymond and F. D. Toste, *Science*, 2015, **350**, 1235–1238.
66 M. Otte, *ACS Catal.*, 2016, **6**, 6491–6510.
67 M. D. Levin, D. M. Kaphan, C. M. Hong, R. G. Bergman, K. N. Raymond and F. D. Toste, *J. Am. Chem. Soc.*, 2016, **138**, 9682–9693.
68 C. M. Hong, D. M. Kaphan, R. G. Bergman, K. N. Raymond and F. D. Toste, *J. Am. Chem. Soc.*, 2017, **139**, 8013–8021.
69 J. D. Evans, C. J. Sumby and C. J. Doonan, *Chem. Soc. Rev.*, 2014, **43**, 5933–5951.
70 C. K. Brozek and M. Dincă, *Chem. Soc. Rev.*, 2014, **43**, 5456–5467.
71 L. Chen, R. Luque and Y. Li, *Chem. Soc. Rev.*, 2017, **46**, 4614–4630.
72 M. Hoshino, A. Khutia, H. Xing, Y. Inokuma and M. Fujita, *IUCrJ*, 2016, **3**, 139–151.
73 Q. Du, J. Peng, P. Wu and H. He, *TrAC - Trends Anal. Chem.*, 2018, **102**, 290–310.
74 W. J. Gee, *Dalton Trans.*, 2017, **46**, 15979–15986.
75 E. J. Carrington, I. J. Vitórica-Yrezábal and L. Brammer, *Acta Crystallogr. Sect. B*, 2014, **70**, 404–422.
76 T. L. Easun, F. Moreau, Y. Yan, S. Yang and M. Schröder, *Chem. Soc. Rev.*, 2017, **46**, 239–274.
77 S. Lee, E. A. Kapustin and O. M. Yaghi, *Science*, 2016, **353**, 808–811.
78 S. M. Cohen, *Chem. Rev.*, 2012, **112**, 970–1000.
79 C. K. Brozek and M. Dincă, *J. Am. Chem. Soc.*, 2013, **135**, 12886–12891.
80 E. D. Bloch, L. J. Murray, W. L. Queen, S. Chavan, S. N. Maximoff, J. P. Bigi, R. Krishna, V. K. Peterson, F. Grandjean, G. J. Long, B. Smit, S. Bordiga, C. M. Brown and J. R. Long, *J. Am. Chem. Soc.*, 2011, **133**, 14814–14822.
81 A. W. Stubbs, L. Braglia, E. Borfecchia, R. J. Meyer, Y. Román- Leshkov, C. Lamberti and M. Dincă, *ACS Catal.*, 2018, **8**, 596–601.
82 C. K. Brozek and M. Dincă, *Chem. Sci.*, 2012, **3**, 2110–2113.
83 S. T. Madrahimov, J. R. Gallagher, G. Zhang, Z. Meinhart, S. J. Garibay, M. Delferro, J. T. Miller, O. K. Farha, J. T. Hupp and S. T. Nguyen, *ACS Catal.*, 2015, **5**, 6713–6718.
84 M. P. Byrn, C. J. Curtis, Y. Hsiou, S. I. Khan, P. A. Sawin, S. K. Tendick, A. Terzis and C. E. Strouse, *Am. Chem. Soc.*, 1993, **115**, 9480–9497.
85 T. R. Ramadhar, S. L. Zheng, Y. S. Chen and J. Clardy, *Chem. Commun.*, 2015, **51**, 11252–11255.
86 T. R. Ramadhar, S. L. Zheng, Y. S. Chen and J. Clardy, *Acta Crystallogr. Sect. A Found. Crystallogr.*, 2015, **71**, 46–58.
87 T. R. Ramadhar, S. L. Zheng, Y. S. Chen and J. Clardy, *CrystEngComm*, 2017, **19**, 4528–4534.
88 G. H. Ning, Y. Inokuma and M. Fujita, *Chem. - An Asian J.*, 2014, **9**, 466–468.
89 A. G. O-Brien, A. Maruyama, Y. Inokuma, M. Fujita, P. S. Baran and D. G. Blackmond, *Angew. Chem. - Int. Ed.*, 2014, **53**, 11868–11871.
90 N. Zigon, M. Hoshino, S. Yoshioka, Y. Inokuma and M. Fujita, *Angew. Chem. - Int. Ed.*, 2015, **54**,

9033–9037.
91 S. Matsuzaki, T. Arai, K. Ikemoto, Y. Inokuma and M. Fujita, *J. Am. Chem. Soc.*, 2014, **136**, 17899–17901.
92 S. Yoshioka, Y. Inokuma, V. Duplan, R. Dubey and M. Fujita, *J. Am. Chem. Soc.*, 2016, **138**, 10140–10142.
93 Y. Inokuma, S. Yoshioka, J. Ariyoshi, T. Arai and M. Fujita, *Nat. Protoc.*, 2014, **9**, 246–252.
94 Y. Inokuma and M. Fujita, *Bull. Chem. Soc. Jpn.*, 2014, **87**, 1161–1176.
95 S. Yoshioka, Y. Inokuma, M. Hoshino, T. Sato and M. Fujita, *Chem. Sci.*, 2015, **6**, 3765–3768.
96 G. H. Ning, K. Matsumura, Y. Inokuma and M. Fujita, *Chem. Commun.*, 2016, **52**, 7013–7015.
97 K. Yan, R. Dubey, T. Arai, Y. Inokuma and M. Fujita, *J. Am. Chem. Soc.*, 2017, **139**, 11341–11344.
98 Y. Inokuma, K. Matsumura, S. Yoshioka and M. Fujita, *Chem. - An Asian J.*, 2017, **12**, 208–211.
99 M. P. Byrn, C. J. Curtis, S. Khan, P. A. Sawin, R. Tsurumi and C. E. Strouse, *J. Am. Chem. Soc.*, 1990, **112**, 1865–1874.
100 J. Juan-Alcañiz, J. Gascon and F. Kapteijn, *J. Mater. Chem.*, 2012, **22**, 10102–10119.
101 C. Kaes, A. Katz and M. W. Hosseini, *Chem. Rev.*, 2000, **100**, 3553–3590.
102 M. R. Madsen, J. B. Jakobsen, M. H. Rønne, H. Liang, H. C. D. Hammershøj, P. Nørby, S. U. Pedersen, T. Skrydstrup and K. Daasbjerg, *Organometallics*, 2020, **39**, 1480–1490.
103 B. Saavedra, N. González-Gallardo, A. Meli and D. J. Ramón, *Adv. Synth. Catal.*, 2019, **361**, 3868–3879.
104 N. Elgrishi, M. B. Chambers, X. Wang and M. Fontecave, *Chem. Soc. Rev.*, 2017, **46**, 761–796.
105 N. Queyriaux, D. Sun, J. Fize, J. Pécaut, M. J. Field, M. Chavarot-Kerlidou and V. Artero, *J. Am. Chem. Soc.,* 2020, **142**, 274-282
106 C. A. Kent, B. P. Mehl, L. Ma, J. M. Papanikolas, T. J. Meyer and W. Lin, *J. Am. Chem. Soc.*, 2010, **132**, 12767–12769.
107 C. A. Kent, D. Liu, L. Ma, J. M. Papanikolas, T. J. Meyer and W. Lin, *J. Am. Chem. Soc.*, 2011, **133**, 12940–12943.
108 C. A. Kent, D. Liu, T. J. Meyer and W. Lin, *J. Am. Chem. Soc.*, 2012, **134**, 3991–3994.
109 C. Wang, J. L. Wang and W. Lin, *J. Am. Chem. Soc.*, 2012, **134**, 19895–19908.
110 B. An, L. Zeng, M. Jia, Z. Li, Z. Lin, Y. Song, Y. Zhou, J. Cheng, C. Wang and W. Lin, *J. Am. Chem. Soc.*, 2017, **139**, 17747–17750.
111 C. Wang, K. E. Dekrafft and W. Lin, *J. Am. Chem. Soc.*, 2012, **134**, 7211–7214.
112 M. H. Xie, X. L. Yang, C. Zou and C. De Wu, *Inorg. Chem.*, 2011, **50**, 5318–5320.
113 C. Wang, Z. Xie, K. E. Dekrafft and W. Lin, *J. Am. Chem. Soc.*, 2011, **133**, 13445–13454.
114 T. L. Easun, J. Jia, T. J. Reade, X. Z. Sun, E. S. Davies, A. J. Blake, M. W. George and N. R. Champness, *Chem. Sci.*, 2014, **5**, 539–544.
115 T. J. Reade, T. S. Murphy, J. A. Calladine, R. Horvath, I. P. Clark, G. M. Greetham, M. Towrie, W. Lewis, M. W. George and N. R. Champness, *Philos. Trans. R. Soc. A Math. Phys. Eng. Sci.,* 2016, **375**: 20160033
116 T. L. Easun, J. Jia, J. A. Calladine, D. L. Blackmore, C. S. Stapleton, K. Q. Vuong, N. R. Champness and M. W. George, *Inorg. Chem.*, 2014, **53**, 2606–2612.
117 K. Manna, T. Zhang and W. Lin, *J. Am. Chem. Soc.*, 2014, **136**, 6566–6569.
118 K. Manna, T. Zhang, F. X. Greene and W. Lin, *J. Am. Chem. Soc.*, 2015, **137**, 2665–2673.
119 M. I. Gonzalez, E. D. Bloch, J. A. Mason, S. J. Teat and J. R. Long, *Inorg. Chem.*, 2015, **54**, 2995–3005.
120 E. D. Bloch, D. Britt, C. Lee, C. J. Doonan, F. J. Uribe-Romo, H. Furukawa, J. R. Long and O. M.

Yaghi, *J. Am. Chem. Soc.*, 2010, **132**, 14382–14384.
121 M. Wang, B. Yuan, T. Ma, H. Jiang and Y. Li, *RSC Adv.*, 2012, **2**, 5528–5530.
122 W. M. Bloch, A. Burgun, C. J. Coghlan, R. Lee, M. L. Coote, C. J. Doonan and C. J. Sumby, *Nat. Chem.*, 2014, **6**, 906–912.
123 M. Huxley, C. J. Coghlan, A. Burgun, A. Tarzia, K. Sumida, C. J. Sumby and C. J. Doonan, *Dalton Trans.*, 2016, **45**, 4431–4438.
124 M. T. Huxley, C. J. Coghlan, W. M. Bloch, A. Burgun, C. J. Doonan and C. J. Sumby, *Philos. Trans. R. Soc. A Math. Phys. Eng. Sci.,* **375**: 20160028
125 A. Burgun, C. J. Coghlan, D. M. Huang, W. Chen, S. Horike, S. Kitagawa, J. F. Alvino, G. F. Metha, C. J. Sumby and C. J. Doonan, *Angew. Chem. Int. Ed.*, 2017, **56**, 8412–8416.
126 M. T. Huxley, A. Burgun, H. Ghodrati, C. J. Coghlan, A. Lemieux, N. R. Champness, D. M. Huang, C. J. Doonan and C. J. Sumby, *J. Am. Chem. Soc.*, 2018, **140**, 6416–6425.
127 C. Sun, G. Skorupskii, J.-H. Dou, A. M. Wright and M. Dincă, *J. Am. Chem. Soc.*, 2018, **140**, 17394–17398.
128 S. A. Younis, D. K. Lim, K. H. Kim and A. Deep, *Adv. Colloid Interface Sci.*, 2020, **277**, 102108.
129 J. S. Anderson, A. T. Gallagher, J. A. Mason and T. D. Harris, *J. Am. Chem. Soc.*, 2014, **136**, 16489–16492.
130 P. Z. Moghadam, A. Li, S. B. Wiggin, A. Tao, A. G. P. Maloney, P. A. Wood, S. C. Ward and D. Fairen-Jimenez, *Chem. Mater.*, 2017, **29**, 2618–2625.
131 P. Z. Moghadam, T. Islamoglu, S. Goswami, J. Exley, M. Fantham, C. F. Kaminski, R. Q. Snurr, O. K. Farha and D. Fairen-Jimenez, *Nat. Commun.*, 2018, **9**, 1–8.
132 P. G. Boyd, A. Chidambaram, E. García-Díez, C. P. Ireland, T. D. Daff, R. Bounds, A. Gładysiak, P. Schouwink, S. M. Moosavi, M. M. Maroto-Valer, J. A. Reimer, J. A. R. Navarro, T. K. Woo, S. Garcia, K. C. Stylianou and B. Smit, *Nature*, 2019, **576**, 253–256.
133 C. A. Fernandez, S. K. Nune, H. V. Annapureddy, L. X. Dang, B. P. McGrail, F. Zheng, E. Polikarpov, D. L. King, C. Freeman and K. P. Brooks, *Dalton Trans.*, 2015, **44**, 13490–13497.
134 M. A. Chowdhury, *Rev. J. Chem.*, 2017, **7**, 1–22.
135 Y. Guan, Z. Teng, L. Mei, J. Zhang, Q. Wang and Y. Luo, *J. Colloid Interface Sci.*, 2019, **533**, 207–215.
136 Y. Liu, Y. Wang, J. Huang, Z. Zhou, D. Zhao, L. Jiang and Y. Shen, *AIChE J.*, 2019, **65**, 491–499.
137 E. Lashkari, H. Wang, L. Liu, J. Li and K. Yam, *Food Chem.*, 2017, **221**, 926–935.
138 K. Wu, C. Du, F. Ma, Y. Shen, D. Liang and J. Zhou, *Polymers (Basel).*, 2019, **11**, 947.
139 M. Vassaki, K. E. Papathanasiou, C. Hadjicharalambous, D. Chandrinou, P. Turhanen, D. Choquesillo-Lazarte and K. D. Demadis, *Chem. Commun.*, 2020, **56**, 5166–5169.
140 S. R. Miller, E. Alvarez, L. Fradcourt, T. Devic, S. Wuttke, P. S. Wheatley, N. Steunou, C. Bonhomme, C. Gervais, D. Laurencin, R. E. Morris, A. Vimont, M. Daturi, P. Horcajada and C. Serre, *Chem. Commun.*, 2013, **49**, 7773–7775.
141 M. Sarker and S. H. Jhung, *J. Mol. Liq.*, 2019, **296**, 112060.
142 M. Zhang, R. Qiao and J. Hu, *Nanomaterials*, 2020, **10**, 1134.
143 S. Diring, A. Carné-Sánchez, J. Zhang, S. Ikemura, C. Kim, H. Inaba, S. Kitagawa and S. Furukawa, *Chem. Sci.*, 2017, **8**, 2381–2386.
144 C. Kim, S. Diring, S. Furukawa and S. Kitagawa, *Dalton Trans.*, 2015, **44**, 15324.
145 C. Orellana-Tavra, R. J. Marshall, E. F. Baxter, I. A. Lázaro, A. Tao, A. K. Cheetham, R. S. Forgan and D. Fairen-Jimenez, *J. Mater. Chem. B*, 2016, **4**, 7697–7707.
146 H. D. Lawson, S. P. Walton and C. Chan, *ACS Appl. Mater. Interfaces*, 2021, **13**, 7004–7020.

147 J. Chen, D. Sheng, T. Ying, H. Zhao, J. Zhang, Y. Li, H. Xu and S. Chen, *Nano-Micro Lett.*, 2020, **13**, 23

Chapter Two: Manganese carbonyl photochemistry

2.1 Introduction

2.1.1 Carbon monoxide in chemical synthesis and medicine

Carbon monoxide (CO) is an important C1 building block in organic synthesis and is a crucial signalling molecule in the human body.[1] Despite its value in both synthesis and medicine, the use of CO has been limited to large scale industrial processes, including the Cativa™ and the Fischer-Tropsch processes to make acetic acid and methanol respectively (Figure 2.1). This has mainly been due to safety concerns surrounding the use of CO.[2] CO is a tasteless, odourless, and colourless gas, toxic to humans with the reputation of the "silent killer". Inhaled CO reaches the lungs and enters the bloodstream where it binds to haemoglobin to form carboxyhaemoglobin. CO is a stronger ligand than oxygen when coordinating to the iron(II) in haemoglobin, with approximately 230 times the affinity, therefore restricting the transportation of oxygen around the body.[3] Therefore, the use of CO as both a therapeutic agent and chemical building block has been stymied by its health risks.

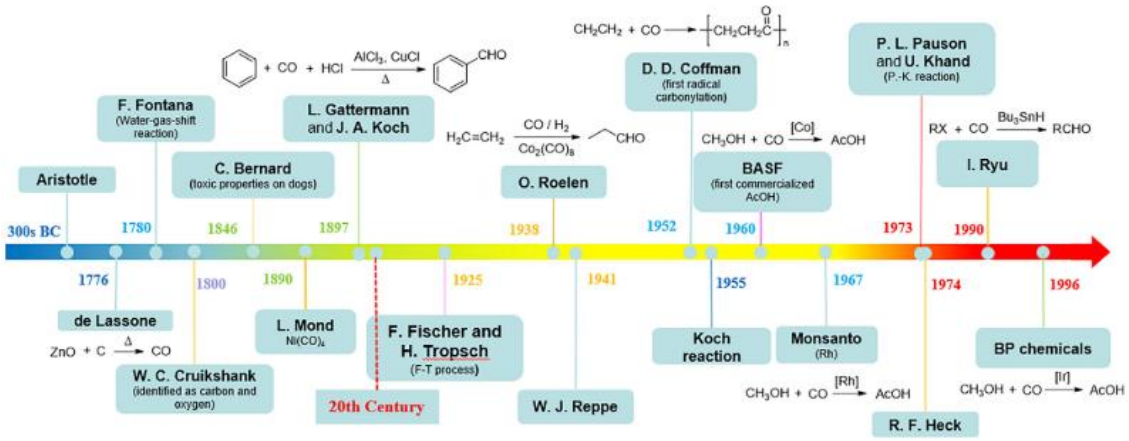

Figure 2.1. Timeline of the use of carbon monoxide in chemical synthesis.[4]

Despite these risks, a large family of reactions incorporating CO into organic molecules, or carbonylation reactions, have been developed. Due to the strength of the C-O triple bond, the strongest known chemical bond with a bond dissociation energy of 1,072 kJ/mol, CO needs to be activated before use.[4] One of the most common ways to do so is through coordination of the CO to a transition metal. As such, industrial

processes such as the Cativa™ process to synthesise acetic acid from methanol rely on the use of an iridium catalyst and high temperatures and pressures (180 °C and 30-50 bar).[5] In this process, CO coordinates to $Ir(CO)I_3(COCH_3)$ and undergoes a migratory insertion and reductive elimination to produce acetyl iodide, which then further reacts with water to form acetic acid (Figure 2.2). This has proven to be highly effective and is used to manufacture approximately 7.2 million tonnes of acetic acid per year.[6,7]

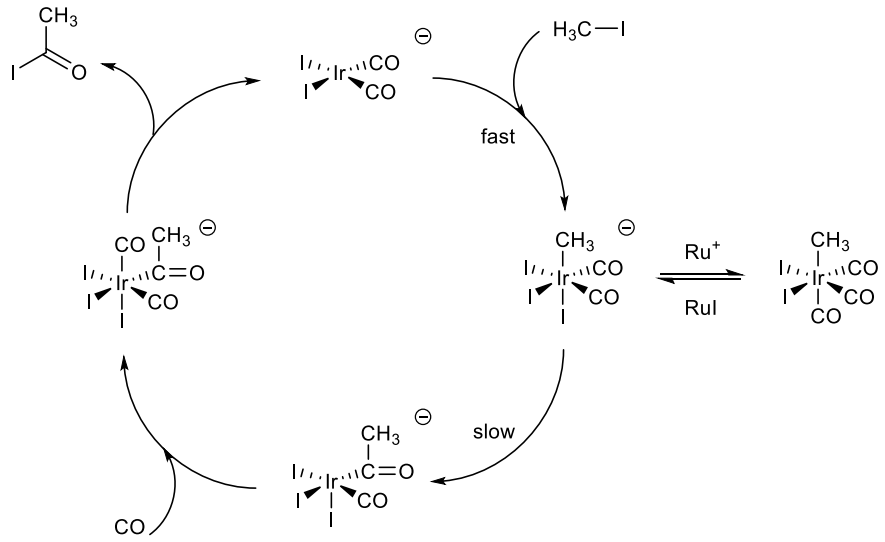

Figure 2.2. Catalytic cycle for the Cativa™ process for the carbonylation of methanol.[5]

Carbonylation reactions are also used to valorise bulk and fine chemicals from olefins, generating aldehydes, alcohols and carboxylic acids.[8,9] Use of carbonylation reactions for the synthesis of more complex organic molecules has been comparatively limited.[2,10] In order to avoid the necessity of using CO gas, alternative sources of the CO group have been developed including formates, formamides, formic anhydride, dichlorocarbene, aldehydes, organosilanes and metal carbonyls.[8] These methods use solid or liquid precursors which either generate CO *in situ* or from carbonyl complexes with metal catalysts (Figure 2.3). Although they avoid the need for a gas bottle of CO, they often require higher temperatures, longer reaction times or extra reagents in the form of acids, bases, or metal catalysts. These present additional problems in reagent compatibilities and product purification. Despite these issues, the use of *in situ* generation of CO has placed carbonylation reactions within the toolbox of the synthetic chemist.

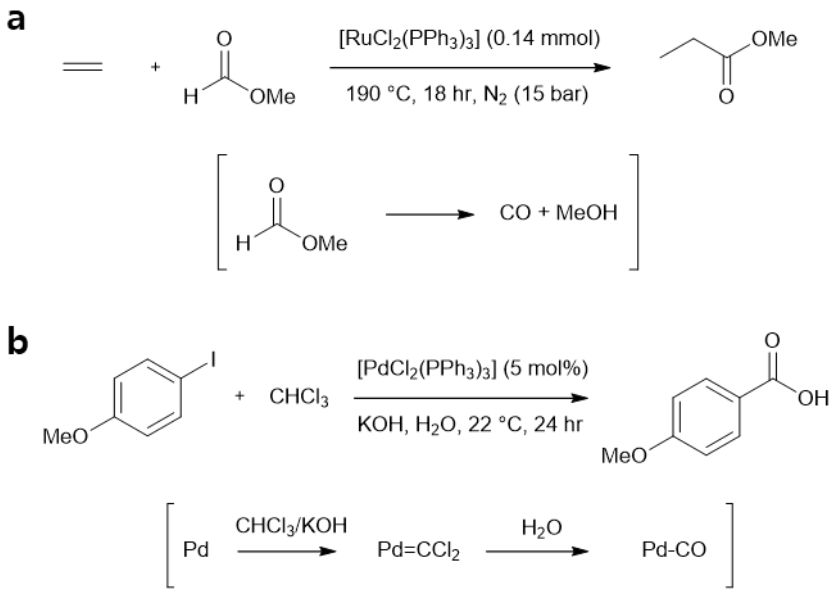

Figure 2.3. a) Ru-catalysed hydroesterification using methyl formate as a source of CO **b)** Pd-catalysed hydroxycarbonylation using chloroform/KOH to form a dichlorocarbene intermediate, then a Pd-carbonyl complex.[8]

In the human body, CO is generated by haem oxygenase,[11,12] and has several functions including modulating inflammatory responses, platelet aggregation, neurovascular responses and cell death via apoptosis.[13,14] In addition, cancer cells have been found to upregulate the haem oxygenase system under exposure to stresses, such as anti-cancer agents, radiation therapy or oxidative stress.[15] Using CO as a therapeutic agent has important implications for treatments of asthma, organ transplants and cancer.[16,17] CO has been found to sensitise cancer cells to chemotherapy treatments, without harming normal cells.[18,19] The quantity of CO and exposure time are the most critical factors to avoiding harmful toxic effects, and regulating this is difficult when CO is administered via inhalation (Figure 2.4).[1,17] Carbon monoxide releasing molecules (CORMs) have been investigated over the last two decades as a platform for the controlled transportation and delivery of CO to the target tissues.[20,21]

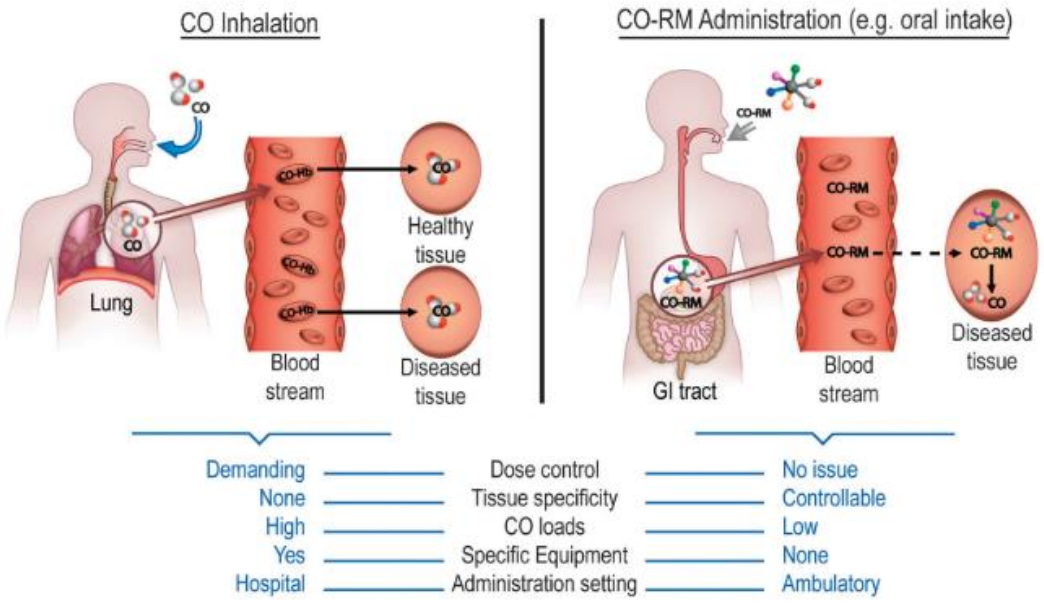

Figure 2.4. Therapeutic delivery pathways for CO and their main advantages and disadvantages.[3]

Initial testing showed simple transition metal carbonyl complexes such as $Mn_2(CO)_{10}$, $Fe(CO)_5$ and $[Ru(CO)_3Cl_2]_2$ to be effective at releasing CO, but problems were encountered with the release mechanism, solubility, toxicity and biological deactivation.[21,22] Since then a large family of CORM complexes have been made, using a range of transition metals (Ru, Fe, Mn, V, Co, Ir, Mo and W) and modified ligand sets which have improved the solubilities and stabilities.[23] While many CORMs rely on simple thermal or hydrolysis activation to release CO, some have been developed to achieve controllable and specific CO delivery by activation through internal or external triggers such as enzymes or photoactivation.[24] Photoactivated CORMs (photoCORMs) allow for a high degree of control over the release of CO; however, as with all CORMs, after CO release an inactivated metal-ligand complex is generated which may have adverse physiological effects.[24]

2.1.2 Metal carbonyl CORMs

In both chemical synthesis and therapeutic applications, metal-carbonyl complexes have been used as CO sources to avoid the use of gaseous CO. The carbonyl ligand bonds strongly to transition metals due to the combination of a ligand-to-metal electron donation from the 3σ-CO σ-orbital and metal-to-ligand back-donation from the metal d_π orbital to the ligand π* orbital (Figure 2.5).[4] Lower valent metals with

available d-electrons contribute to stronger π-back bonding interactions; thus the majority of stable carbonyl complexes are with low-valent metals.[25] Occupation of the CO π* orbital upon metal backdonation leads to a lowering of the bond order between the carbon and oxygen atoms, resulting in a longer bond length and a lower carbonyl stretching frequency in the IR spectrum compared to free CO gas.

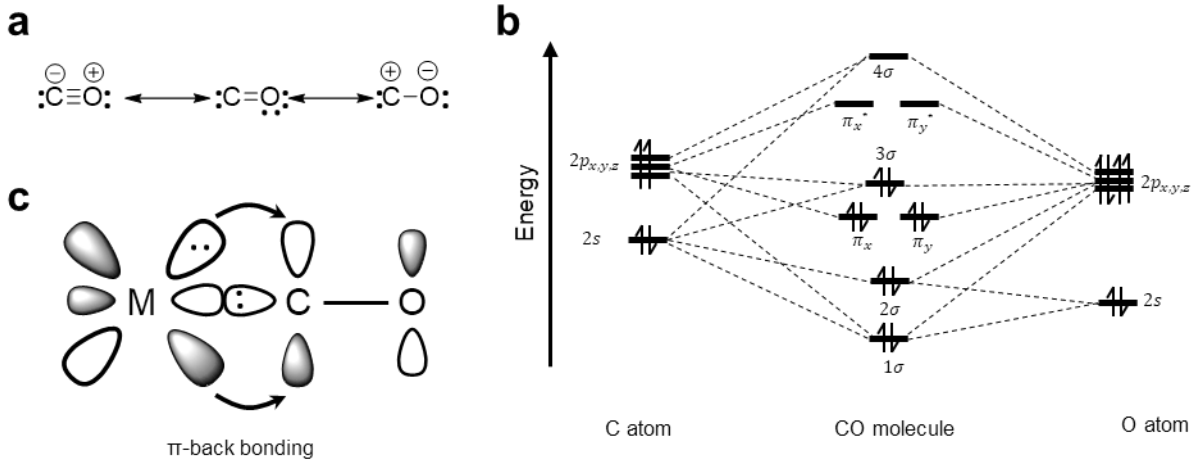

Figure 2.5. Bonding of CO to transition metals with a) three resonance structures of CO, b) orbital filling diagram for the CO molecule and c) σ bonding and π-back bonding in a metal-carbonyl bond.[4]

Most reported metal carbonyl CORMs release CO through passive thermodynamic mechanisms, generally by oxidation of the metal in aqueous media leading to less π-back bonding, the rates of which can be modulated, but not actively controlled, through modification of ancillary ligands.[26,27] In contrast, the group 7 and 8 transition metals, Mn, Re and Ru, in +1 and +2 oxidation states respectively can form photoactive carbonyl complexes. The absorption of a photon causes a metal-to-ligand charge transfer (MLCT) process, which is allowed due to the low spin d^6 configuration of these metals. This causes a transfer of electron density from the metal d-orbital to the π* molecular orbital of the CO ligand, resulting in the labilisation of the metal to ligand bond.[28] Ancillary ligands can be used to tune the wavelength of light needed to labilise the M-CO bond, as well as the reaction rate by modifying the energy gap between the orbitals involved in photoexcited electron transfer (the HOMO and LUMO). For the photoexcitation to be effective in the visible spectrum the HOMO-LUMO gap should be as narrow as possible, and this can be achieved by using ancillary ligands with conjugated bidentate aromatic groups or π-donor atoms bound directly to the metal. Examples of the former include nitrogen heterocyclic ligands such as bipyridine,

which can stabilise the LUMO associated with the MLCT while halide anions such as Cl^- and Br^- are examples of the latter.[29]

CORMs containing the facially coordinated $[Mn(CO)_3]^+$ motif have garnered significant attention due to their photodissociation under visible light, ease of functionalisation and relatively low cost compared to Re and Ru carbonyl complexes.[30]

2.1.3 Mn(I) PhotoCORMs

The first Mn(I) carbonyl compound to be used as a photoCORM was the commercially available $Mn_2(CO)_{10}$ (Figure 2.6a).[21] This; however, only released one of the carbonyl ligands and presented solubility issues. The addition of bi- or tri-dentate ancillary ligands to produce *fac*-$Mn(CO)_3X$ complexes has resulted in a large library of Mn(I) photoCORMs which release CO under irradiation with visible light and through which the chemical and physical properties may be tuned (Figure 2.6d).[31] The complex *fac*-$[Mn(his)(CO)_3]$ (Hhis=histidine) utilised the amino acid L-histidine as a tripodal ligand to produce a water soluble and photoactive CORM (Figure 2.6b). However, a myoglobin assay to quantify the released CO showed only one carbonyl ligand out of the three being released to react with the myoglobin.[32] Despite many Mn photoCORMs having been developed, the reaction mechanism and products remained unexplored for several years.

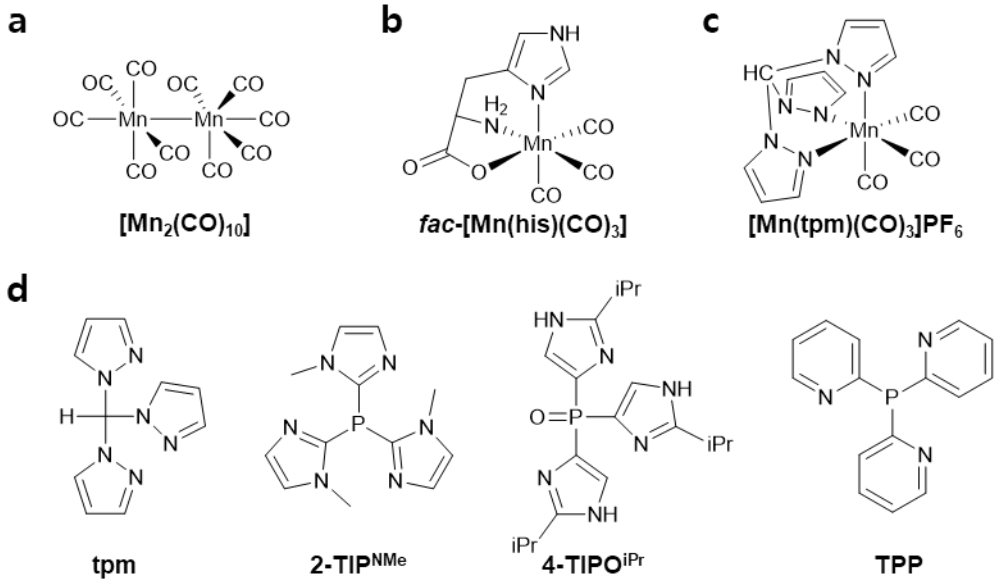

Figure 2.6. A selection of Mn(I) photoCORMs and ligands. **a)** The first Mn photoCORM studied, $Mn_2(CO)_{10}$, **b)** the water soluble fac-[Mn(his)$(CO)_3$] complex only loss of one CO ligand after irradiation, **c)** Mn photoCORM used to study reaction intermediates by Berens *et al*, **d)** selection of tripodal ligands used to make $Mn(CO)_3$ photoCORMs.

Berends *et al.* were the first to study the reaction intermediates and products of Mn photoCORM decarbonylations. They noted that previous studies which used myoglobin assays to quantify the amount of CO released by *fac*-Mn(I) tricarbonyl complexes reported incomplete CO release, with only 1-2 CO molecules released per manganese centre.[33] It was concluded, that due to the instability of mono- or di-carbonyl Mn(I) complexes in the aqueous environments, further reactions must be taking place. Using the photoCORMs [$Mn(CO)_3$(tpm)](PF_6) (tpm = tris(pyrazolyl)methane)(**1**) (Figure 2.6c) and [$Mn(CO)_3$(bpzaa)](**2**) (Hbpzaa = bis(pyrazolyl)acetic acid), Berends *et al* monitored the CO release by UV/vis, IR and EPR spectroscopy, as well as the traditional myoglobin assay. The IR spectra showed the formation of a carbonyl band at 1850 cm^{-1} associated with the formation of a solvated manganese(I) cis-dicarbonyl species. The second stretch expected for this species was obscured under the parent bands. The dicarbonyl band was observed to increase in intensity between 3-10 min of irradiation, then decrease and disappear after 30 min of irradiation.

After 30 min no CO bands were observed, indicating that all metal bound CO ligands had been lost. EPR analysis showed the formation of a mononuclear Mn(II) compound and 5 min of irradiation with the signals increasing in intensity and reaching a maximum after 30 or 10 min of irradiation (for compounds **1** and **2** respectively). After this the bands decreased and no new EPR features were observed; in addition, no

mononuclear Mn(III) was detected in parallel mode. The authors stated that dinuclear Mn(III) complexes were the most likely final reaction products. The proposed reaction pathway was presented: (steps 1 and 2) excitation of the photoCORM causing the release of one CO ligand and coordination of a solvent molecule; (step 3) the dicarbonyl species then lost a further two CO ligands and (step 4) underwent oxidation with an unknown oxidation agent to form a Mn(II) tri-solvated species; which was (step 5) further oxidised to form a Mn(III) dimer (Figure 2.7).

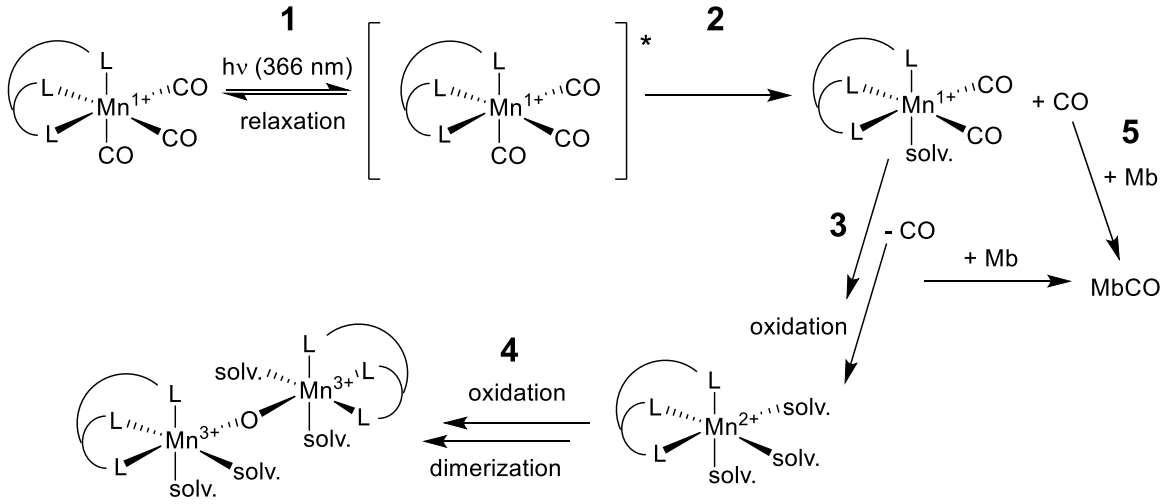

Figure 2.7. Carbon monoxide release pathway proposed by Berends *et al* involving photoexcitation followed by loss of CO to form a cis-dicarbonyl intermediate, then further loss of CO and oxidation of the Mn(I) to Mn(III). Released CO reacted with deoxy-myoglobin to form carbonmonoxy-myoglobin.[33]

In order to better identify photoCORM intermediates, Nagel *et al* used the tetradentate ligand tpa (tris(2-pyridylmethyl)amine) coordinated in a tripodal fashion to form the photoactive species *fac*-[Mn(CO)$_3$(tpa-κ^{3}N)]Br.[34] It was postulated that upon release of a CO ligand, the non-coordinated pyridyl group could occupy the vacant site, thus producing a well-defined intermediate. What was found, through a combination of IR and DFT analysis, was that the initially-formed vacant site immediately coordinated to a water molecule from the (non-anhydrous) DMSO solution. The coordinated water was subsequently displaced by the pendant pyridyl group to form a *cis*-Mn(CO)$_2$ moiety with IR stretches at 1896 and 1860 cm^{-1}. Loss of a further molecule of CO lead to water binding to the vacant site, resulting in a final reaction product of [Mn(CO)(OH$_2$)(tpa-κ^{4}N)], which saw no further loss of CO over the course of the reaction.

Further mechanistic insights were provided by Pordel and White, who employed *fac*-[Mn(NN)(CO)$_3$(L)]$^{n+}$ complexes {NN = 4,4′-dimethylester-2,2′-bipyridine (dmebpy), 2,2′-bipyridine (bpy), or 4,4′-dimethyl-2,2′-bipyridine (Me$_2$bpy), L = Br$^-$ or pyridine (py)}

to probe the impact of NN and L on the photochemical ligand exchange mechanism.[35] It was found that replacing a π-donor ligand (Br^-) with a π-accepting ligand (pyridine) stabilised the Mn(I) HOMO and changed the location of the first photo-released CO from the equatorial site (Br^-) to the axial site *trans* to L (pyridine). It was also found that both bromide and pyridine coordinated species underwent ligand exchange with acetonitrile to form a dicarbonyl intermediate with two coordinated acetonitrile molecules at the axial sites (Figure 2.8).

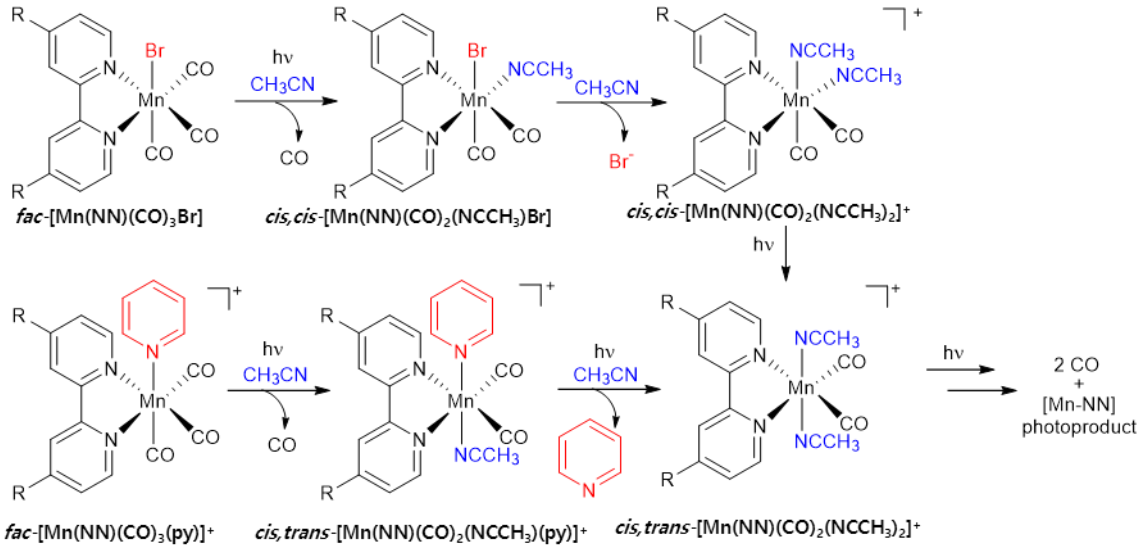

Figure 2.8. Stepwise photochemical ligand disassociation and intermediate formations for bromide and pyridine coordinated complexes. R = H, Me or COOMe[35]

Fac-tricarbonyl Mn(I) photoCORMs have been shown to lose all three carbonyl ligands under irradiation with visible light. For medicinal applications, the solubility of photoCORMs in aqueous media is a key consideration.[36] This has mainly been achieved by forming ion-pair complexes, where the use of bulky and/or multidentate ligands and non-coordinating anions has been effective.[37,38] Photolysis of the luminescent complex $[Mn(Imdansyl)(CO)_3(phen)](CF_3SO_3)$ (where, Imdansyl = dansylimidazole and phen = 1,10-phenanthroline) dissolved in acetonitrile under an ambient atmosphere produced Mn(II) complexes coordinated to phen and water ligands.[38] This complex was found to be effective at entering human colorectal adenocarcinoma cells (HT-29) and causing cell death after irradiation with visible light, with minimal cell damage to healthy cells or to the HT-29 cells without irradiation. A manganese carbonyl complex, $[Mn(CO)_3(phen)(PTA)]CF_3SO_3$ (phen = 1,10-phenanthroline, PTA = 1,3,5-triza-7-phosphaadamantane) was even shown to sensitise *cis*-platin resistant ovarian cancer cell lines.[19] This was found to be mediated in part by the CO inhibition of cystathionine

β-synthase, an enzyme overexpressed in ovarian cancer tissues and associated with cis-platin resistance.

A charge-separated species was synthesised using a bis-pyrazolyl, heteroscorpionate type ligand to make the *fac*-[Mn(CO)$_3$(bdmpze)]Br (bdmpze = 2,2-bis(3,5-dimethyl-1-pyrazolyl) ethanol) ion pair complex (Figure 2.9).[37] This complex was water soluble and released three equivalents of CO gas when irradiated with light of 405 or 470 nm wavelengths.

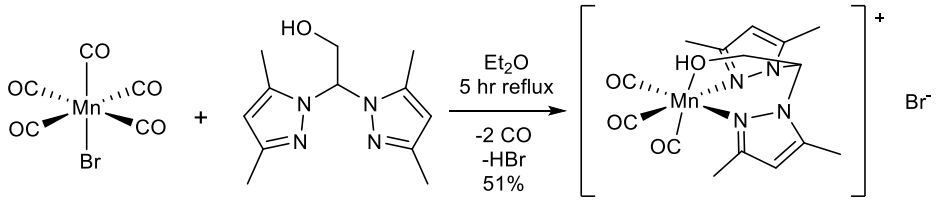

Figure 2.9. Charge-separated photoCORM [Mn(CO)$_3$bdmpze]Br (bdmpze = 2,2-bis(3,5-dimethyl-1-pyrazolyl) ethanol).[37]

The *fac*-[Mn(CO)$_3$(bdmpze)]Br ion pair complex was stable in the solid-state, but solutions in methanol decomposed through a disproportionation reaction resulting in a Mn(II)(bdmpze)$_2$ cationic complex and a [Mn(-I)(CO)$_5$]$^-$ anion, along with the formation of several other decomposition products. The structure of the decomposition product (iCORM4) was confirmed by a single crystal X-ray structure (Figure 2.10).

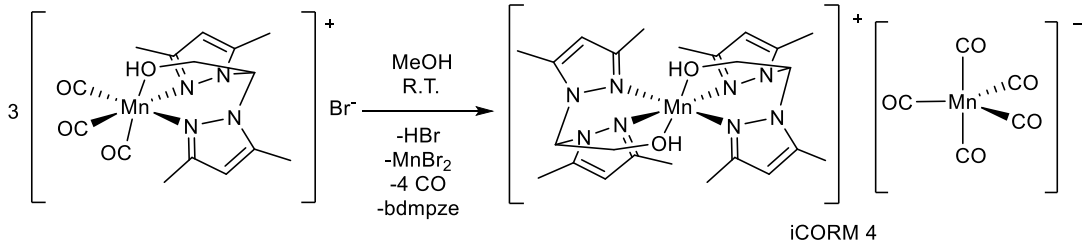

Figure 2.10. Decomposition pathway for [Mn(CO)$_3$bdmpze]Br (bdmpze = 2,2-bis(3,5-dimethyl-1-pyrazolyl) ethanol).[37]

Fac-tricarbonyl Mn(I) photoCORMs have been shown to deliver gaseous CO upon irradiation with visible or UV light. The decarbonylation reaction pathways were studied for several species which were found to undergo either complete decarbonylation with concomitant oxidation of the Mn(I) to Mn(III), disproportionation of Mn(I) to Mn(II) and Mn(0), or partial decarbonylation resulting in the formation of mono- or di-carbonyl moieties.

2.1.4 Mn(I) carbonyl complexes in MOFs

Mn(I) carbonyl complexes have been of interest not only as CORMs for medical applications, but also as catalysts, especially for the reduction of CO_2.[39] The electrochemical reduction of CO_2 by rhenium carbonyl complexes is well known and has been studied since 1985;[40] but the far greater natural abundance of manganese makes it a more attractive catalyst. Manganese(I) carbonyl complexes can undergo a two electron reduction *in situ* to form a five coordinate Mn(-1) anionic complex. This then enters a catalytic cycle which converts CO_2 to CO. Again, auxiliary ligand modification allows for the properties of the complex to be tuned, with bulky ligands used to prevent dimerization and incorporate photosensitisers which encouraged the reduction of the Mn centre.[39] One strategy to prevent catalyst deactivation by dimerization is to tether the Mn(I) complex to a support.[41,42] This has been demonstrated using the MOF (UiO-67-bpy), where a *fac*-[$Mn(CO)_3Br$] complex was tethered in a post-synthetic process to vacant N,N-bpy chelation sites. The resulting crystals were then soaked in a solution with a ruthenium photosensitiser and a sacrificial electron donor. The material reacted with CO_2 under irradiation with visible light to produce formate with 96% selectivity and moderate turnovers, performing better than analogous homogeneous systems (Figure 2.11).[43]

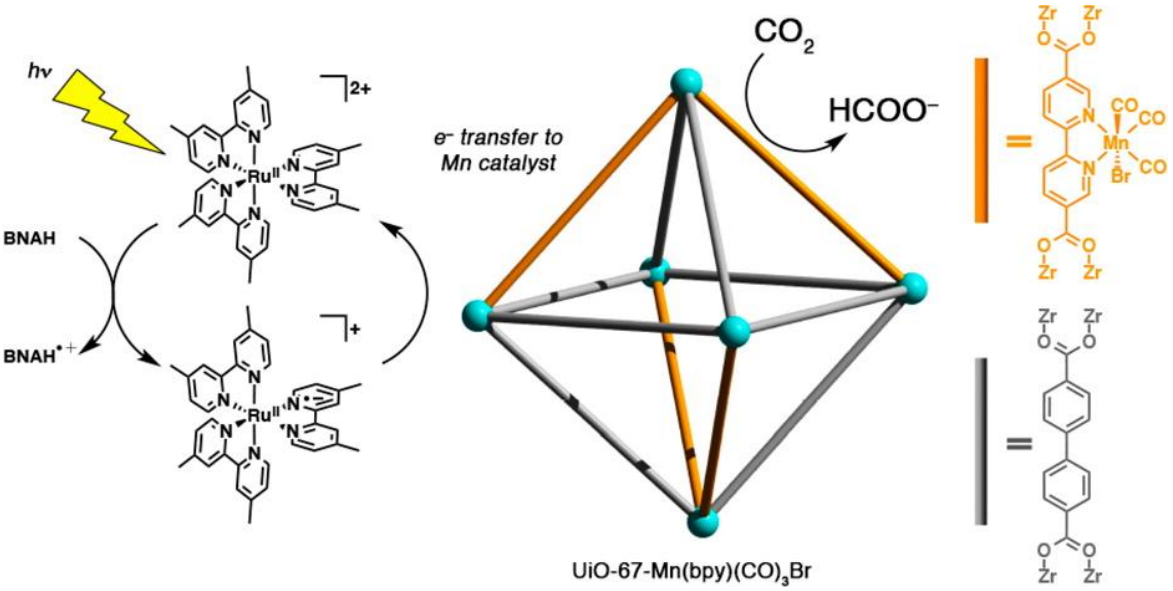

Figure 2.11. Photocatalytic reduction of CO_2 to formate using $Mn(CO)_3Br$ complex tethered to free bipyridine coordination sites in UiO-67.[43]

Tethering Mn(I) carbonyl complexes to MOFs has also been used to study their photoreactive properties. The ligand bpydc (2,2′-bipyridine-5,5′-dicarboxylate) was reacted with $Mn(CO)_5Br$ to form *fac*-[$Mn(CO)_3$bpydcBr], which was then used to form MOFs by reaction with MnX_2 (X = Cl or acetate) in DMF.[44] This formed an air-stable, close-packed 3D framework containing the N,N-chelated *fac*-[$Mn(CO)_3Br$] moiety. Single crystals suitable for analysis by single crystal X-ray diffraction were produced, allowing the photoreactivity to be studied by time-resolved IR spectroscopy and photocrystallography. Photoexcitation by an Xe lamp led to loss of a CO ligand; however, due to the close-packed nature of the framework the free CO rapidly recombined with the metal centre. This manifested as the formation of two ν(CO) bands indicative of a metal-dicarbonyl species in the IR spectrum, which were bleached as the free CO recombined with the manganese centre, regenerating stretches corresponding to tricarbonyl complexes. Unusually, the CO recombination generated a mixture of *mer*-tricarbonyl and *fac*-tricarbonyl complexes, with approximately 25% of the regenerated tricarbonyl corresponding to the new *mer*-isomer (Figure 2.12). Both isomers could be observed using single-crystal x-ray crystallography, demonstrating a powerful new technique for 3D elucidation of reaction intermediates. The incorporation of a manganese photoCORM within a crystalline MOF forced the complex into an unusual reaction environment, promoting the formation of disfavoured species which could be structurally characterised using crystallography.

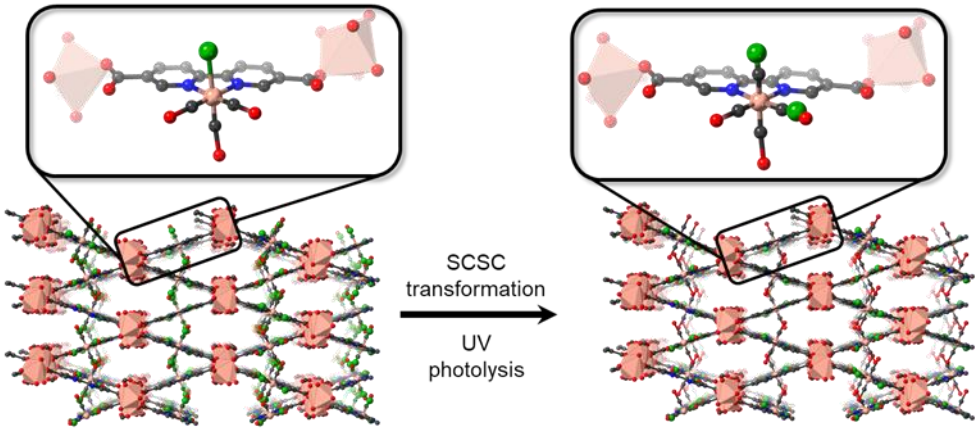

Figure 2.12. Single crystal to single crystal transformation of [M(L)$(CO)_3$X] complexes (where L = 2,2'-bipyridine-5,5'-dicarboxylic acid; M= Mn(I) or Rh(I), X = Br^- or Cl^-) tethered to Mn under photoexcitation leading to isomerisation of the [M(2,2'-bipy)$(CO)_3$X] group, resulting in both *fac*- and *mer*-isomers.[36] (Mn , beige; Cl, green; C, grey; O,- red; N,-blue)

The MOF UiO-67-bpy, which features accessible N,N-chelation sites, was employed by Diring *et al* to tether a *fac*-$Mn(CO)_3Br$ complex and produce a photoCORM. Post-synthetic metalation was used to incorporate the manganese carbonyl species into vacant bipyridine binding sites to produce UiO-67[$Mn(CO)_3Br$] (Figure 2.13).[45] The use of solid-state photoCORMs was proposed to avoid potentially complex ligand systems needed to solubilise poorly soluble Mn(I) CORMs and prevent toxic side effects from reaction products. Irradiation with 460 nm light resulted in a near complete bleaching of the carbonyl band in the IR spectrum and the detection of released CO gas through myoglobin assays. No loss of CO was observed for the molecular analogue, $Mn(CO)_3$(dmbpy)Br (dmbpy = 5,5′-dimethyl-2,2′-bipyridine), despite having identical coordination environments and MLCT absorption bands to UiO67-bpy[$Mn(CO)_3Br$]. This indicates that the difference in reactivity must be caused by the physical separation of the complexes within the MOF. The site-isolation of the Mn(I) atoms combined with the porosity of the MOF allows for egress of the released CO molecules. A key finding of this study was that light penetration into the crystals was a limiting factor in the photo-efficiency of the compound. Small crystals (260 ± 80 nm) with a 69% loading of Mn(I) carbonyl complex released CO with a greater efficiency than the same size crystals with 95% loading, and larger crystals (1200±180 nm) with 60% loading. Due to the small size of the MOF crystals, structural characterisation of the initial complex or any reaction products was not possible.

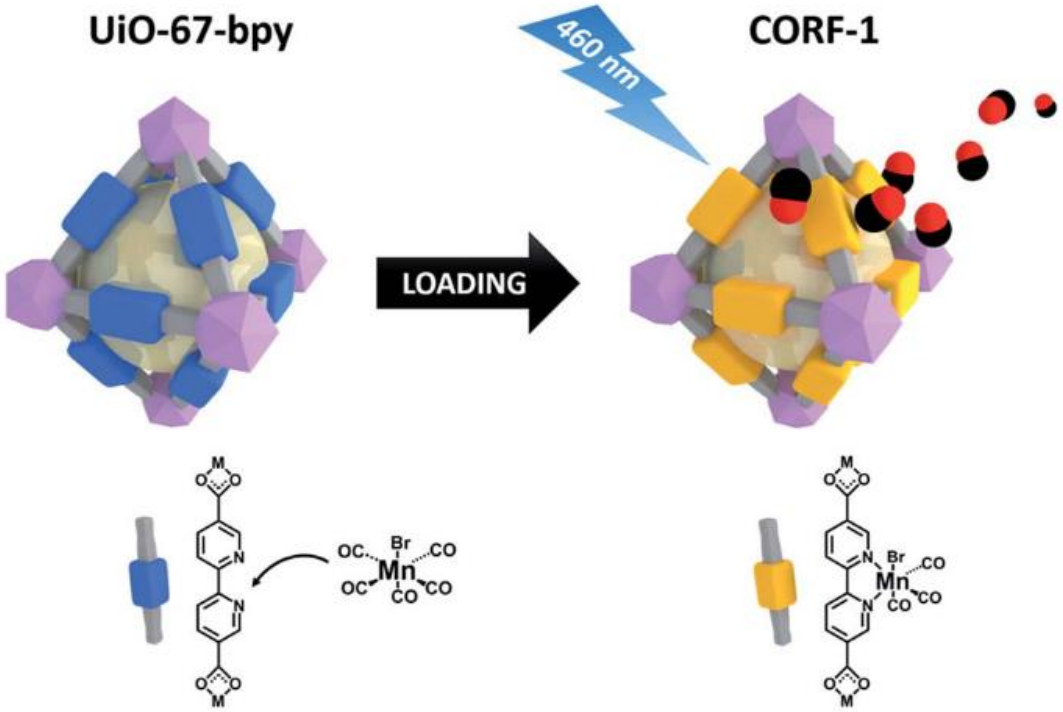

Figure 2.13. Schematic representation of UiO-67-bpy metalated with $Mn(CO)_5Br$ and photolysed to release CO gas.[45]

Mn(I) carbonyl complexes have been shown to have important applications as therapeutic agents and as catalysts. Despite this, the reaction mechanisms surrounding their photolysis are not fully understood. Incorporation into solid-state materials such as MOFs allows solid-state analysis techniques such as X-ray crystallography to be applied, while granting access to new and unusual reaction intermediates and products.

2.1.4 Manganese MOF (MnMOF)

The quantitative metalation of MnMOF with $Mn(CO)_5Br$ has been previously reported, and the metalated MOF, MnMOF·$[Mn(CO)_3X]Y$ (X = solvent and Y = Br, or X = Br), has been used to demonstrate protecting group free site-selective click reactions and solvent-induced isomer interconversions.[46,47] The MOF structure, formulated as $[Mn_3L_2L']$, is comprised of Mn(II) trinuclear nodes coordinated to L (Figure 2.14), where L is coordinatively saturated through bonding to the Mn nodes but L′ is coordinated solely through the carboxylate donors, thus providing a vacant bis-pyrazole site for metalation post-synthetically. This bis-pyrazole site is connected by a methylene bridge,

which imparts remarkable flexibility while maintaining single crystallinity during post-synthetic metalation and subsequent chemical transformations.

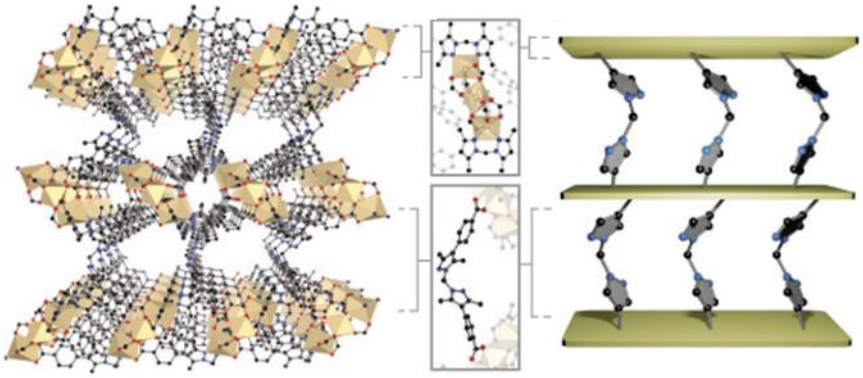

Figure 2.14. MnMOF, showing from left to right, solvent accessible channels linked by trinuclear Mn(II) clusters and the ligand L', with the un-coordinated bis-pyrazole sites. [48]

MnMOF is an ideal platform for studying photoactivated decarbonylation reactions of Mn(I) photoCORMs by photocrystallography due to its facile metalation behaviour, low-symmetry space group and flexibility, accommodating changes in coordination environments whilst retaining crystallinity.

2.2 Aims

The photoactivated decarbonylation pathways of MnMOF[$Mn(CO)_3X$]Y (X,Y = Br^- or solvent) were studied using photocrystallography and IR spectroscopy, in an effort to identify reaction intermediates and products. The influence of solvent and coordination sphere were investigated, and the behaviour compared to analogous small molecule manganese(I) carbonyl complexes.

2.3 Results and Discussion

2.3.1 Synthesis and characterisation of MnMOF[Mn(CO)$_3$X].Y

The ligand precursor H_2L {4,4'-(methylenebis(3,5-dimethyl-1H-pyrazole-1,4-diyl)}dibenzoic acid)[49–51] and MnMOF[48] were synthesised according to literature procedures with the following modifications. When synthesising 1,1-methylenebis(4-iodo-3,5-dimethyl-1H-pyrazole) the reaction mixture was stirred at room temperature overnight rather than for 30 min, as it was found that a longer reaction time was necessary to achieve a high yield (29% vs 71%). After the mixture was poured into water the resulting suspension was chilled overnight in the fridge, then filtered and recrystallised from ethanol to remove all residual unreacted iodine. When synthesising MnMOF, attempts to increase the reaction scale or perform the reaction in a re-usable vessel were found to produce a 2D MOF phase, which is close packed and unable to be metalated (Appendix 2.6.1). As such, all MnMOF was made in individual batches according to the literature method, which could be split or combined as necessary for post-synthetic procedures (Figure 2.15a).

MnMOF was post-synthetically metalated with [Mn(CO)$_5$Br] in ethanol at 50 °C overnight, according to the method published by Huxley *et al* (Figure 2.15b).[46] Overnight heating of the MOF in the manganese carbonyl solution, rather than for 48 hrs, was found to give quantitative loadings through EDX analysis, established by comparing the manganese to bromine elemental ratios. Lower temperatures of 30 °C and 40 °C gave lower metalation loadings of 52% and 71% respectively, while increasing the temperature to 60 °C gave quantitative metalation, but analysis by IR spectroscopy gave qualitative evidence for some loss of CO (Table 2.1).

Table 2.1. MnMOF metalation with $Mn(CO)_5Br$ at varying temperatures analysed by EDX

Temperature (°C)	Metalation efficiency (%)
30	52
40	71
50	116
60	95

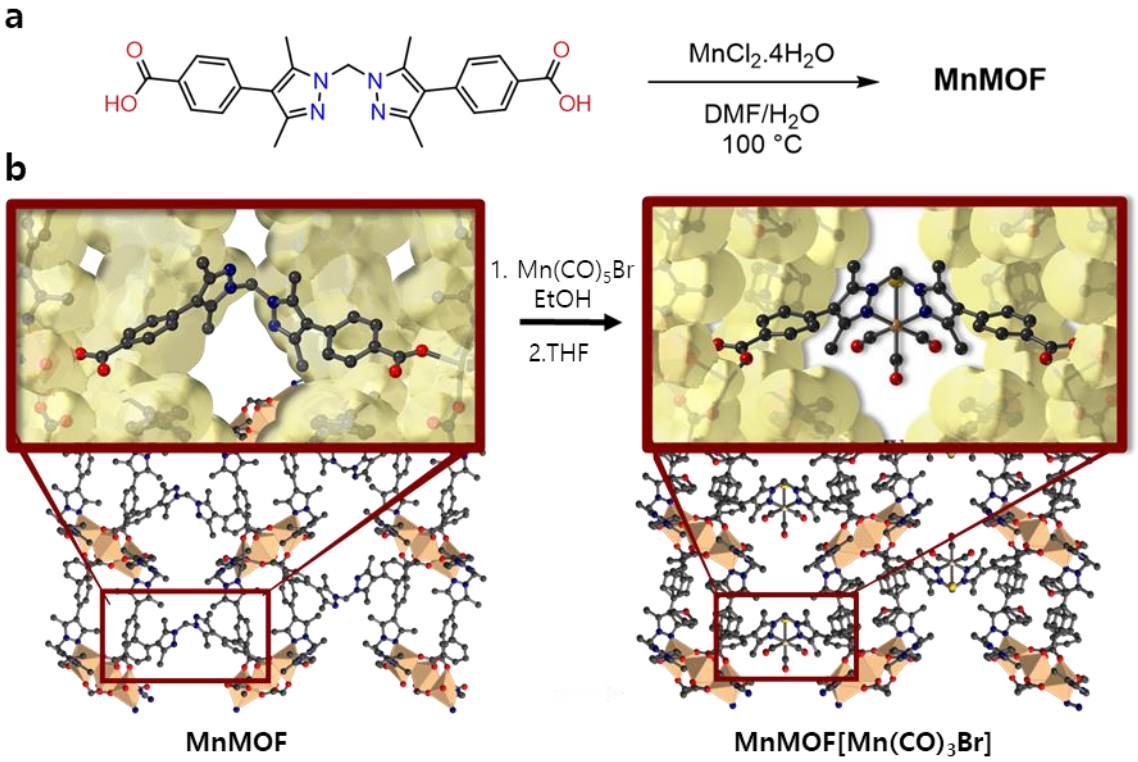

Figure 2.15.a) MnMOF synthesis from ligand L and manganese chloride in DMF and water. **b)** Metalation with $Mn(CO)_5Br$ in ethanol and subsequent solvent exchange with non-polar solvents produces MnMOF[$Mn(CO)_3Br$] complex. (C, grey; Br, yellow; Mn, beige; O, red; N, blue)

The metalation product (MnMOF[$Mn(CO)_3$OHEt].Br]) could be observed through single crystal X-ray diffraction and is formed in the charge-separated state, with the bromide anion residing in the MOF pore and the Mn(I) metal centre coordinated to 3 carbonyl ligands, the chelating bis-pyrazole ligand from the MOF, and a solvent molecule in the axial position *trans* to the methylene bridge. All metalated MnMOF structures, and subsequent single crystal to single crystal transformations, produced structures in the $P2_1/m$ space group. In the *as-synthesised* state the coordinated solvent is a mixture of ethanol and water, as the metalation conditions do not exclude water (Figure 2.16a).

Through investigation of the IR spectrum and single crystal X-ray diffraction experiments it was found that the coordination environment around the manganese(I) cation underwent a series of solvent induced isomerisations through single crystal to single crystal processes. Solvent exchange to one with a higher dielectric constant, acetonitrile, led to replacement of the coordinated ethanol or water with acetonitrile (Figure 2.16b). The coordinated acetonitrile molecule could be modelled crystallographically, with a Mn-N bond length of 1.86(2) Å compared to the original complex which displayed Mn-O (O = OH_2 or $OHCH_2CH_3$) bond length of 2.21(2) Å. Exchange with the polar, but more bulky solvent, benzonitrile caused a rearrangement of the coordination sphere resulting in benzonitrile occupying the less sterically hindered coordination site adjacent to the methylene bridge (Figure 2.16c, Table 2.2). The phenyl-ring of the benzonitrile was significantly disordered but could be modelled with geometrically optimised bond lengths and angles. The coordinated benzonitrile molecule displayed a Mn-N (N≡C-Ph) bond length of 2.02(3) Å and coordinated at a 179(3)° angle (Mn-N-C).

Finally, solvent exchange with THF, which has a lower polarity than ethanol, led to displacement of coordinated H_2O/ethanol by bromide, thus forming a charge-neutral complex with a Mn-Br bond length of 2.57(3) Å (Figure 2.16d). Although the carbonyl ligands could be modelled in the respective X-ray structure after each exchange, they displayed a significant degree of thermal motion due to the freedom graned by the MOF pore and the number of single-crystal-to-single crystal transformations endured, which impact crystal quality. As such, differences in the carbonyl bond lengths and angles between isomers cannot be meaningfully resolved. Instead, IR spectroscopy was employed to probe the behaviour of the carbonyl ligands during these isomerisations.

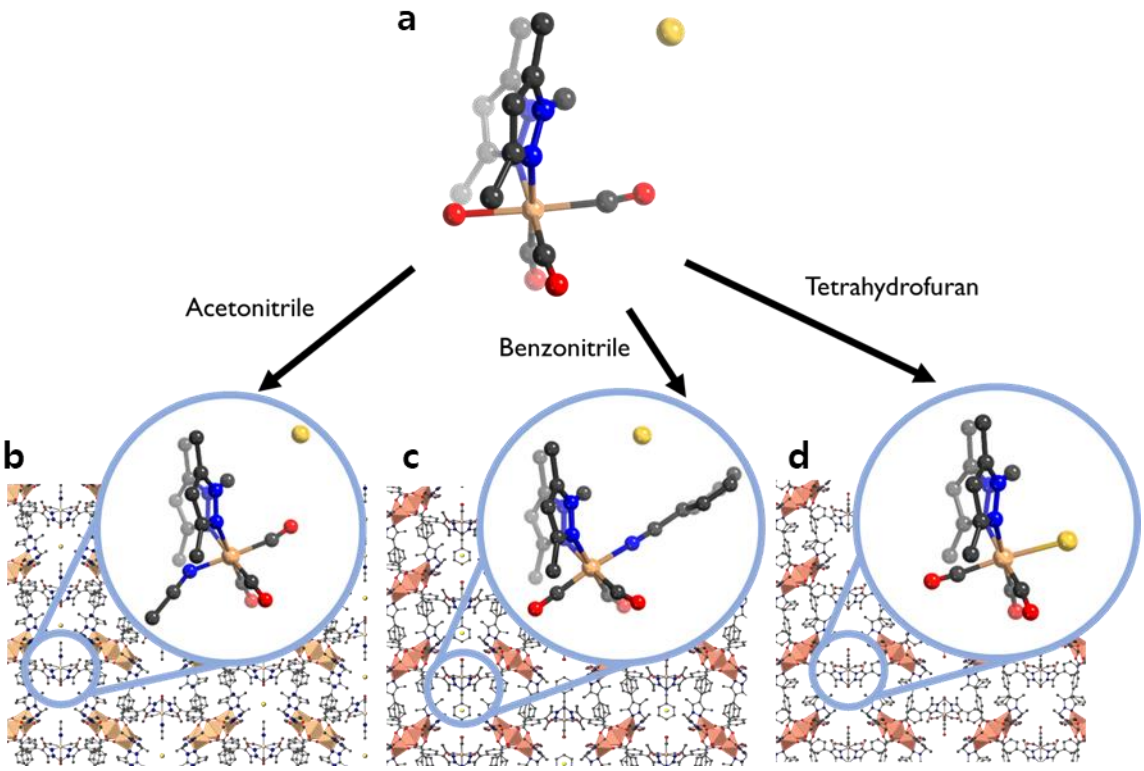

Figure 2.16. Solvent-induced isomerisations in the coordination sphere of $Mn(CO)_3(L')X.Y$ **a)** As-synthesised charge-separated complex in ethanol/water (EtOH ε = 24.5, water ε = 78.4), **b)** solvent exchange with acetonitrile (ε = 37.5), with coordinated acetonitrile, **c)** solvent exchange with benzonitrile (ε = 26), with coordinated solvent at axial position syn to methylene bridge and **d)** solvent exchange with THF (ε = 7.58) producing a charge-neutral complex with coordinated Br^-.(C, grey; Br, yellow; Mn, beige; O, red; N, blue)

Table 2.2. Selected bond lengths for solvent induced isomers of MnMOF$[Mn(CO)_3X]Y$ (X, Y = Br, solvent)

Solvent	Ethanol	Acetonitrile	Benzonitrile	Tetrahydrofuran
Bond lengths	*Å*	*Å*	*Å*	*Å*
Mn-CO(eq)	1.78(2)	1.87(2) (CO)	1.99(3)	1.82(1)
Mn-CO(ax)	2.11(4)	1.92(2)	1.79(2)	1.86(2)
C-O(eq)	1.10(2)	1.16(2)	1.10(2)	1.12(1)
C-O(ax)	1.07(6)	1.01(2)	1.13(2)	1.02(2)
Mn-X(ax)	2.21(2) (OH_2)	1.86(2) (MeCN)	2.02(3) (BzCN)	2.57(3) (Br)
eq = equatorial with respect to L′				
ax = axial with respect to L′				

The position of the carbonyl bands in the IR spectrum are sensitive to changes in the coordination sphere arising from solvent coordination and re-arrangement (Figure 2.17). Samples were dried before analysis, but not activated, leaving solvent in

the pores of the MOF. The parent tricarbonyl complex MnMOF·[$Mn(CO)_3Br$] exhibits three strong absorbance bands in the infrared spectrum, at approximately 2020, 1945, 1890 cm^{-1}, the positions of those bands varying slightly depending on the solvent and coordination environment (whether Br or solvent is coordinated), as previously reported,[47] and due to temperature (Table 2.3). These absorbance bands correspond to the A′ and A′′ symmetric stretches and A′ asymmetric stretch of the *fac*-tricarbonyl complex, assuming C_s point group symmetry (Figure 2.17a).[52]

Table 2.3. Effect of solvent dielectric constant (ε) on ν(CO) for MnMOF[$Mn(CO)_3X$]Y (X, Y = Br^-, solvent)

Solvent	ε	ν (CO) (cm^{-1})	Form
MeCN	37.5	2041, (2029*), 1953, 1921	Ion pair (coordinated NCMe)
BzCN	26	2021, 1937, 1909	Ion pair (coordinated NCBz)
EtOH	24.5	2040, 1951, 1921	Ion pair (coordinated OH_2 or $OHCH_2CH_3$)
THF	7.58	2029, 1951, 1906	Neutral complex

* Shoulder

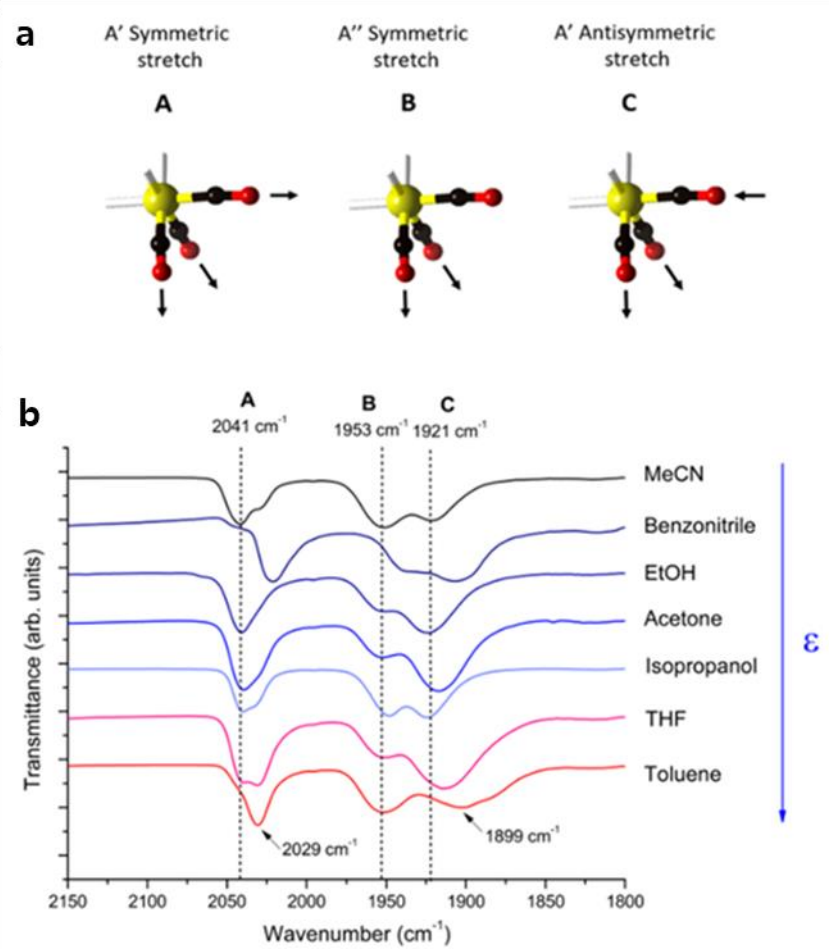

Figure 2.17. a) IR active stretching modes for manganese tricarbonyl complex in MnMOF and **b)** changes in IR carbonyl stretches associated with solvent induced isomerisations.[47]

To follow the exchange of solvents within the MOF pores, samples of the MOF crystals were removed from the bulk at designated time points. Each portion was digested with deuterated hydrochloric acid, and the solution analysed via ^{1}H NMR spectroscopy to determine the proportion of each solved species in the MOF pores, thereby providing an insight into the extent of solvent exchange at each time point. The exchange of solvent in the pores was complete after 3 washes and a total of 45 min of soaking the crystals; however, the isomerisation of the Mn(I) complex was a slower process. Full conversion, as revealed by careful analysis of the carbonyl stretching bands in the IR spectrum, was only seen 24 hrs after solvent exchange (Figure 2.18).

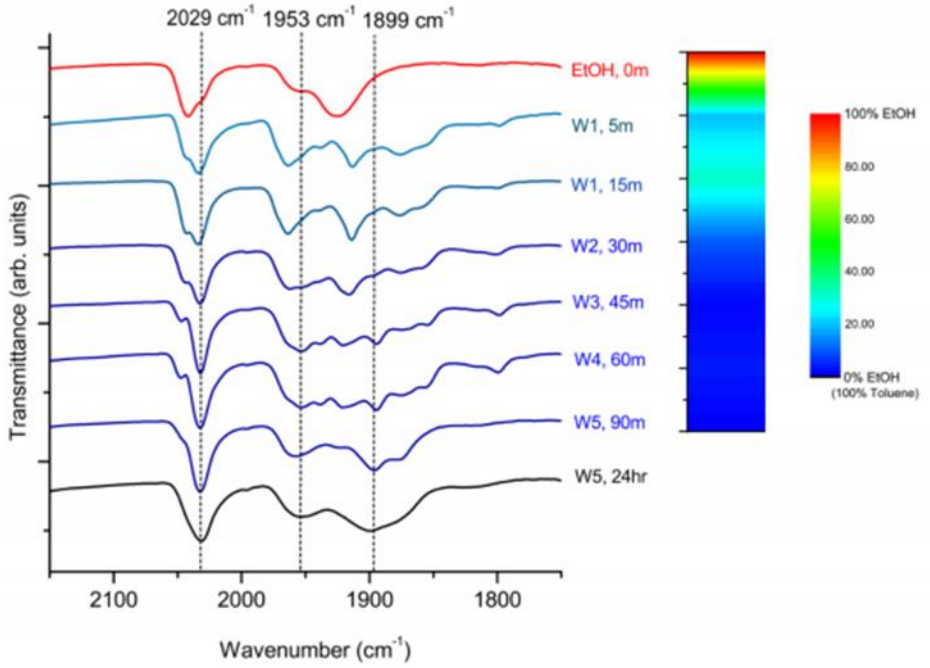

Figure 2.18. Carbonyl stretching region of the IR spectrum during solvent induced isomerisation of the charge-separated complex in ethanol to the charge-neutral complex in toluene. A sample of MnMOF[$Mn(CO)_3(H_2O)$]Br in ethanol was washed a total of five times with dry toluene over the course of 90 min. After each wash a portion of MOF was dried under Ar and analysed by both IR and NMR spectroscopy (digested in D_6-DMSO/DCl).[47]

The *fac*-tricarbonyl Mn(I) complex, $[Mn(CO)_3X]Y$ (X = solvent or Br^-, Y = solvent or Br^-), was coordinated to MnMOF in a quantitative yield at 50 °C through post-synthetic metalation of the vacant bis-pyrazolyl binding site. The coordination environment of the complex could be manipulated through changing the solvent environment in the MOF pore, resulting in a series of isomerisations with retention of crystallinity and long-range order. As such, the behaviour of the Mn(I) complex in the solid-state MOF can mimic that seen in molecular species in solution.

2.3.2 Characterisation and photolysis of $[Mn(bdpm)(CO)_3Br]$

A model complex, $[Mn(bdpm)(CO)_3Br]$ (bdpm = bis(3,5-dimethyl-1H-pyrazol-1-yl)methane), was synthesised from the reaction of bdpm with $[Mn(CO)_5Br]$ in ethanol using a literature procedure.[46] Large yellow block-shaped crystals suitable for single crystal X-ray structure (SCXRD) determination were obtained. The complex crystalised in the *Pnma* space group and the asymmetric unit contains half the complex, with a mirror plane running through the methylene bridge and bisecting the Mn(I) atom and its axial CO and Br ligands. In contrast to the MOF, the bromide anion resides in the

axial position adjacent to the methylene bridge and has a Mn-Br bond length of 2.582(6) Å. A distance 2.53 Å between the bromide and the CH_2 hydrogen on the methylene bridge indicates the presence of a hydrogen bond which preferentially promotes the formation of this isomer. The intermolecular interaction between the Br atom and the *anti*-methylene hydrogen of an adjacent molecule which is 2.85 Å and with a hydrogen-bonding angle of 174.7° (C-H·····Br), and could be classified as a non-classical hydrogen bonding interaction.[53,54] The model complex crystal does not contain any solvent molecules and the complex packs in an alternating zig-zag pattern (Figure 2.19).

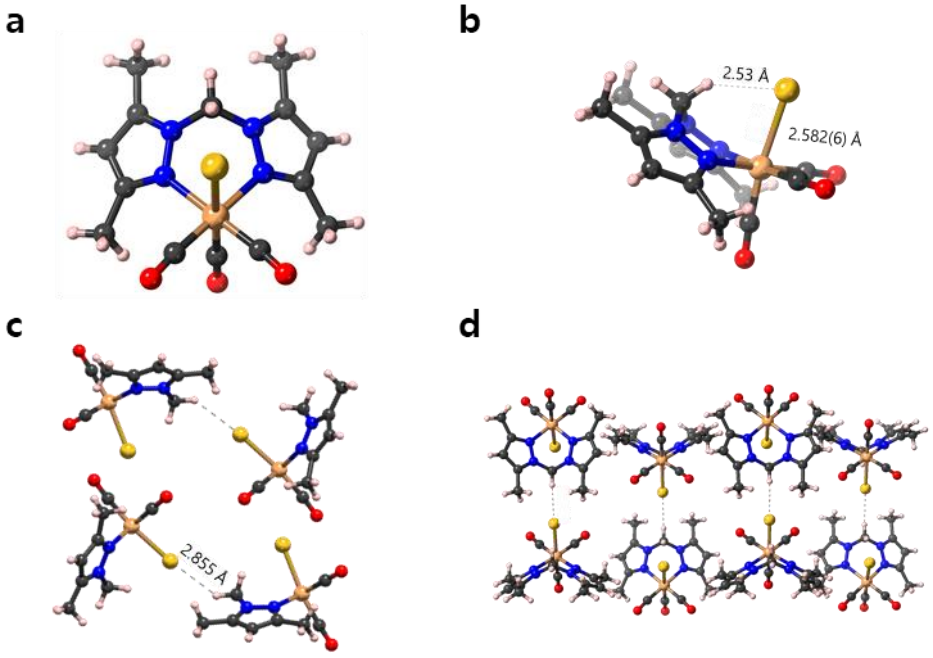

Figure 2.19. Structure and packing of model complex [Mn(bdpm)$(CO)_3$Br] from SCXD, **a)** top view, **b)** side view showing Mn-Br bond length and C-H·····Br hydrogen bond. **c)** Crystal packing diagram viewed down the y-axis and **d)** along the ac plane showing intermolecular hydrogen bonding. (C, grey; Br, yellow; Mn, beige; O, red; N, blue; H, pink)

Given that photolysis of [Mn(diimine)$(CO)_x$Br] entities, in which the diimine is a bispyrazole donor set have seldom been explored, the response of the model complex to irradiation was investigated. Solid-state samples of Mn(bdpm)$(CO)_3$Br display no change in the IR spectrum or crystal structure upon irradiation with visible or UV light. When dissolved in organic solvents and irradiated; however, the complex rapidly reacts, losing the CO IR bands (Figure 2.20, Table 2.4). The behaviour of the complex dissolved in both THF and DCM after irradiation with visible light is very similar, with both samples losing all three carbonyl bands. A small free CO gas band is observed in both solvents, with the band in THF being broader than that in DCM. The photo-decarbonylation reaction also occurred faster in DCM, with complete loss of coordinated CO observed

after only 45 sec, compared to 2 min in THF. This may be due to the slightly higher dielectric constant of DCM (ε = 9.08, compared to THF ε = 7.52)[55] resulting in more favourable coordination and energetically favouring the photoproduct, or the DCM may have been less dry than the THF and adventitious water ligated the Mn(I) centre during photolysis.

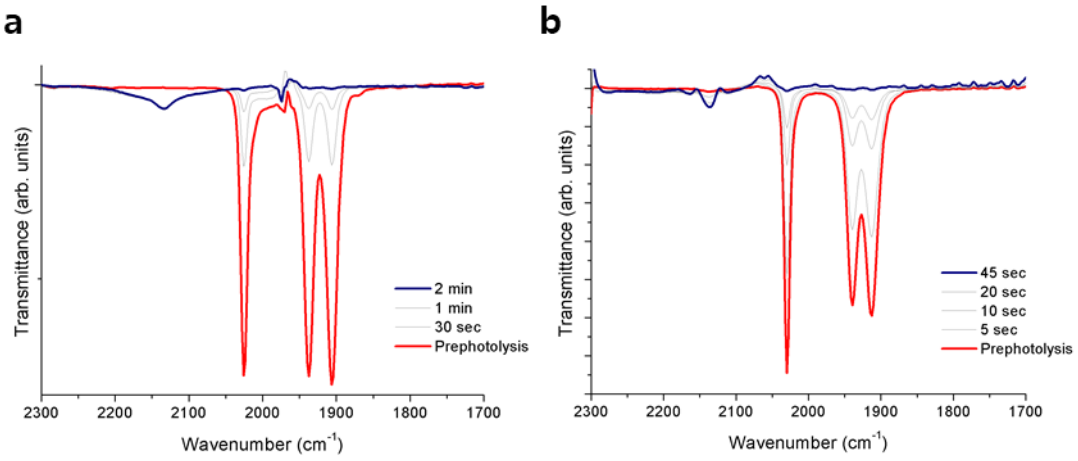

Figure 2.20. IR spectra of model complex Mn(bdpm)$(CO)_3$Br dissolved in **a)** THF and **b)** DCM before (red) and after photolysis (grey, blue).

Table 2.4. IR peak assignments and changes upon photolysis for the model complex Mn(bdpm)$(CO)_3$Br dissolved in THF and DCM

Peaks in THF (Wavenumber cm^{-1})	**Peaks in DCM** (Wavenumber cm^{-1})	**Change with photolysis**	**Assignment**
1904	1913	Decreasing	Tricarbonyl (A' asym)
1935	1939	Decreasing	Tricarbonyl (A'')
2025	2030	Decreasing	Tricarbonyl (A' sym)
2132	2136	Increasing	CO (free)

In summary, the molecular model complex Mn(bdpm)$(CO)_3$Br was synthesised and its photochemical behaviour assessed. In its solid form the complex is stable and does not react under irradiation, with no observed changes in the infrared spectrum or single crystal X-ray diffraction data. When dissolved in THF or DCM the complex quickly loses all three of the coordinated carbonyl ligands under photolysis, with only minor variations observed in the different solvents.

2.3.3 Photolysis of bulk samples of MnMOF[$Mn(CO)_3X$]Y

MnMOF[$Mn(CO)_3Br$] has a strong absorbance band at 373 nm corresponding to the metal to ligand charge transfer absorption band (MLCT), and therefore absorbs UV and blue light (Figure 2.21). The response of the MOF-bound Mn(diimine)$(CO)_3Br$ complex to UV and short wavelength visible irradiation was investigated by solid-state IR and UV-visible spectroscopy, as well as probing the release kinetics via residual gas analyser (RGA) mass spectrometry.

UV-Vis spectroscopy revealed that photolysis of dried MnMOF[$Mn(CO)_3Br$]·THF was accompanied by a distinct colour change of the sample from yellow to white. For the following experiments, "dried" MOF crystals were used, meaning that excess solvent was removed from the crystal surfaces under a flow of nitrogen gas until the sample was a free-flowing powder, but the MOF was not activated, so solvent molecules remained in the MOF pores. The absorbance maxima at 373 nm disappeared, accompanied by an increase in broad peaks in the 400-700 nm range likely attributable to a Mn(II) d-d transition (discussed in Section 2.3.6) (Figure 2.21b). The adsorption corresponding to the MOF in the region 200-300 nm does not exhibit any significant change.

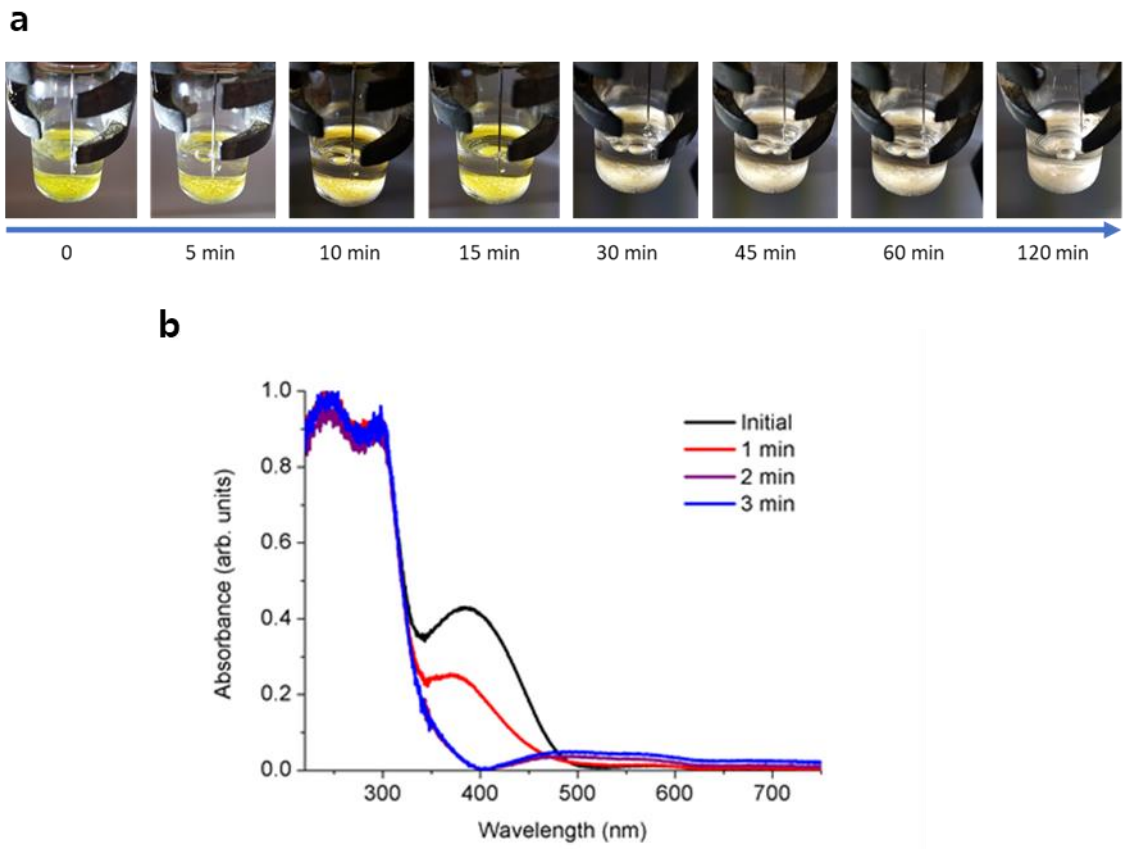

Figure 2.21. a) Changes in the colour of the MnMOF[$Mn(CO)_3Br$]·THF crystals during bulk photolysis under solvent. **b)** Solid-state UV-Vis reflectance spectra of MnMOF[$Mn(CO)_3Br$]·THF, before (black), during (red) and after (purple/blue) photoinduced decabonylation.

The changes in the IR spectrum upon irradiation were investigated under a range of conditions including irradiation in air, under solvent and under vacuum. For irradiation in air the sample was dried in the dark under a flow of inert gas (nitrogen or argon) and then placed in an ATR diamond anvil sample holder. After the initial spectrum was collected the anvil removed and the sample irradiated with a visible wavelength torch. The anvil was replaced to collect spectra at each timepoint, and the irradiation was continued until no changes were observed between two following timepoints. For these samples the three parent tricarbonyl bands disappear, indicating that all three carbonyl ligands permanently dissociate from the Mn(I) centre under photolysis (Figure 2.22).

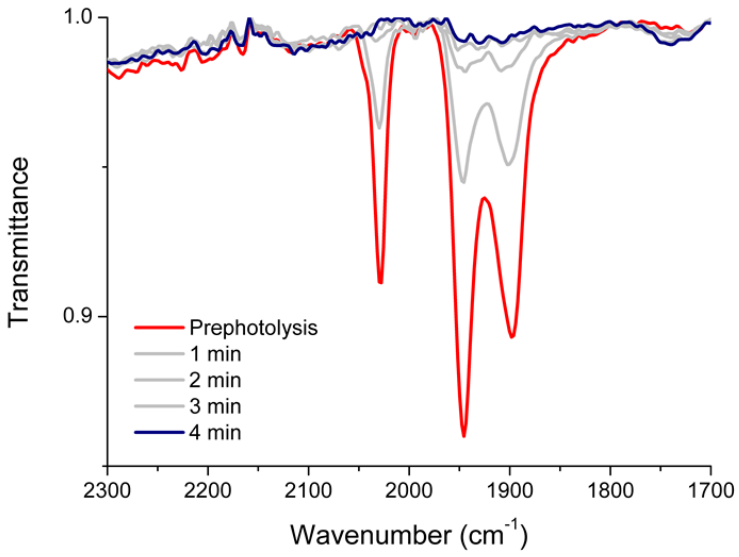

Figure 2.22. ATR-IR spectra of MnMOF[$Mn(CO)_3Br$]·THF before (red), during (grey) and after (blue) photolysis with visible light.

To limit exposure to air and water, photolysis of bulk MnMOF[$Mn(CO)_3X$]Y samples was undertaken in dry solvents. The MOF samples were washed with the freshly distilled solvent of interest (THF or MeCN) using the procedure outlined in Section 2.3 in order to form either the charge-neutral or charge-separated complex. The sample was then irradiated with a visible wavelength torch in the vial under a stream of argon bubbled through the surrounding solvent. Small quantities of sample were removed at designated time intervals, dried under a stream of argon, and placed in nujol oil between NaCl disks for the IR spectroscopy studies. A nujol mull of the compound was used to limit sample exposure to the atmosphere between removal from the vial and when the spectra were recorded. Spectra were normalised to the MOF peaks (ν(C=C) 1607 and 1548 cm^{-1}) to be comparable between time points. Both samples (in THF and MeCN) showed complete loss of the carbonyl peaks in similar time periods (Figure 2.23). IR spectra of a THF solvated sample collected after irradiation for 1 hr showed diminished *fac*-tricarbonyl CO stretches, with a broadened peak around 1929 cm^{-1}, then complete loss of CO peaks after 2 hrs of irradiation. In the case of the MeCN solvated sample, IR spectra collected after 1 hr of irradiation showed two distinct small peaks at 2047 and 2033 cm^{-1}, with one broad peak at 1945 cm^{-1}. Complete loss of the CO stretches took slightly longer for this sample, requiring an extra 30 min of irradiation time. The irradiation times in these experiments are significantly longer than those required for the photolysis of smaller sample quantities with more direct irradiation.

The reaction set-up also may have contributed to the longer reaction times, due to variations in the alignment of the torch with the sample. Thus, comparisons of reaction rates here are only qualitative.

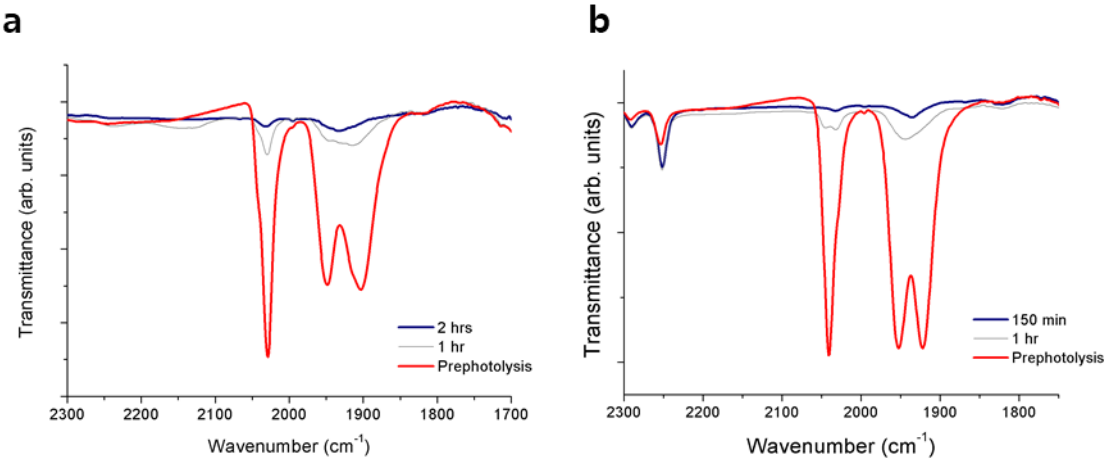

Figure 2.23. IR spectra recorded from the bulk photolysis under solvent of **a)** MnMOF[$Mn(CO)_3Br$]·THF and **b)** MnMOF[$Mn(CO)_3MeCN$]Br. Note the free acetonitrile peaks at 2291 and 2250 cm^{-1} are residual pore and surface solvent and are not of interest.

Unlike the results obtained during photolysis in air, the changes in the carbonyl stretching frequencies observed at intermediate times in the bulk photolysis experiments suggest the presence of isomers like those observed previously in the solvent induced isomerisations (Section 2.3.1). No free CO gas is observed due to constant bubbling of argon through the solution, which displaces any CO released into solution.

Release of CO from a dried sample of MnMOF[$Mn(CO)_3Br$]·THF under UV irradiation and heating was also examined by residual gas analysis mass spectroscopy (RGA-MS), by monitoring the m/z 28 peak (Figure 2.24). Initially, the sample was monitored at room temperature in the dark to assess the stability of the carbonyl complex. No CO was detected at m/z 28 under those conditions. Upon heating to 80 °C (Figure 2.24a) or irradiating the sample with UV light (Figure 2.24b) an immediate, sharp increase in the m/z 28 peak was observed, which continued to increase for a period (13 min) before plateauing. For the heated sample, some of the increase in pressure can be attributed to the increase in temperature as well as the release of CO. Both samples exhibited a slow decrease over the remaining timescale of the experiment due to sampling of the reaction headspace. The time for the complete photolysis of this sample (until no further increase in the m/z 28 peak was observed) was longer than previously observed in the IR experiments due to less direct irradiation of the sample.

This was unavoidable in this reaction set-up due to the size of the sapphire window into the reaction cell and the surface area of sample exposed to the light. Notably, no ongoing gradual increase in CO concentration was observed, as might be expected if CO gas trapped in MOF crystals was being slowly released.

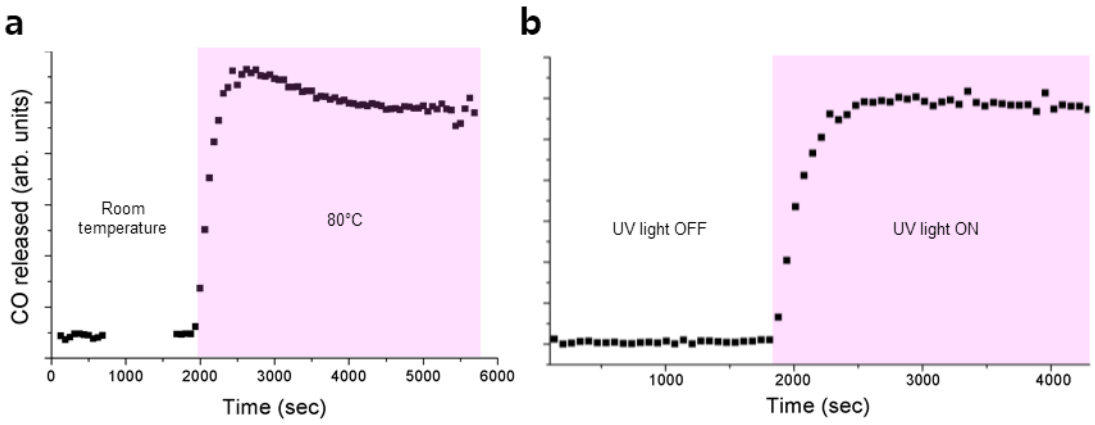

Figure 2.24. RGA-MS of the m/z = 28 peak corresponding to CO released from MnMOF[$Mn(CO)_3Br$]·THF under **a)** thermolysis at 80 °C and **b)** photolysis with UV light.

Together these observations show that in the bulk state, unlike some other Mn(diimine)(CO)Br complexes, irradiation with blue or UV light causes the permanent dissociation of all three carbonyl ligands from the Mn centre within MnMOF. This is distinct from the molecular analogue which does not release CO in the solid-state. Furthermore, the CO gas is not trapped in the MOF crystals or on the crystal surface but is released readily into the surrounding atmosphere.

2.3.4 Matrix isolated time-resolved-IR photolysis of MnMOF[$Mn(CO)_3Br$]·THF

To elucidate the steps involved in this photodissociation reaction, matrix isolated time-resolved infrared spectroscopy (TR-IR) was employed. For this technique, MOF samples solvated with THF and dried under a flow of nitrogen gas were mixed with a salt (NaCl or KBr) and pressed into a transparent disk (9 x 0.5 mm) under 6 tonnes of pressure in the dark. The disks were then placed between lead gaskets in a sealed chamber with CaF_2 windows. The cell was placed under a vacuum shroud and evacuated to approx. 1 x 10^{-6} mbar. The photolysis reaction was then examined at room and low-temperature (190 K) under irradiation with a high-powered UV-vis Hg lamp. No significant changes were observed in the IR spectra upon cooling, indicating that no

structural changes or rearrangements occurred due to the lower temperature (Figure 2.25).

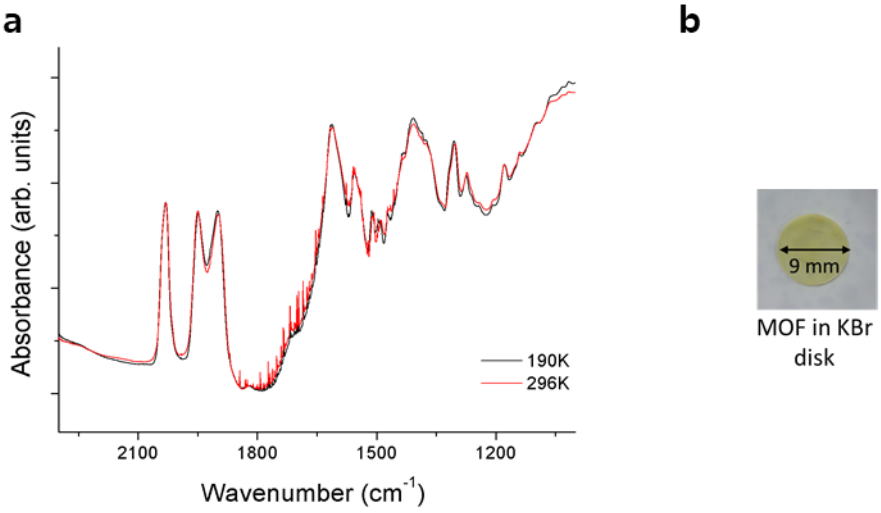

Figure 2.25. a) Matrix isolated IR spectra of MnMOF[$Mn(CO)_3Br$]·THF in a KBr disk at room temperature (296K, red) and cooled to 190K (black) and **b)** photo of MnMOF[$Mn(CO)_3Br$]·THF pressed in a KBr disk.

To ensure that the MOF had not been destroyed by the processes involved in disk preparation, cooling to 190K, exposure to vacuum and irradiation, powder X-ray diffraction experiments were undertaken. For the MOF PXRD pattern to be observable against that of the crystalline salt matrix, a much higher loading of MOF had to be used compared to that used for the IR experiments (50 mg MOF/200 mg salt). Even with this higher loading, the MOF PXRD pattern was low in intensity, but observable in the disk sample. The most significant low angle peaks corresponding to the MOF were present in the disk and not appreciably changed after photolysis (Figure 2.26).

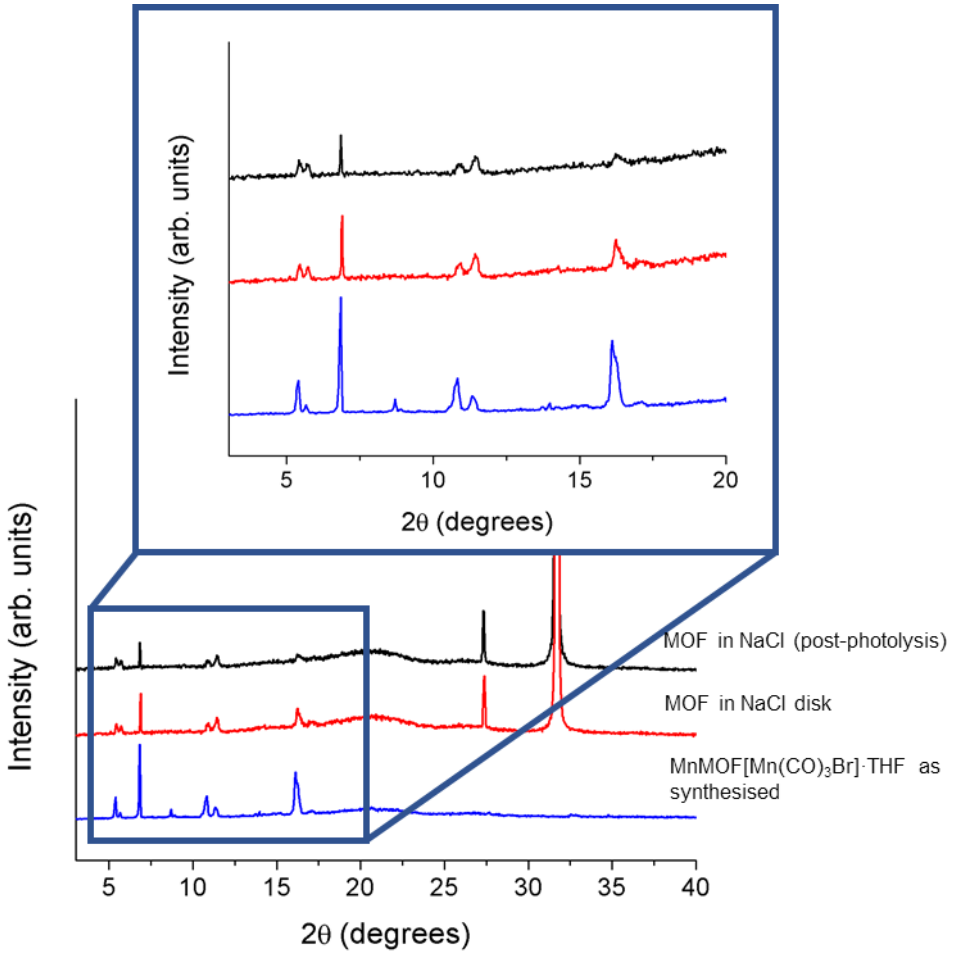

Figure 2.26. PXRD patterns of MnMOF[$Mn(CO)_3Br$]·THF as synthesised (blue), incorporated into an NaCl disk for matrix isolated IR studies (red) and in the NaCl disk after photolysis on the matrix isolated IR apparatus (black).

The combination of incorporating the MOF into a salt matrix, cooling the sample and limiting the exposure to light due to the apparatus windows resulted in slower decarbonylation reactions and allowed reaction intermediates to be observed by IR spectroscopy.

MnMOF[$Mn(CO)_3Br$]·THF in NaCl at 190K

MnMOF[$Mn(CO)_3Br$]·THF was gently dried under a flow of nitrogen until it became a freely flowing powder, then mixed with finely ground sodium chloride (not anhydrous) and pressed into a disk. The sample was then irradiated with a Hg lamp, with IR spectra collected after 1, 5, 15, 35, 75 and 135 min of irradiation (Figure 2.27, Table 2.5). During this experiment, the three original carbonyl bands decrease in

intensity, with the bands at 2033 and 1912 cm^{-1} decreasing at the same rate, while the band at 1947 cm^{-1} decreasing at a slower rate. Meanwhile, bands develop at 2129, 1891, 1850 and 1821 cm^{-1}. The 2129 cm^{-1} band is smaller than the other peaks and corresponds to free CO trapped in the MOF/salt matrix. This is consistent with the literature, where CO trapped in an ice matrix was observed at 2139 cm^{-1} compared to 2143 cm^{-1} for unconfined gaseous CO.[56] The further shift to lower wavenumbers indicates the presence of some interactions with the MOF or salt matrix. The remainder of the new peaks correspond to dicarbonyl complexes formed from the loss of one CO ligand. As discussed earlier, a *fac*-dicarbonyl species with coordinated solvent would show two IR bands at lower wavenumber compared to the tricarbonyl complex due to more back-donation from the metal centre to the equatorially coordinated carbonyls.

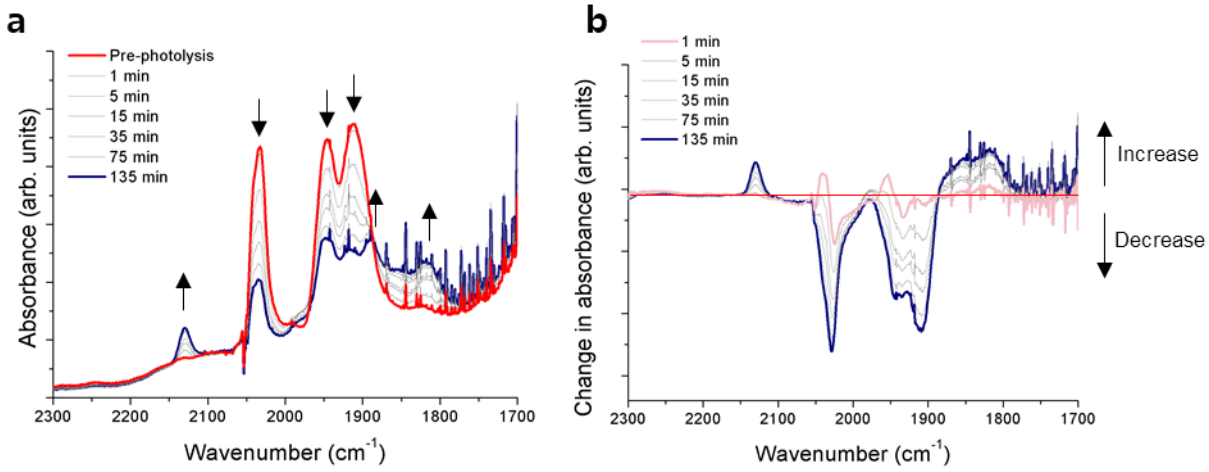

Figure 2.27. a) Carbonyl region of IR spectrum for photolysis in matrix isolated MnMOF[$Mn(CO)_3Br$] sample dried from THF and incorporated into a NaCl disk at 190 K. **b)** Difference spectra showing the change in absorbance from parent complex.

Table 2.5. Peaks in the carbonyl region of IR spectrum during photolysis in matrix isolated MnMOF[$Mn(CO)_3Br$]·THF sample incorporated into a NaCl disk at 190K

Peak (cm^{-1})	Change with photolysis	Species
2129	Increasing	Free CO
2035	Decreasing	Tricarbonyl (a′ sym)
1947	Decreasing	Tricarbonyl (A′′)
1916	Shift	Tricarbonyl
1911	Decreasing	Tricarbonyl (A′ asym)
1891	Increasing	Dicarbonyl (overlapping)
1854	Increasing	Dicarbonyl
1821	Increasing	Dicarbonyl

Kinetic analysis of the loss of the tricarbonyl bands reveals that the band at 1947 cm^{-1} decreases at a slower rate than the other two bands, thus indicating the presence of another dicarbonyl band growing beneath it, resulting in four dicarbonyl bands in total (Figure 2.28). Due to the overlap of the peaks the rate of change of the dicarbonyl peak at 1891 cm^{-1} could not be plotted. The intensity of the dicarbonyl peaks do not increase appreciably over time, therefore indicating that they are transient and that there is a steady state concentration of these species after the initial photolysis step. As the NaCl matrix was not anhydrous in this instance, it is likely that the dicarbonyl bands correspond to a mixture of $[Mn(CO)_2(L')(THF)]Br$ and $[Mn(CO)_2(L')(H_2O)]Br$.

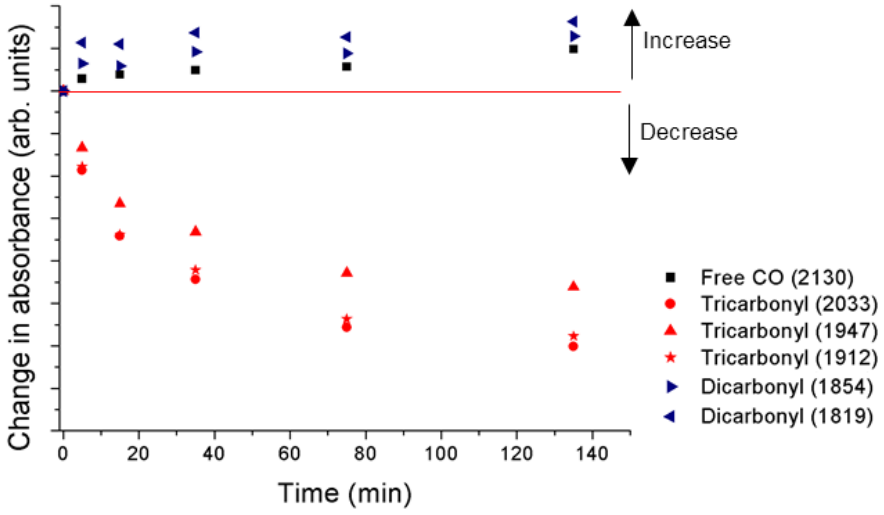

Figure 2.28. Rate of change in absorbance of carbonyl peaks of MnMOF$[Mn(CO)_3Br]$·THF in NaCl at 190 K during photolysis. Note the tricarbonyl peak at 1947 cm^{-1} (red triangle) decreases at a different rate to the other two tricarbonyl peaks.

MnMOF$[Mn(CO)_3Br]$·THF in KBr at 190 K

To prevent reactions with water the matrix material was changed to anhydrous potassium bromide. The MnMOF$[Mn(CO)_3Br]$·THF sample in KBr was then prepared and analysed in the same way as described in the previous section to give the following results (Figure 2.29, Table 2.6). Like the previous sample, the three carbonyl bands associated with the tricarbonyl parent complex decreased with irradiation and a small band associated with free CO gas increased. In contrast with the previous sample, only one clear dicarbonyl band is observed at 1830 cm^{-1}.

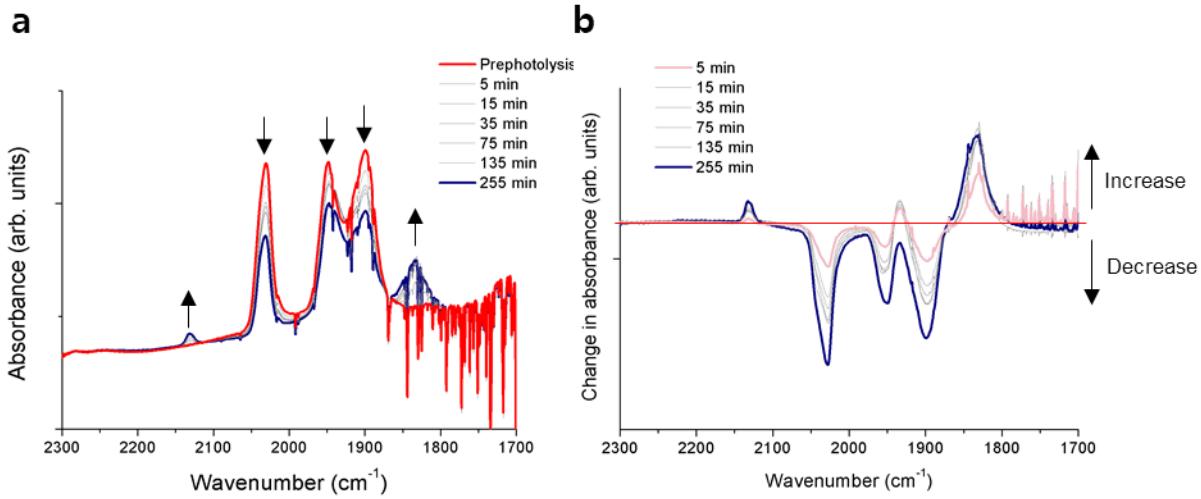

Figure 2.29. a) Time-resolved matrix isolated IR of the carbonyl region during the photolysis of MnMOF[Mn(CO)3Br]·THF in a KBr disk at 190K. **b)** Difference spectra showing the change in absorbance between time points.

Table 2.6. Peaks in the carbonyl region of IR spectrum during photolysis in matrix isolated MnMOF[$Mn(CO)_3Br$]·THF incorporated into a KBr disk at 190K

Peak (cm^{-1})	Change with photolysis	Species
2131	Increasing	Free CO
2033	Decreasing	Tricarbonyl
1948	Decreasing	Tricarbonyl
1901	Decreasing	Tricarbonyl
1832	Increasing	Dicarbonyl

Kinetic analysis of the change in the band intensities over time shows fewer clear trends in comparison to the spectra recorded in NaCl (Figure 2.30). Issues with the correction due to imperfect alignment of the sample with the spectrometer likely account for unexpectedly positive or negative changes observed in the trendline. Despite this, valuable information may still be extracted from this analysis. While only one dicarbonyl band was observed, all three tricarbonyl bands decreased at different rates, indicating the presence of at least one other band increasing in the same region. Dicarbonyl complexes of the form MnMOF[$Mn(CO)_2X$] are expected to exhibit two carbonyl bands;[33,44,57] therefore, it is probable that in addition to the band at 1832 cm^{-1}, a second dicarbonyl band lies between 1901-1948 cm^{-1}. Previous studies found the transient dicarbonyl complex [Mn(diimine)$(CO)_2$Br], tethered to a Mn(II) based MOF, exhibited ν(CO) bands at 1839 and 1908 cm^{-1}.[44] The expected position of the second

dicarbonyl band could be investigated through computation experiments; however, these were out of the scope of this project. The intensity of the dicarbonyl band at 1832 cm^{-1} increased rapidly with the initial photolysis step, then slowly declines over time, indicating that this species is transient.

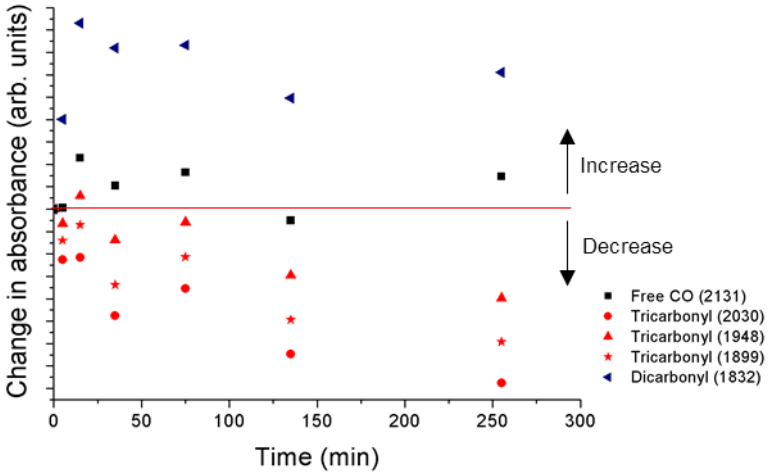

Figure 2.30. Rate of change in absorbance of carbonyl peaks of MnMOF[$Mn(CO)_3Br$]·THF in KBr at 190 K during photolysis.

Photolysis of MnMOF[$Mn(CO)_3Br$]·THF in anhydrous KBr at 190K showed different behaviour to the previously discussed sample in non-anhydrous NaCl matrix. In the absence of significant quantities of water, a single band at 1832 cm^{-1} can be observed due to the formation of an intermediate dicarbonyl species with coordinated THF.

MnMOF[$Mn(CO)_3Br$]·THF in KBr at 296K

Finally, the photolysis MnMOF[$Mn(CO)_3Br$]·THF in KBr at room temperature (296K) was studied. This produced spectra very similar to those conducted on the bulk samples discussed in Section 2.3.3 (Table 2.7). The intensity of the tricarbonyl peaks decreased, although did not disappear on the time scale of the experiment (Figure 2.31). Despite the higher temperature, loss of CO was significantly slower than during photolysis in a vial or on a small sample in air, most likely due to incorporation in the salt matrix and the reaction set up. Only a small free CO peak was observed at 2131 cm^{-1}, with the higher temperature allowing released CO to escape the matrix. Development of peaks from reaction intermediates were very small, but observable at 1857 and 1816 cm^{-1}. These peaks do not match those observed at 190K and there are

several possibilities for their origin. They may be caused by a mixture of dicarbonyl isomers, which are forming due to either the loss of CO from different positions or thermally induced rearrangement after the loss of a CO ligand. They may also result from further loss of CO, forming monocarbonyl intermediates, which may exist as several different isomeric arrangements, each with a single IR band. As these peaks are small and do not continue to grow to an appreciable extent with further photolysis, they are attributed to unstable intermediates which reacted further.

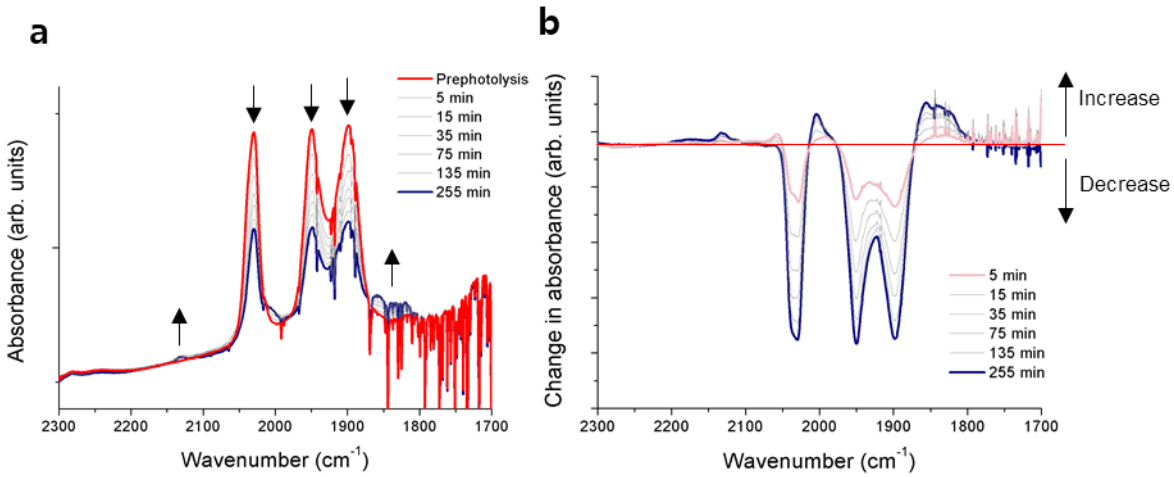

Figure 2.31. a) Time-resolved matrix-isolated IR of the carbonyl region during the photolysis of MnMOF[$Mn(CO)_3Br$]·THF in a KBr disk at 296K. **b)** Difference spectra showing the change in absorbance between time points.

Table 2.7. Peaks in the carbonyl region of IR spectrum during photolysis in matrix isolated MnMOF[$Mn(CO)_3Br$]·THF incorporated into a KBr disk at 296K

Peak (cm^{-1})	Change with photolysis	Species
2131	Increasing	Free CO
2032	Decreasing	Tricarbonyl
1949	Decreasing	Tricarbonyl
1899	Decreasing	Tricarbonyl
1857	Increasing	Monocarbonyl
1816	Increasing	Monocarbonyl

Kinetic analysis of the change in peak intensities demonstrated for the first time that all three tricarbonyl peaks decreased at the same rate, indicating that there are no dicarbonyl reaction-intermediate peaks masked beneath them. This suggests that the peaks (1857 and 1816 cm^{-1}) are caused by two or more monocarbonyl species (Figure

2.32). These bands are unusually low in frequency and should be investigated further through computational studies. This suggests that the dicarbonyl species observed at 190K is very unstable at room temperature and hence loss of the second carbonyl ligand occurs rapidly. The monocarbonyl peaks reach a steady state after 35 min of photolysis, after which they only increase minimally over the course of the experiment. This indicates that at room temperature under matrix isolated conditions the monocarbonyl species is also transient and the Mn(I) complex undergoes complete decarbonylation.

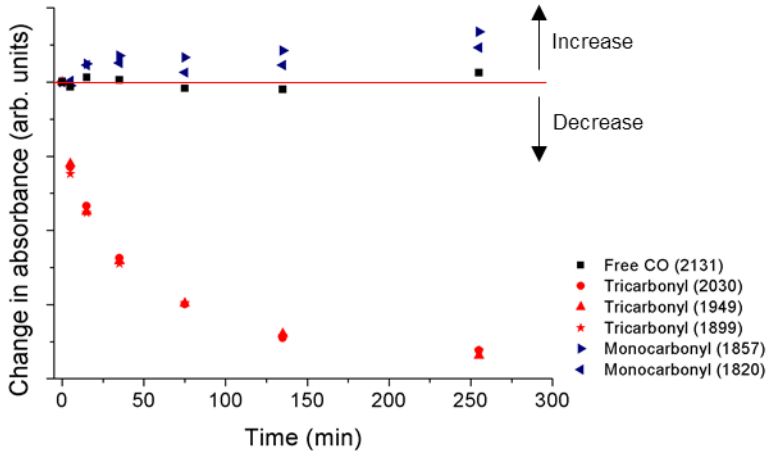

Figure 2.32. Rate of change in absorbance of carbonyl peaks of MnMOF[$Mn(CO)_3Br$]·THF in KBr at 296 K during photolysis.

Studies of MnMOF[$Mn(CO)_3Br$]·THF by matrix isolated IR spectroscopy showed that the photoactivated loss of CO is stepwise, with initial formation of dicarbonyl solvated intermediates where the vacant coordination site is occupied by THF or water. These species are transient and at room temperature rapidly undergo further carbonyl loss to give more than one monocarbonyl isomer, which are longer lived at room temperature. These monocarbonyl species are also transient and undergo loss of the final carbonyl ligand. Free CO gas can be observed to be trapped temporarily in the matrix, especially at 190K, with a peak at 2131 cm^{-1}, before being removed from the matrix under vacuum.

2.3.5 Photocrystallography of MnMOF[$Mn(CO)_3X$]Y

The photoinduced decarbonylation of the Mn(I) complex in MnMOF was followed by a series of X-ray diffraction "snapshots". In previous work conducted by a collaborator, these studies were initially conducted on a single crystal of the THF solvated sample MnMOF·[$Mn(CO)_3Br$]·THF, with multiple data collections following the specified periods of irradiation.[59] The experiment was conducted with irradiation from a visible LED light source at 270 K and data collections at 150 K, with the crystal slowly warmed up and cooled down between each cycle of irradiation and collection. Initially the structure of the MOF-bound complex contains the *fac*-[$Mn(CO)_3Br$] entity, with the Br^- anion residing on the less hindered axial site of the complex adjacent to the methylene bridge of the bis-pyrazole ligand (Figure 2.33a). After 30 min of irradiation, a change in the Mn(I) coordination sphere is evident (Figure 2.33b). The axial Br- and CO ligands remain largely unaffected, but the equatorial sites are now disordered between CO and THF ligands. While the earlier matrix isolated IR results show that a dicarbonyl complex is initially formed at low-temperature, the presence of a mirror plane results in the dicarbonyl complex being disordered across both equatorial positions. Therefore, the two equatorial sites are occupied by a lone THF molecule and the remaining CO ligand, with both disordered across the mirror plane which bisects the complex, indicating the formation of a *cis*-dicarbonyl species. The loss of an equatorial CO before the axial CO is expected due to the competition of the two equatorial carbonyls for back-bonding, combined with the π-accepting capability of the bis-pyrazole ligand, increasing the lability of these Mn-C(O) bonds in comparison to the analogous bond for the carbonyl *trans* to the bromide anion, which is not competing for π-backbonding.[58] While computational experiments were outside the scope of this study, these may show the difference in ν(CO) bands expected from *cis*- or *trans*-dicarbonyl complexes, to compare this finding to the previous IR studies.

After 50 min of photolysis, further changes to the coordination sphere are evident (Figure 2.33c). Two THF molecules are clearly coordinated to the equatorial positions, but disorder of the Br over the axial positions prevents determination of the structure, which could be a monocarbonyl complex or Mn complex without coordinated CO. Analysis of the axial position adjacent to the methylene bridge shows that the Br anion has become disordered over both axial positions, suggesting some dissociation

of the third CO axial ligand, but whether it was released completely or recombined to form a conformational isomer could not be confirmed. Further photolysis did not provide any additional clarification of the structure. It is notable that in the late-stage photolysis structures, the occupancy of the manganese atom decreases and a reduction in the electron density of the ligands complicates the interpretation.

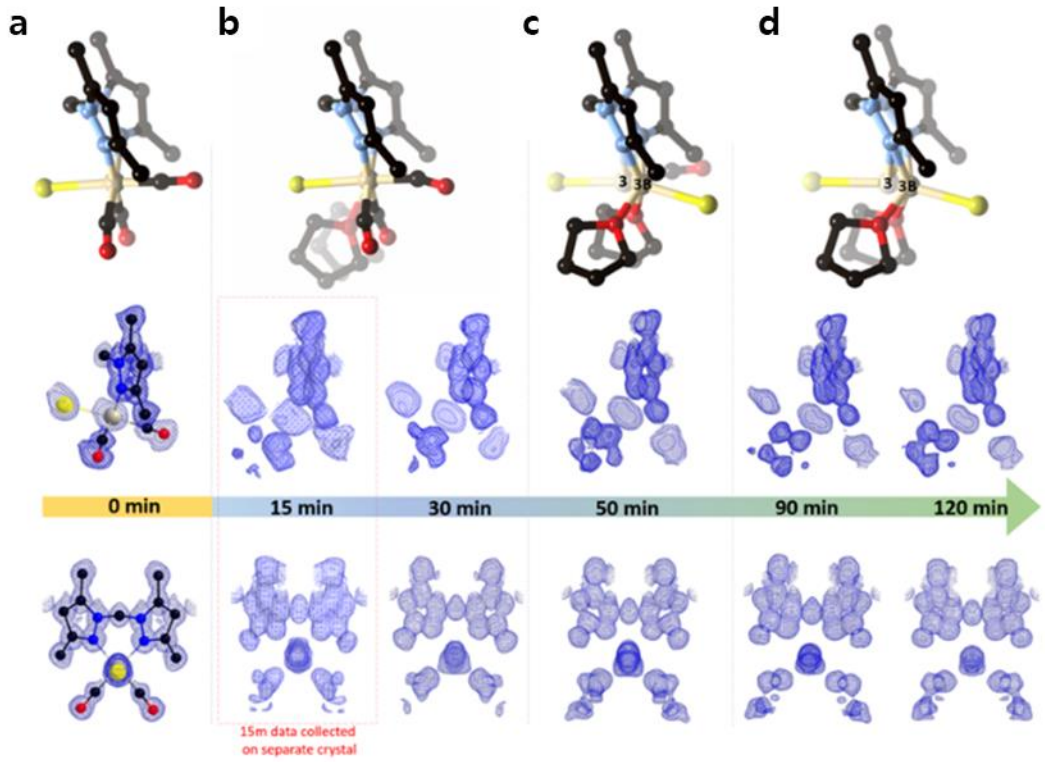

Figure 2.33. Photodecarbonylation pathway for MnMOF[$Mn(CO)_3Br$]·THF, including F_{obs} maps with data collections taken **a)** pre-photolysis, **b)** after 30 min of irradiation with visible light, **c)** after 50 min of irradiation and **d)** after 120 min of irradiation[59]

Given that the proposed MnMOF[$Mn(THF)_3Br$] final photoproduct was not able to be modelled, the photocrystallography of MnMOF[$Mn(CO)_3NCMe$]Br solvated in acetonitrile was investigated. Acetonitrile, in contrast to THF, has a higher dielectric constant (ε=37.5 vs ε=7.58)[55] and a higher coordinating affinity, resulting in the initial manganese carbonyl complex being charge-separated, with the anion residing in the pore of the MOF. In order to examine the charge-separated complex and analyse the final photoproduct, single crystals of acetonitrile solvated MnMOF[$Mn(CO)_3NCMe$]Br were mounted in Fomblin oil and cooled to 100K before collecting an pre-photolysis data set. The crystals were exposed to as little light as possible during the mounting process; however, it was impossible to prevent some light exposure due to the need to

use an optical microscope to pick and mount the crystal. It was also found that the acetonitrile solvated crystals were much more easily damaged and prone to solvent loss than the same compound solvated in THF or ethanol. As such, to prevent damage to the crystals during transport to the Diamond Light Source and to ensure the absence of water, the crystals were first solvent exchanged and stored in dry THF. Solvent exchange with dry acetonitrile was then performed on site, 12 hrs before collection.

The initial pre-photolysis structure shows the *fac*-[$Mn(CO)_3NCMe$] complex, with the coordinated acetonitrile ligand in the axial position opposite the methylene bridge. The bromide anion resides in the MOF pore approximately 2.87 Å from the coordinated acetonitrile and 4.01 Å from the axial carbonyl ligand of the adjacent complex in the channel of the MOF (Figure 2.34a). After collecting the initial set of data, the crystal was irradiated with UV/visible light with diffraction data collections taken every 10 min for a total of 30 min. The use of UV/visible irradiation in this instance was dictated by the availability of light sources at the synchrotron. Unlike the previous experiment with the THF solvated MOF, no temperature changes were made during the irradiation and data collection process. This was due to a combination of a more powerful UV/Vis light source, time constraints and the desire to minimise damage to the crystal from several cycles of warming and cooling. Analysis of the F_{obs} maps (Figure 2.34) shows the changes in electron density arising from the ligands around the Mn(I) metal centre and from the bromide anion during photolysis.

After 10 min of UV photolysis, the electron density map revealed changes in the equatorial ligands and the position of the bromide anion (Figure 2.34b). Electron density associated with coordinated acetonitrile at the equatorial positions can be observed, although like the THF sample discussed previously, the presence of the mirror plane down the centre of the complex means that the observed electron density represents a superposition of coordinated carbonyl and acetonitrile ligands. The equatorial ligands were modelled in two parts as acetonitrile and carbonyl with fixed U_{iso} parameters as their occupancies were allowed to freely refine. They were then fixed at 75% (MeCN) and 25% (CO) and their U_{iso} were allowed to freely refine. Refinement of the Br anion at a full occupancy led to large displacement parameters than the pre-photolysis structure, which indicated that these values were compensating in the least-squares fit for an over-estimated site occupancy. The occupancy of the anion was, therefore, modelled at 75%, now 3.93 Å from the axial carbonyl. Attempts to model the electron

density at other low-occupancy sites where the Br^- was situated were problematic due to the low electron density associated with these positions. The Mn-CO bond length for the axial carbonyl shortened slightly from the pre-photolysis structure (1.92(2) Å to 1.87(1) Å), while the equatorial Mn-C bond lengthened from 1.87(2) Å to 2.04(2) Å.

After 20 min of photolysis the electron density corresponding to the Br^- anion in the pore decreased and was modelled at 66% (Figure 2.34c). Bromide coordinated to the Mn atom was modelled, with a bond length of 2.77(2) Å, within error of the Mn-Br bond of 2.82(6) Å observed in the model complex. Extra regions of electron density at this position were modelled as a carbonyl ligand. The U_{iso} of both the carbonyl and bromide were fixed and the occupancies allowed to freely refine, resulting in 33% occupancy for the Br^- and 25% occupancy for the carbonyl. Attempts to adjust the occupancies to ensure the position was fully occupied resulted in over-assigned electron density based on the displacement parameters, so this may be due to this coordination site being vacant for some of the complexes in the crystal. Due to deteriorating crystal quality and low signal to noise ratios assignment of electron density must be carefully considered to avoid problematic overinterpretation of the data. The equatorial and axial acetonitrile ligands were modelled at 100% occupancy and were coordinated to the Mn atom at bonding angles (Mn-N-C) of 160(1)° (axial) and 165(1)° (equatorial).

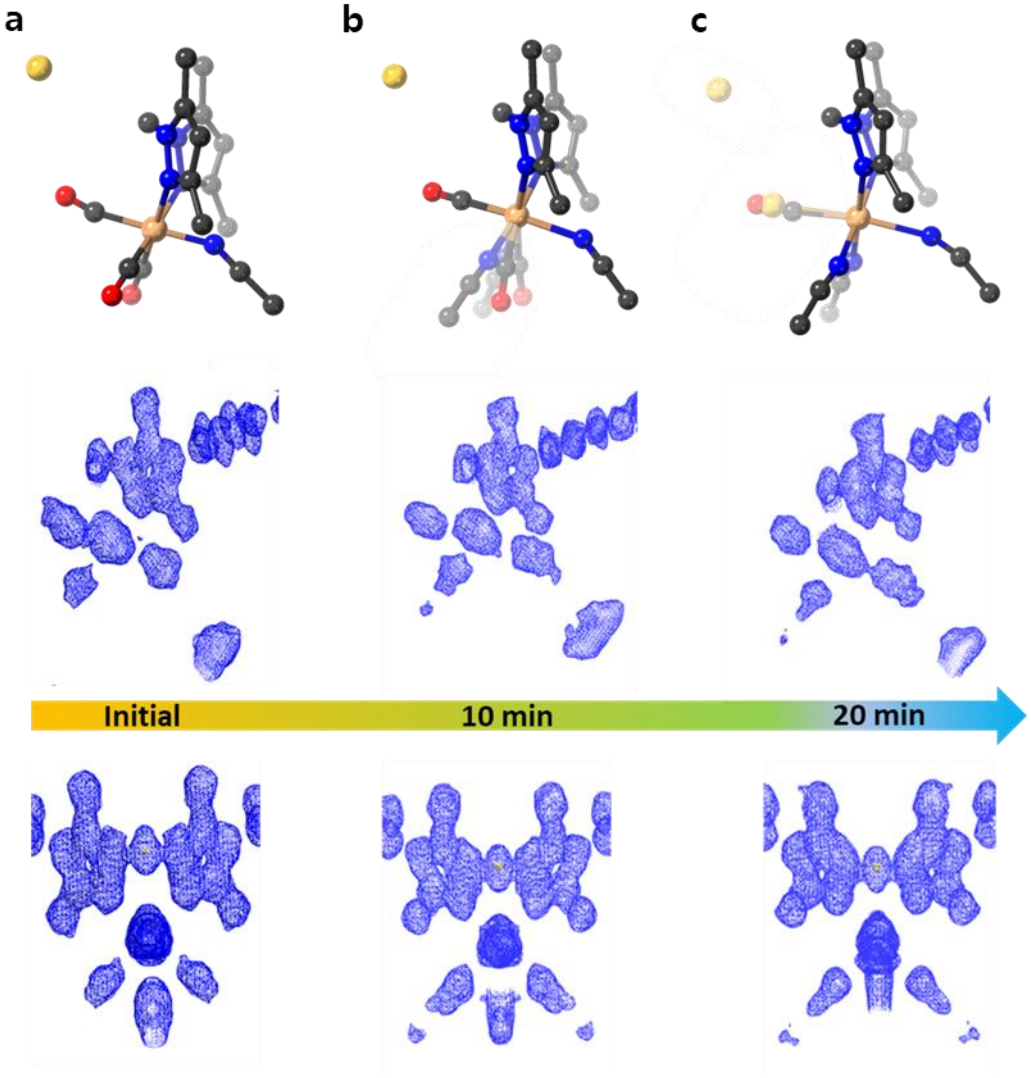

Figure 2.34. Photodecarbonylation of a single crystal of MnMOF[$Mn(CO)_3MeCN$]Br including F_{obs} maps with data collections taken **a)** pre-photolysis, **b)** after 10 min of irradiation with UV light and **c)** after 20 min of irradiation. The equatorial ligands in (b) (MeCN and CO) are disordered, with occupancies of 75% and 25% respectively. In (c) the occupancy of the Br^- in the pore is modelled at 33%, while the coordinated Br^- is at 25%. Occupancy of the axial carbonyl is fixed at 25%. (Mn, beige; C, grey; N, blue; O, red; Br, yellow)

The crystal was irradiated for a further 10 min and a data set collected, but the structure was unable to be solved due to damage to the crystal and a much-reduced overall data quality. A crystallographic 'snapshot' of the final photochemically decarbonylated manganese complex could, therefore, not be achieved; however, the series of photocrystallography experiments conducted with MnMOF[$Mn(CO)_3NCMe$]Br provided valuable insights into the reaction intermediates. The identity of the final photoproduct corresponding to the loss of all three carbonyl ligands, observed by spectroscopy in the bulk phase experiments, could not be determined due to low crystallographic occupancy of this species and disorder.

2.3.6 Controlled atmosphere IR spectroscopy of MnMOF[Mn(CO)$_3$X]Y

To characterise the terminal photoproduct, a custom-made IR cell was built to study the photolysis reaction under a controlled atmosphere. The cell contains of two NaCl disks, between which the solid MOF sample can be held. This assembly is enclosed within a sealed stainless-steel cell fitted with two *Swagelok* valves which can be connected to vacuum or gas lines as required. The cell has two sodium chloride windows which align with the sample and allow in-situ IR spectroscopy data to be collected under a controlled atmosphere. The photolysis of MnMOF[Mn(CO)$_3$Br]·THF and MnMOF[Mn(CO)$_3$MeCN]Br with visible light was performed under vacuum and monitored by IR spectroscopy at regular intervals. Once the reaction was complete, indicated by the complete disappearance of the CO bands, the cell was placed under a CO atmosphere at 1 bar. After 30 min, an IR spectrum was collected which confirmed the formation of new CO bands (2057, 2049, 2041 and 2033 cm^{-1}) at higher wavenumbers than those of the parent complex (2027, 1951 and 1892 cm^{-1}) (Figure 2.35). This new manganese carbonyl complex did not show any response to irradiation with visible light, but the bands disappeared after the cell was opened to the atmosphere or after remaining under vacuum for 72 hrs.

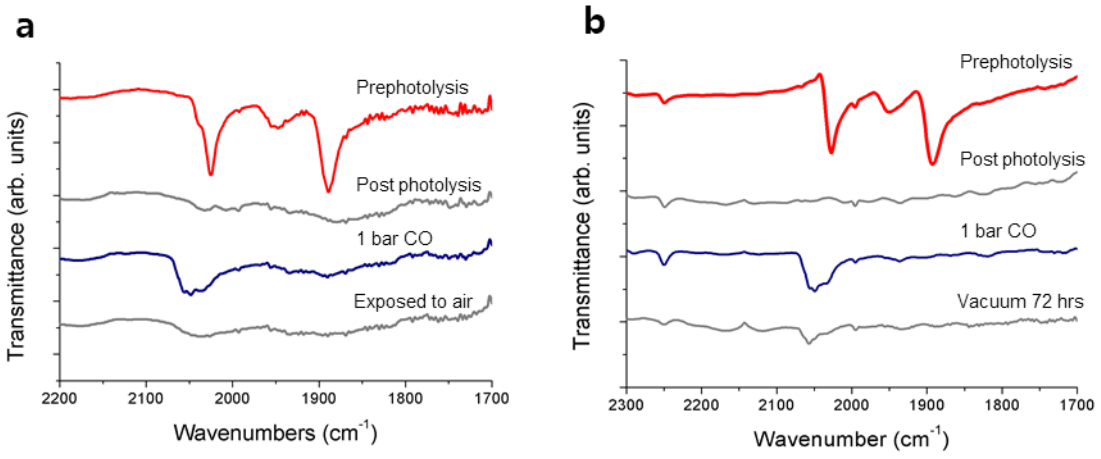

Figure 2.35. MnMOF[Mn(CO)3X]Y samples photolyzed with visible light in a controlled atmosphere IR cell then placed under CO gas **a)** MnMOF[Mn(CO)$_3$Br]·THF and **b)** MnMOF[Mn(CO)$_3$MeCN]Br. Note that the intensity of the parent tricarbonyl band at 1951 cm^{-1} is weaker in intensity compared to the other two bands than seen in pervious experiments due to background corrections from the cell.

The formation of these new bands after exposure to CO gas was unexpected. As CO is a better ligand than either THF or acetonitrile it was hypothesised that adding CO to the photolyzed MOF would reform the original complex, which obviously did not

occur. While Mn(II) carbonyl complexes are rare, they have been previously reported[60,61] and exhibited IR stretches at 2124 (s), 2085 (m) and 2032 (vs) cm^{-1}. Previously described Mn(II) tricarbonyl species were reported to be green, red or violet in colour and were electrochemically oxidised from *fac*-[Mn(I)$(CO)_3$dpmX] (dpm = $Ph_2PCH_2PPh_2$, X = Cl, Br) in the presence of $NOPF_6$ to give low spin *mer*-[Mn(II)$(CO)_3$dpmX]PF_6 (X= Cl^-, Br^-) complexes. These complexes were then reduced, either electrochemically or by solvent to give the *mer*-Mn(I)$(CO)_3$dpmX (X= Cl, Br) isomer, which rapidly decomposed via unknown intermediates to a product with no coordinated carbonyl ligands.[60] This suggests that the complex formed after exposure to CO gas is a Mn(II)$(CO)_x$ complex, most likely in a mixture of isomers. Unlike the IR bands reported in the literature, the new bands observed were all roughly equal in intensity and overlapping, supporting the presence of multiple isomers. The appearance of these peaks at lower wavenumber than those in the literature would be expected for the formation of mono- or di-carbonyl Mn(II) complexes. These complexes are very unstable, are strong oxidising agents and can be reduced, and decomposed when exposed to water vapour in air. Despite the CO bands supporting the formation of Mn(II) species, the source of the oxidation of Mn(I) to Mn(II) is unknown. Possible mechanisms include disproportionation of all Mn(I) atoms to Mn(0) and Mn(II) during the decarbonylation reaction, trace quantities of oxygen or water causing the oxidation during decarbonylation, or the CO gas (or impurities within) acting as the oxidising agent.

2.3.7 Manganese leaching post-photolysis

The proposed redox pathway for the fully photolyzed manganese carbonyl complex was investigated in a series of leaching studies. A bulk sample of MnMOF[$Mn(CO)_3$X].Y (THF and MeCN solvated) was dried under a stream of argon and photolyzed with visible light until no CO stretches were observable in the IR spectrum. The crystals were re-solvated and one equivalent of $CoCl_2$ added. The samples were left overnight, the solvent removed, and the crystals were analysed by SEM/EDX (Table 2.8). Samples which underwent the same procedure but without photolysis were analysed as controls. For the photolyzed MnMOF[$Mn(CO)_3$Br]·THF sample there was no significant replacement of the manganese with cobalt compared to the control, indicating that any loss of manganese from the binding site after photolysis was only due to the lability of

the Mn complex and not due to the photolysis reaction. For MnMOF[$Mn(CO)_3NCMe$]Br, significant replacement of Mn for Co was seen in the photolyzed sample compared to the control. The post-photolysis sample showed a 20% higher replacement, with over 50% of the metal centres replaced with cobalt. The control also displayed higher Mn/Co exchange compared to THF, commensurate with the greater ability of acetonitrile to coordinate to Mn(I). It may be inferred therefore that approximately 20% of metalation occupancy is lost during the photolysis reaction in acetonitrile. This; however, does not confirm or disprove any oxidation state changes occurring at the Mn(I) centre during the photo-decarbonylation reaction.

Table 2.8 Manganese leaching study by substitution with $CoCl_2$, analysed by SEM/EDX

	Co Occupancy	**Standard error**
THF control	17%	5%
Post photolysis THF	20%	4%
MeCN control	32%	3%
Post Photolysis MeCN	52%	3%

2.3.8 Investigation into oxidation state changes by X-ray photoelectron spectroscopy

To investigate any oxidation state changes occurring at the manganese (I) centres during photo-decarbonylation, X-ray photoelectron spectroscopy (XPS) was employed. Due to a lack of stability, no reference XPS spectra for Mn(I) could be found in the literature. Therefore, it was imperative to collect good reference spectra for both Mn(I) and Mn(II) oxidation states to identify any changes occurring during photolysis of the MOF tethered complexes. This experiment was further complicated by the presence of framework Mn(II) atoms which were three times more abundant than the chelated Mn(I) (assuming 100% occupancy of the metalation site). Initially [$Mn(CO)_5Br$] was selected as the reference for Mn(I); however, under the high vacuum environment of the XPS apparatus the complex sublimed and could not be analysed. The model complex [$Mn(dpzm)(CO)_3Br$] was then chosen, along with un-metalated MnMOF to act as the references for Mn(I) and Mn(II) respectively. Samples were prepared by drying to a free-flowing powder under a flow of nitrogen gas, then placed on an adhesive carbon tab on the sample holder. This was then placed as quickly as possible in the apparatus

where it was placed under vacuum and pumped down to a pressure of 1 x 10^{-9} mbar. For the light sensitive MnMOF[$Mn(CO)_3X$]Y (X = Br^- or NCMe, Y = THF or Br^-) samples all preparation was carried out in the dark and all openings on the reaction apparatus were covered with aluminium foil. Both the THF solvated and MeCN solvated samples were analysed, with XPS spectra collected from the un-photolyzed samples before the samples were irradiated with a visible torch through a window in the reaction apparatus. For all samples, a flood gun was used to prevent overcharging and damage to the samples from the X-ray beam. Although the decarbonylation of the complex due to the high vacuum and X-ray beam was a concern, an immediate increase in the chamber pressure (from 1 x 10^{-9} to 2.5 x 10^{-8} mbar) was observed when the light was turned on, indicating that CO was released from the MOF only under irradiation conditions. This confirmed that the initial spectrum collected for each sample arose from the parent complex. Since there was no means to perform *in situ* IR spectroscopy, the samples were photolyzed until the chamber pressure returned to pre-photolysis levels, indicating that all CO had been removed. Although the C-O peak in the C 1s region could be observed in the Mn(I) reference, it could not be seen in the MOF samples due to the confounding presence of the other C-X bonds. Therefore, only the Mn regions of the spectrum were of interest in comparing the pre- and post-photolysis samples (Figure 2.36).

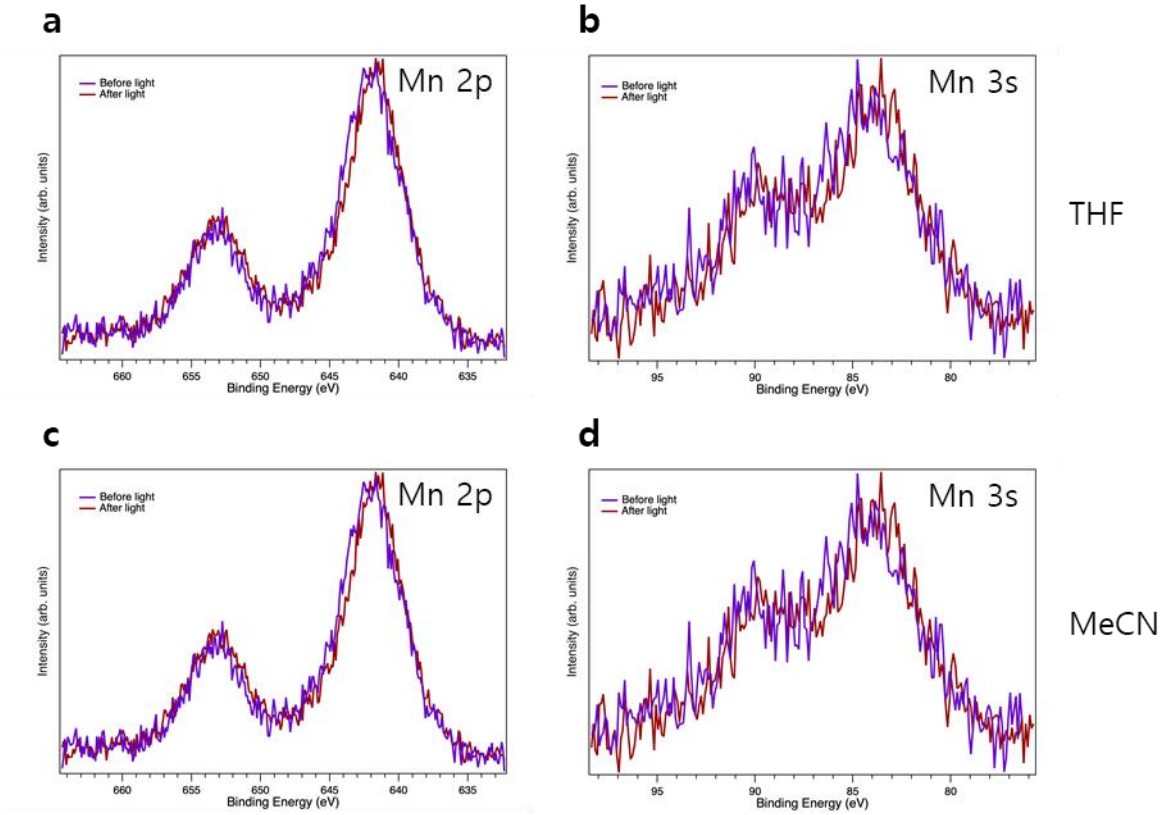

Figure 2.36. XPS spectra of MnMOF[$Mn(CO)_3X$]Y samples before (purple) and after (red) photolysis of the **a)** sample dried from THF Mn 2p region and **b)** Mn 3s region and the sample dried from MeCN **c)** 2p and **d)** 3s region.

From the XPS data collected it is evident that both MnMOF[$Mn(CO)_3X$]Y samples contain both Mn(II) and Mn(I) components. There was no measurable difference in the Mn spectra after photolysis, suggesting that no change in oxidation state occurred as a result of the decarbonylation reaction. Peak 8 in Table 2.9 is the main indicator of the presence of Mn(I) in the MOF samples. This peak is not present in the Mn(II) reference and, although it is shifted slightly in the MOF compared to the Mn(I) reference, this is likely due to the weakness of the Mn(I) component compared to the Mn(II) component leading to some ambiguity.

Table 2.9. Peaks fitted to the Mn 2p XPS spectra

Mn 2p	**Binding Energy (eV)**							
	Peak 1	**Peak 2**	**Peak 3**	**Peak 4**	**Peak 5**	**Peak 6**	**Peak 7**	**Peak 8**
MnO[62]	639.28	640.32	641.08	641.96	643.04	644.13	646.16	637.63
Mn(I)	638.46	639.9	641.22		642.66	644.34	647.34	635.82
Mn(II)	638.82	640.26	641.58		643.02	644.7	646.84	-
Mn-THF	638.74	640.18	641.5		642.94	644.62	646.76	636.94
Mn-MeCN	638.18	639.62	640.94		642.38	644.06	646.2	636.38

The XPS results showed that the photolysis of MnMOF[$Mn(CO)_3X$]Y does not lead to oxidation state changes in the manganese atoms present. As the exposure of the samples to the air when preparing and loading them was unavoidable, this also discredits the second theory expounded in Section 2.3.6, that the formation of Mn(II) was from exposure to the atmosphere during sample preparation. It is therefore likely that either trace oxygen impurities in the gas cylinder acted as the oxidation agent to form the Mn(II) carbonyl species described earlier, or a new, unknown Mn(I) carbonyl species was formed.

2.4 Conclusions and Future Directions

A photoactive *fac*-[Mn(I)$(CO)_3$X] (X=Br or MeCN) was tethered to MnMOF by post-synthetic metalation. This was achieved in a quantitative yield with retention of long-range order, and so the material was suitable to be studied by single crystal X-ray diffraction. The photo-decarbonylation reaction was studied by photocrystallography, IR spectroscopy and XPS after irradiation with visible or UV light. While UV or visible light sources were used in different experiments, this was due to availability of equipment and no study was made of the effect of irradiation wavelength or power on the photolysis reactions. Future studies investigating these parameters may be of interest to further probe the kinetics and mechanism of the reaction. The photolysis reaction of MnMOF[Mn$(CO)_3$X]Y (X= Br^- or solvent, Y = Br^- or solvent) proceeded in a stepwise fashion, involving three CO release steps. The complex was stable at room temperature in the dark; however, it underwent solvent induced isomerisations in the presence of solvents of varying coordinating abilities. As such, both the charge-separated species in which the X coordination site was occupied by a solvent molecule and the charge-neutral species, where X was a bromide anion, were studied. For both the charge-neutral and charge-separated complexes the first CO loss was from the equatorial position, as shown by photocrystallography, to form complexes 2a and 2b (Figure 2.37). This is due to the competition for π-backbonding between the two equatorial positions due to the π-accepting character of the bis-pyrazole ligands positioned *trans* to the equatorial CO sites, lowering the Mn-CO bond order. This led to the formation a *cis*-dicarbonyl intermediate which was observed by matrix isolated IR spectroscopy at 190K. The second carbonyl loss also occurred from the equatorial position, leaving an axially coordinated monocarbonyl intermediate (3a and 3b).

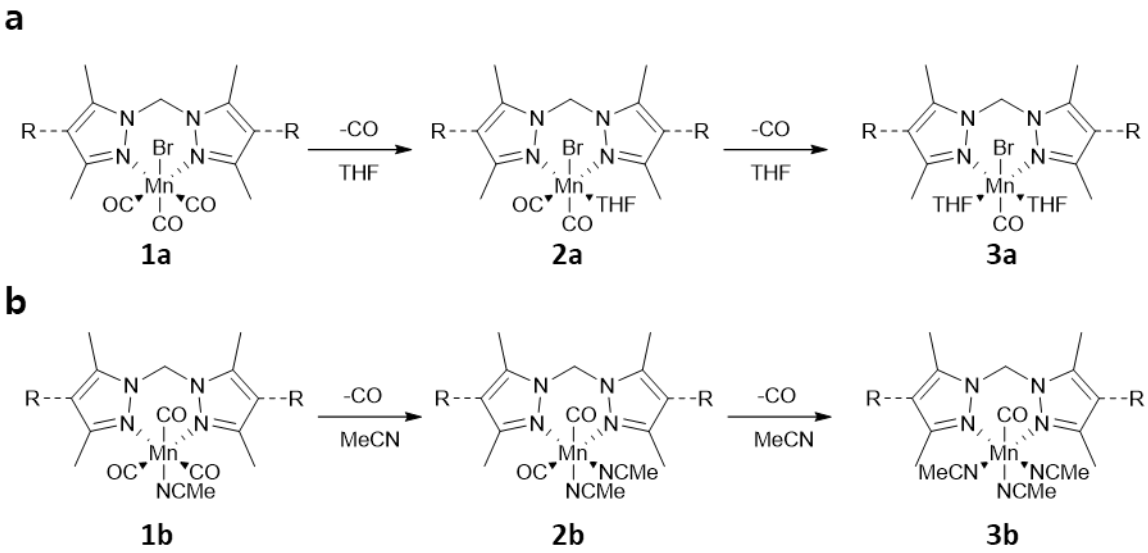

Figure 2.37. Reaction pathway for the photo-decarbonylation of fac-tricarbonyl Mn(I) complexes in MnMOF **a)** in the presence of THF and **b)** in the presence of MeCN, following the stepwise loss of two carbonyl ligands to form mono-carbonyl intermediates.

The first two decarbonylation steps followed the same pathway for the charge-neutral and charge-separated species, but differences were observed in the loss of the final carbonyl ligand (Figure 2.38). For the THF solvated, charge-neutral species, at either the mono-carbonyl intermediate or after the loss of the final carbonyl ligand, the bromide anion becomes disassociated from the manganese centre. The bromide anion then re-coordinates to form isomers in which the bromide anion could occupy either axial position (4a or 5a). This resulted in a disordered structure, where the occupancy of the final coordination site was uncertain. The observation of multiple monocarbonyl bands in the matrix isolated TR-IR data presented in Section 2.3.4 indicates that the loss and rearrangement of the anion occurs at the monocarbonyl intermediate stage. In contrast, the photocrystallography studies of MnMOF[$Mn(CO)_3NCMe$]Br revealed that coordination of the bromide anion occurs after loss of the final carbonyl ligand, resulting in a MnMOF[$Mn(MeCN)_3Br$] complex.

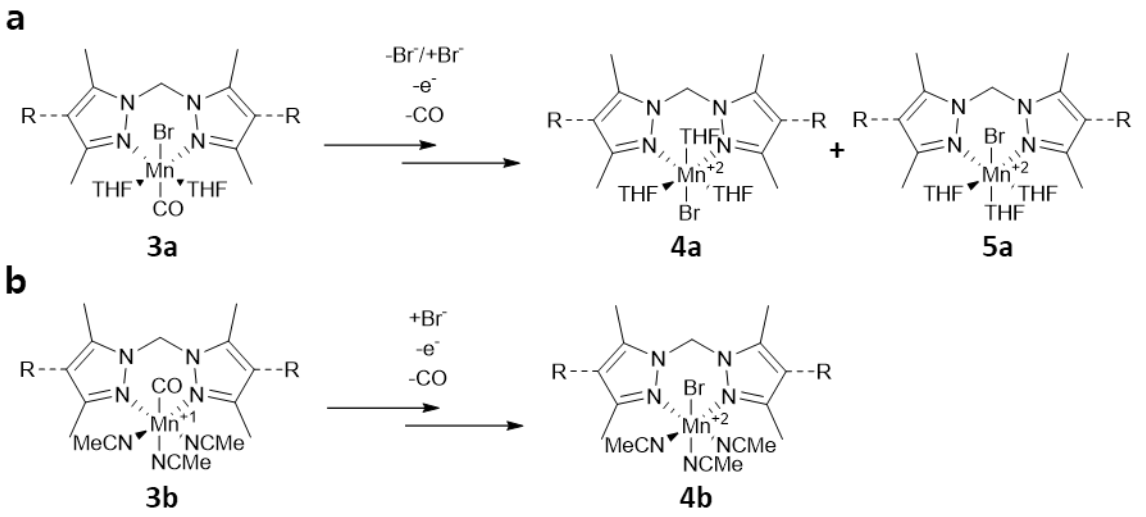

Figure 2.38. Proposed multi-step reaction pathway for loss of the third carbonyl ligand and oxidation to Mn(II) for MnMOF[Mn(CO)$_3$X]Y in the presence of **a)** THF and **b)** acetonitrile.

While the oxidation of Mn(I) to Mn(II) in a dark process after or associated with the loss of the final carbonyl ligand has been shown by EPR spectroscopy previously for Mn(I) photoCORMs,[33] this is the first time that a photochemically produced Mn(II) complex has been observed by IR spectroscopy through the formation of a Mn(II) carbonyl complex in the absence of electrochemical oxidation. The identity of the oxidising agent is still unknown, as XPS studies did not show any changes in the manganese oxidation states after photolysis under high vacuum. It can therefore be assumed that an environmental oxidation agent is required, and an intramolecular redox process is not the cause of the Mn(I) oxidation. Therefore, further studies are required to identify the cause and mechanism of the oxidation, and whether it occurs simultaneously with CO loss, or as a separate process.

In the same way as observed by Diring et al, the solid-state photochemical behaviour of the *fac*-[Mn(L)(CO)$_3$Br] complex is different in the MOF to its corresponding molecular analogue. It is; however, comparable to the molecular analogue's behaviour in the solution-state meaning that the MOF environment is producing a pseudo-solution-state in the pores of the solid-state material.

This study demonstrated that the isolating of a Mn(I) photoCORM in a MOF can be a powerful tool to study the photodissociation process by crystallographic methods and to study reactions in the solid-state which are not observed for comparable discrete organometallic complexes. These compounds have many potential applications as CO releasing materials for chemical synthesis or therapeutic agents, or as catalysts for

reactions such as the reduction of carbon dioxide. There are still many avenues to explore in investigating the chemical and electronic effects of changing the auxiliary ligands, modifying the wavelength of light needed for CO release and solvent environments. There are also physical properties that need to be considered now that these reactions are occurring in the solid-state, such as particle size and shape, metal leaching and crystallinity.

2.5 Experimental

2.5.1 General experimental

All chemicals were obtained from commercial sources and used as received unless otherwise stated. Dry solvents were distilled (acetonitrile over calcium hydride, THF over sodium/benzophenone, and ethanol over magnesium) and degassed with argon before use. The ligand L (L = bis(4-carbonxyphenyl-3,5-dimethylpyrazolyl) methane), MnMOF, MnMOF[$Mn(CO)_3X$]Y (where X/Y = Br^- or solvent)[48] and the model complex bromotricarbonyl(bis(3,5-dimethyl-1H-pyrazol-1-yl)methane)manganese(I)[46] were prepared by previously reported methods. MnMOF[$Mn(CO)_3X$] was stored in the dark and handled with minimal exposure to light.

NMR spectra were recorded on a Varian 500 MHz spectrometer at 23 °C using a 5 mm probe or Brucker DPX400, AV400 or AV(III)400 400 MHz spectrometers with BBFO probes. ^1H NMR spectra recorded in $CDCl_3$ were referenced to the internal standard, Me_4Si (0 ppm) or to the solvent peak.

A FEI Quanta 450 high resolution, field emission scanning electron microscope was used to collect images and perform energy-dispersive X-ray spectroscopy (EDX). EDX was collected with an Oxford Ultim X-Max Large Area SDD detector with Oxford Aztec EDX processing software.

Solid-state UV/Vis spectra were obtained on a Cary 5000 UV/Vis/NIR spectrophotometer with a Harrick Praying Mantis diffuse reflectance spectroscopy attachment on samples distributed in KBr.

Bulk photolysis was performed on 20-30 mg of sample in 5 mL of dry solvent, under constant flow of argon with an LEDlenser M14 400 lm visible torch. The sample and torch were wrapped in foil and the vial was agitated every 10 min to ensure even irradiation.

Room temperature infrared (IR) spectra were collected on a Bruker Alpha FTIR spectrometer with an ATR attachment. Room temperature-controlled atmosphere measurements were conducted on a PerkinElmer Spectrum Two spectrophotometer, with the sample dispersed between two NaCl disks inside a custom built sealed stainless steel cell with NaCl windows, which allows for the sample to be placed under vacuum or a pressure of gas. Samples were placed under vacuum for analysis. Samples exposed

to CO were placed under vacuum, then 1 bar CO added before placed under vacuum again for analysis. Matrix isolated IR spectra were collected on a Thermo Nicolet Avatar 360 spectrophotometer with the sample dispersed in dry NaCl or KBr and pressed into a disk (8 mm diameter, 0.5 mm thickness) under 6 tonnes of pressure. The disk was placed into a copper cell with CaF_2 windows, which was sealed and placed inside a vacuum shroud, before cooled to the analysis temperature. Photolysis was performed with a Philips HPK medium pressure 125W mercury arc lamp (see Section 2.5.6).

Single crystals were mounted in Fomblin or Paratone-N oil on a MiTeGen micromount. Data for MnMOF[$Mn(CO)_3Br$]·THF was collected on the MX1 beamline at the Australian Synchrotron at 100K for the initial structure and 150K for intermediate photolysis and processed using XDS software (λ = 0.7108).[63] Data for MnMOF[$Mn(CO)_3MeCN$]Br was collected on the i19 beamline at Diamond Light Source (λ = 0.6889) at 100K and processed using Xia2 software.[64] Absorption corrections were applied using empirical methods and the structures were solved by direct methods using SHELXS or SHELXT and refined by full-matrix least-squares by SHELXL,[65] interfaced through XSeed or Olex2.[66] Unless stated otherwise, all non-hydrogen atoms were refined anisotropically and hydrogen atoms were included as invariants at geometrically estimated positions. The SQUEEZE routine of PLATON was used to subtract electron density corresponding to disordered solvent molecules where stated.[67] CrystalMakerX[68] and ShelXle[69] were used to produce the figures. F_{obs} maps were produced at a resolution of 1.00 e/Å^3. Further details on crystallographic solution and refinement are found in Sections 2.6.2 and 2.6.3.

PXRD data was collected on a Bruker Advance D8 powder diffractometer (parallel X-ray) equipped with a capillary stage and using Cu Kα radiation (λ = 1.5418 Å), or on a Bruker Endeavour D4 powder diffractometer (parallel X-ray, flat plate loaded) using Co Kα radiation (λ = 1.789 Å).

2.5.2 Synthesis of Ligand L

Synthesis of 2 (Figure 2.39):[48] Dimethyl pyrazole (5g, 52.02 mmol) was dissolved in DMSO (30 mL) before KOH (11.68g, 208.08 mmol) was added. The suspension was stirred vigorously for 1.5 hrs at 60 °C before dibromomethane (4.52 g, 26.01 mmol) in DMSO (20 mL) was added dropwise over 30 min. The reaction mixture was stirred at 60

°C for an additional 4 hrs, then poured into water (300 mL) and extracted with chloroform (6x30 mL). The extract was washed with water (2x20mL) and dried over anhydrous calcium chloride. The solvent was removed under reduced pressure to give the product (5.012 g, 95%, NMR data were in accord with reported values).

Synthesis of 3:[50] A suspension of 2 (4.99 g, 24.7 mmol), finely powdered iodine (4.97 g, 19.76 mmol) and iodic acid (1.74 g, 9.88 mmol) in an mixture of glacial acetic acid (50 mL) and 30% sulfuric acid (5 mL) was stirred overnight at room temperature until the iodine colour disappeared. The mixture was poured into water (250 mL) and cooled in the fridge overnight. If no precipitate formed NaOH was added to induce precipitation. The precipitate was filtered, dried and if necessary recrystallised from ethanol to give fine white needle crystals (7.91 g, 70%, NMR data were in accord with reported values).

Synthesis of Ligand L:[48] Compound 3 (1.5 g, 3.29 mmol), 4-carboxyphenyl boronic acid (1.64 g, 9.88 mmol) and aqueous K_2CO_3 (6.60 g, 47.8 mmol, 38 mL) were combined in DMF (180 mL). After degassing the mixture with Ar for 30 min, $Pd(PPh_3)_4$ (0.57g, 0.49 mmol, 0.15 equiv) was added. The resulting mixture was further degassed for 30 min, then heated at 90 °C for 20 hrs. The reaction mixture was cooled to room temperature, then distilled water (200 mL) was added. The mixture was filtered over celite and washed with DCM (5x50 mL). The aqueous layer was acidified with 20% HNO_3 to pH 3 to afford a white precipitate which was isolated, washed with ethanol and dried to give a white solid (1.237g, 85%, NMR data were in accord with reported values)

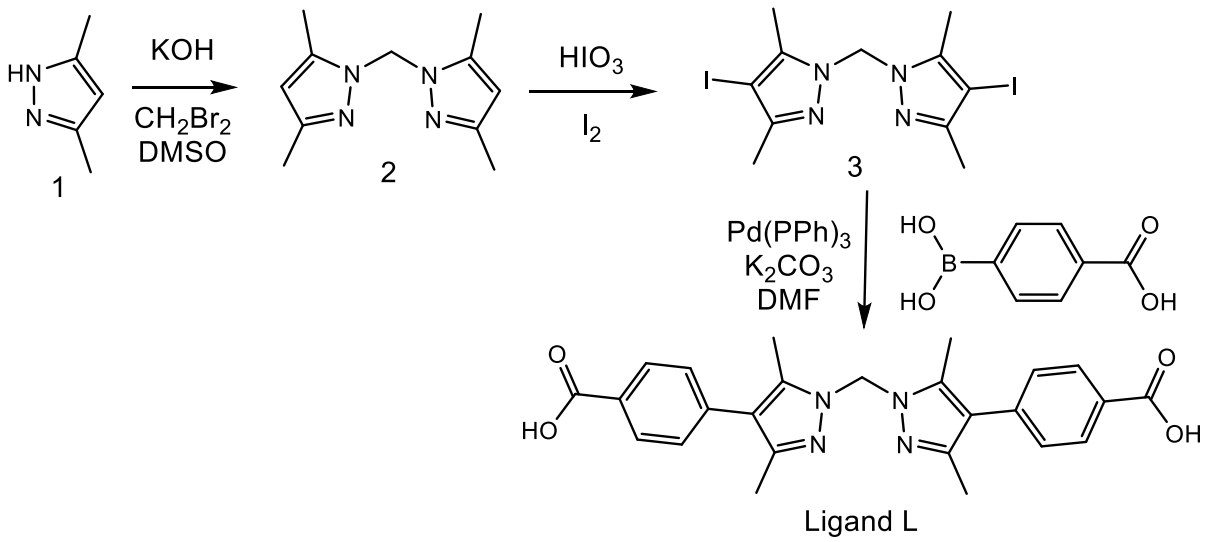

Figure 2.39. Reaction scheme for the synthesis of ligand L (4,4'-{methylenebis(3,5-dimethyl-1H-pyrazole-1,4-diyl)}dibenzoic acid).

2.5.3 Synthesis of [Mn(bdpm)(CO)$_3$Br] model complex[46]

Bdpm (100 mg, 0.49 mmol) was dissolved in ethanol (15 mL) under nitrogen. $Mn(CO)_5Br$ (170 mg, 6.3 mmol, 1.3 equiv.) was then added and the solution heated to 90 °C for 5 hrs in the dark. The solution was then left to cool overnight, forming a yellow precipitate. This was isolated by filtration, washed with cold ethanol and crystallised from slow evaporation of chloroform (in the dark) to give the $Mn(CO)_3Br$ model complex as large yellow block crystals (178 mg, 86%) (Figure 2.40).

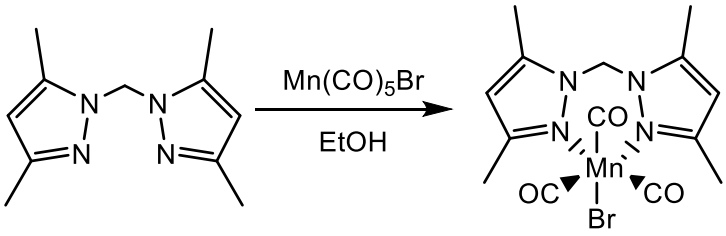

Figure 2.40. Reaction scheme for the synthesis of [Mn(bdpm)(CO)$_3$Br] model complex.

2.5.4 MnMOF

Ligand L (31.6 mg, 0.07 mmol) dissolved in DMF (4 mL) added to $MnCl_2.4H_2O$ (24.7 mg, 0.12 mmol) dissolved in water (2 mL) in a 20 mL screw cap vial and heated at 100 °C for 2 days. The colourless crystals were then washed with DMF (x5) (NMR, IR, PXRD and SCXRD data were in accord with reported values).[48]

To synthesize MnMOF[$Mn(CO)_3OH_2$]Br, MnMOF crystals were washed in ethanol (x5) before an excess of $Mn(CO)_5Br$ was added. The vial was wrapped in foil to exclude light and heated at 50 °C overnight, after which the bright yellow crystals were washed with ethanol (x8). To perform solvent exchanges, the sample was washed with the new, freshly distilled, solvent (x5) and left to soak overnight before analysis.

2.5.5 Manganese leaching experiment

MnMOF[$Mn(CO)_3Br$]·THF [6 mg] was dried under argon, then photolyzed for 2 hrs under a flow of argon. Dry THF and $CoCl_2.10H_2O$ (1 mg) was added and left overnight. The MOF was then washed with THF (x3), dried and analysed by SEM/EDX. The same procedure was followed for the acetonitrile solvated sample, MnMOF[$Mn(CO)_3$MeCN]Br, with THF replaced by MeCN. Unphotolyzed control samples were prepared by soaking the MnMOF[$Mn(CO)_3X$].Y (X = Br or MeCN, Y = THF or Br) (6

mg) with $CoCl_2.10H_2O$ (1 mg) in the dark overnight, before washing them (x3) and drying them for EDX analysis.

2.5.6 Matrix isolated IR

MnMOF[$Mn(CO)_3X$].Y samples (2 mg) were incorporated into finely ground salt (KBr or NaCl) (200 mg), then pressed into a 9 x 0.5 mm disk under 6 tonnes of pressure in the dark. The disk was then placed into the sample chamber with a lead gasket. The sample chamber was sealed, placed on the instrument as seen in Figure 2.41.

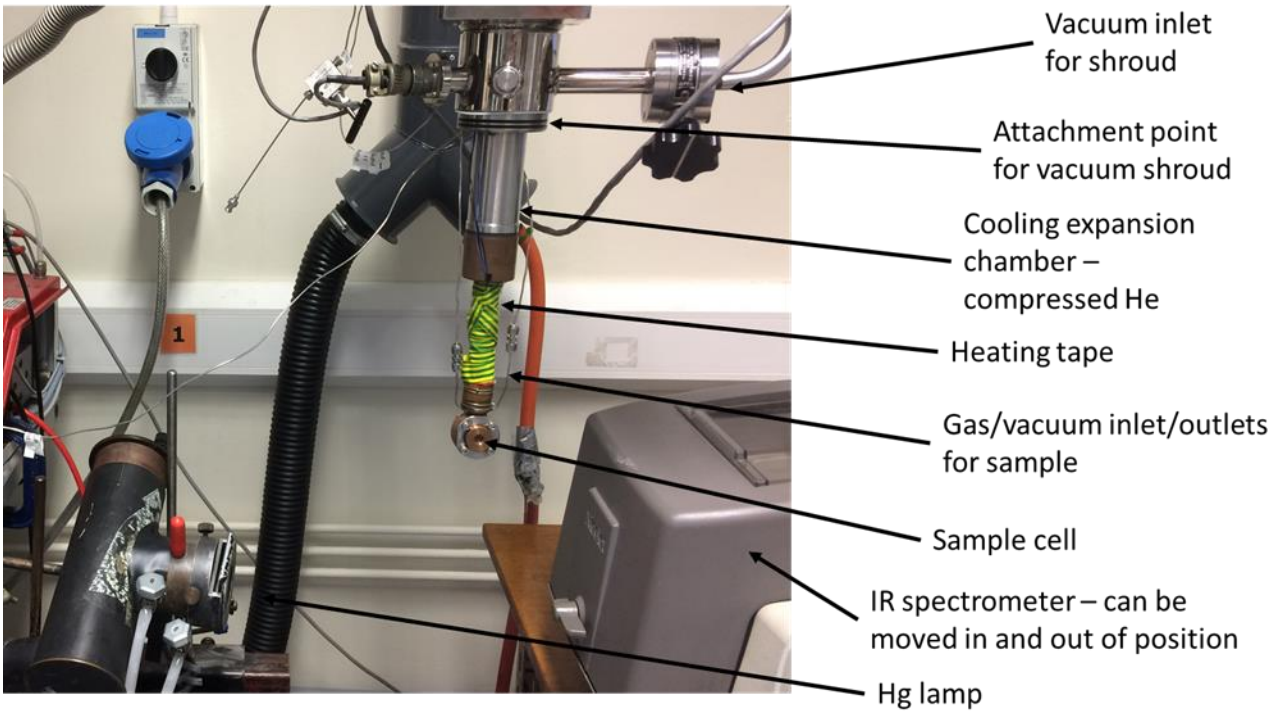

Figure 2.41. Reaction set-up employed for matrix isolated IR spectroscopy.

2.6 Appendix

2.6.1 2D Mn coordination polymer

The 2D layered coordination polymer, $[Mn_2L_2(H_2O)_2]$, was formed as a by-product from the synthesis of MnMOF. It crystallised in the spacegroup *C2/c* as large colourless block crystals (Structure **2.1**). The asymmetric unit contains half a ligand molecule, one Mn atom and a water molecule coordinated to the manganese. This results in a distorted 5-coordinate square pyramidal geometry around the manganese atom with four bonds to a carboxylate oxygen of four molecules of ligand L. The fifth, axial, coordination site is occupied by a water molecule. This forms a zig-zag chain of manganese atoms bridged by carboxylates to form 2D sheets, capped by water molecules. The pyrazole rings are uncoordinated and in an *anti*-configuration (Figure 2.42a). The sheets packed in an alternating fashion, so that the manganese chain of one layer resided beneath the centre of the ligand in the next layer (Figure 2.42b-d). The sheets were close-packed, and the coordination polymer could not be metalated.

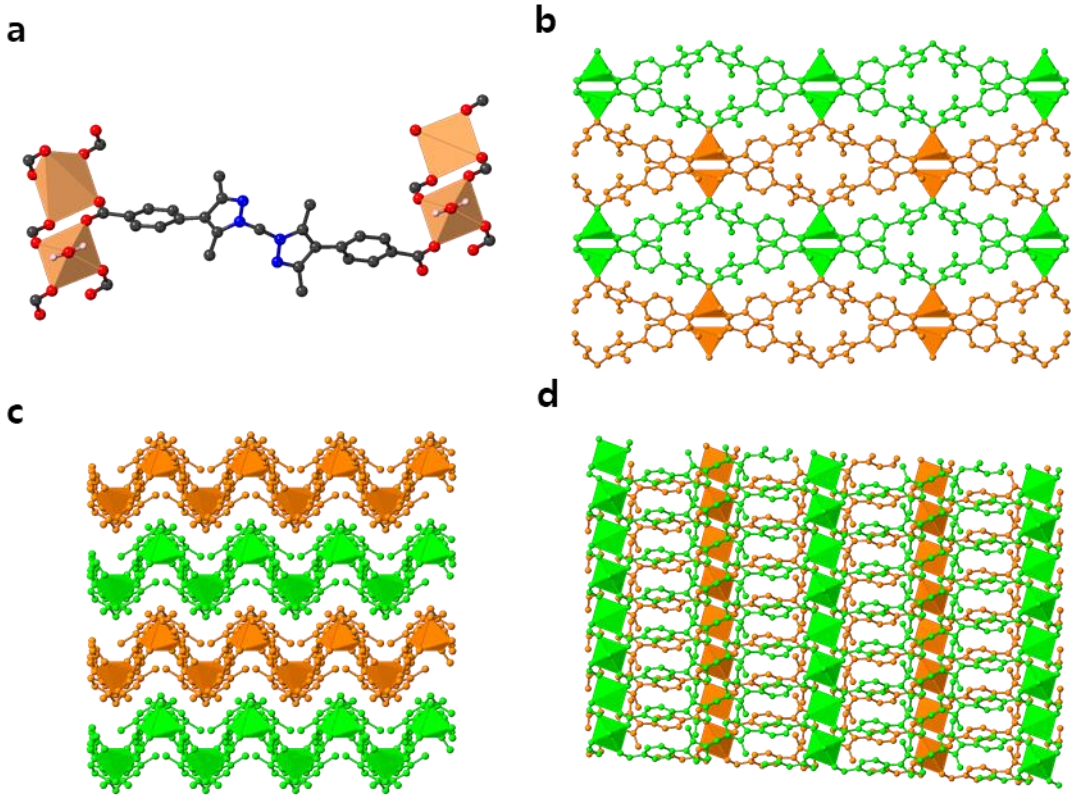

Figure 2.42. $[Mn_2L_2(H_2O)_2]$ MOF made from scaled up MnMOF reaction. **a)** Ligand coordination showing uncoordinated anti-configuration of pyrazoles, **b)** packing view along the z-axis, **c)** packing view along the x-axis and **d)** packing view along the y-axis showing 2D zig-zag sheets.

Optimised conditions for the synthesis of this coordination polymer were not investigated, as it was an unwanted product of attempts to increase the scale of MnMOF

forming reactions. Despite this, it may be of interest in the future if the sheets can be delaminated, as the uncoordinated bis-pyrazolyl may be metalated if they become accessible. Therefore, this may be suitable for further investigations into post-synthetically metalated nanosheets.

2.6.2 SCXRD refinement details

SCXRD structures will be named according to Table 2.10. Note that structures **2.4** and **2.5** were refined and finalised by Prof. Christopher Sumby and Dr. Witold Bloch and published in Huxley *et al.*[47] As such, the refinement details will not be discussed here.

Supplementary crystallographic data may be found at https://figshare.com/s/0081af3a1baddad98b6b.

Table 2.10. Naming scheme for crystal structures

Crystal structure reference	Sample	Location in chapter	Figure reference (Thermal ellipsoid plot)
2.1	MnL(OH_2) 2D coordination polymer	2.3.1	Figure 2.43
2.2	MnMOF[$Mn(CO)_3OH_2$]Br·EtOH	2.3.1	Figure 2.44
2.3	MnMOF[$Mn(CO)_3$MeCN]Br	2.3.1	Figure 2.45
2.4	MnMOF[$Mn(CO)_3$BzCN]Br	2.3.1	Figure 2.46
2.5	MnMOF[$Mn(CO)_3$Br]·THF	2.3.1	Figure 2.47
2.6	[Mn(bdpm)$(CO)_3$Br] model complex	2.3.2	Figure 2.48
2.7	MnMOF[$Mn(CO)_3$MeCN]Br photolyzed for 10 min	2.3.5	Figure 2.49
2.8	MnMOF[$Mn(CO)_3$MeCN]Br photolyzed for 20 min	2.3.5	Figure 2.50

MnMOF[Mn(CO)$_3$OH$_2$]Br·EtOH (2.2)

To subtract the contribution of the disordered solvent (EtOH), the SQUEEZE routine of PLATON was applied to the data, which generated a new HKL file. The number of located electrons was 520, which equates to approximately 20 ethanol molecules per unit cell, and 5 per asymmetric unit. This has been added to the reported formula. Note that it is likely that the coordinated solvent molecule is either water or ethanol, but due to disorder, only the coordinated oxygen atom common to both molecules was modelled at 100% occupancy.

RIGU restraints were used in the refinement of axial carbonyl ligand (2 restraints in total).

MnMOF[Mn(CO)$_3$MeCN]Br (2.3)

To subtract the contribution of the disordered solvent (MeCN), the SQUEEZE routine of PLATON was applied to the data, which generated a new HKL file. The number of located electrons was 328, which equates to approximately 15 acetonitrile molecules per unit cell, and 3.75 per asymmetric unit. This has been added to the reported formula. The occupancy of the bromide anion in MOF pore was fixed at 75% to fit with the electron density map.

DFIX and RIGU restraints were used in the refinement of carbonyl and acetonitrile ligands and the disordered phenyl rings in the MOF ligands (15 restraints in total).

SIMU constraints were used in the refinement of the Mn(I) complex (5 constraints in total)

MnMOF[Mn(CO)$_3$MeCN]Br photolyzed for 10 min (2.7)

To subtract the contribution of the disordered solvent (MeCN), the SQUEEZE routine of PLATON was applied to the data, which generated a new HKL file. The number of located electrons was 354, which equates to approximately 16 acetonitrile molecules per unit cell, and 4 per asymmetric unit. This has been added to the reported formula. The occupancy of the bromide anion in MOF pore was fixed at 75% to fit with the

electron density map. The equatorial ligands were modelled as 75% acetonitrile and 25% carbonyl.

A series of DFIX and RIGU restraints were used in the refinement of carbonyl and acetonitrile ligands and the disordered phenyl rings in the MOF ligands (15 restraints in total).

EADP, SIMU and EQUIV constraints were used in the refinement of the Mn(I) complex (6 constraints in total)

MnMOF[Mn(CO)$_3$MeCN]Br photolyzed for 20 min (2.8)

To subtract the contribution of the disordered solvent (MeCN), the SQUEEZE routine of PLATON was applied to the data, which generated a new HKL file. The number of located electrons was 372, which equates to approximately 17 acetonitrile molecules per unit cell, and 4.25 per asymmetric unit. This has been added to the reported formula. The occupancy of the coordinated bromine anion was fixed at 33%, while the uncoordinated bromine anion was fixed at 66% to best fit the electron density map. The occupancy of the axially coordinated carbonyl ligand was fixed at 25%. Attempts to increase this occupancy, or the occupancy of the bromine anion at this position lead to over occupation of the site according to the electron density, therefore it is assumed that the position is partially vacant. Both acetonitrile ligands were modelled at 100% occupancy.

A series of DFIX, DANG and RIGU restraints were used in the refinement of carbonyl and acetonitrile ligands (14 restraints in total).

SIMU constraints were used in the refinement of the Mn(I) complex (3 constraints in total)

2.6.3 Thermal ellipsoid plots

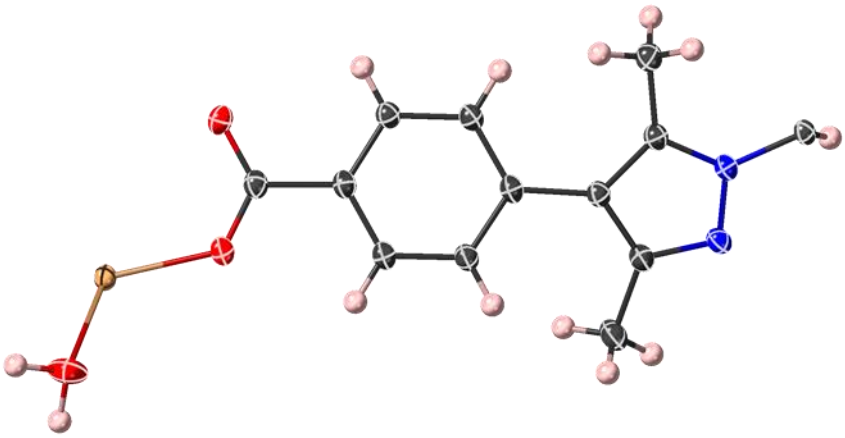

Figure 2.43. Asymmetric unit of 2D MnMOF (**2.1**), with all non-hydrogen atoms represented by ellipsoids at the 50% probability level. (C, grey; Mn, beige; O, red; N, blue; H, pink)

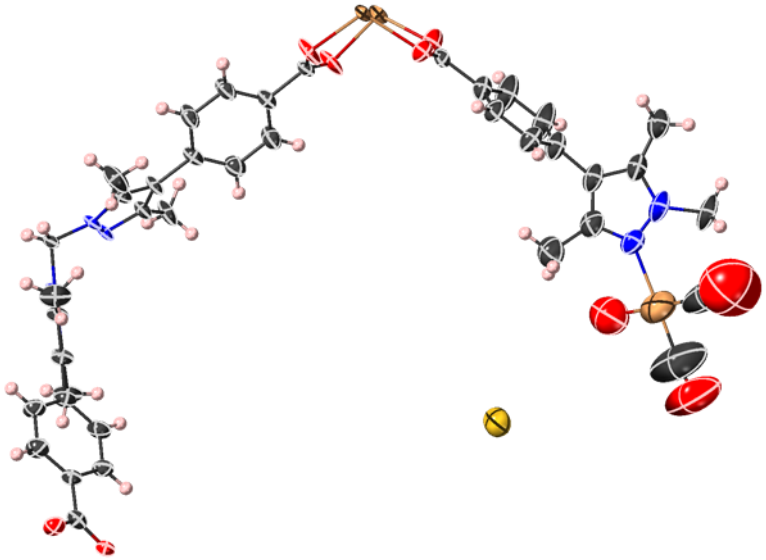

Figure 2.44. Asymmetric unit of MnMOF[$Mn(CO)_3OH_2$]Br (**2.2**), with all non-hydrogen atoms represented by ellipsoids at the 50% probability level. (C, grey; Br, yellow; Mn, beige; O, red; N, blue; H, pink)

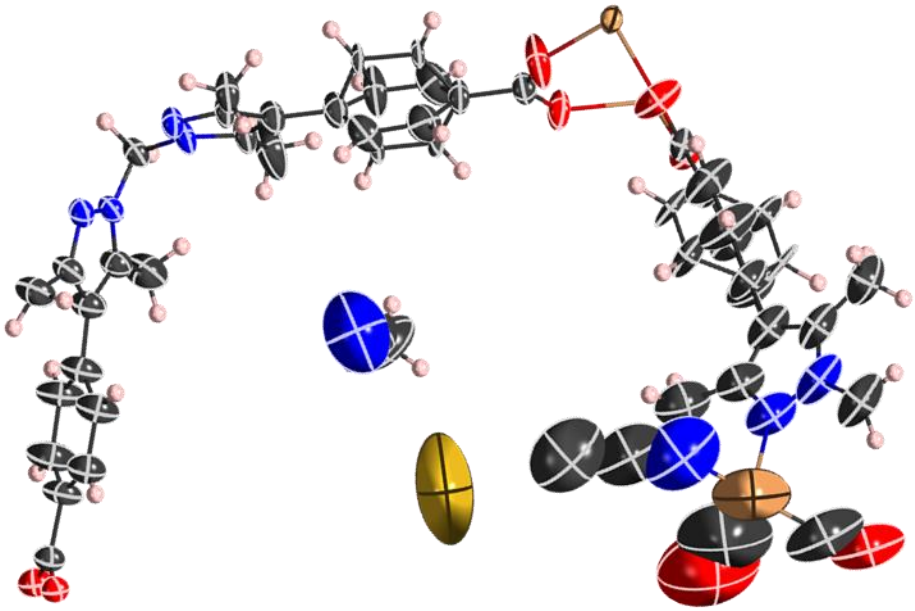

Figure 2.45. Asymmetric unit of MnMOF[Mn(CO)$_3$MeCN]Br (**2.3**), with all non-hydrogen atoms represented by ellipsoids at the 50% probability level. (C, grey; Br, yellow; Mn, beige; O, red; N, blue; H, pink)

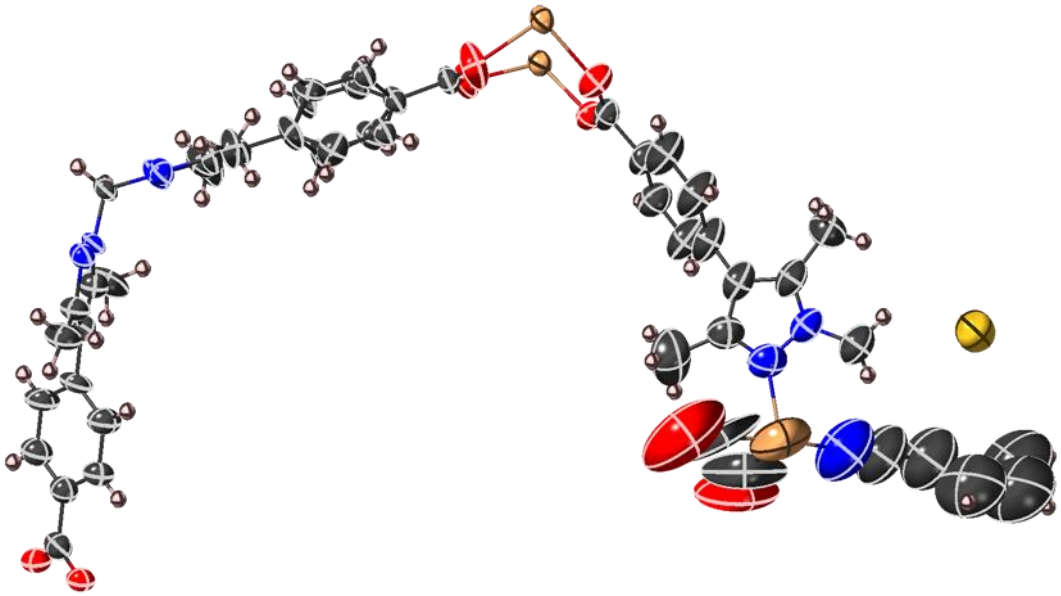

Figure 2.46. Asymmetric unit of MnMOF[Mn(CO)$_3$BzCN]Br (**2.4**), with all non-hydrogen atoms represented by ellipsoids at the 50% probability level. (C, grey; Br, yellow; Mn, beige; O, red; N, blue; H, pink)

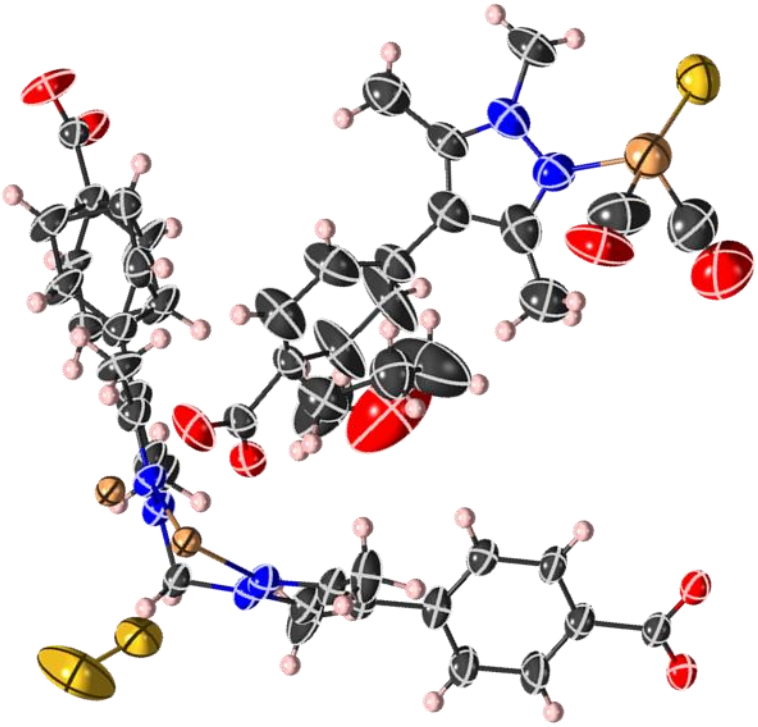

Figure 2.47. Asymmetric unit of MnMOF[$Mn(CO)_3Br$]·THF (**2.5**), with all non-hydrogen atoms represented by ellipsoids at the 50% probability level. (C, grey; Br, yellow; Mn, beige; O, red; N, blue; H, pink)

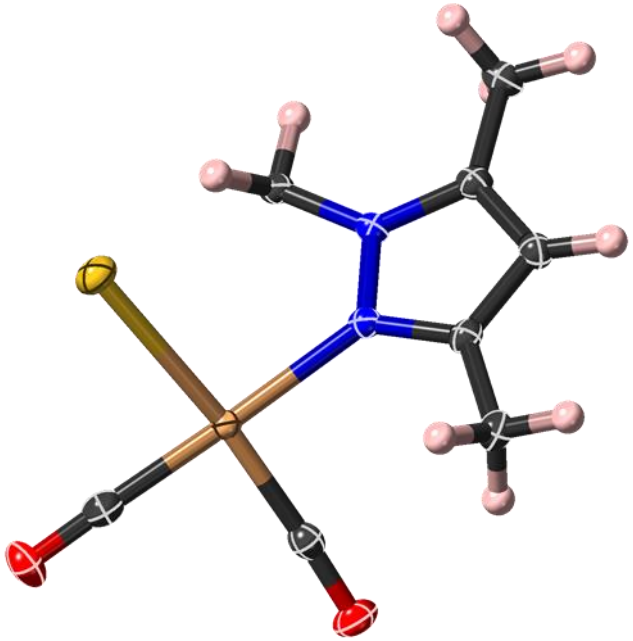

Figure 2.48. Asymmetric unit of [Mn(dpzm)$(CO)_3Br$] (**2.6**), with all non-hydrogen atoms represented by ellipsoids at the 50% probability level. (C, grey; Br, yellow; Mn, beige; O, red; N, blue; H, pink)

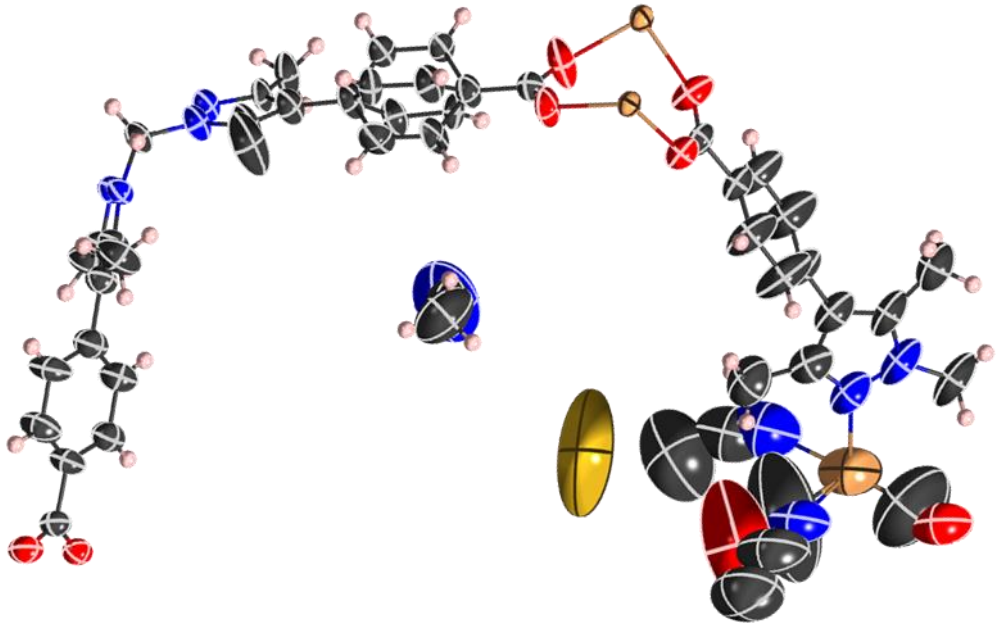

Figure 2.49. Asymmetric unit of MnMOF[$Mn(CO)_3MeCN$]Br photolyzed for 10 min (**2.7**), with all non-hydrogen atoms represented by ellipsoids at the 50% probability level. (C, grey; Br, yellow; Mn, beige; O, red; N, blue; H, pink)

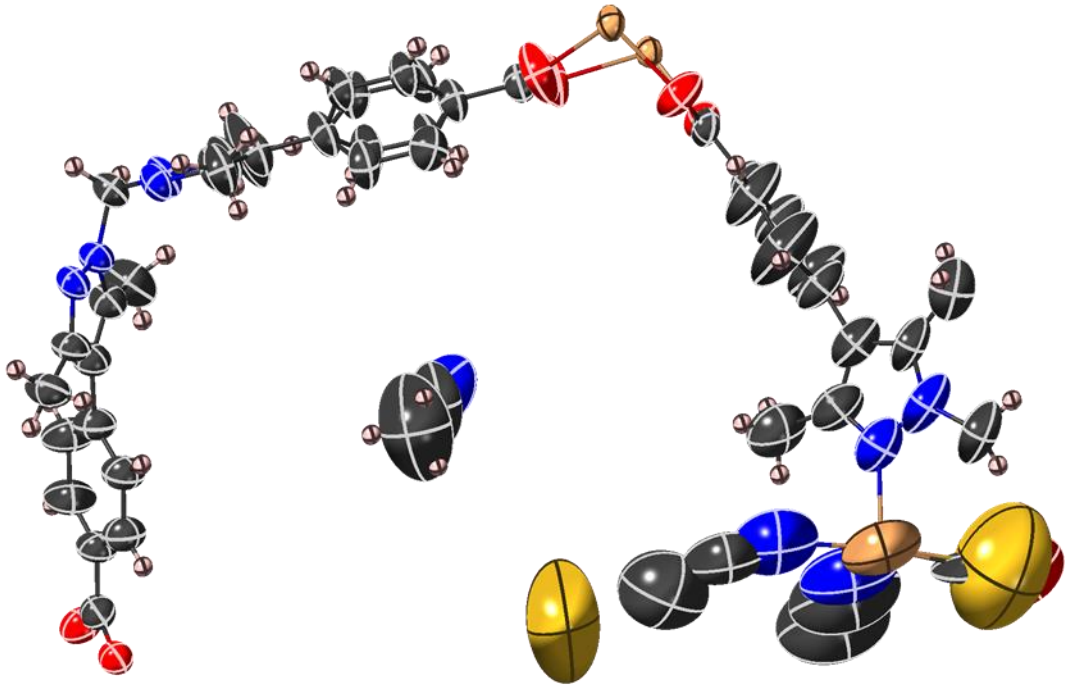

Figure 2.50. Asymmetric unit of MnMOF[$Mn(CO)_3MeCN$]Br photolyzed for 20 min (**2.8**), with all non-hydrogen atoms represented by ellipsoids at the 50% probability level. (C, grey; Br, yellow; Mn, beige; O, red; N, blue; H, pink)

Table 2.11. Crystal data and structure refinement details

Sample	**2.1**	**2.2**	**2.3**	**2.4**	**2.5**
Empirical formula	$C_{50}H_{48}Mn_2N_8O_{10}$	$C_{49}H_{61}Br_{0.5}Mn_3N_6O_{14}$	$C_{49}H_{46.75}Br_{0.5}Mn_{2.5}N_{11.25}O_{7.5}$	$C_{42.5}H_{35.5}N_{6.5}O_{7.5}Mn_2Br_{0.5}$	$C_{43}H_{42}Br_{0.5}Mn_2N_6O_9$
Formula weight	1030.84	1122.82	1050.53	907.11	936.66
Temperature/K	153(2)	120(2)	100.0 (2)	120(2)	100(1)
Crystal system	monoclinic	monoclinic	monoclinic	monoclinic	monoclinic
Space group	*C2/c*	*P2₁/m*	*P2₁/m*	*P2₁/m*	*P2₁/m*
a/Å	20.900(4)	12.4337(4)	12.4134(13)	12.4262(8)	12.337(3)
b/Å	14.678(3)	33.9583(11)	33.362(4)	33.687(2)	32.664(7)
c/Å	7.6360(15)	12.9228(5)	12.9953(13)	12.9813(9)	12.964(3)
α/°	90	90	90	90	90
β/°	93.70(3)	99.229(4)	95.565(9)	98.017(7)	93.65(3)
γ/°	90	90	90	90	90
Volume/Å³	2337.6(8)	5385.7(3)	5356.4(10)	5380.9(6)	5213.6(18)
Z	2	4	4	4	4
ρ_{calc}*g/cm³*	1.465	1.114	1.135	1.120	1.193
μ/mm⁻¹	0.610	5.050	0.821	4.635	0.918
F(000)	1068.0	1832.0	1871.0	1854.0	1926.0
Crystal size/mm³	0.2 × 0.15 × 0.1	0.301 × 0.150 × 0.005	0.30 × 0.10 × 0.04	0.448 × 0.104 × 0.021	0.22 × 0.03 × 0.01
Radiation/Å	MoKα (λ = 0.71073)	CuKα (λ = 1.54184)	Synchrotron (λ = 0.6889)	CuKα (λ = 1.54184)	Synchrotron (λ = 0.7109)
2Θ range for data collection/°	3.906 to 63.808	6.93 to 148.04	2.366 to 72.142	5.246 to 150.59	2.494 to 63.536
Index ranges	-28 ≤ h ≤ 28, -20 ≤ k ≤ 20, -11 ≤ l ≤ 11	-15 ≤ h ≤ 15, -42 ≤ k ≤ 31, -15 ≤ l ≤ 16	-20 ≤ h ≤ 20, -53 ≤ k ≤ 56, -21 ≤ l ≤ 22	-11 ≤ h ≤ 15, -37 ≤ k ≤ 41, -16 ≤ l ≤ 15	-17 ≤ h ≤ 17, -47 ≤ k ≤ 47, -17 ≤ l ≤ 17
Reflections collected	20031	40762	111480	40784	88020
Independent reflections	3457 [R_{int} = 0.0653, R_{sigma} = 0.0411]	10850 [R_{int} = 0.0856, R_{sigma} = 0.0670]	25824 [R_{int} = 0.1912, R_{sigma} = 0.3712]	10920 [R_{int} = 0.1440, R_{sigma} = 0.1060]	14336 [R_{int} = 0.0585, R_{sigma} = 0.0412]
Data/restraints/parameters	3457/0/163	10850/6/517	25824/74/627	10920/118/573	14336/1/605
Goodness-of-fit on F²	1.076	1.051	0.944	1.462	1.531
Final R indexes [I>=2σ (I)]	R_1 = 0.0748, wR_2 = 0.2451	R_1 = 0.0975, wR_2 = 0.2673	R_1 = 0.1271, wR_2 = 0.3426	R_1 = 0.1640, wR_2 = 0.4297	R_1 = 0.1271, wR_2 = 0.3824
Final R indexes [all data]	R_1 = 0.0820, wR_2 = 0.2573	R_1 = 0.1129, wR_2 = 0.2803	R_1 = 0.2798, wR_2 = 0.3864	R_1 = 0.1963, wR_2 = 0.4545	R_1 = 0.1540, wR_2 = 0.3956
Largest diff. peak/hole / e Å⁻³	2.81/-0.98	1.12/-1.67	1.45/-1.30	1.34/-1.71	1.61/-3.55

Table 2.12. Crystal data and structure refinement details

Sample	**2.6**	**2.7**	**2.8**
Empirical formula	$C_{14}H_{16}BrMnN_4O_3$	$C_{49.25}H_{47.5}N_{12.25}O_{6.75}Br_{0.5}Mn_{2.5}$	$C_{50.6}H_{46.75}Br_{0.5}Mn_{2.5}N_{12.75}O_{6.13}$
Formula weight	423.16	1056.30	1081.04
Temperature/K	120.0	100(2)	100(2)
Crystal system	orthorhombic	monoclinic	monoclinic
Space group	*Pnma*	$P2_1/m$	$P2_1/m$
a/Å	10.0695(4)	12.4072(8)	12.4279(11)
b/Å	14.5722(7)	33.106(2)	33.146(3)
c/Å	11.3525(4)	12.9591(9)	12.9816(13)
α/°	90	90	90
β/°	90	95.378(6)	95.071(8)
γ/°	90	90	90
Volume/Å³	1665.81(12)	5299.5(6)	5326.6(9)
Z	4	4	4
ρ_{calc}*g/cm³*	1.687	0.044	1.131
μ/mm⁻¹	9.430	0.055	0.822
F(000)	848.0	69.0	1855.0
Crystal size/mm³	1 × 0.4 × 0.05	0.30 x 0.10 x 0.04	0.3 x 0.1 x 0.04
Radiation/Å	CuKα (λ = 1.54184)	Synchrotron (λ = 0.6889)	Synchrotron (λ = 0.6889)
2Θ range for data collection/°	9.876 to 148.938	2.384 to 72.144	2.382 to 72.118
Index ranges	-12 ≤ h ≤ 8, -17 ≤ k ≤ 17, -13 ≤ l ≤ 14	-20 ≤ h ≤ 20, -53 ≤ k ≤ 56, -22 ≤ l ≤ 21	-20 ≤ h ≤ 20, -53 ≤ k ≤ 56, -21 ≤ l ≤ 21
Reflections collected	6827	110674	109385
Independent reflections	1736 [R_{int} = 0.0363, R_{sigma} = 0.0270]	25681 [R_{int} = 0.1759, R_{sigma} = 0.4775]	25698 [R_{int} = 0.1779, R_{sigma} = 0.5271]
Data/restraints/parameters	1736/0/114	25681/45/611	25698/75/599
Goodness-of-fit on F²	1.130	0.955	0.982
Final R indexes [I>=2σ (I)]	R_1 = 0.0299, wR_2 = 0.0782	R_1 = 0.1283, wR_2 = 0.3461	R_1 = 0.1372, wR_2 = 0.3646
Final R indexes [all data]	R_1 = 0.0333, wR_2 = 0.0808	R_1 = 0.3158, wR_2 = 0.3978	R_1 = 0.3594, wR_2 = 0.4185
Largest diff. peak/hole / e Å⁻³	0.76/-0.53	1.19/-1.30	1.23/-0.96

Table 2.13. Selected bond lengths and angles

	2.2 (EtOH)	**2.3 (MeCN)**	**2.4 (BzCN)**	**2.5 (THF)**	**2.6 (Model complex)**	**2.7 (MeCN 10 min photolysis)**	**2.8 (MeCN 20 min photolysis)**
Bond lengths	Å	Å	Å	Å	Å	Å	Å
Mn-CO(eq)	1.78(2)	1.869(17) (CO)	1.99(3)	1.818(13)	1.800(3)	2.035(2)	
Mn-CO(ax)	2.11(4)	1.916(15)	1.787(19)	1.86(2)	1.793(4)	1.871(3)	2.100(3)
C-O(eq)	1.10(2)	1.16(2)	1.096(18)	1.117(14)	1.152(3)	1.34806(7)	
C-O(ax)	1.07(6)	1.01(2)	1.126(18)	1.02(2)	1.144(5)	0.989(11)	1.15837(12)
Mn-X(ax-solvent)	2.21(2) (OH_2)	1.857(16) (MeCN)	2.02(3)			2.266(12)	2.386(11)
Mn-N(eq-ac)		-				2.175(10)	2.181(10)
N-C(ax-ac)		1.141(8)	1.138(9) (BzCN)			1.063(10)	1.123(8)
C-C(ax-ac)		1.427(9)	1.444(8) (BzCN)			1.357(14)	1.464(9)
Mn-Br				2.571(3)	2.821(6)		2.771(16)
O···Br(ax, through space)	4.596	4.012	4.436 (to *anti*-axial CO)			3.931	3.849
Bond angles	°	°	°	°	°	°	°
Mn-C-O(eq)	164(5)	171(3)	164(5)	173.4(13)	174.5(2)	175.53(7)	
Mn-C-O(ax)	179(3)	168(3)	179(3)	176.5(19)	176.5(3)	175.15(5)	174.27(7)
Mn-N-C(ax-solvent)		153(3)	179(3)			146.3(12)	160.1(15)
Mn-N-C(eq-ac)						174.0(10)	165.1(11)
N-C-C(ax-ac)		178(2)	178(2)			177.2(9)	166.8(15)

eq = equatorial with respect to L'

ax = axial with respect to L'

ac = acetonitrile

2.6.4 Calculation to determine Co occupancy

Co occupancy in Section 2.5.5 was calculated by the following formula

c = #Co atoms

m = #Mn atoms

t= total number of Mn and Co atoms

$r = \frac{c}{m}$ (measured atomic ratio of Co to Mn)

$\therefore c = rm$

$t = c + m$

$= rm + m$

$= (r + 1)m$

Proportion of sites occupied $= \frac{c+m}{4}$ (as there are 4 potential sites for metal atoms to occupy)

$= \frac{(r+1)m}{4}$

Co occupancy $= \frac{c}{Proportion\ of\ sites\ occupied}$

$= \frac{4c}{(r+1)m}$ (as c=rm)

$= \frac{4rm}{(r+1)m}$

Therefore, Co occupancy = $\frac{4r}{r+1}$

2.7 References

1 M. Knauert, S. Vangala, M. Haslip and P. J. Lee, *Oxid. Med. Cell. Longev.*, 2013, 360815

2 L. Wu, Q. Liu, R. Jackstell and M. Beller, *Angew. Chem. Int. Ed.*, 2014, **53**, 6310–6320.

3 C. C. Romão, W. A. Blättler, J. D. Seixas and G. J. L. Bernardes, *Chem. Soc. Rev.*, 2012, **41**, 3571–3583.

4 J. B. Peng, H. Q. Geng and X. F. Wu, *Chem*, 2019, **5**, 526–552.

5 In *Homogeneous Catalysis*, Springer, Dordrecht, 2004.

6 G. J. Sunley and D. J. Watson, *Catal. Today*, 2000, **58**, 293–307.

7 C. Le Berre, P. Serp, P. Kalck and G. P. Torrence, in *Ullmann's Encyclopedia of Industrial Chemistry*, Wiley-VCH Verlag GmbH & Co. KGaA, Weinheim, Germany, 2014, pp. 1–34.

8 T. Morimoto and K. Kakiuchi, *Angew. Chem. Int. Ed.*, 2004, **43**, 5580–5588.

9 A. Brennführer, H. Neumann and M. Beller, *Angew. Chem. Int. Ed.*, 2009, **48**, 4114–4133.

10 K. Ma, B. S. Martin, X. Yin and M. Dai, *Nat. Prod. Rep.*, 2019, **36**, 174–219.

11 M. Suematsu, N. Goda, T. Sano, S. Kashiwagi, T. Egawa, Y. Shinoda and Y. Ishimura, *J. Clin. Investig.*, 1995, **96**, 2431–2437.

12 A. Verma, D. J. Hirsch, C. E. Glatt, G. V. Ronnett and S. H. Snyder, *Science*, 1993, **259**, 381–384.

13 S. W. Ryter, J. Alam and A. M. K. Choi, *Physiol. Rev.*, 2006, **86**, 583–650.

14 M. Kajimura, R. Fukuda, R. M. Bateman, T. Yamamoto and M. Suematsu, *Antioxidants Redox Signal.*, 2010, **13**, 157–192.

15 T. Yamamoto, N. Takano, K. Ishiwata, M. Ohmura, Y. Nagahata, T. Matsuura, A. Kamata, K. Sakamoto, T. Nakanishi, A. Kubo, T. Hishiki and M. Suematsu, *Nat. Commun.*, 2014, **5**, 160.

16 L. Vítek, H. Gbelcová, L. Muchová, K. Váňová, J. Zelenka, R. Koníčková, J. Šuk, M. Zadinova, Z. Knejzlík, S. Ahmad, T. Fujisawa, A. Ahmed and T. Ruml, *Dig. Liver Dis.*, 2014, **46**, 369–375.

17 R. Motterlini and L. E. Otterbein, *Nat. Rev. Drug Discov.*, 2010, **9**, 728–743.

18 B. Wegiel, D. Gallo, E. Csizmadia, C. Harris, J. Belcher, G. M. Vercellotti, N. Penacho, P. Seth, V. Sukhatme, A. Ahmed, P. P. Pandolfi, L. Helczynski, A. Bjartell, J. L. Persson and L. E. Otterbein, *Cancer Res.*, 2013, **73**, 7009–7021.

19 B. Kawahara, S. Ramadoss, G. Chaudhuri, C. Janzen, S. Sen and P. K. Mascharak, *J. Inorg. Biochem.*, 2019, **191**, 29–39.

20 R. Motterlini, P. Sawle, S. Bains, J. Hammad, R. Alberto, R. Foresti and C. J. Green, *FASEB J.*, 2005, **19**, 1–24.

21 R. Motterlini, J. E. Clark, R. Foresti, P. Sarathchandra, B. E. Mann and C. J. Green, *Circ. Res.*, 2002, **90**, 17-24

22 I. Chakraborty, S. J. Carrington, G. Roseman and P. K. Mascharak, *Inorg. Chem.*, 2017, **56**, 1534–1545.

23 B. E. Mann, *Top. Organomet. Chem.*, 2010, **32**, 247–285.

24 S. García-Gallego and G. J. L. Bernardes, *Angew. Chem. Int. Ed.*, 2014, **53**, 9712–9721.

25 M. Wrighton, *Chem. Rev.,* 1974, **74**, 4, 401-430

26 E. Kottelat and F. Zobi, *Dalton Trans.,* 2016, **45**, 6920-6927

27 L. Hewison, S. H. Crook, B. E. Mann, A. J. H. M. Meijer, H. Adams, P. Sawle and R. A. Motterlini, *Organometallics*, 2012, **31**, 5823–5834.

28 I. Chakraborty, S. J. Carrington and P. K. Mascharak, *Acc. Chem. Res.*, 2014, **47**, 2603–2611.

29 E. Kottelat, A. Ruggi and F. Zobi, *Dalton Trans.*, 2016, **45**, 6920–6927.

30 M. A. Gonzales and P. K. Mascharak, *J. Inorg. Biochem.*, 2014, **133**, 127–135.

31 A. M. Mansour, C. Steiger, C. Nagel and U. Schatzschneider, *Eur. J. Inorg. Chem.*, 2019, **2019**,

4572–4581.
32 F. Mohr, J. Niesel, U. Schatzschneider and C. W. Lehmann, *Zeitschrift fur Anorg. und Allg. Chem.*, 2012, **638**, 543–546.
33 H.-M. Berends and P. Kurz, *Inorganica Chim. Acta*, 2012, **380**, 141–147.
34 C. Nagel, S. McLean, R. K. Poole, H. Braunschweig, T. Kramer and U. Schatzschneider, *Dalton Trans.*, 2014, **43**, 9986-9997
35 S. Pordel and J. K. White, *Inorganica Chim. Acta*, 2020, **500**, 119206.
36 R. D. Rimmer, A. E. Pierri and P. C. Ford, *Coord. Chem. Rev.*, 2012, **256,** 1509–1519.
37 R. Mede, J. Traber, M. Klein, H. Görls, G. Gessner, P. Hoffmann, M. Schmitt, J. Popp, S. H. Heinemann, U. Neugebauer and M. Westerhausen, *Dalton Trans.*, 2017, **46**, 1684–1693.
38 J. Jimenez, I. Chakraborty, A. Dominguez, J. Martinez-Gonzalez, W. M. C. Sameera and P. K. Mascharak, *Inorg. Chem.*, 2018, **57**, 1766–1773.
39 A. Sinopoli, N. T. La Porte, J. F. Martinez, M. R. Wasielewski and M. Sohail, *Coord. Chem. Rev.*, 2018, **365**, 60–74.
40 B. P. Sullivan, C. M. Bolinger, D. Conrad, W. J. Vining and T. J. Meyer, *J. Chem. Soc. Chem. Commun.*, 1985, **20**, 1414–1416.
41 X. Wang, I. Thiel, A. Fedorov, C. Copéret, V. Mougel and M. Fontecave, *Chem. Sci.*, 2017, **8**, 8204–8213.
42 M. Stanbury, J. D. Compain and S. Chardon-Noblat, *Coord. Chem. Rev.*, 2018, **361**, 120–137.
43 H. Fei and S. M. Cohen, *Chem. Commun.*, 2014, **50**, 4810–4812.
44 A. J. Blake, N. R. Champness, T. L. Easun, D. R. Allan, H. Nowell, M. W. George, J. Jia and X. Z. Sun, *Nat. Chem.*, 2010, **2**, 688–694.
45 S. Diring, A. Carné-Sánchez, J. Zhang, S. Ikemura, C. Kim, H. Inaba, S. Kitagawa and S. Furukawa, *Chem. Sci.*, 2017, **8**, 2381–2386.
46 M. T. Huxley, A. Burgun, H. Ghodrati, C. J. Coghlan, A. Lemieux, N. R. Champness, D. M. Huang, C. J. Doonan and C. J. Sumby, *J. Am. Chem. Soc.*, 2018, **140**, 6416–6425.
47 M. T. Huxley, R. J. Young, W. M. Bloch, N. R. Champness, C. J. Sumby and C. J. Doonan, *Organometallics*, 2019, **38**, 3412–3418.
48 W. M. Bloch, A. Burgun, C. J. Coghlan, R. Lee, M. L. Coote, C. J. Doonan and C. J. Sumby, *Nat. Chem.*, 2014, **6**, 906–912.
49 A. S. Potapov and A. I. Khlebnikov, *Polyhedron*, 2006, **25**, 2683–2690.
50 A. S. Potapov, A. I. Khlebnikov and S. F. Vasilevskii, *Russ. J. Org. Chem.*, 2006, **42**, 1368–1373.
51 W. M. Bloch, C. J. Doonan and C. J. Sumby, *CrystEngComm*, 2013, **15**, 9663–9671.
52 B. S. Ault, T. M. Becker, G. Q. Li and M. Orchin, *Spectrochim. Acta - Part A Mol. Biomol. Spectrosc.*, 2004, **60**, 2567–2572.
53 B. Zha, J. Li, J. Wu, X. Miao and M. Zhang, *New J. Chem.*, 2019, **43**, 17182–17187.
54 L. Brammer, E. A. Bruton, and P. Sherwood, *Crys. Growth Des.*, 2001, 1, **4**, 277-290
55 Common Solvents Used in Organic Chemistry: Table of Properties, https://organicchemistrydata.org/solvents/, (accessed 21 March 2021).
56 P. A. Gerakines, W. A. Schutte, J. M. Greenberg and E. F. Van Dishoeck, *Astron. Astrophys.,* 1995, **296**, 810-818
57 J. A. Calladine, S. B. Duckett, M. W. George, S. L. Matthews, R. N. Perutz, O. Torres and K. Q. Vuong, *J. Am. Chem. Soc*, 2011, **133**, 2303–2310.
58 M. Dalal, in *A Textbook of Inorganic Chemistry*, Dalal Institute, 1st edn., 2012.
59 M. Huxley, PhD thesis, University of Adelaide, 2019.

60 A. M. Bond, R. Colton and M. J. McCormick, *Inorg. Chem.*, 1976, **16**, 155–159.

61 A. M. Bond, B. S. Grabaric and Z. Grabaric, *Inorg. Chem.*, 1978, **17**, 1013–1018.

62 E. S. Ilton, J. E. Post, P. J. Heaney, F. T. Ling and S. N. Kerisit, *Appl. Surf. Sci.*, 2016, **366**, 475–485.

63 T. M. McPhillips, S. E. McPhillips, H. J. Chiu, A. E. Cohen, A. M. Deacon, P. J. Ellis, E. Garman, A. Gonzalez, N. K. Sauter, R. P. Phizackerley, S. M. Soltis, and P. Kuhn, *J. Synchrotron Rad.*, 2002, **9**, 401-406

64 H. Nowell, S. A. Barnett, K. E. Christensen, S. J. Teat, and D. R. Allan, *J. Synchrotron Rad.*, 2012, **19**, 435-441

65 G. M. Sheldrick, *Acta Crys. A*, 2008, **64**, 1, 112-122

66 O. V. Dolomanov, L. J. Bourhis, R. J. Gildea, J. A. K. Howard and H. Puschmann., *J. Appl. Cryst.*, 2009, **42**, 339- 341.

67 A. L. Spek, *Acta Crystallogr. Sect. C Struct. Chem.*, 2015, **71**, 9–18.

68 CrystalMakerX©, CrystalMaker Software Ltd, Oxford, England, www.crystalmaker.com

69 C. B. Hubschle, G. M. Sheldrick, and B. Dittrich, *J. Appl. Cryst.,* 2011, **44**, 1281-1284

Chapter Three: Potential applications of CO loaded MOFs

3.1 Introduction

3.1.1 MOFs in medicine and fine chemical synthesis

With large internal surface areas allowing for the storage of guest molecules, many MOFs have been investigated for applications in which they act as reservoirs of these molecules for drug delivery[1–4] and gas storage and release,[5,6] as well as storage for energy, industrial and environmental applications.[7–10] There are several reasons why the storage and release of a gas from a solid-state material is advantageous. Among these reasons are the safety benefits of storage in a solid-state material over more traditional tank storage which requires higher or lower pressures. Additionally, there is an ease of handling a solid, especially in small quantities, compared to using a gas.[9] The general methods through which MOFs can be utilised for these applications were outlined in Chapter 1.5, and hence specific applications will now be expanded upon.

For a MOF to be used as a storage vessel, both the uptake and the release of the guests must be studied. For gases this is often studied through adsorption isotherms, where the difference between adsorption and desorption traces can indicate the working capacity of the host material (Figure 3.1). Crucially, the delivery of the payload under the conditions in which the material is to be used is a significant indicator of the applicability of a material.[11] While pressure changes are one method for triggering the release of a gas from a MOF, other stimuli such as increased temperature, chemical treatment or irradiation with light may be used.[5,6,8]

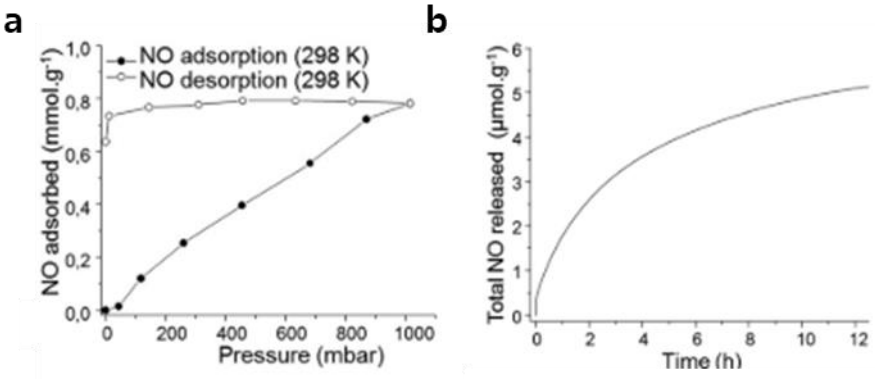

Figure 3.1. Controlled delivery of NO was achieved with a porous Ca-MOF in which NO was bound to coordinatively unsaturated sites. **a)** NO isotherm showing a large hysteresis between the adsorption and desorption traces, indicating chemisorption, and **b)** NO release from the MOF triggered by hydrolysis.[12]

The class of signalling molecules called gasotransmitters are prime candidates for MOF-bound therapeutic agents.[13] These gases, namely nitric oxide, carbon monoxide and hydrogen sulfide, act as messengers between cells, triggering physiological and chemical transformations.[14] Despite their therapeutic benefits, all three agents present challenges in delivery due to acute toxicity at high concentrations, location dependant activities, and their gaseous nature. The storage and release of nitric oxide (NO) from MOFs has been pioneered by the group of Morris (Figure 3.2). Investigations by this research group explored different methods of storing the gas, including in the pores,[15] bound to unsaturated metal sites[12,16,17] and post-synthetic modification of the organic linkers.[18] The release kinetics have also been tuned through metal substitution,[16,17] pore size modification[17] and structural flexibility.[19] The NO released from these materials has been reported to stimulate the relaxation of smooth muscles in porcine arteries and inhibit the aggregation of human blood platelets.[20] The synergistic loading of complementary therapeutic agents, including NO, ruthenium anticancer drugs and bactericidal agents, has also been demonstrated.[21,22] This has resulted in the ability to control the release of the different agents at different rates and to allow for different therapeutic activities.

Figure 3.2. Activation, loading and release cycle of NO carrier M-CPO-27 (M = Co or Ni), where NO is bound to coordinatively unsaturated metal sites.[20]

As with any therapeutic agent, the process through which a MOF becomes a final medicinal product, or formulation, must be carefully considered.[23] MOFs and coordination polymers are generally obtained as crystalline powders, but the solid-state properties of particle size, shape, surface area and morphology all affect their activities.[24] As such, for MOFs to be tailored for specific applications, their shaping must also be considered in addition to their chemistry and topology.[25,26] For biomedical applications, the formulation of MOFs into monoliths, gels, ointments and thin films have been considered as viable pathways.[23]

The application of MOFs in chemical synthesis is a less well-developed field; however, they have been investigated for use in separations and purifications[27,28] and catalysis in bulk and continuous flow systems. MOF-508 was used in a gas chromatographic column for the highly selective separation of alkanes[27] and a silica-UiO-66 composite was demonstrated to separate positional isomers of ethylbenzene and xylene.[28] Heterogenous catalysts in flow systems can allow for reaction and separation to occur simultaneously, as the reactants flow through a fixed packed or coated column. Mechanical degradation of the catalyst is minimal due to lack of stirring and very high surface area to volume ratios can be achieved.[29] Both MOF-as-catalyst and catalyst-in-MOF systems have been reported to be used for catalytic continuous flow reactions.[30,31]

An as-yet unexplored application for MOFs is the controlled release of reagent gases for chemical synthesis. The ability of MOFs to store and release gases from the solid-state presents untapped opportunities, especially for continuous flow systems, where it would be plausible to introduce a gas from a "MOF cartridge", which can then be replaced and/or regenerated when empty. Ideally, the MOF would have the ability for the gas release to be finely controlled and be able to be switched on and off by an external trigger.[32]

3.1.2 Carbon monoxide in chemical synthesis

As discussed in Chapter 2, carbon monoxide is an incredibly powerful building block for chemical synthesis. Carbonylation reactions allow for the direct installation of synthetically important functional groups such as carboxylic acids, esters, aldehydes, ketones and amides, and are used in the industrially relevant Monsanto, Cativa and Fischer-Tropsch processes to produce acetic acid and liquid hydrocarbons.

Despite its synthetic usefulness, CO is not widely used in laboratory scale and fine chemical synthesis. This is largely due to the safely concerns arising from using such a toxic and flammable gas and, as CO is a colourless and odourless gas, accidental exposure is a serious risk.[34] Laboratory scale CO generating materials have been of interest in the last decade and are now commercially available, although expensive.[35] The COware/COgen system developed by the Skrydstrup group involves the palladium catalysed decarbonylation of tertiary acid chlorides in a two-chamber system, where the CO is generated in one chamber and is used in a range of amino-,[36,37] alkoxy-,[38] thio-[39] and reductive[40] carbonylations along with Suzuki-Miyaura and other coupling reactions (Figure 3.3).[41]

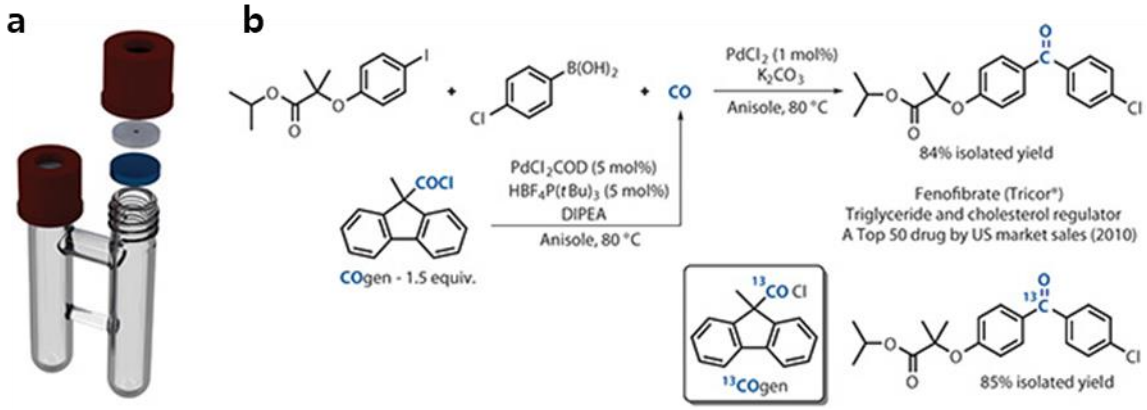

Figure 3.3. a) COware two chamber reaction vessel and **b)** Suzuki-Miyaura coupling with carbonyl insertion using Cogen source.[41]

Other CO sources have also been explored for small scale *in-situ* generation of carbon monoxide including aldehydes with ruthenium catalysts,[42,43] formates and formamides with palladium catalysts,[44–48] and metal carbonyl complexes ($Ni(CO)_4$, $W(CO)_6$ and $Mo(CO)_6$) with bases in protic solvents.[49–51]Despite being promising for small scale chemistry, these CO sources have been deemed too toxic, atom inefficient or expensive for larger scale reactions.[52] For example, the metal carbonyl complex CO

sources were used as 4 equivalents of CO bound to $Ni(CO)_4$ (1:1 reactant to complex ratio),[49] 2 equivalents of CO bound to $W(CO)_6$[50] and 6 equivalents of CO bound to $Mo(CO)_6$[51] in order to achieved yields >80%.

Another approach to utilise CO more safely in chemical synthesis has been the development of continuous flow reactor systems. In these systems, higher interfacial areas, mass and heat transfer rates have allowed for poorly soluble gases such as CO to react with near stoichiometric equivalents (1.2 equivalents)[53] and at lower pressures[54] than with batch methods. Despite these advances, pressurised gases are still required, albeit with less risk to the chemist. To eliminate the need for CO gas cylinders, Brancour *et al.* connected *in-situ* CO generation with a tube-in-tube flow reactor to perform carbonylation reactions (Figure 3.4).[55] Gaseous CO was generated by the dehydration of formic acid with sulfuric acid. A similar method was used for the carbonylation of alcohols and despite reporting little improvement in yield compared to the batch procedure, the reaction could be scaled up to the multi-gram scale.[56] Unlike a gas bottle, the CO generation of these materials cannot be switched on and off as simply as opening a valve, and hence fine control over the CO release is limited.

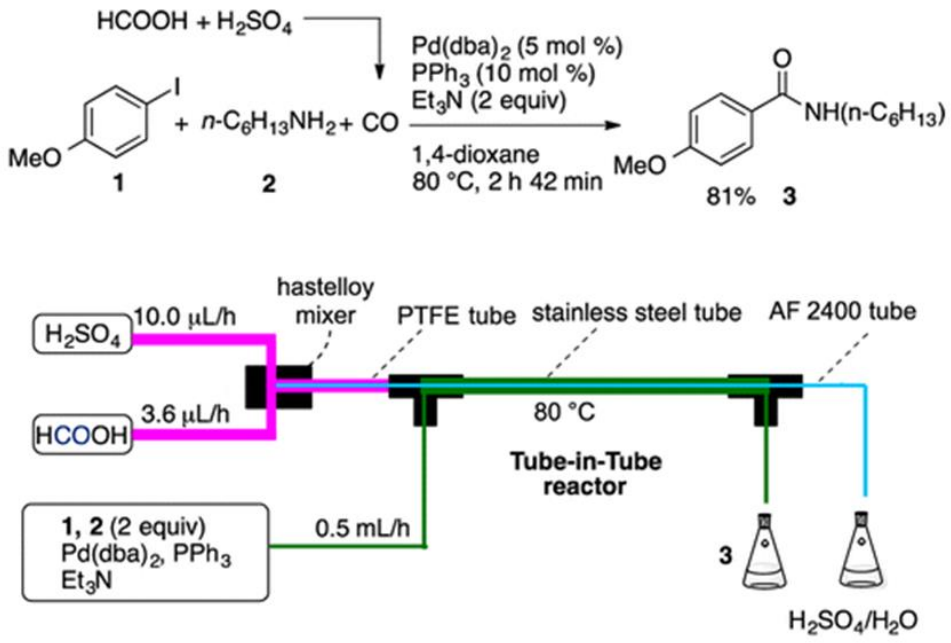

Figure 3.4. In-situ generation of CO from the dehydration of formic acid with sulfuric acid for an aminocarbonylation reaction in a tube-in-tube flow reactor.[55]

As a chemical building block, CO is highly desirable to use in fine and bulk chemical synthesis. To this end, carbonylation reactions are carried out with high efficiencies at very large scales, using gaseous CO, and on very small scales, using *in*- or *ex-situ* CO generating materials. The development of a CO generating material for use in medium scale flow systems which is safe, re-usable and tuneable whilst having the ability to turn on and off the release of CO would be advantageous.

3.1.3 Carbon monoxide in medicine

For many years carbon monoxide (CO) has had a reputation as a toxic gas which can be fatal to humans. Recently, it has been found to have a key role in the human body as a signalling molecule and has the potential to be used therapeutically in treating asthma, organ failure, sepsis and organ transplant rejection.[57,58] The difficulty in utilising CO, is in the application, due to its state as a gas, and in avoiding the serious complications involved in carbon monoxide poisoning. This topic was introduced in Chapter 2.1.1, as was a possible solution in the form of carbon monoxide releasing molecules (CORMs). CORMs circumvent the need to administer CO in its gaseous form by binding it to a pro-drug molecule, one class of which are metal carbonyl complexes. A subset of these complexes releases CO on irradiation with light and may be referred to as photoCORMs. These molecules have been extensively studied but the molecular species are typically unsuitable for therapeutic use due to fast diffusion rates, resulting in toxicity to untargeted healthy tissues, and enzymatic degredation.[59,60] MOFs provide a means by which these photoCORMs can be immobilised, enabling them to be used in the solid-state, and providing high loading efficiencies and tuneable photoactivated delivery kinetics.[61]

3.1.4 Carbon monoxide releasing MOFs

Despite many examples of MOFs used to release other small gaseous signalling molecules such as NO and H_2S, there are only a few examples in the literature of CO releasing MOFs. The first such study by Ma *et al*, utilised unsaturated coordination sites within the iron MOFs, MIL-88B and NH_2-MIL-88B, to coordinate to CO (Figure 3.5).[62]

The MOFs were first activated by heating above 373K under vacuum to remove coordinated water molecules, then exposed to a CO atmosphere at 93K. The trapped CO was then released through the dissolution of the parent framework in a phosphate buffer solution. The loading capacity of these MOFs was limited, with only 9 and 17% of the iron sites coordinating to CO in MIL-88B and NH_2-MIL-88B respectively, leading to CO release of 0.36 and 0.69 mmol g^{-1}.

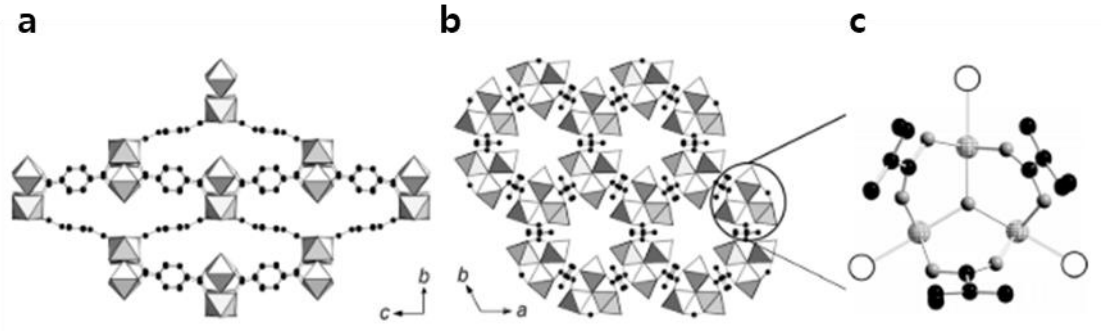

Figure 3.5. CO storage and release by coordination to the metal nodes of MIL-88B **a)** viewed down the a axis, **b)** viewed down the c-axis and **c)** iron secondary building unit with vacant coordination sites represented by open circles. (Fe, light grey; O, grey; C, black)[62]

The encapsulation of a molecular photoCORM into the pores of a MOF was an approach developed by the group of Barea.[63] The first example of this method involved the incorporation of $[Mn(tacn)(CO)_3]^+$ (tacn = 1,4,7-triazacyclononane) into the pores of an anionic framework, $[Zn_8(adeninate)_4(bpdc)_6]$ (bpdc = 4,4′-biphenyl dicarboxylate), by cation exchange. Although the guest complex released CO upon irradiation with light (0.25 mmol g^{-1}) unfortunately, the majority of the photoCORM complexes leached into solution when placed into water. Later studies utilised a one pot method in which a photoCORM, $[Mo(CNCMe_2CO_2H)_3(CO)_3]$, was encapsulated within the mesopores of a hierarchically porous MOF, MOF-74(Zn) $[Zn_2(dhtp)]$ (dhtp = 2,5-dihydroxyterephthalate).[64] Quantities of CO released were much lower than the non-encapsulated CORM. The same photoCORM was also encapsulated into a series of aluminium based MOFs, where it was reported that smaller channels led to lower leaching of the CORM in solution and demonstrated the release CO of upon irradiation.[61]

The problem of a pore bound CORM leaching from the MOF can be addressed by chemical attachment of the CO donor to the MOF. Diring *et al* utilised a zirconium MOF, UiO-67-bpy, constructed from a 2,2′-bipyridine linker to construct a light activated CO releasing material (Figure 2.13).[59] The MOF had free chelating nitrogen donor sites, which when exposed to a solution of bromopentacarbonylmanganese(I) bound the manganese to the framework. The material was then irradiated with visible light at 460 nm to release CO to cell cultures, with a maximum release of 4.7 mmol g^{-1}. This release is near the theoretical maximum CO loading capacity of 14.6 wt.% (corresponding to 5.2 mmol g^{-1}) for the MOF metalated at 95% of available sites.

While these were the only studies examining CO *release* from MOFs, there have been many others investigating the *adsorption* of CO in MOFs.[65,66] These MOFs must be assumed to also be able to release the stored CO as well, except when the MOF is used as a CO reaction catalyst;[67] however, this has not been explored in these cases. These studies demonstrated that MOFs can bind and control the release of carbon monoxide for therapeutic use, but further work is required to tune the photo-release to longer wavelengths of light, as these will have higher physiological penetration, and to extend the library of photoCORM containing MOFs.

One starting point for extending this library is other MOFs constructed from the same 2,2′-bipyridine dicarboxylate linker that was successfully used in UiO-67-bpy. DUT-5, [Al(OH)(bpdc)] (bpdc = 4,4′-biphenyldicarboxylate), is such a MOF, in which the biphenyl linkers can easily be substituted for bipyridyl groups. This 3D framework is constructed of aluminium ion chains linked by hydroxyl groups and bridging carboxylates, producing rectangular channels 11.1 x 11.1 Å in size.[68] This MOF has been synthesised on gram scales as a microcrystalline powder and post-synthetically modified to bind to metals including Co(II), Mn(II) and Mn(III) for catalysis (Figure 3.7).[69] This is, therefore, an ideal MOF for anchoring metal carbonyl photoCORMs, with a theoretical maximum CO carrying capacity of 16.6 wt.% (5.9 mmol g^{-1}), if metalated with $Mn(CO)_3Br$ and assuming quantitative loading.

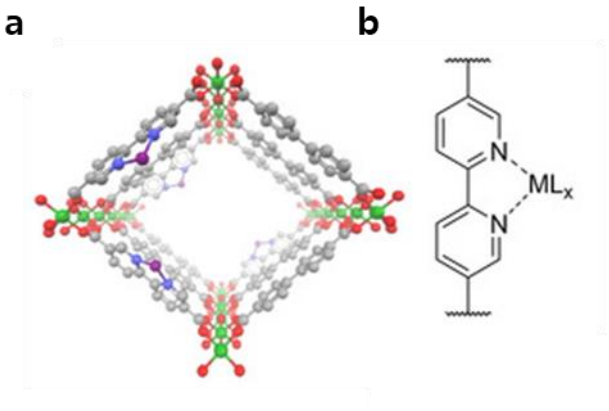

Figure 3.7. a) Schematic representation of the MOF DUT-5 (bipy), (bipy = 2,2'-bipyridine dicarboxylate), containing manganese (II/III) or cobalt (II) ions bound through PSMet to the framework. **b)** Bipyridine chelating binding site for metals.[69]

3.1.4 Structuralising MOFs

Like the structures of proteins, the structures of MOFs can be considered on four levels (Figure 3.8). The first level is the chemical building blocks, the metal node and organic linker. The second is the secondary building unit (SBU), which is the coordination of multiple ligands around a metal ion or cluster, producing a unit with a relatively rigid geometry. The third level is the linking of SBUs to form an extended network, which can be described by its topology and can contain open pores or channels. The last level of MOF structure is the morphology of the particle and is controlled by the growth of the structure. The fourth level encompasses the particle size, shape and orientation.[25] Much of this thesis is focussed on the first three levels of MOF structure, in manipulating the building blocks and chemistry inside a MOF structure; however, it would be remiss to ignore the effects of morphology.

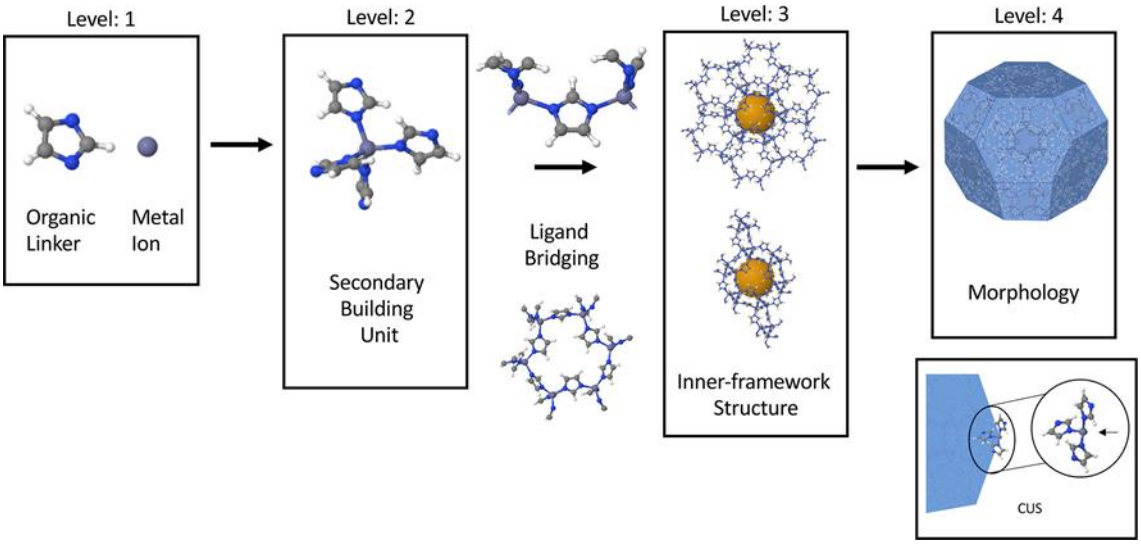

Figure 3.8. Structural levels of MOF composition with Level 1, organic linker and metal node; Level 2, secondary building unit; Level 3, structural topology and; Level 4, particle morphology[25]

As crystalline powders, MOFs have several disadvantages for applications in medicine or flow chemistry, including poor processability, safety concerns from dust formation, and difficulties in separating and reusing the frameworks.[70,71] In addition, the diameters of MOF pores are typically smaller than 2 nm, due to a higher propensity for framework collapse upon de-solvation for larger pore sizes. Incorporating hierarchical porosity in materials allows for tuneable multiple functions for which their effectiveness together could be greater than the sum of their parts.[72]

This can be achieved through adding a fifth structural level and assembling many individual crystals into 0D (hollow capsules or spheres), 1D (nanorods or fibres), 2D (membranes or films) or 3D superstructures (Figure 3.9).[73] The formation of these superstructures can be achieved through a number of methods including bottom-up (templating, interfacial reactions, reaction confinement etc.) and top-down (delamination, dip coating, electrospinning, etching etc.) approaches.

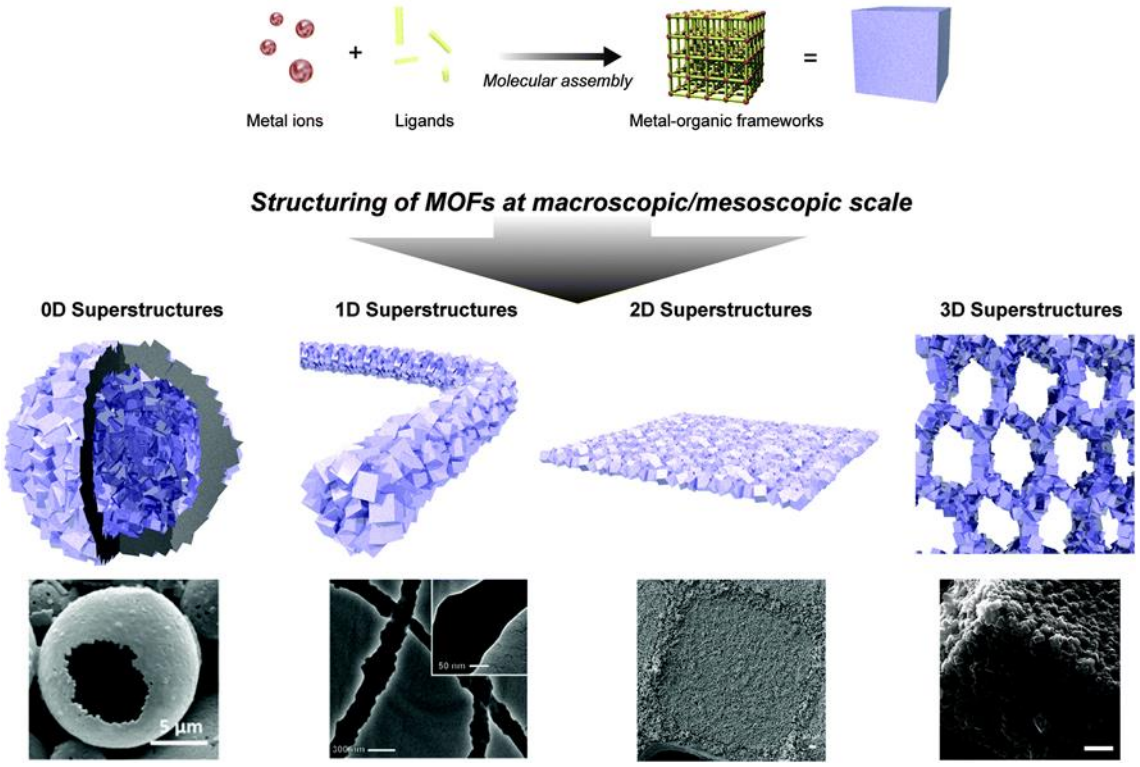

Figure 3.9. Classifications for MOFs structuralised at the macroscopic and mesoscopic scales.[73]

The formation of MOFs into 3D superstructures and monoliths may allow for the incorporation of macro- or meso-porosity, increasing the rates of diffusion of guest molecules. The presence of smaller crystallites incorporated into a 3D superstructure also allows for higher external surface areas,[74] while still allowing for convenient separation and recovery of the MOF, and reduced safety risks inherent to fine particles. One method for 3D structuralisation is solid-liquid synthesis using a sacrificial solid template. One such class of templates are metal oxide sol-gels, which are formed from a chemical process which first forms a colloidal suspension or sol, followed by the addition of a catalyst to form a gel. A gel is a continuous solid which can support its own weight, but which encloses a liquid phase. If the solvent is removed under normal conditions, capillary pressure causes shrinkage of the gel network and a substance known as a xerogel or ceramic is formed.[75] If the solvent is removed under conditions with no capillary pressure (e.g. supercritical drying), the resulting substance is known as an aerogel, and generally minimal shrinkage is observed (Figure 3.10a).

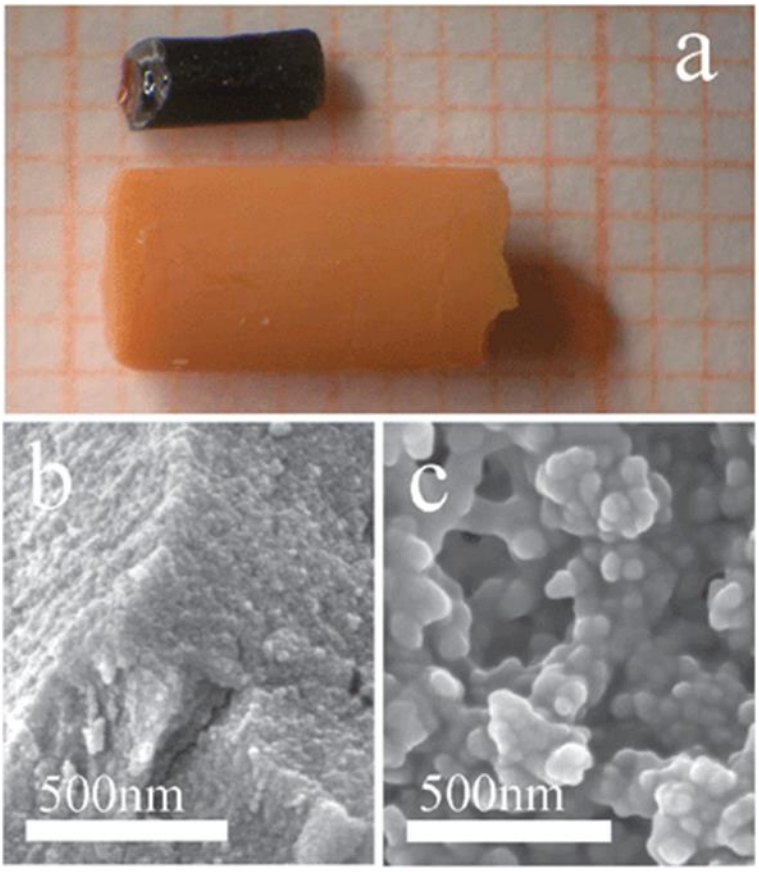

Figure 3.10. Iron (III) and 1,3,5-benzene-tricarboxylate MOFs formed as a **a)** xerogel (top) and aerogel (bottom). SEM images of the **b)** xerogel and **c)** aerogel showed the aerogel to be lower density and contains a high degree of macro-porosity compared to the xerogel.[76]

Both xerogels and aerogels may have high porosities and surface areas. As such sol-gel derived metal oxide templates may allow for the structuring of MOFs at the meso- and macro-scales and the creation of higher order superstructures, with enhanced properties compared to conventionally synthesised MOFs.[76,77] Therefore the meso- and macro-scopic structuralisation of MOFs for CO delivery applications may allow for greater diffusion, ease of use and processability.

3.2 Aims

This project aimed to utilise MnMOF as a safe and easily controlled *ex-situ* source of CO for carbonylation reactions. The photoactivated decarbonylation behaviour studied in Chapter 2.3 was applied to trigger CO generation by irradiation with visible light. This behaviour was also investigated to see if it extended to other MOFs which are unable to be studied by SCXRD. The behaviour of these MOFs (UiO-67-bpy and DUT-5-bpy) were compared to MnMOF in order to begin to develop a library of CO releasing MOFs and to identify key factors in controlling CO release.

In endeavouring to enhance the utility of MnMOF as a CO source, 3D structuralised MnMOF was synthesised from sol-gel derived manganese oxide templates. The synthesis and morphology of the templates were explored, as were the conditions for MOF formation. The structuralised MnMOF was then characterised, and its post-synthetic metalation and CO release properties were investigated and applied for use in carbonylation reactions.

Results and Discussion

3.3 Using MOFs to deliver CO for chemical synthesis

3.3.1 Reaction design

Both *in-situ* and *ex-situ* CO generating materials have been reported in the literature, but it was evident that *ex-situ* methods would present easier separation of the MOF from the reactants and provide the ability to characterise and regenerate the MOF after use in a reaction. The separation of the MOF from the reaction products was also postulated to limit degradation of the MOF due to exposure to the reactants and the heat of the reaction. MnMOF[$Mn(CO)_3$OHEt]Br (1) was chosen as an initial CO source, due to the understanding of the photochemistry developed in Chapter 2. Although MnMOF[$Mn(CO)_3$EtOH]Br releases CO upon both irradiation with light and heating to above 50 °C (Chapter 2.x), only photoinitiated CO release was investigated in this study due to the better-known understanding of the photochemistry and to time constraints. The aminocarbonylation reaction of 4-iodoanisole and n-hexylamine was chosen as a test reaction due to its prevalence in the literature for testing other CO releasing materials (Figure 3.11a).[36,38,55,78]

Several reaction formats were considered including a two-armed 25 mL tube with a single neck, two separate flasks connected by tubing and a single flask containing a vial with a perforated lid. These were ruled out due to difficulties in introducing reactants, poor transport of released CO to the reagents and the inability to separately irradiate or heat the chambers, respectively. Based on these experiments, a custom 10 mL H-tube was made, allowing for separate temperature and light conditions for each chamber, while minimising the headspace for CO to diffuse through (Figure 3.11b). The MOF was placed in an open glass vial containing a stirrer bar in the second arm, along with 1 mL of dioxane (between the vial and the wall of the H-tube) to avoid condensing and hence solvent loss from the higher temperature solution of the reaction arm. The reaction arm was placed in an oil bath to heat to the reaction temperature (80 °C), while a 2000 lumen LED torch in the visible spectrum was aligned with the MOF containing arm and wrapped in foil to maximise exposure to the light.

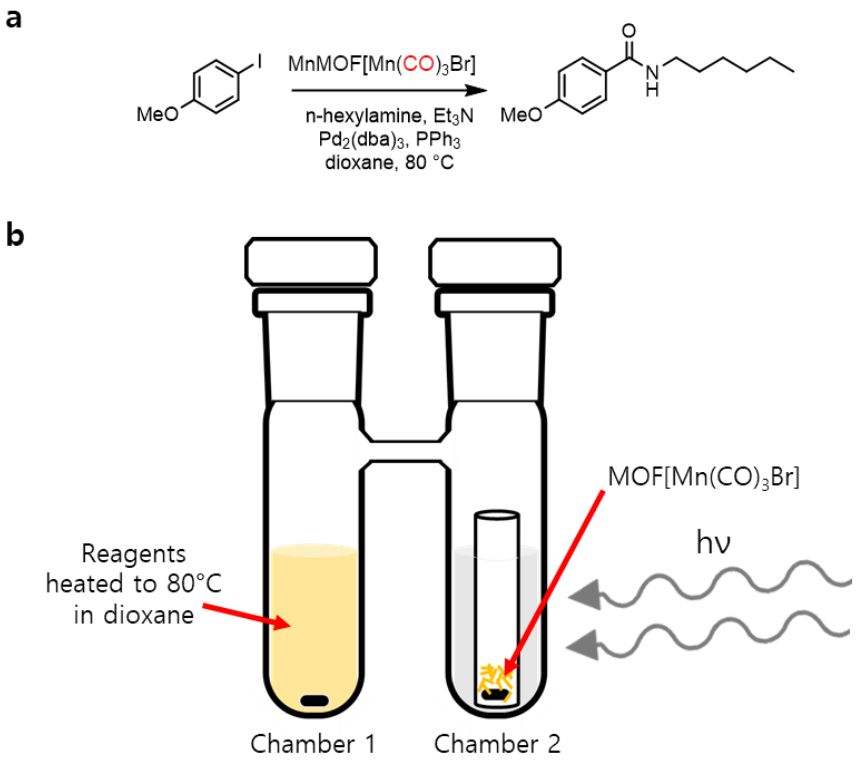

Figure 3.11. a) Aminocarbonylation reaction using MnMOF[$Mn(CO)_3Br$] as a source of carbon monoxide in **b)** a two-chamber reaction vessel where the reactants are dissolved and heated in one arm and the solid-state MOF is irradiated in the other with a bridge allowing the movement of released CO.

3.3.2 MnMOF[$Mn(CO)_3(EtOH)$]Br (CORMat-1) as CO source for chemical synthesis

MnMOF post-synthetically metalated with [$Mn(CO)_3Br$] was synthesised as described in Chapter 2.3.1 to give CORMat-1 (carbon monoxide releasing material). With quantitative loading, CORMat-1 contained 4.9 wt.% CO, equivalent to 1.8 mmol g^{-1}, assuming that all loaded CO was released. To determine the effectiveness of using $Mn(CO)_3Br$ loaded MOFs as a source of CO for aminocarbonylation reactions small scale test reactions were carried out with 20 mg of 4-iodoanisole and varying quantities of MOF . CORMat-1 was washed with ethanol (x5) then dried under a flow of nitrogen in the dark, before being weighed and placed into the reaction set-up. The number of equivalents of CO delivered to the reaction was calculated based on quantitative loading of the MOF and hence 4.9 wt. % of the total MOF mass being CO. Complete release of CO from the MOF was also assumed, although in some cases as will be described later, this was not the case. It should also be noted when considering the quantity of CO delivered from the MOF to the reaction, that this is occurring in equilibrium with the

gaseous headspace of the reaction vessel and the solubility of CO in the reaction solvent (dioxane). It is then logical to assume that excess CO is necessary due to these limitations. While the reaction product was able to be isolated after purification by column chromatography, the conversion percentage is calculated from analysis of the NMR spectra of the crude product, where the integration of the product peak (2H - aromatic, d, 6.93) was compared to the corresponding peak of the starting material (2H-aromatic, d, 6.69). The downfield shift in this peak is due to the replacement of the adjacent iodine with the amide group, resulting in a de-shielding effect.

The aminocarbonylation reaction with 1 equivalent of CO from CORMat-1 resulted in a conversion of 36%, with the conversion increasing to 68% with 1.21 equivalents and 82% with 1.57 equivalents of CO (Table 3.1, Figure 3.12a). IR spectra taken after these reactions showed no CO peaks in the carbonyl region between 1700-2100 cm^{-1}, indicating that complete loss of CO was achieved (Figure 3.12b). Increasing the amount of CORMat-1 to provide 2.60 equivalents of CO resulted in a lower conversion than for the previous experiment (1.57 equivalent). Although the IR spectrum, again, showed no CO peaks post-reaction, it was observed that with the large quantity of MOF required for this experiment (118 mg) mixing in the vial was impeded. As this experiment was not repeated due to time constraints, this result could be an anomaly, or it could be a result of ineffectual irradiation due to the large quantity of MOF, resulting in a slower release of CO, causing the lower conversion. To test this theory, the reaction should be repeated and if the decrease in conversion efficiency is again observed, a larger reaction vessel could be employed, hence allowing for a larger stir bar and more efficient mixing which will allow all crystals equal exposure to light.

Table 3.1. Conversion efficiencies achieved in aminocarbonylation reactions using varying quantities of MnMOF[$Mn(CO)_3$EtOH]Br (CORMat-1) as a photoactivated source of CO.

Mass of CORMat-1 (mg)	Equivalents of CO	Conversion (%)
47	1.04	36
55	1.21	68
71	1.57	82
118	2.60	72

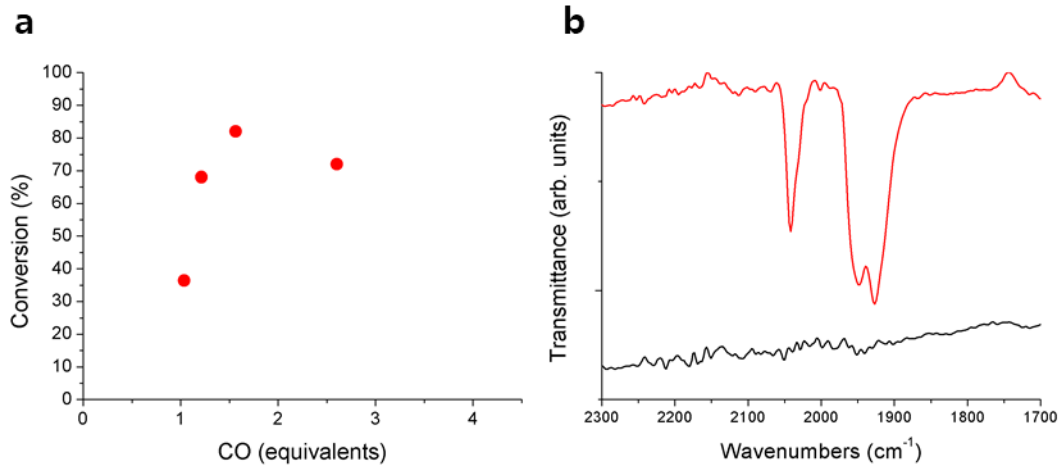

Figure 3.12. a) Conversion efficiencies achieved in aminocarbonylation reaction plotted against the equivalents of CO generated from CORMat-1. **b)** Representative IR spectra of the carbonyl region of MnMOF[$Mn(CO)_3EtOH$]Br before (red) and after (black) use in aminocarbonylation reaction.

As discussed in Chapter 2.3.6, the manganese (I) carbonyl complexes cannot be regenerated through addition of CO gas. In an attempt to re-use CORMat-1 as a CO source, the MOF was taken after the aminocarbonylation reaction and re-suspended in ethanol. Fresh bromopentacarbonylmanganese(I) was added and the MOF was treated to the same metalation conditions as previously. IR analysis of this sample (Figure 3.13) showed the presence of the same carbonyl peaks as the initial compound, with lower intensity, relative to the MOF peaks. This indicates that some of the post-CO release manganese complex is able to be displaced by [$Mn(CO)_3Br$], but the conditions tested did not allow for full exchange.

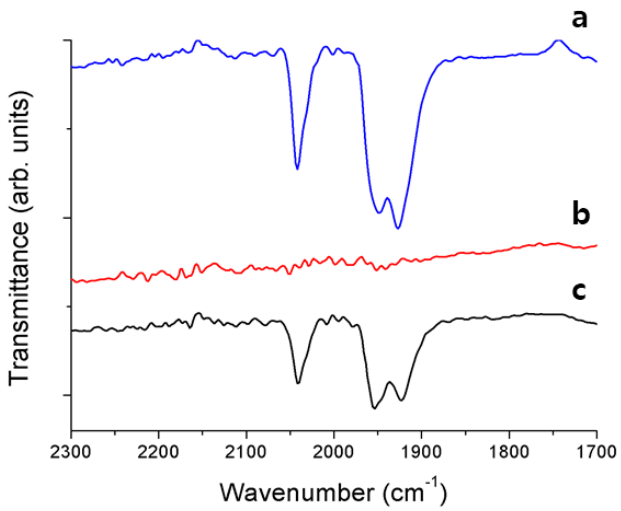

Figure 3.13. CORMat-1 **a)** before photolysis, **b)** after photolysis and **c)** after re-metalation. Peak heights are normalised to MnMOF framework C=C peak at 1603 cm^{-1}.

3.3.3 CO insertion reactions with UiO-67-bpy[Mn(CO)$_3$Br] and DUT-5-bpy[Mn(CO)$_3$Br]

Due to the inherently low loading of CO in CORMat-1 (4.9 wt.%, 1.88 mmol g^{-1}), other MOFs with higher CO loading capacities were tested. As discussed earlier (Section 3.1.4), MOFs synthesised from the ligand bpydc (2,2′-bipyridine-5,5′-dicarboxylate) have been metalated with *fac*-Mn(CO)$_3$X (X=Br or Cl) complexes and shown to release CO under irradiation. As such, the MOFs UiO-67-bpy and DUT-5-bpy were chosen, as both could be synthesised from bpydc, offering a vacant coordination site for Mn(I) in every ligand. Due to this, quantitative loading is unlikely due to the high density of sites leading to steric crowding.[59] Both MOFs were synthesised according to literature procedures as microcrystalline powders and metalated using the same method as CORMat-1. SEM analysis showed that DUT-5-bpy was synthesised as irregularly shaped crystallites 1.14 (±1 SD) μm in size, while the UiO-67-bpy crystallites were more uniformly shaped and sized, 326 (±69 SD) nm in diameter (Appendix 3.9).

Metalation success was measured by SEM/EDX using the ratios of manganese to the framework metal. Unlike CORMat-1 these MOFs did not allow quantitative metalation; however, the CO content of both MOFs were still higher. DUT-5-bpy metalated 43% (±2% SE) of available sites and so had a CO loading of 7.14 wt.% (2.75 mmol g^{-1}), while UiO-67-bpy achieved 80% (±3% SE) metalation, resulting in a 11.7 wt.% (4.5 mmol g^{-1}) loading of CO. The phase purity of the metalated MOFs was confirmed by PXRD (Appendix 3.9). Irradiation with visible light showed the same complete loss of CO peaks as CORMat-1 (Appendix 3.9), so these MOFs were considered suitable to test as CO sources in the aminocarbonylation reaction. Unlike CORMat-1, no Mn(II) carbonyl peaks were observed after the photolyzed MOFs were placed under 1 bar of CO gas.

DUT-5-bpy[Mn(CO)$_3$OHEt]Br (CORMat-2) was an effective source of CO, with conversions of 91% with 1.64 equiv. CO and 96% for 3.47 equiv. CO (Table 3.2 and Figure 3.14a). Complete decarbonylation was not achieved, with the IR spectrum still showing carbonyl peaks after overnight irradiation under the reaction conditions (Figure 3.14c). This was likely due to the crystallite size being much smaller than CORMat-1 (1.14 (±1) μm compared to >100 μm), causing the crystals to stick together and to the sides of the vial, preventing efficient mixing and hence resulting in a proportion of the

crystals not exposed to the light. Thus, the effective equivalents of CO released and available for reaction would be lower than those calculated from the mass of MOF added to the vessel. Despite this, high yields were achieved with only a minor excess of CO in the MOF and significantly less mass of MOF compared to CORMat-1 is needed to achieve this.

Table 3.2. Conversion efficiencies achieved in aminocarbonylation reactions using varying quantities of DUT-5[$Mn(CO)_3Br$] (CORMat-2) as a photoactivated source of CO.

Mass of CORMat-2 (mg)	CO equivalents	Conversion (%)
14	0.45	31
25	0.80	76
51	1.64	91
108	3.47	96

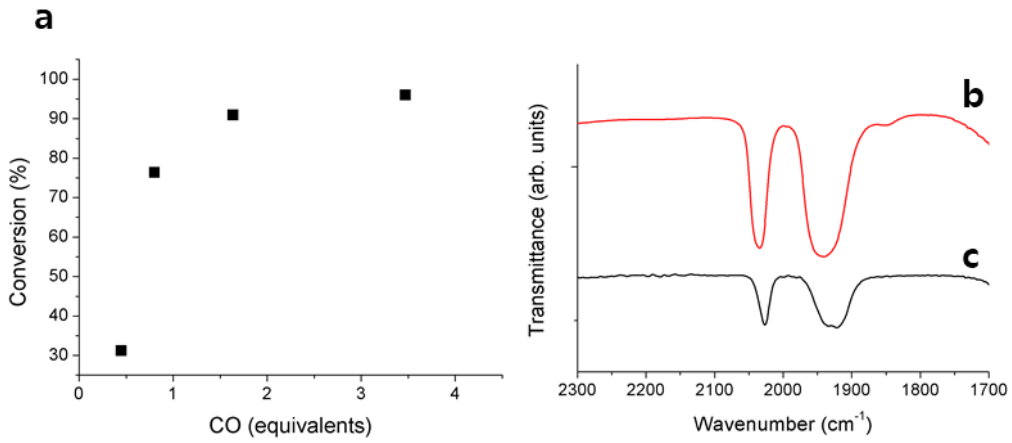

Figure 3.14. a) Conversion efficiencies achieved from using CORMat-2 as an *ex-situ* source of CO for aminocarbonylation reactions plotted against the equivalents of CO in the reaction vessel. IR spectra of DUT-5[$Mn(CO)_3EtOH$]Br **b)** before use in the aminocarbonylation reaction and **c)** after photolysis and use in the reaction. Peak heights were normalised to C=C framework peak at 1620 cm^{-1}.

UiO-67-bpy[$Mn(CO)_3OHEt$]Br (CORMat-3) had the highest CO loading by weight of the MOFs tested at 11.7%. It too was an effective source of CO, with up to 90% conversion efficiencies (Table 3.3). Like CORMat-2, full decarbonylation was not achieved with carbonyl peaks remaining in the IR spectrum after reaction (Figure 3.15b). This was not surprising, as the UiO-67-bpy crystals were 326 (±69) nm in diameter, and so similarly difficult to expose all crystals to the light using the reaction format developed

here. It may be possible to achieve more complete CO release by further optimisation of the reaction design or by tuning the crystal morphology.

Table 3.3. Conversion efficiencies achieved in aminocarbonylation reactions using varying quantities of UiO-67-bpy[$Mn(CO)_3Br$] (CORMat-3) as a photoactivated source of CO.

Mass of CORMat-3 (mg)	CO equivalents	Conversion (%)
12	0.63	19
31	1.63	61
51	2.69	74
85	4.48	90

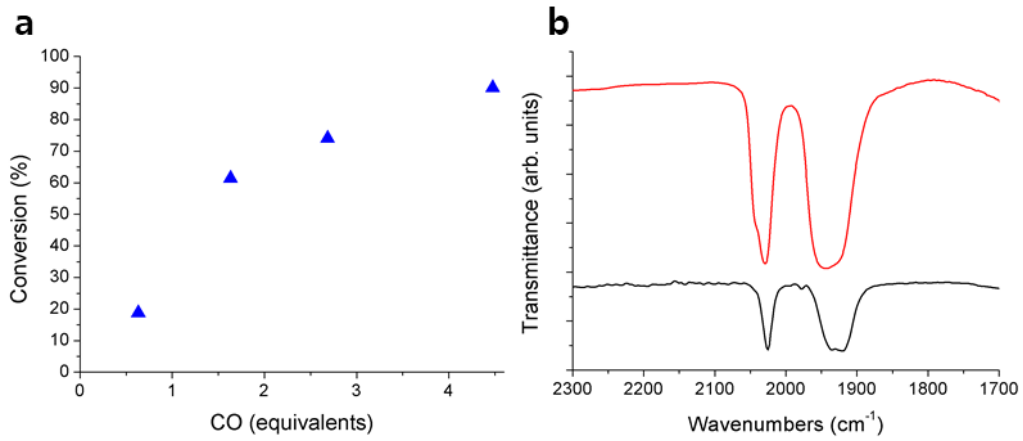

Figure 3.15. a) Conversion efficiencies achieved from using CORMat-3 as an *ex-situ* source of CO for aminocarbonylation reactions plotted against the equivalents of CO in the reaction vessel. **b)** IR spectra of CORMat-3 (UiO-67[$Mn(CO)_3EtOH$]Br) before use in the aminocarbonylation reaction (red) and after (black) photolysis under reaction conditions. Peak heights were normalised to the ν(C=C) MOF peak at 1595 cm^{-1}.

In the same way as described for CORMat-1, re-metalation of CORMat-3 was attempted by placing a photolyzed sample in ethanol with [$Mn(CO)_5Br$] and heating to 50 °C overnight. The sample was then washed (x5) and analysed by IR spectroscopy, where carbonyl peaks very similar to the starting material were observed (Figure 3.16). The quantity of replaced and regenerated sites was not determined, but this is a promising indication that this material may be re-usable.

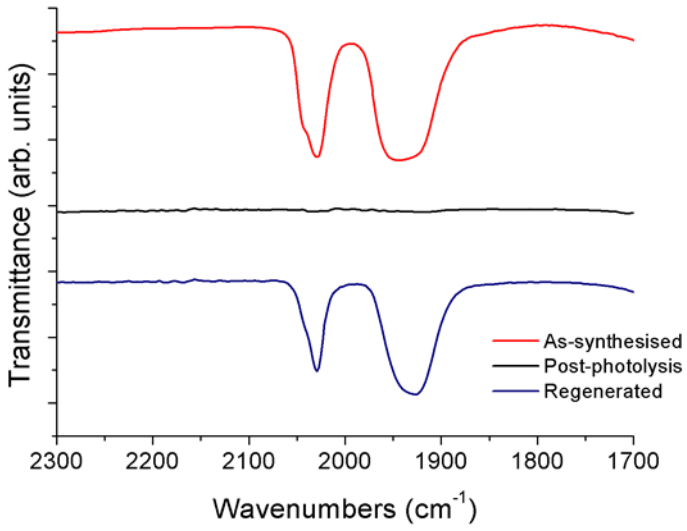

Figure 3.16. IR spectra of CORMat-3 before (red) and after (black) photolysis, then after re-metalation with $[Mn(CO)_5Br]$ (blue).

Comparing the behaviour of the three MOFs tested shows that the MOF type, including the coordination environment and crystal size can have a significant impact on their use as *ex-situ* CO sources (Figure 3.17). CORMat-2 (DUT-5) demonstrated the highest conversion efficiencies by both equivalents of CO and MOF mass, despite having only 43% of sites metalated and not undergoing complete decarbonylation. CORMat-1 (MnMOF) was the second-best performing MOF, with high conversion for low excess of CO and complete decarbonylation, but conversion dropped for higher CO equivalents due to low loadings resulting in large quantities of MOF needed which are difficult to fully irradiate. CORMat-3 (UiO-67-bpy) gave the lowest conversions and did not completely decarbonylate. High conversions were achieved by using over 4 equivalents of CO, with no drop in efficiency like that seen in CORMat-1 due to small crystal sizes and higher CO loadings.

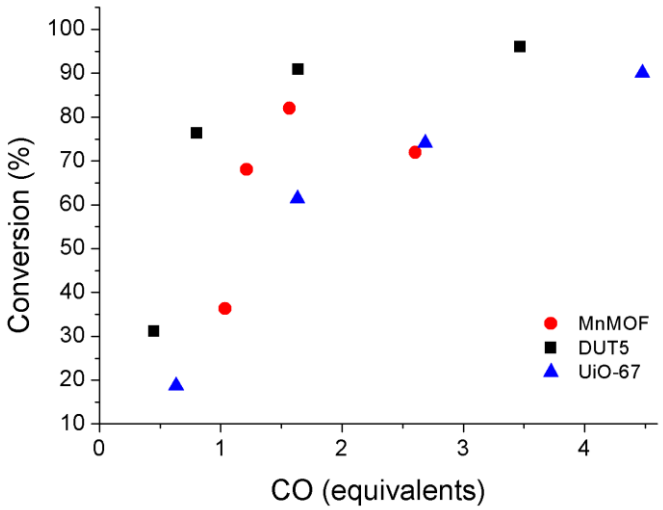

Figure 3.17. Comparison of the conversion efficiencies of the manganese carbonyl metalated MOFs as *ex-situ* sources of CO for an aminocarbonylation reaction. Red circles- CORMat-1, black squares – CORMat-2, blue triangles – CORMat-3.

The demonstrated importance of crystal morphology on CO delivery performance reinforces the motivations for improving ease of use, processability and diffusion through structuralising MOFs into higher dimensional superstructures. These results show that to tune the CO release behaviour of MOFs, all structural levels, from the chemical building blocks to the crystal morphology, must be considered.

3.4 Manganese oxide sol-gels

3.4.1 Manganese oxide sol-gel synthesis and washing

Sacrificial manganese oxide sol-gel templates were chosen as a route to synthesise 3D MnMOF superstructures and monoliths. Manganese oxide (MnOx) sol-gels were synthesised using a modified procedure from Ching *et al.*[79] Potassium permanganate was first dissolved in water followed by the slow addition of maleic acid with rapid stirring in a 3:1 molar ratio. Maleic acid was used instead of fumaric acid due to its availability and no noticeable difference in reactivity was observed. The solution rapidly turned from purple to brown and was stirred for 10 min with dinitrogen bubbling under a mild vacuum, created by an aspirator or low vacuum pump. The vacuum and nitrogen gas bubbling were found to be essential for creating stable gel monoliths by helping to remove carbon dioxide bubbles created from the redox reaction.[80] Removal of either the dinitrogen bubbling or vacuum, or if the solution was stirred for a longer period of

time, resulted in flocculation of the manganese oxide into small particles. While this material may still be useful for MOF formation, this research was directed at gel monoliths, and hence the modified procedure was used. The gel was poured into moulds (generally 2 mL glass or plastic vials) and set after 30-60 min (Figure 3.18a). The gel was then left to cure overnight, during which time it would contract to approximately half its original size and sink to the bottom of the vial. The gel was then washed with water 5 times, with one wash left to soak overnight. Subsequent solvent exchanges followed the same procedure. Exchange directly to less polar solvents such as hexane, THF or even diethyl ether was not effective, so stepwise solvent exchanges decreasing in polarity were used (water to acetone to diethyl ether to hexane). With each solvent exchange the gel monolith shrunk further, with the hexane solvated monoliths approximately 1/8 of their original size and, although delicate, were stable enough to be handled and transferred between containers (Figure 3.18b). After the monolith was dried, depending on the method, it could further shrink to approximately 5% of its original size (Figure 3.18c).

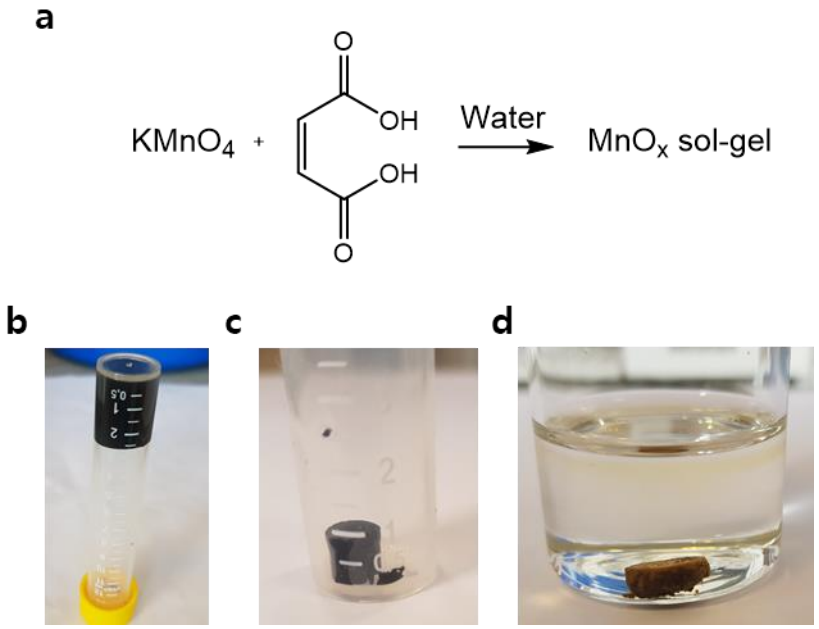

Figure 3.18. a) MnOx sol-gel reaction scheme and **b)** MnOx sol-gel after setting in a centrifuge tube mould. **c)** MnOx gel monolith after being washed and solvent exchanged with hexane. The solvent has been removed, but the monolith has not been dried. **d)** Monolith after being dried from hexane in the air and with surface conversion to MnMOF.

3.4.2 Templated MnOx sol-gels

The formation of regular and controlled macro-porosity was attempted by the use of templates; however, the introduction of templates such as 20 µm polyethylene granules disrupted monolith formation and hence all attempts at forming macro-porous manganese oxide ceramic monoliths were unsuccessful. The millimetre sized MnOx particles formed in the presence of PE granules were washed with water and dried overnight at 150 °C before being analysed by SEM. The heating process caused some of the polymer to melt and form clumps of 27.6 (± 9.1) µm in size (Figure 3.19a and b), coated by a polymer film and adhered to one another (Figure 3.19c). Inside these clumps was low density manganese oxide, with micron sized channels (Figure 3.19d). The use of a polymer template may be an effective route to micro-porous structuralised MnMOF, but due to time constraints this avenue was not explored further.

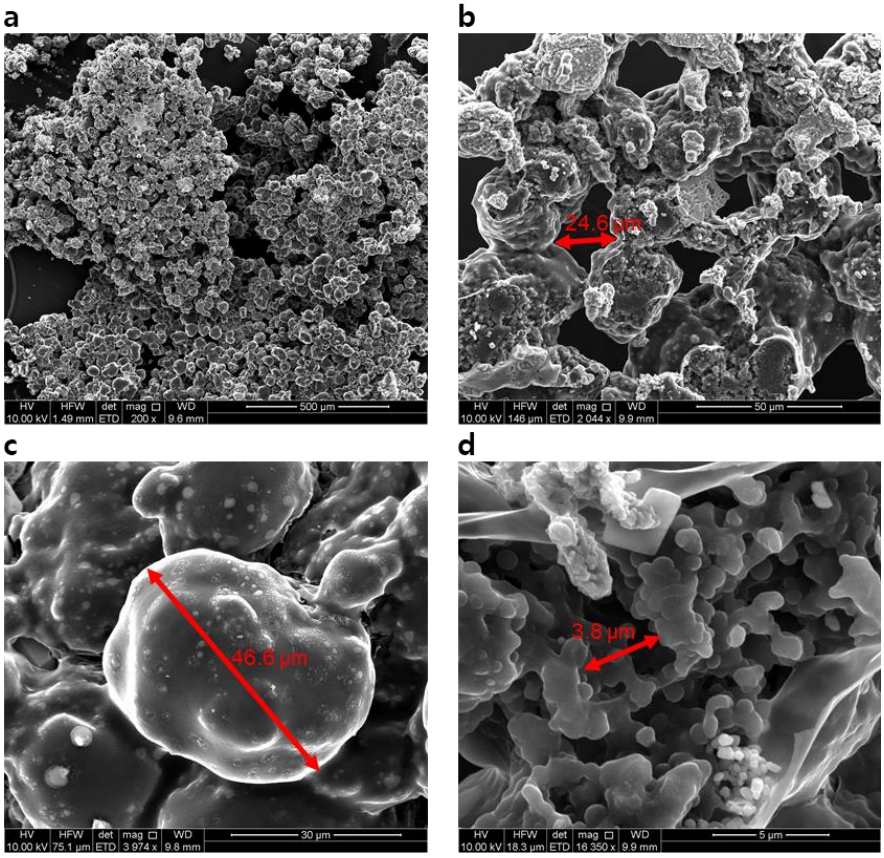

Figure 3.19. Polyethylene templated manganese oxide ceramic from sol-gel. **a)** Manganese oxide clusters coated with melted PE stuck together in extensive networks with large gaps. **b)** Higher magnification image where regions of exposed MnOx are visible. **c)** Polyethylene coated particle with melted film and unmelted particles visible and **d**) manganese oxide inside polymer coated cluster, showing microporosity.

Due to the extensive shrinkage the sol-gel undergoes during the curing and washing processes, attempts to manipulate the shape and macroscopic surface structure of the sol-gels were unsuccessful. In an effort to control the macroscopic shape, manganese oxide nanoparticles were formed as coatings on aluminium oxide foil using a modified method from Kulinich *et al* (Figure 3.20a).[81] A piece of aluminium foil was placed in an aqueous solution of potassium permanganate and sodium tetraborate. The solution was either heated to 100 °C overnight, or left at room temperature for 3 days, after which the foil acquired a gold-coloured coating (Figure 3.20b) and was analysed by SEM/EDX. Heating the solution to 100 °C resulted in an even coating of nanoparticles approximately 185 (±99) nm in diameter (Figure 3.20c and d).

Leaving the solution for longer at room temperature produced a thicker coating of manganese oxide, with larger, but less uniform, particles sizes of 896 (±783) nm (Figure 3.20e and f). In this sample, some very large manganese oxide particles formed, with diameter of up to 10 μm (Figure 20e). Although the thickness of the coating was not determined, EDX analysis showed that the ratio of manganese to aluminium was on average 22 times greater in the 3 day sample than the overnight sample, and excluding the large particles was 12 times greater (Table 3.10 in Appendix 3.9.1). Despite successfully producing manganese oxide coatings onto aluminium oxide foil, attempts to use this as a basis for structuralised MOFs were unsuccessful. A possible reason for this could be insufficient quantities of manganese oxide, in which case investigating thicker coatings may be of interest. Another possibility may be poor adhesion of the manganese oxide to the foil surface, causing preferential detachment of the nanoparticles when in MOF forming conditions to form non-structuralised MOF.

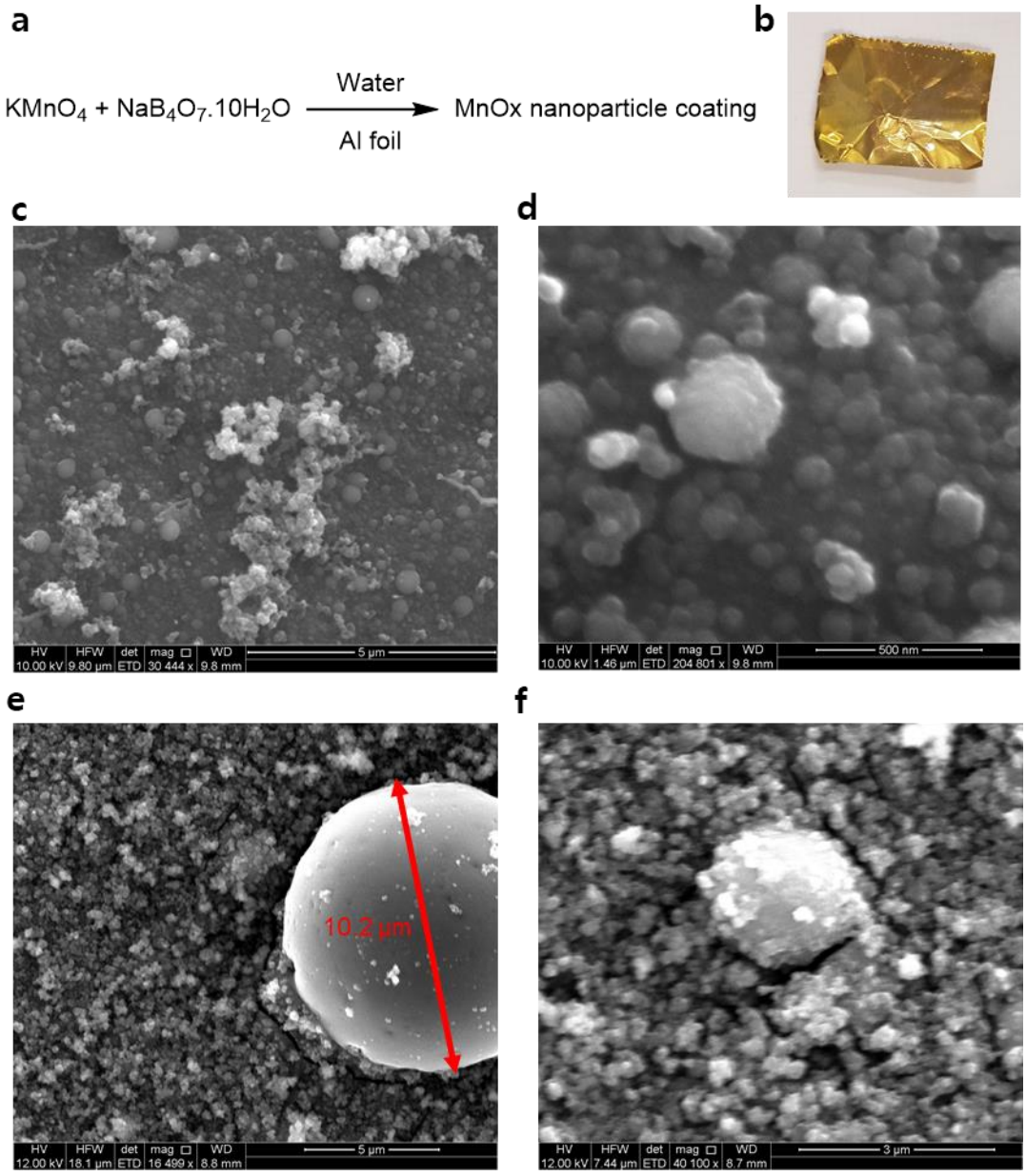

Figure 3.20. Manganese oxide nanoparticles coating aluminium foil. **a)** reaction scheme for the nanoparticle formation, **b)** optical photograph of the 3 day nanoparticle coating. **c)** and **d)** SEM images of the nanoparticle coating after reacting overnight at 100 °C and **e)** and **f)** after reacting for 3 days at room temperature.

While some macro-structural control was able to be achieved using polymer and aluminium foil templates, the manganese oxide samples produced were not suitable for conversion to MnMOF. Further optimisation is required if either method is to be used to synthesise structuralised MnMOF.

3.4.3 MnOx sol-gel drying methods

Several methods were investigated for drying the MnOx sol-gels described in Section 3.4.1 into xerogels. According to reports in the literature drying the ceramics from lower surface tension solvents result in higher porosity.[75] To examine this, the sol-gels were dried from both water (surface tension = 72.75 mN m^{-1})[82] and hexane (surface tension = 19 mN m^{-1}).[83] The hexane solvated gels were dried either under vacuum or in a 100 °C oven, while the water solvated gels were dried in the oven. Wet gels solvated with DMF and water solvated gels dried under ambient conditions were also used (Table 3.4). The ceramics were then analysed by SEM (Figure 3.21) and PXRD (Figure 3.22) before being used to make structuralised MnMOF.

Table 3.4. Sol-gel derived MnOx sample names and preparation methods

Sample name	Solvent	Drying method
MnOx-1	Water	Heating at 100°C
MnOx-2	Hexane	Vacuum
MnOx-3	Hexane	Heating at 100°C
MnOx-4	DMF	None (wet gel)
MnOx-5	Water	None (wet gel)
MnOx-6	Hexane	None (wet gel)

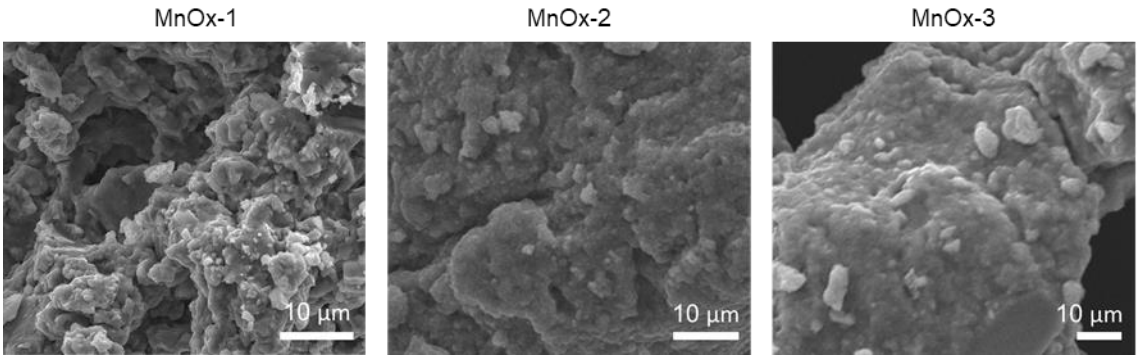

Figure 3.21. Sol-gel derived MnOx ceramics MnOx-1 (solvated in water and dried at 100°C), MnOx-2 (solvated in hexane then dried under vacuum) and, MnOx-3 solvated in hexane and dried at 100°C.

Samples were dried as monoliths then crushed before analysis. SEM revealed dense and relatively featureless materials. The samples dried from hexane (MnOx-2 and -3) displayed greater surface topological features than that dried from water (MnOx-1), as expected due to the lower surface tension of hexane leading to faster drying times

and hence less pore collapse. There were few observable differences between the samples dried in the oven and under vacuum. The surface features of MnOx-2 and -3 were approximately 5-10 μm in size and did not appear to be part of an interconnecting pore network. This was disappointing, as this would preclude MOF formation in the interior of the ceramic, limiting the structuralisation to the surface features. Literature methods for synthesising more porous sol-gel derived ceramics rely on solvent exchange and drying from supercritical carbon dioxide; however, supercritical solvents were not available for this study.[75] To access a lower density MnOx starting material for structuralisation, DMF solvated gels (MnOx-4) were used directly for MOF synthesis without drying in addition to the dried MnOx ceramics (MnOx-1,2,3 and 5).

EDX analysis of the ceramics revealed an approximate 2:1 ratio of oxygen to manganese, which correlates to the literature analysis that Mn(IV) is the predominant oxidation state.[79] The literature procedure for producing a MnOx ceramic dried from water states that the material is microporous, with channels 4.6 Å in diameter in which potassium ions reside. The ceramics dried from hexane (MnOx-2 and -3) had a higher percentage of potassium ions present than that dried from water (MnOx-1) (Table 3.5), likely due to deionised water having a low pH as a result of dissolved carbonic acid, and hence H^+ ions providing some of the charge balance, but no gas adsorption studies were undertaken to provide pore size distribution data. All MnOx ceramic samples were amorphous, with featureless PXRD patterns (Figure 3.22).

Table 3.5. EDX analysis of MnOx sol-gel ceramics

Sample name	Solvent	Drying conditions	Mn:O ratio (SE)	Molar percentage of potassium K% (SE)
MnOx-1	Water	Oven	1 : 2.20 (0.44)	3.62 (0.28)
MnOx-2	Hexane	Vacuum	1 : 1.88 (0.36)	5.86 (0.38)
MnOx-3	Hexane	Oven	1 : 1.82 (0.30)	5.71 (0.44)

Sol-gel derived MnOx ceramics were made from the drying of solvated sol-gels through heating or vacuum. Despite the different drying methods employed, few observable differences were exhibited in the morphology, crystallinity or elemental make-up. The ceramics were amorphous and the predominant manganese oxidation state was found to be Mn(IV), with a small percentage of potassium ions.

3.5 Synthesis of structuralised MnMOF from sol-gel derived MnOx

3.5.1 Reagents needed for structuralised MnMOF

Structuralised MnMOF was synthesised from the MnOx sol-gels and ceramics described in Section 3.4 by combining the ligand (L) with the manganese oxide, DMF, water and ascorbic acid and heating to 100 °C in the same way as synthesising conventional MnMOF. The ascorbic acid acted as a mild reducing agent, as a variety of oxidation states of manganese (mostly Mn(IV) were present in the sol-gels and as Mn(II) is required for MnMOF formation. 1, 2, 4 and 10 molar equivalents (compared to moles of ligand) of ascorbic acid were used, with 2 and 4 molar equivalents both forming crystalline material while maintaining the macro-structural properties of the MnOx template (Table 3.6 and Figure 3.22). 10 equivalents; however, produced larger crystals that did not maintain the shape of the original MnOx ceramic, while 1 equivalent did not produce any significant crystalline material. From this point, 2 molar equivalents of ascorbic acid were used in all MnMOF structuralisation experiments as it was postulated that less reducing agent would slow the reaction and allow for coordination replication of the manganese oxide, as it was necessary for the rate of MOF formation to be faster than the rate of dissolution of the MnOx template.

Table 3.6. Reducing agent quantities used in strucMnMOF forming reactions

Molar equivalents of ascorbic acid (to ligand L)	**Crystallinity**	**Structuralised**
1	No	No
2	Yes	Yes
4	Yes	Yes
10	Yes	No

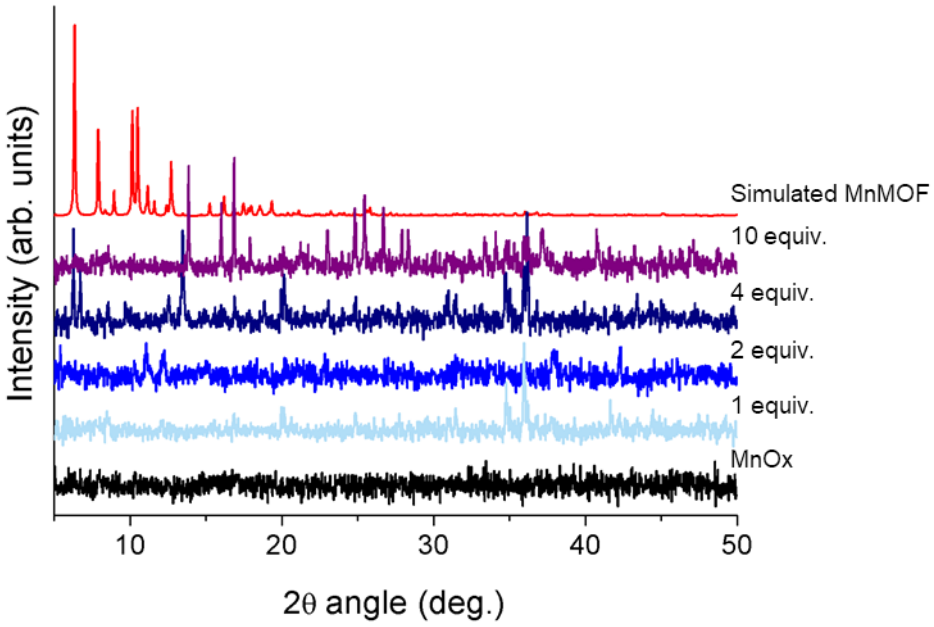

Figure 3.22. PXRD pattens of MOF converted MnOx samples after reacting with various equivalents of ascorbic acid reducing agent. (Black – unreacted MnOx, purple – 1 equivalent, blue – 2 equivalents, green – 4 equivalents, yellow – 10 equivalents)

None of the converted MnOx PXRD patterns match what would be expected for MnMOF, even allowing for orientation effects, nor do they match the close packed, 2D coordination polymer discussed in Chapter 2. Due to the very small quantity of crystalline material produced and hence the low intensity of any diffraction peaks, identification of these phases was not possible. Nevertheless, the formation of off-white material on the surface of the MnOx particles and the presence of PXRD peaks indicated that a crystalline coordination polymer was being formed under these reaction conditions, and hence further investigations were carried out.

Scanning electron microscopy (SEM) was used to follow the structuralisation of MnMOF on MnOx wet gels and ceramics, with the aim to determine optimal condition to produce a thin coating of MnMOF on the MnOx support, without loss of the 3D macro-structural properties of the support. The structuralised MOFs will be named according to Table 3.7.

Table 3.7. Structuralised MnMOF sample names and preparation method for MnOx templates

Sample name	MnOx support	MnOx solvent	MnOx drying method
StrucMnMOF-1	MnOx-1	Water	Heating at 100°C
StrucMnMOF-2	MnOx-2	Hexane	Vacuum
StrucMnMOF-3	MnOx-3	Hexane	Heating at 100°C
StrucMnMOF-4	MnOx-4	DMF	None (wet gel)
StrucMnMOF-5	MnOx-5	Water	None (wet-gel)
StrucMnMOF-6	MnOx-6	Hexane	None (wet-gel)
StrucMnMOF-7	MnOx-7	Water	Ambient conditions

3.5.2 Structuralised MnMOF: Crystal growth

To study the crystal growth of MnMOF on MnOx sacrificial templates, samples were analysed by SEM after reacting under MOF forming conditions for 2, 4 and 20 hrs (Figure 3.23). The MnOx templates were synthesised as described in Section 3.4, dried and crushed into sub-millimetre pieces before placed in the MOF forming reaction. It was found that despite the lack of variation in the morphologies of MnOx1-3 (Figure 3.21), the crystal growth from these templates varied. After 2 hrs only small spherical crystals grown from nucleation sites (361 ± 93 nm) were visible on MnOx-1, where the underlying MnOx-1 surface topology was visible as 2-4 µm spherical aggregates. For MnOx-2 and MnOx-3, crystal growth was further developed after 2 hrs, displaying 3.20 (± 0.97) µm and 4.62 (±1.59) µm plate crystals, respectively. A 4 hr time point was not taken for strucMnMOF-1; however, after 3 hrs it could be observed that indistinctly shaped MOF crystallites now coated the MnOx-1 surface. In contrast, after 4 hrs, well defined plate crystals had now grown to 16.5 (± 7.83) µm and 24.1 (± 11.3) µm for StructMnMOF-2 and StrucMnMOF-3. Finally, after 20 hrs well defined plate crystals, 2.15 (± 0.82) µm were visible on MnOx-1, while MnOx-2 displayed very large crystals 63.7 (± 31.8) µm in size and MnOx-3 12.0 (± 7.23) µm sized crystals.

Crystal growth on MnOx-1 appears to follow a linear progression of nucleation and growth, and after 20hrs resulted in crystals two orders of magnitude smaller than those synthesised under conventional conditions. The appearance of the indistinctly shaped intermediate stages of growth after 2 and 3 hrs may provide interesting insights

into crystal growth of MnMOF in general, and further work would aid in uncovering these growth mechanisms. The crystal growth behaviours of MnOx-2 and MnOx-3 are less straightforward, especially at the 20 hr timepoint. For the 2 and 4 hr timepoints the crystals formed on these two supports are similar (within error). After 20 hrs structMnMOF-2 is formed as large plate crystals adjacent to regions of exposed MnOx-2, whereas the crystals of structMnMOF-3 are smaller than those at the 4-hr time point and uniformly coating the oxide surface. The reasons behind these differences may be determined through observation of the MOF-oxide composites at larger scales.

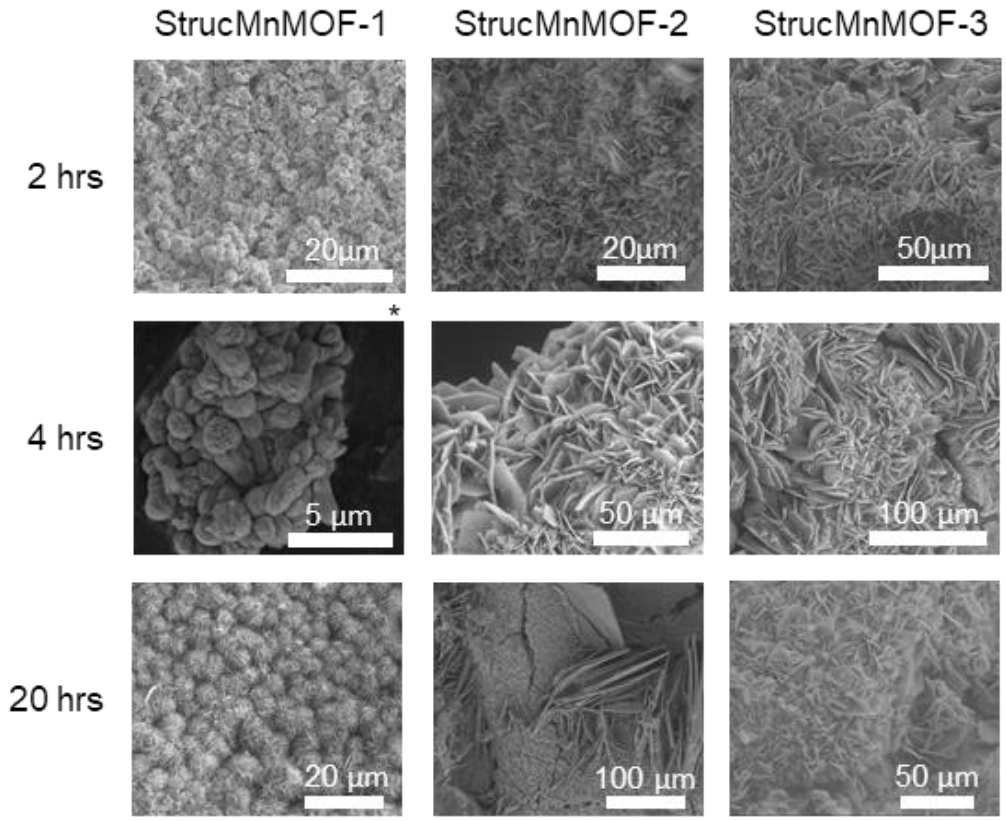

Figure 3.23. Representative images of MnMOF crystal growth on sacrificial sol-gel derived MnOx supports after 2, 4 and 20 hrs of reaction. *A 4hr time point was not taken for this sample, instead this image is from a 3-hr time point.

The crystal growth of strucMnMOF on sol-gel derived MnOx sacrificial supports was shown to follow a pattern of nucleation on the oxide surface followed by crystal growth from indistinct aggregates into plate shaped crystals. Crystal growth was slower on MnOx-1, which was dried from water, than on MnOx-2 and MnOx-3, which were dried from hexane. Coverage of the MnOx support in well-defined plate crystals was achieved after 2 hrs for strucMnMOF-2 and strucMnMOF-3 and between 4-20 hrs for strucMnMOF-1.

3.5.3 Structuralised MnMOF: Macroscale morphology

The morphology of the structuralised MnMOF samples was also analysed on the macroscopic scale (i.e., whole particles) (Figure 3.24). The lack of large, interconnected solvent accessible channels in the MnOx supports resulted in the majority of crystal growth occurring on the particle surface. For MnOx-1, after 2 hrs only the topology of the oxide substrate is visible and after 3 hrs a thin layer (approx. 1 μm) of MOF can be seen. The thickness of the MOF coating after 2 hrs for the MnOx-2 and MnOx-3 samples could not be measured due to no observable gaps where the underlying substrate could be seen; however, most of the exposed surfaces are covered by relatively uniform strucMnMOF. After 4 hrs (MnOx-2 and MnOx-3) or 20 hrs (MnOx-1) cracking in the MOF surfaces appeared. These cracks are due to the growing MOF crystals requiring more space than is available on the substrate surface. These cracks developed further, resulting in sheets of strucMnMOF peeling off from the oxide particles. This resulted in exposure of unreacted MnOx surfaces to the MOF reactants, which were observed after the overnight reactions (discussed further in Section 3.5.5).

The freshly exposed surfaces then underwent the same cycle of crystal nucleation and growth that occurred at earlier time points, resulting in the strucMnMOF-2 and -3 observations noted in Section 3.5.2. StrucMnMOF-2 showed a mixture of large crystals which had not yet come away from the surface and freshly exposed MnOx-2, whereas strucMnMOF-3 showed plate crystallites sized between the earlier 2-4 hr time points, indicating that sheets of strucMnMOF-3 had detached from the particle surface at 16-18 hr of reaction time. The formation of strucMnMOF was also visible to the eye, with an off-white coating forming on the black MnOx particles, and white sheets of MOF visible after they detached.

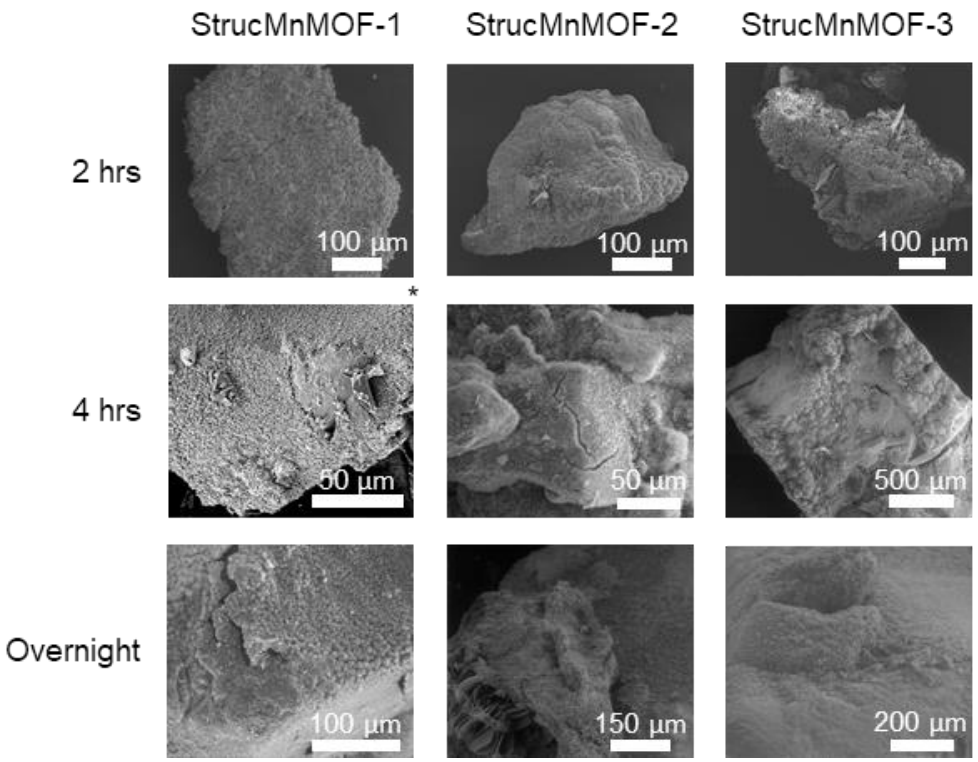

Figure 3.24. SEM images of the macrostructural properties of strucMnMOF. *A 4hr time point was not taken for this sample, instead this image is from a 3-hr time point.

MnMOF crystal nucleation and growth occurs across the surface of MnOx substrates, resulting in coatings of small, well defined plate crystals. As the crystals increase in size, they come away from the oxide surface as sheets, revealing unreacted MnOx which undergoes a new cycle of MnMOF crystal nucleation and growth. The MOF sheets remained intact and could be several hundred micrometres in length, although very fragile (Figure 3.25). This process was especially evident for the solvated MnOx substrates (MnOx-4, -5, and -6), for which it was apparent that the formation and detachment of MOF sheets had occurred several times over 20 hrs, due to the number of sheets visible in the sample vials. As the MOF crystallites occur on both sides of the sheets, it can be assumed that either the growth of the crystals on the inside face occurs between a crack forming and the sheet detaching, or that there are enough manganese ions in solution for continued crystal growth after the detachment of the sheet.

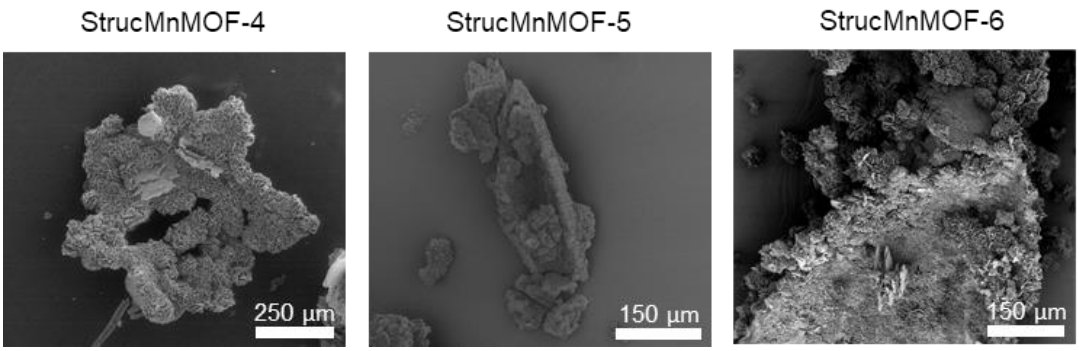

Figure 3.25. Sheets of strucMnMOF samples detached from the surfaces of the MnOx particles derived from solvated sol-gels (MnOx-4, DMF solvated; MnOx-5, water solvated; MnOx-6, hexane solvated) reacted for 20 hrs.

These studies show that strucMnMOF can be grown on the surface of sol-gel derived MnOx substrates, retaining the macrostructural properties of the template until a point at which the crystals grow too large and detach from the particle surface. Short reaction times or slowing of reaction rates are therefore necessary to synthesise controlled, uniform coatings of MOF on substrates of this type. The growth of MOF micro-sheets was not the purpose of this study; however, their formation may present opportunities for further explorations of high external surface area MnMOF.

3.5.4 Structuralised MnMOF: Crystal growth abnormalities

The results discussed in Section 3.5.2-3 described the bulk samples and the most common crystal morphologies observed in each sample, however, abnormalities were also seen and will be discussed here. The most common anomaly observed was the formation of much larger crystals than the bulk, surrounding a region of unreacted MnOx (Figure 3.26). This was only seen in a small percentage of particles (not quantified), and was encountered in all MnOx-1, MnOx-2, and MnOx-3 samples at the 2-hr reaction time point (Figure 3.26).

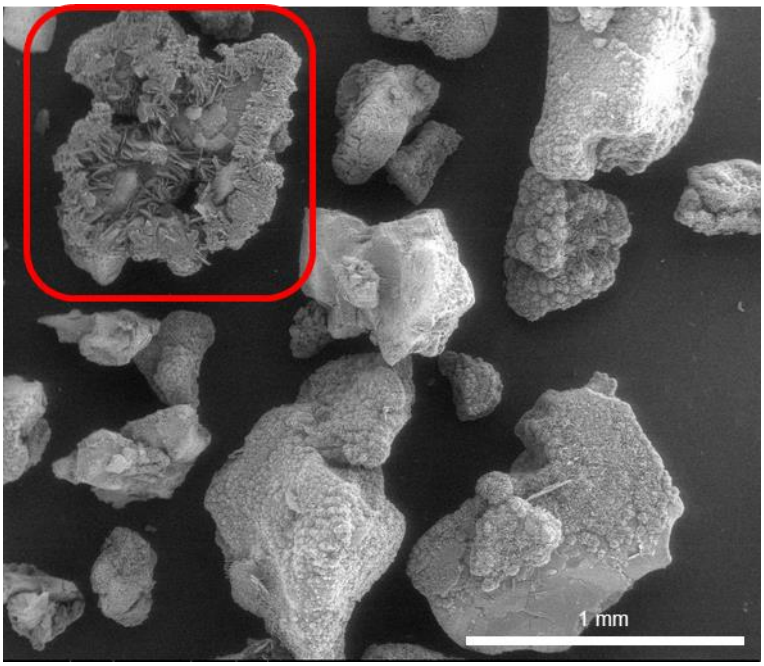

Figure 3.26. Several particles of strucMnMOF-2 after 4 hrs of reaction, showing one particle with abnormally large crystals surrounding a region of unreacted MnOx.

These crystals were most evident in the 2 hr time point for MnOx-1, where the majority of crystallites were sub-micron sized. In contrast, several regions of plate crystals 82.2 (± 26.6) µm could be seen. For MnOx-2 and MnOx-3 the size difference between the bulk and the large crystals was smaller (Table 3.8), but the regions of unreacted MnOx that these large crystals bordered were more obvious (Figure 3.27). The topology of those regions of MnOx appeared to be denser and smoother than other areas of MnOx observed in the samples.

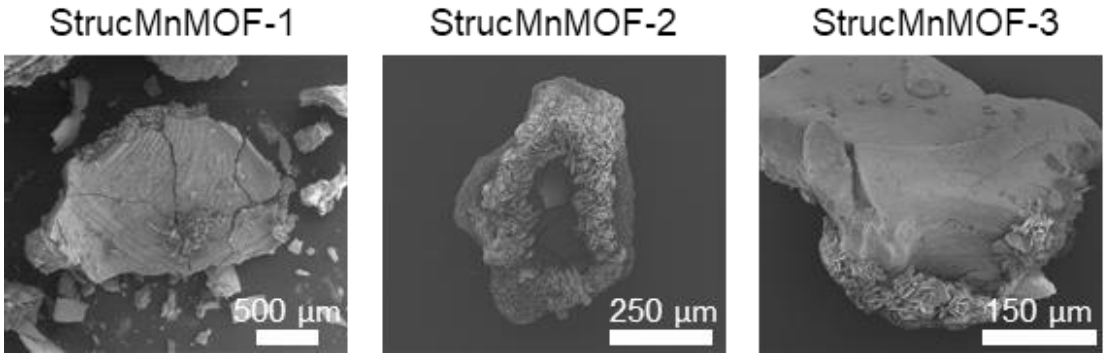

Figure 3.27. Unusual large crystals observed in strucMnMOF-1, strucMnMOF-2 and strucMnMOF-3 at the 2-hr time point. These large crystals border regions of unreacted MnOx.

Table 3.8. Crystal size comparison for the majority of the crystals compared to the anomalous large crystals seen at edges of regions of unreacted MnOx

	MnOx-1		**MnOx-2**		**MnOx-3**	
	Length (µm)	SD	Length (µm)	SD	Length (µm)	SD
Bulk	0.361	0.093	3.20	0.97	4.62	1.59
Large crystals	82.2	26.0	27.7	12.8	18.5	6.19

The growth of these abnormal crystals is likely caused by the nature of the manganese oxide surface, with several possible explanations. Although the MnOx substrates are amorphous, as shown by PXRD, the arrangement of the atoms may have some degree of local order, leading to some faces of MnOx being more or less susceptible to hydrolysis, oxidation or coordination by the reactants in solution. This may lead to unreacted surfaces in the latter case and edges where MOF growth can occur rapidly in the former case. Another reason may be the arrangement of MnOx particles in the reaction vial. It is possible that the large crystals grew at the interface between the face of a MnOx particle and the vial. This would result in an unreacted region of MnOx due to restricted access of available reactants arising from the contact between the glass vial and the MnOx particle. A final reason could be due to the drying method of the MnOx supports. It is likely that when the MnOx monoliths were dried, the chemical and physical properties of the surface were different to the internal properties. Therefore, when these monoliths were crushed, for the MnMOF forming reaction, some surfaces were less reactive than others. This is related to the first hypothesis, but reactivity is not inherent to the MnOx, but as a result of the drying process. Both the first and last explanations may give clues to the underlying nature of the MnOx substrate; however, more work is needed to confirm or disprove any of these hypotheses.

3.5.5 Structuralised MnMOF: MnOx supports

Six different MnOx supports were used to form structuralised MnMOF, as discussed in Section 3.5.2-4. The supports were shown to control the rate of crystal nucleation and growth, as well as the macroscopic structural properties. The dried MnOx ceramics were shown to be fairly smooth and dense prior to further reaction (Section 3.4.3). The morphology of the MnOx revealed after MOF growth is very variable between the samples (Figure 3.28). In general, the surface of the MnOx, revealed after the detachment of a sheet of MOF, is comprised of spherical aggregates, the size of which vary. As these aggregates were not observed on these scales before the reaction, they may be due to weathering from the reaction conditions. These regions of exposed MnOx appear as though they may be meso- and/or macro-porous and hence it would be of interest to perform gas adsorption studies on these samples in the future.

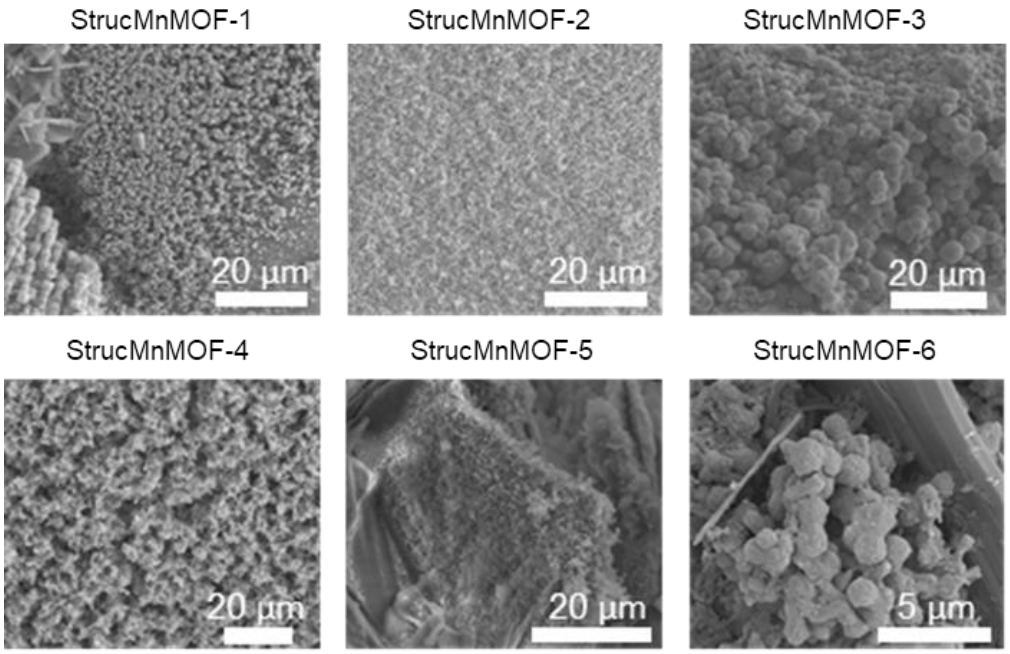

Figure 3.28. Exposed MnOx revealed after 20 hrs of MOF forming reaction

The growth of MOF crystals on the micron-scale MnOx aggregates allows for the addition of another degree of dimensionality into the MOF structuralisation, adding to crystal size and macroscopic superstructure. It is evident, however, that as the MOF crystals grow, they lose this structural information, and hence growth rate must be carefully controlled if this property is to be exploited.

3.5.6 Optimised conditions for the synthesis of strucMnMOF

The desired properties for structuralised MnMOF were high external surface areas from small crystals, micro-scale and macro-scale structural control through the use of a sacrificial MnOx template and the formation of a consistent and complete MOF coating. As such, MnOx sol-gel solvated in hexane and dried under vacuum (MnOx-2), then reacted with 2 equivalents of ascorbic acid under MOF forming conditions for 4 hours fulfilled most of these criteria; thus, these conditions were selected as the best of the tested conditions. However, there is still room for optimisation, especially in the formation of manganese oxide supports, but the structuralised MnMOF samples were deemed suitable for further testing as CO delivery vessels.

.

3.6 Structuralised MnMOF as a CO delivery vessel

3.6.1 Characterisation of structuralised MnMOF

The strucMOFs were characterised by powder X-ray diffraction, SEM/EDX and gas adsorption measurements. As discussed earlier, the MnOx ceramics generated from sol-gel methods were amorphous and hence displayed a featureless PXRD pattern (Figure 3.29a). After reacting an MnOx-3 under MnMOF forming conditions for 3 hrs, SEM imaging showed a coating of crystallites over the oxide surface (discussed in Section 3.5.2). The PXRD of this sample (Figure 3.29c) shows two sharp peaks, with one of these at a low angle, suggestive of MOF formation. Although a thin MOF coating such as this is desirable for structuralisation purposes, the quantity of crystalline material was simply too small to attain good quality PXRD data of these samples. A more fully converted sample, MnOx-5 converted to strucMOF-5 over 2 days, was analysed and displayed a diffraction pattern with several sharp low angle peaks (Figure 3.29d). The peaks in this pattern match those from the 3 hr sample, as well as containing several other smaller peaks and a significant sharp peak at 6.5° (2θ) which matches a peak in the simulated MnMOF pattern. The converted MOF patterns are not a good match for the simulated MnMOF pattern; however, this is often the case for MnMOF PXRD patterns, as they can display a wide range of patterns due to the flexibility of the framework and strong orientation effects. What can be shown from the diffraction of strucMnMOF-5 is that crystalline MOFs are being produced from this reaction.

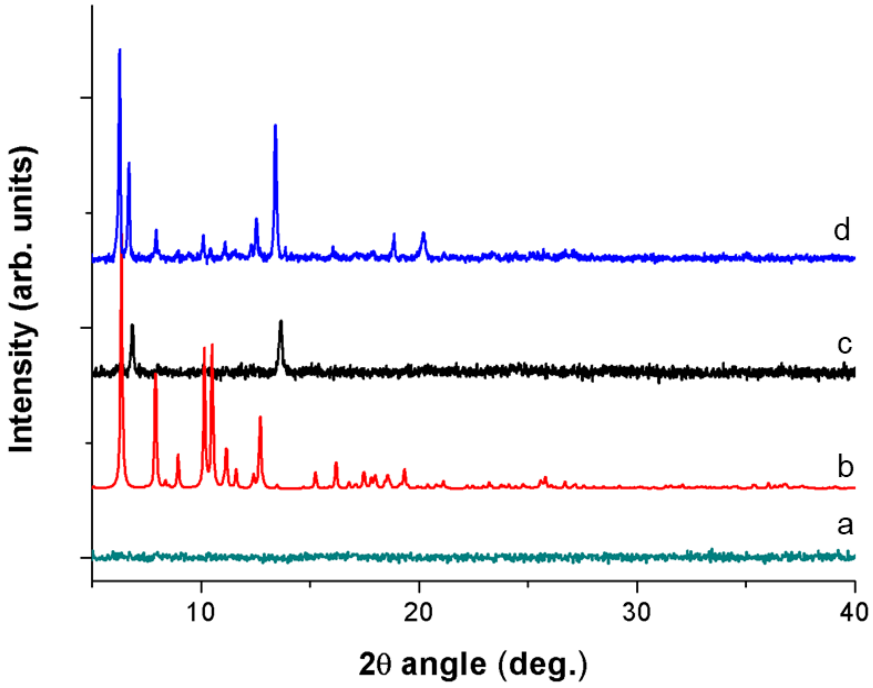

Figure 3.29. PXRD patterns of **a)** representative pattern of a manganese oxide ceramic synthesised from MnOx sol-gels, **b)** simulated pattern for MnMOF, **c)** strucMOF-3 after 3 hrs of reaction and **d)** strucMOF-5 after 2 days of reaction.

EDX analysis of converted MnMOF crystals showed the presence of nitrogen (Table 3.9), but the nitrogen to manganese atomic ratio was highly variable depending on the location on the sample that the data was collected from. This is due to several factors, firstly that the depth of EDX analysis may be deeper than the depth of the MOF layer, therefore including underlying manganese oxide. From previous discussions it has been evident that the rate of the MOF formation is dependent on the MnOx support and so some particles developed thicker MOF coatings than others (Figure 3.30a). The samples were coated in carbon to be conductive enough to perform SEM; however, this precludes analysis of carbon ratios and results in the presence of a much larger carbon peak directly adjacent to the nitrogen peak, which prevents reliable quantification of both the carbon and nitrogen content (Figure 3.30b). Therefore, the SEM/EDX analysis shows that the crystals formed from the MnOx sol-gel contain manganese and nitrogen which must come from Ligand L, although this technique is unable to confirm the atomic ratio of these species.

Table 3.9. EDX analysis of converted MnMOF synthesised from MnOx sol-gel reacted for 2 days. Locations of data collection correspond to image in Figure 3.30a.

	Atomic %					N:Mn
	C	N	O	Mn	Si	
Spectrum 1	31.82	1.48	46.6	20.09		**0.074**
Spectrum 2	63.16	16.13	15.48	5.23		**3.08**
Spectrum 3	63.49	11.05	12.81	12.64		**0.87**
Spectrum 4	66.05	12.96	14.35	6.64		**1.95**
Spectrum 5	45.13	3.09	32.24	19.53		**0.16**
Spectrum 6	59.56	10.36	11.14	17.88	1.06	**0.58**

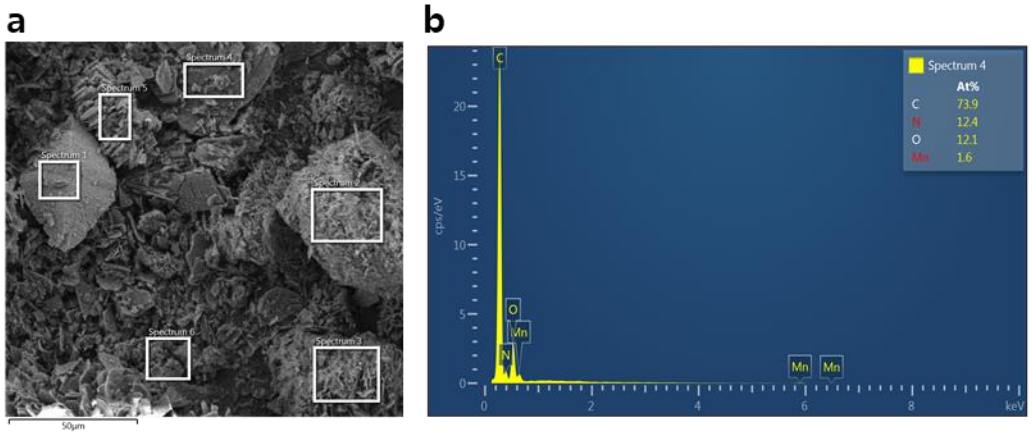

Figure 3.30. SEM/EDX analysis of strucMnMOF with **a)** spectrum collection locations for Table 3.9 and **b)** representative EDX spectrum for strucMOF, showing the close proximity of carbon and nitrogen peaks.

A nitrogen gas adsorption isotherm at 77K was undertaken on the same 2 day converted sample as shown in Figure 3.29d (strucMnMOF-5). The sample was washed with DMF (x5) and methanol (x5) then dried under a flow of nitrogen gas and activated under vacuum at 100 °C for 1.5 hr. This is an established method for activating MnMOF. The isotherm shows the characteristic gate-opening behaviour of MnMOF between P/P_0 of 0.005-0.06 due to the flexibility of the methylene bridge in Ligand L (Figure 3.31 a and b inset).[84] The total uptake of N_2 was 208 cm^3g^{-1}, less than the 250 cm^3g^{-1} reported for pure MnMOF due to incomplete conversion of the MnOx, resulting in the sample containing both microporous MOF and manganese oxide (Figure 3.31). There is no evidence of mesopores in the isotherm, but the increase in N_2 uptake after P/P_0 0.95 indicates the condensation of nitrogen in the voids between particles. This isotherm,

combined with the data from SEM/EDX and PXRD, indicates that the crystalline material formed from the MnOx conversion reactions is MnMOF.

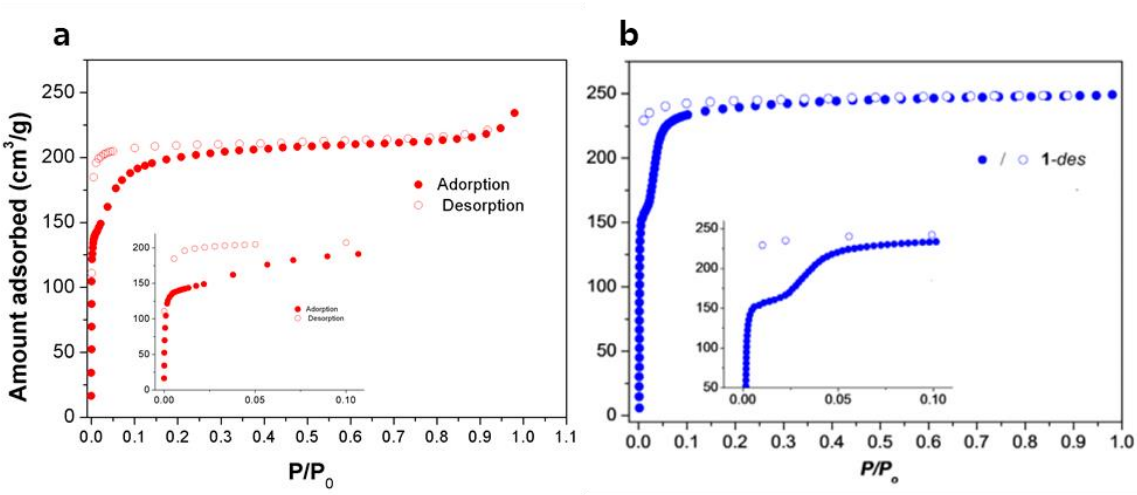

Figure 3.31. Nitrogen adsorption isotherms for **a)** converted MnMOF from MnOx sol-gel reacted for 2 days and activated from methanol and **b)** conventionally synthesised MnMOF from Bloch *et al*.[84] Inset are enlarged around the region of gate-opening due to the flexible methylene hinge in ligand L.

3.6.2 Metalation of structuralised MnMOF

The strucMnMOF-2 (reacted for 3 hrs) was metalated with bromopentacarbonylmanganese (I) in ethanol at 50 °C overnight in the same way as conventional MnMOF. The sample was then washed with ethanol and analysed by SEM/EDX and infrared spectroscopy. EDX analysis showed a Br:Mn ratio of 0.30 (±0.02 SE), indicating complete metalation. Obtaining EDX data from these samples was more problematic compared to conventionally synthesised MOF crystals, as a high energy electron beam is needed for EDX; however, due to high surface areas and poor conduction to the surface, beam damage was often sustained. It was found that the best EDX data could be obtained from particles in close contact with the carbon surface, allowing for good conductivity and less room for movement.

The IR spectrum of the metalated sample displayed the same carbonyl bands as the conventionally synthesised metallated MnMOF (Figure 3.32a). After photolysis with visible light in the sealed IR cell, the carbonyl bands had disappeared after 4 min of irradiation (Figure 3.32b). Subsequent exposure to CO gas (1.5 bar) resulted in the formation of several bands at 2057, 2047, 2040 and 2035 cm^{-1}. These bands increase in intensity between 30 min and 2 hrs of exposure, after which they did not change, even

after remaining exposed to 1.5 bar of CO for 72 hrs. These bands are very similar to those that appeared in the conventionally synthesised MnMOF after undergoing the same procedure, although of different relative intensities (Chapter 2.3.6).

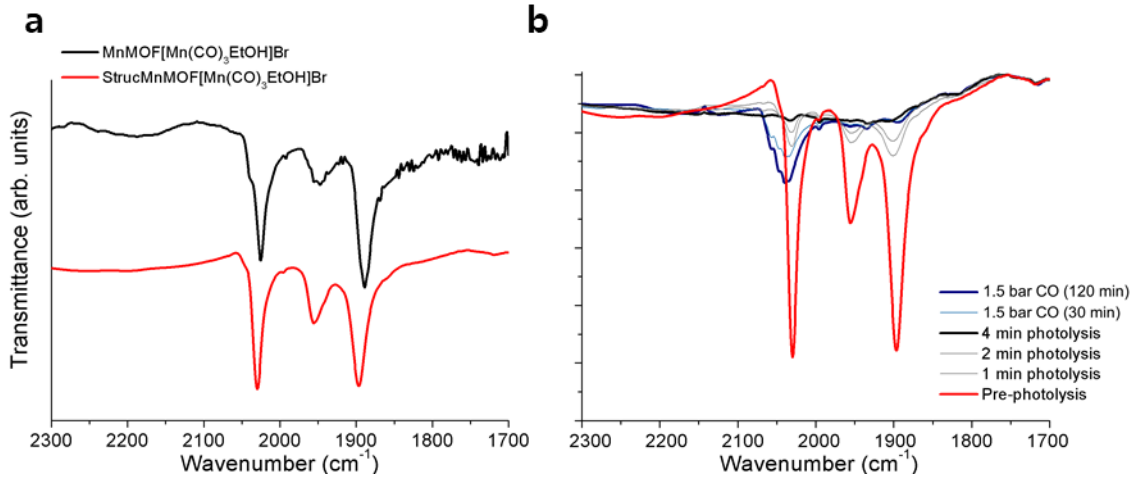

Figure 3.32. IR spectra of strucMnMOF[$Mn(CO)_3Br$].THF. **a)** strucMnMOF[$Mn(CO)_3Br$]·THF in IR cell (red) and conventionally synthesised MnMOF[$Mn(CO)_3Br$]·THF (black) in the same cell. **b)** After irradiation with visible light in cell and subsequent exposure to 1.5 bar CO gas.

The presence of nitrogen, along with the change in morphology, powder diffraction, adsorption and metalation behaviour confirm that the structuralised MOF is the same material as MnMOF.

3.6.3 CO delivery from structuralised MnMOF

MnOx-2 was reacted under the conditions outlined in Section 3.5.6 for 3 hrs to form strucMnMOF-2, which was metalated with [$Mn(CO)_5Br$] and then used as a source of CO for the aminocarbonylation reaction described in Section 3.3.2. The equivalents of CO loaded in the strucMnMOF-2 were not able to be calculated due to the unknown percentage of unconverted MnOx in the sample, but modest conversions of 15 and 10% were achieved using 51 and 44 mg of strucMnMOF-2 respectively. This is significantly lower than the conversions achieved with the same masses of pure MOFs and is due to a large proportion of the mass being MnOx. For better results, it would be desirable for the structuralised MnMOF to be more macro-porous and with a higher percentage of MOF as a thin coating on the support. This may be achieved though further exploration of the templating methods discussed in Section 3.4.2, or through supercritical drying of MnOx sol-gels to form aerogels.

3.7 Conclusions and Future Directions

3.7.1 MOFs as a CO source for chemical synthesis

MnMOF[$Mn(CO)_3$OHEt]Br (CORMat-1) was demonstrated to deliver gaseous CO through irradiation with visible light in an *ex-situ* manner to perform an aminocarbonylation reaction in a two-chamber reactor. After testing several reactor designs, some design features presented themselves as necessary for the successful use of CORMats as *ex-situ* CO sources. These were, limited headspace to allow for efficient use of released CO, the ability to control the temperatures of the two chambers separately and the means to remove the CORMats after reaction without additional filtration steps. High levels of conversion (up to 82%) were achieved with only a 1.57 excess of CO, less than that reported for other metal carbonyl CO sources.[49–51]

DUT-5-bpy and UiO-67-bpy synthesised with 2,2′-bipyridine-5,5′-dicarboxylate were metalated with [$Mn(CO)_5Br$] (to give CORMat-2 and -3 respectively) and demonstrated to be effective CO sources for the same aminocarbonylation reaction. High levels of conversion were achieved, 91% with 1.6 equiv. of CO from CORMat-2 and 90% with 4.5 equiv. of CO from CORMat-3. The variation in the behaviour of these two MOFs allude to the influence of particle shape and size on the release of CO. These MOFs may be more suitable than MnMOF for reaction scale-up as they are synthesised from cheaper components in larger scales; however, further study of the effects of crystal morphology is needed.

A limiting factor for the use of MOF samples is ensuring all crystals are exposed to the irradiation, and hence crystal size and morphology plays an important role and should be investigated further. Reactor design will also be an important consideration for scale up to larger batch or continuous flow systems, in ensuring even and complete irradiation, effective transport of released CO and easy removal of the MOF for regeneration and replacement. Further examination of temperature-controlled release of CO would also be of interest, as this may allow for uniform decarbonylation of larger quantities of MOFs but may be slower to switch on and off the release.

Although the regeneration of the CO releasing MOFs could not be achieved through addition of CO gas (Chapter 2.3.6), the re-metalation of photolyzed samples of CORMat-1 and CORMat-3 showed the presence of carbonyl peaks in the same regions as the original samples. While this was not pursued further, this presents an interesting

opportunity for these MOFs to be used as reusable CO sources. An alternative pathway to investigate is the metalation and CO release of other metal carbonyl compounds such as Ni, Re or Fe, which may have alternative photolysis mechanisms and allow for regeneration through exposure to CO gas.

3.7.2 Structuralisation of MnMOF

The results of the CO delivery experiments in Section 3.3 showed that MOF morphology plays an important role in CO delivery, as well as being an important consideration for the application of MOFs outside of research settings. Sol-gel derived sacrificial manganese oxide supports were synthesised in order to produce MnMOF as three-dimensional superstructures. These MnOx materials were amorphous and predominantly contained the Mn(IV) oxidation state. As such a reducing agent was required for MOF synthesis and the use of 2 equivalents of ascorbic acid was found to provide an adequate balance between MnOx reaction and MnMOF formation.

The nature of the MnOx scaffold was found to have a large impact on the rate of MOF formation and subsequent crystal size and macrostructural morphology. MOF growth also only occurred at the surface of the MnOx particles, resulting in the cyclical formation of sheets of strucMnMOF growing and detaching from the particle surfaces. Therefore, it was found that short reaction times were needed to achieve surface conversion of the MnOx particles, without loss of the substrate structure.

Unfortunately, the MnOx sol-gels were too fragile to have a controllable macrostructure through the use of templates, although surface converted cylindrical monoliths were able to be formed. The limitation of surface conversion only was seen when the strucMnMOF was used as a CO source for an aminocarbonylation reaction, where low yields for the mass of the composite material were seen compared to the pure MOF. As such, other methods of templating and constructing MnOx scaffold should be pursued to create more effective 3D superstructures.

Despite this, the structuralised MnMOF displayed the same properties as conventionally synthesised MnMOF, showing gate opening gas adsorption and the ability to be post-synthetically metalated. This presents an opportunity for the morphological properties of MnMOF to be tuned for all applications previously studied

in this MOF. Another, unexpected, result was the ability to synthesis larger quantities of MnMOF than the conventional method, which forms a different 2D framework (Chapter 2.6.1) when scaled-up.

3.8 Experimental

3.8.1 General experimental

Single crystals of MnMOF were prepared as previously reported.[84] Unless stated otherwise, all chemicals were purchased from commercial vendors and used as-received. NMR spectra were recorded on a Varian 500 MHz spectrometer at 23 °C using a 5 mm probe or Brucker DPX400, AV400 or AV(III)400 400 MHz spectrometers with BBFO probes. ^{1}H NMR spectra recorded in $CDCl_3$ were referenced to the internal standard, Me_4Si (0 ppm) or to the solvent peak. A FEI Quanta 450 scanning electron microscope was used to collect images and perform energy-dispersive X-ray spectroscopy (EDX), with low vacuum mode (60 Pa) used when needed. EDX was collected with an Oxford Ultim Max Large Area SDD detector with Oxford Aztec EDX processing software. Powder X-ray diffraction (PXRD) data was collected using a Cu Kα (λ = 1.540562 Å) source on a Bruker D8, Advanced X-ray powder diffractometer (parallel X-ray, capillary loaded) and a Co Kα (λ = 1.78895 Å) Bruker D4, Endeavour X-ray powder diffractometer (parallel X-ray, flat plate loaded).

A FEI Quanta 450 high resolution, field emission scanning electron microscope was used to collect images and perform energy-dispersive X-ray spectroscopy (EDX). EDX was collected with an Oxford Ultim X-Max Large Area SDD detector with Oxford Aztec EDX processing software. Crystal size distributions were obtained by measuring 20-40 crystals at random in an image using Eleif Photomeasure software and calculating the average and standard deviation.

Ambient atmosphere infrared (IR) spectra were collected on a PerkinElmer Spectrum Two, with the sample distributed between two NaCl disks or on a Bruker Alpha FTIR with an ATR attachment. Room temperature-controlled atmosphere measurements were collected on a PerkinElmer Spectrum Two spectrophotometer, with the sample dispersed between two NaCl disks inside a custom built sealed stainless steel cell with NaCl windows, which allows for the sample to be placed under vacuum or a pressure of gas. Samples were placed under vacuum for analysis. Samples exposed to CO were placed under vacuum, then 1 bar CO added before placed under vacuum again before analysis. Gas adsorption isotherm measurements were performed on an ASAP 2020 Surface Area and Pore Size Analyzer. Activation of samples was carried out as described.

MnMOF,[84] UiO-67-bpy[85] and DUT-5-bpy[86] were synthesised according to literature procedures, and metalated with an excess of $Mn(CO)_5Br$ in ethanol at 50 °C overnight in the dark then washed with ethanol (x5) and dried under nitrogen. Extent of metalation was verified by SEM/EDX.

3.8.2 Reaction procedures

UiO-67-bpy

$ZrCl_4$ (24.5 mg, 0.105 mmol), bipyridyl-dicarboxylic acid (26 mg, 0.105 mmol) and benzoic acid (384.7 mg, 3.15 mmol, 30 equiv) were dissolved in DMF (10 mL) in a 20 mL glass scintillation vial and the solution heated at 120 °C overnight. The resulting white suspension was centrifuged and washed with DMF (5 times) and ethanol (5 times), before metalation with $Mn(CO)_5Br$ at 50 °C overnight. The resulting orange powder was centrifuged and washed with ethanol (x5) or until the solution was colourless. Characterisation is discussed in Section 3.9.2.

DUT-5-bpy

Bipyridyl-dicarboxylic acid (38.3 mg, 0.15 mmol) and $AlCl_3.6H_2O$ (37.8 mg, 0.15 mmol) were dissolved in DMF (2.5 mL) and heated at 120 °C overnight in a 20 mL glass scintillation vial. The resulting precipitate was then washed with DMF (x5) and ethanol (x5) before metalation with $Mn(CO)_5Br$ overnight at 50 °C. Characterisation is discussed in Section 3.9.2.

Aminocarbonylation reaction

4-iodoanisole (20 mg, 0.085 mmol) was placed in the reaction chamber with n-hexylamine (23 µL, 0.171 mmol, 2 equiv.), triethylamine (24 µL, 0.171 mmol, 2 equiv.) and triphenylphosphine (2.2 mg, 8.5 x 10^{-6} mol, 10%) (Figure 3.33). Dioxane was added (0.5 - 1 mL) and the mixture degassed with argon for 10-20 min. $Pd(dba)_2$ (2.5 mg, 4.3 x 10^{-6} mol, 5%) was then added and the MOF (>1 equiv. CO) added to the other MOF chamber. The reaction mixture was heated at 80 °C for the duration of the reaction (overnight). The solvent was removed and the residue purified by column chromatography (silica, 20% EtOAc/Hexane, Rf: ~0.3, ^1H NMR ($CDCl_3$) 7.73 (2H, d, 8.8 Hz, C-H aromatic), 6.93 (2H, d, 8.8 Hz, C-H aromatic), 6.01 (1H, s, N-H), 3.86 (3H, s, O-CH_3), 3.45 (2H, m, N-C-H_2), 1.60 (4H, m, 2 x CH_2), 1.34 (4H, m, 2 x CH_2), 0.91 (3H, m,

CH_3) and ^{13}C NMR ($CDCl_3$) to give a yellow solid (6.6 mg, 33%). Conversion efficiencies were calculated from ^1H NMR analysis of the crude product before purification.

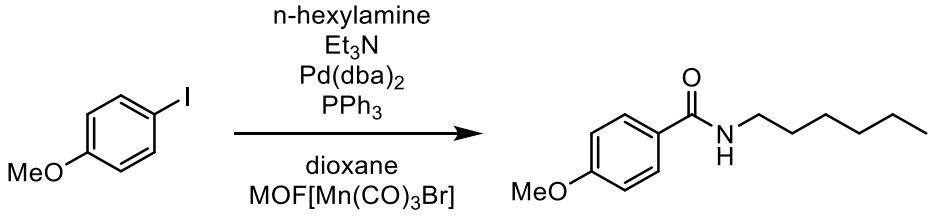

Figure 3.33. Reaction scheme for the aminocarbonylation of 4-iodoanisole.

Manganese oxide sol-gel

Potassium permanganate (500 mg, 3.16 mmol, 3 equiv.) was dissolved in water (30 mL), then maleic acid (122 mg, 1.05 mmol, 1 equiv.) was added slowly. The solution was stirred for 5 min, then degassed vigorously with nitrogen while applying a mild vacuum for 20 min. The gel was then poured into moulds and left to cure overnight, before being washed with water (x3), acetone (x3), diethyl ether (x3) and hexane (x3). One wash of each solvent type was left to soak overnight before being exchanged for the next solvent. The gel could then be air, heat or vacuum dried, or used as a wet gel.

Manganese oxide nanoparticles on aluminium

Potassium permanganate (79 mg, 0.05 mmol) was dissolved in water (10 mL) and mixed with an aqueous solution of sodium tetraborate (95 mg, 0.025 mmol, 9 mL). Aluminium foil was cleaned with ethanol, dried and added to the solution. The vessel was then either heated to 100 °C or left at room temperature for 1-3 days before the foil was removed and washed with water, resulting in a gold-copper coloured coating of manganese oxide nanoparticles.

MnMOF conversion

MnOx (40 mg) was crushed and placed in a scintillation vial with Ligand L (25 mg, 0.056 mmol) and ascorbic acid (20 mg, 0.11 mmol). DMF (4 mL) and water (2 mL) were added, and the vial heated at 100 °C. After the sample was cooled it was washed with DMF (x5).

IR Photolysis and CO exposure

Metalated MOF was solvent exchanged with dry THF (x5) then dried under nitrogen and transferred to the IR cell. The cell was then evacuated under high vacuum

and the initial IR spectrum recorded. The photolysis was performed with a broad spectrum visible torch through the potassium bromide windows of the cell, with IR spectra recorded at several timepoints. After this the cell was evacuated then placed under 1.5 bar CO gas, and IR spectra recorded again at several time points. Before the spectra were recorded the CO was removed by placing the cell under vacuum, then placed back under CO, as the CO_{gas} bands obscure the carbonyl bands.

3.9 Appendix

3.9.1 MnOx foil SEM/EDX

Manganese oxide nanoparticles grown onto aluminium foil were analysed by SEM/EDX in order to measure the quantity of manganese relative to aluminium (Table 3.10 and Figure 3.34).

Table 3.10. Manganese to aluminium elemental ratios from EDX analysis of MnOx nanoparticles on aluminium foil reacted for 1 day and 3 days.

Mn:Al	1 day (SE)	3 days (SE)
Average	0.12 (0.03)	2.32 (0.50)
Large particles only		4.65 (0.69)
Excluding large particles		1.34 (0.42)

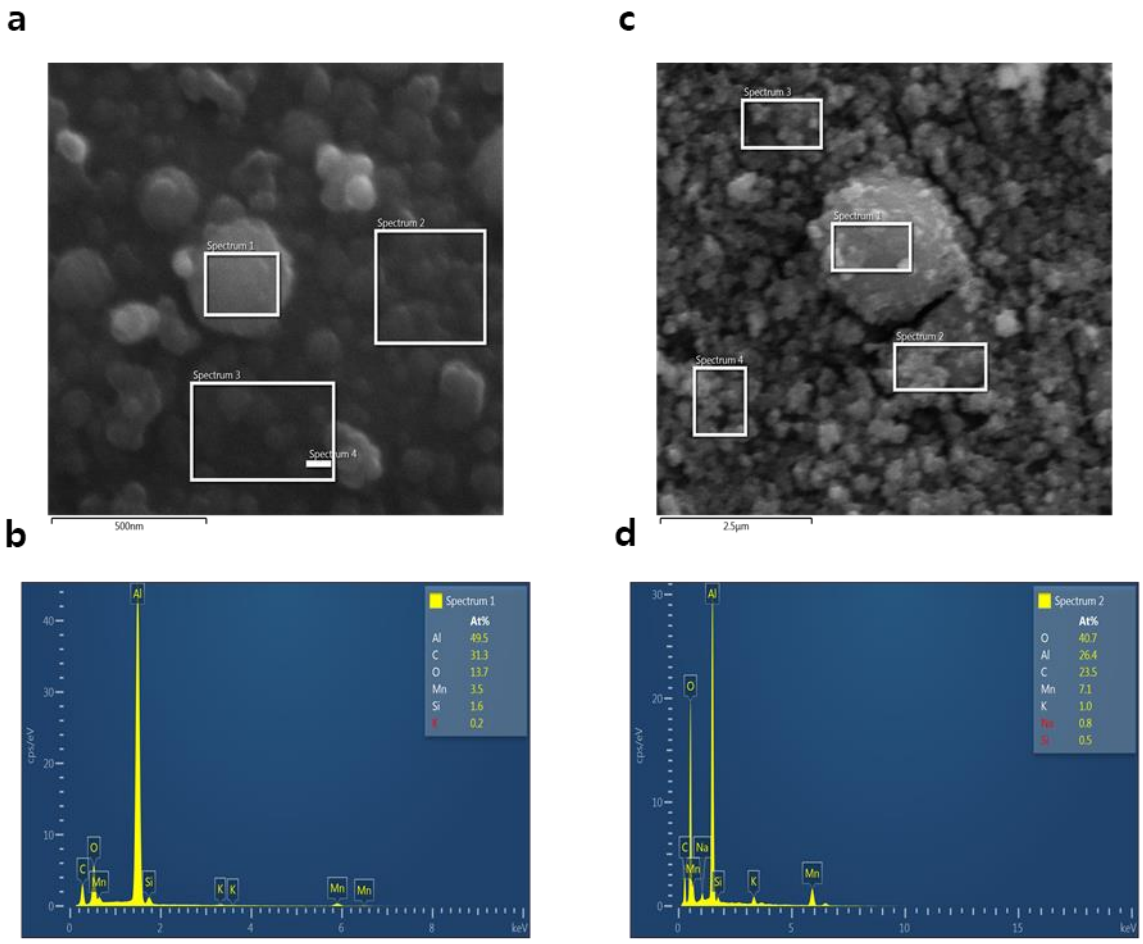

Figure 3.34. Representative SEM images and EDX spectra recorded for MnOx nanoparticles on Al foil reacted for **a/b)** 1 day and **c/d)** 3 days

3.9.2 UiO-67 and DUT-5 characterisation

As microcrystalline powders, UiO-67-bpy and DUT-5-bpy were metalated with $[Mn(CO)_5Br]$ and characterised through SEM/EDX (Figure 3.35), PXRD (Figure 3.36) and IR spectroscopy (Figure 3.37).

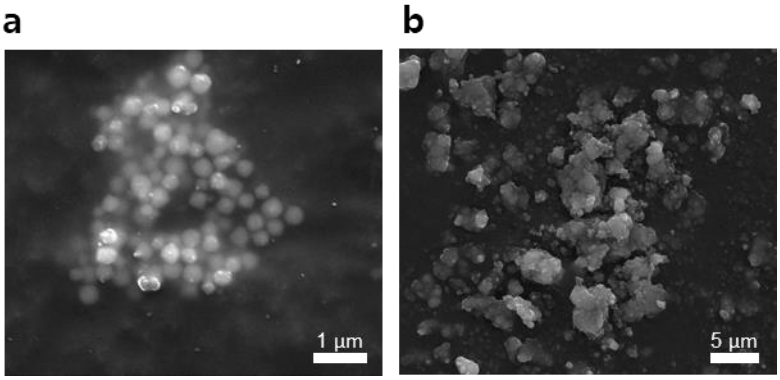

Figure 3.35. SEM images of metalated **a)** UiO-67-bpy$[Mn(CO)_3Br]$ and **b)** DUT-5-bpy$[Mn(CO)_3Br]$

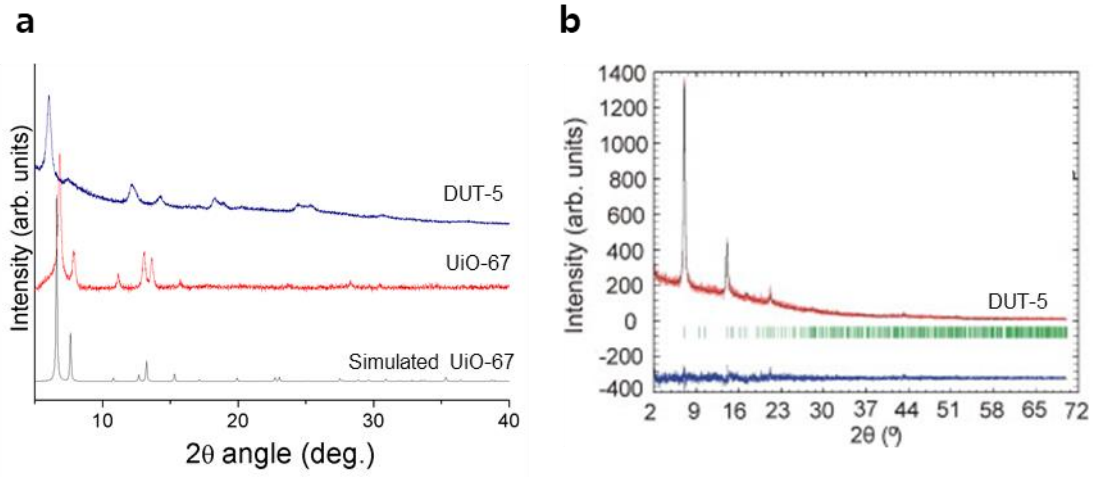

Figure 3.36. PXRD for **a)** DUT-5 (blue), UiO-67 (red) and simulated UiO-67 (black) using Co (λ = 1.7902 Å) radiation. No single crystal structures of DUT-5 have been reported, so it may be compared to **b)** experimental PXRD for DUT-5 using Cu (λ = 1.5406 Å) radiation reported by Senkovska *et al.*[68]

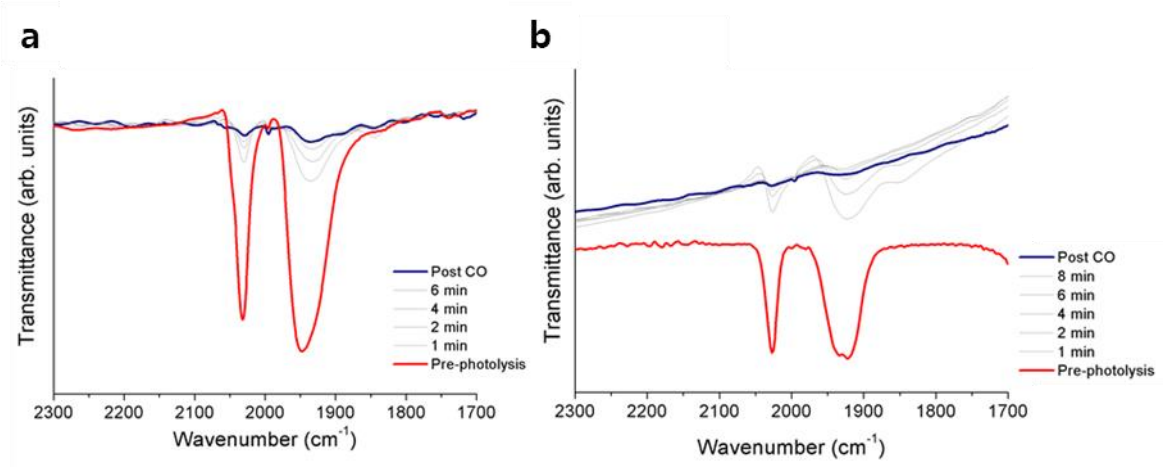

Figure 3.37. IR spectra of **a)** UiO-67[$Mn(CO)_3Br$] and **b)** DUT-5[$Mn(CO)_3Br$] before photolysis (red), during photolysis (grey) and after exposure to CO gas (blue). Note that the spectra in b are not overlaid due to background subtraction problems. The pre-photolysis spectrum was taken from a different sample.

3.10 References

1 L.-L. Tan, H. Li, Y. Zhou, Y. Zhang, X. Feng, B. Wang and Y.-W. Yang, *Small*, 2015, **11**, 3807–3813.

2 J. G. Nguyen, K. K. Tanabe and S. M. Cohen, *CrystEngComm*, 2010, **12**, 2335–2338.

3 M. Vassaki, K. E. Papathanasiou, C. Hadjicharalambous, D. Chandrinou, P. Turhanen, D. Choquesillo-Lazarte and K. D. Demadis, *Chem. Commun.*, 2020, **56**, 5166–5169.

4 Q. Chen, Q. W. Chen, C. Zhuang, P. P. Tang, N. Lin and L. Q. Wei, *Inorg. Chem. Commun.*, 2017, **79**, 78–81.

5 J. Park, D. Yuan, K. T. Pham, J. R. Li, A. Yakovenko and H. C. Zhou, *J. Am. Chem. Soc.*, 2012, **134**, 99–102.

6 H. Bunzen, A. Kalytta-Mewes, L. van Wüllen and D. Volkmer, *Beilstein J. Nanotechnol.*, 2019, **10**, 1851–1859.

7 M. A. Chowdhury, *Rev. J. Chem.*, 2017, **7**, 1–22.

8 Y. Guan, Z. Teng, L. Mei, J. Zhang, Q. Wang and Y. Luo, *J. Colloid Interface Sci.*, 2019, **533**, 207–215.

9 R. E. Morris and P. S. Wheatley, *Angew. Chem. - Int. Ed.*, 2008, **47**, 4966–4981.

10 E. Lashkari, H. Wang, L. Liu, J. Li and K. Yam, *Food Chem.*, 2017, **221**, 926–935.

11 M. Sarker and S. H. Jhung, *J. Mol. Liq.*, 2019, **296**, 112060.

12 S. R. Miller, E. Alvarez, L. Fradcourt, T. Devic, S. Wuttke, P. S. Wheatley, N. Steunou, C. Bonhomme, C. Gervais, D. Laurencin, R. E. Morris, A. Vimont, M. Daturi, P. Horcajada and C. Serre, *Chem. Commun.*, 2013, **49**, 7773–7775.

13 M. Zhang, R. Qiao and J. Hu, *Nanomaterials*, 2020, **10**, 1134.

14 A. Carné-Sánchez, F. J. Carmona, C. Kim and S. Furukawa, *Chem. Commun.*, 2020, **56**, 9750–9766.

15 A. C. McKinlay, J. F. Eubank, S. Wuttke, B. Xiao, P. S. Wheatley, P. Bazin, J. C. Lavalley, M. Daturi, A. Vimont, G. De Weireld, P. Horcajada, C. Serre and R. E. Morris, *Chem. Mater.*, 2013, **25**, 1592–1599.

16 D. Cattaneo, S. J. Warrender, M. J. Duncan, C. J. Kelsall, M. K. Doherty, P. D. Whitfield, I. L. Megson and R. E. Morris, *RSC Adv.*, 2016, **6**, 14059–14067.

17 J. F. Eubank, P. S. Wheatley, G. Lebars, A. C. McKinlay, H. Leclerc, P. Horcajada, M. Daturi, A. Vimont, R. E. Morris and C. Serre, *APL Mater.*, 2014, **2**, 124112.

18 K. Peikert, L. J. McCormick, D. Cattaneo, M. J. Duncan, F. Hoffmann, A. H. Khan, M. Bertmer, R. E. Morris and M. Fröba, *Microporous Mesoporous Mater.*, 2015, **216**, 118–126.

19 B. Xiao, P. J. Byrne, P. S. Wheatley, D. S. Wragg, X. Zhao, A. J. Fletcher, K. M. Thomas, L. Peters, J. S. O. Evans, J. E. Warren, W. Zhou and R. E. Morris, *Nat. Chem.*, 2009, **1**, 289–294.

20 N. J. Hinks, A. C. McKinlay, B. Xiao, P. S. Wheatley and R. E. Morris, *Microporous Mesoporous Mater.*, 2010, **129**, 330–334.

21 S. Rojas, P. S. Wheatley, E. Quartapelle-Procopio, B. Gil, B. Marszalek, R. E. Morris and E. Barea, *CrystEngComm*, 2013, **15**, 9364–9367.

22 A. C. McKinlay, P. K. Allan, C. L. Renouf, M. J. Duncan, P. S. Wheatley, S. J. Warrender, D. Dawson, S. E. Ashbrook, B. Gil, B. Marszalek, T. Düren, J. J. Williams, C. Charrier, D. K. Mercer, S. J. Teat and R. E. Morris, *APL Mater.*, 2014, **2**, 124108.

23 P. Horcajada, R. Gref, T. Baati, P. K. Allan, G. Maurin, P. Couvreur, G. Férey, R. E. Morris and C. Serre, *Chem. Rev.*, 2012, **112**, 1232–1268.

24 R. E. Morris, *Nat. Chem.*, 2011, **3**, 347–348.

25 H. D. Lawson, S. P. Walton and C. Chan, *ACS Appl. Mater. Interfaces*, 2021, **13**, 7004–7020.

26 H. Pham, K. Ramos, A. Sua, J. Acuna, K. Slowinska, T. Nguyen, A. Bui, M. D. R. Weber and F. Tian,

ACS Omega, 2020, **5**, 3418–3427.

27 B. Chen, C. Liang, J. Yang, D. S. Contreras, Y. L. Clancy, E. B. Lobkovsky, O. M. Yaghi and S. Dai, *Angew. Chem. Int. Ed.*, 2006, **45**, 1390–1393.

28 Z. Yan, J. Zheng, J. Chen, P. Tong, M. Lu, Z. Lin and L. Zhang, *J. Chromatogr. A*, 2014, **1366**, 45–53.

29 J. Zhang, J. Chen, S. Peng, S. Peng, Z. Zhang, Y. Tong, P. W. Miller and X. P. Yan, *Chem. Soc. Rev.*, 2019, **48**, 2566–2595.

30 V. Pascanu, P. R. Hansen, A. Bermejo Gómez, C. Ayats, A. E. Platero-Prats, M. J. Johansson, M. À. Pericàs and B. Martín-Matute, *ChemSusChem*, 2015, **8**, 123–130.

31 C. G. Piscopo, M. Schwarzer, M. Herrmann, A. Affini, P. Pelagatti, G. Maestri, R. Maggi and S. Loebbecke, *ChemCatChem*, 2016, **8**, 1293–1297.

32 C. Kim, S. Diring, S. Furukawa and S. Kitagawa, *Dalton Trans.*, 2015, **44**, 15324.

33 J. B. Peng, H. Q. Geng and X. F. Wu, *Chem*, 2019, **5**, 526–552.

34 Airgas, *Carbon Monoxide Sadefy Data Sheet*, 2020.

35 Sigma Aldrich, Application of Carbon Monoxide in Synthesis Made Simple and Safe by Prof. Skrydstrup and Coworkers | Sigma-Aldrich, https://www.sigmaaldrich.com/technical-documents/articles/technology-spotlights/cogen-coware.html, (accessed 23 February 2021).

36 P. Hermange, A. T. Lindhardt, R. H. Taaning, K. Bjerglund, D. Lupp and T. Skrydstrup, *J. Am. Chem. Soc.*, 2011, **133**, 6061–6071.

37 D. U. Nielsen, R. H. Taaning, A. T. Lindhardt, T. M. Gøgsig and T. Skrydstrup, *Org. Lett.*, 2011, **13**, 4454–4457.

38 S. D. Friis, A. T. Lindhardt and T. Skrydstrup, *Acc. Chem. Res.*, 2016, **49**, 594–605.

39 M. N. Burhardt, R. H. Taaning and T. Skrydstrup, *Org. Lett.*, 2013, **15**, 948–951.

40 S. Korsager, R. H. Taaning, A. T. Lindhardt and T. Skrydstrup, *J. Org. Chem.*, 2013, **78**, 6112–6120.

41 A. T. Lindhardt, R. Simonssen, R. H. Taaning, T. M. Gøgsig, G. N. Nilsson, G. Stenhagen, C. S. Elmore and T. Skrydstrup, *J. Label. Compd. Radiopharm.*, 2012, **55**, 411–418.

42 T. Morimoto, K. Fuji, K. Tsutsumi and K. Kakiuchi, *J. Am. Chem. Soc.*, 2002, **124**, 3806–3807.

43 T. Shibata, N. Toshida and K. Takagi, *Org. Lett.*, 2002, **4**, 1619–1621.

44 T. Ueda, H. Konishi and K. Manabe, *Angew. Chem. Int. Ed.*, 2013, **52**, 8611–8615.

45 T. Schareina, A. Zapf, A. Cotté, M. Gotta and M. Beller, *Adv. Synth. Catal.*, 2010, **352**, 1205–1209.

46 S. Cacchi, G. Fabrizi and A. Goggiamani, *J. Comb. Chem.*, 2004, **6**, 692–694.

47 Y. Wan, M. Alterman, M. Larhed and A. Hallberg, *J. Org. Chem.*, 2002, **67**, 6232–6235.

48 J. F. Carpentier, Y. Castanet, J. Brocard, A. Mortreux and F. Petit, *Tetrahedron Lett.*, 1991, **32**, 4705–4708.

49 E. J. Corey and L. S. Hegedus, *J. Am. Chem. Soc*, 1969, **91**, 1233–1234.

50 A. Więckowska, R. Fransson, L. R. Odell and M. Larhed, *J. Org. Chem.*, 2011, **76**, 978–981.

51 J. Lindh, A. Fardost, M. Almeida and P. Nilsson, *Tetrahedron Lett.*, 2010, **51**, 2470–2472.

52 C. J. Mallia and I. R. Baxendale, *Org. Process Res. Dev.*, 2016, **20**, 327–360.

53 H. Akinaga, N. Masaoka, K. Takagi, I. Ryu and T. Fukuyama, *Chem. Lett.*, 2014, **43**, 1456–1458.

54 P. Koos, U. Gross, A. Polyzos, M. O'Brien, I. Baxendale and S. V. Ley, *Org. Biomol. Chem.*, 2011, **9**, 6903–6908.

55 C. Brancour, T. Fukuyama, Y. Mukai, T. Skrydstrup and I. Ryu, *Org. Lett.*, 2013, **15**, 2794–2797.

56 T. Fukuyama, Y. Mukai and I. Ryu, *Beilstein J. Org. Chem*, 2011, **7**, 1288–1293.

57 P. Horcajada, T. Chalati, C. Serre, B. Gillet, C. Sebrie, T. Baati, J. F. Eubank, D. Heurtaux, P. Clayette, C. Kreuz, J. S. Chang, Y. K. Hwang, V. Marsaud, P. N. Bories, L. Cynober, S. Gil, G. Férey, P. Couvreur and R. Gref, *Nat. Mater.*, 2010, **9**, 172–178.

58 M. Knauert, S. Vangala, M. Haslip and P. J. Lee, *Oxid. Med. Cell. Longev.*, 2013, 360815

59 S. Diring, A. Carné-Sánchez, J. Zhang, S. Ikemura, C. Kim, H. Inaba, S. Kitagawa and S. Furukawa, *Chem. Sci.*, 2017, **8**, 2381–2386.

60 I. B. Calhau, A. C. Gomes, S. M. Bruno, A. C. Coelho, C. I. R. Magalhães, C. C. Romão, A. A. Valente, I. S. Gonçalves and M. Pillinger, *Eur. J. Inorg. Chem.*, 2020, **2020**, 2726–2736.

61 F. J. Carmona, C. R. Maldonado, S. Ikemura, C. C. Romão, Z. Huang, H. Xu, X. Zou, S. Kitagawa, S. Furukawa and E. Barea, *ACS Appl. Mater. Interfaces*, 2018, **10**, 31158–31167.

62 M. Ma, H. Noei, B. Mienert, J. Niesel, E. Bill, M. Muhler, R. A. Fischer, Y. Wang, U. Schatzschneider and N. Metzler-Nolte, *Chem. - A Eur. J.*, 2013, **19**, 6785–6790.

63 F. J. Carmona, S. Rojas, P. Purificación, S. Sánchez, H. Jeremias, A. R. Marques, C. C. Romã, D. Choquesillo-Lazarte, J. A. R. Navarro, C. R. Maldonado and E. Barea, *Inorg. Chem.*, 2016, **55**, 6525–6531.

64 F. J. Carmona, S. Rojas, C. C. Romão, J. A. R. Navarro, E. Barea and C. R. Maldonado, *Chem. Commun.*, 2017, **53**, 6581–6584.

65 M. Rivera-Almazo, M. L. Díaz-Ramírez, R. Hernández-Esparza, R. Vargas, A. Martínez, V. Martis, P. A. Sáenz-Cavazos, D. Williams, E. Lima, I. A. Ibarra and J. Garza, *Phys. Chem. Chem. Phys.*, 2021, **23**, 1454–1463.

66 J. G. Bell, S. A. Morris, F. Aidoudi, L. J. McCormick, R. E. Morris and K. M. Thomas, *J. Mater. Chem. A*, 2017, **5**, 23577–23591.

67 Mehar U Nisa, Y. Chen, X. Li and Z. Li, *J. Taiwan Inst. Chem. Eng.*, 2020, **107**, 44–53.

68 I. Senkovska, F. Hoffmann, M. Fröba, J. Getzschmann, W. Böhlmann and S. Kaskel, *Microporous Mesoporous Mater.*, 2009, **122**, 93–98.

69 C. Yildiz, K. Kutonova, S. Oßwald, A. Titze-Alonso, J. Bitzer, S. Bräse and W. Kleist, *ChemCatChem*, 2020, **12**, 1134–1142.

70 P. Cheng, C. Wang, Y. V. Kaneti, M. Eguchi, J. Lin, Y. Yamauchi and J. Na, *Langmuir*, 2020, **36**, 4231–4249.

71 J. Meng, X. Liu, C. Niu, Q. Pang, J. Li, F. Liu, Z. Liu and L. Mai, *Chem. Soc. Rev.*, 2020, **49**, 3142–3186.

72 X. Y. Yang, L. H. Chen, Y. Li, J. C. Rooke, C. Sanchez and B. L. Su, *Chem. Soc. Rev.*, 2017, **46**, 481–558.

73 S. Furukawa, J. Reboul, S. Diring, K. Sumida and S. Kitagawa, *Chem. Soc. Rev.*, 2014, **43**, 5700–5734.

74 K. A. S. Usman, J. W. Maina, S. Seyedin, M. T. Conato, L. M. Payawan, L. F. Dumée and J. M. Razal, *NPG Asia Mater.*, 2020, **12**, 1–18.

75 C. J. Brinker and G. W. Scherer, *Sol-Gel Science: The Physics and Chemistry of Sol-Gel Processing*, Academic Press, San Diego, 1990.

76 M. R. Lohe, M. Rose and S. Kaskel, *Chem. Commun.*, 2009, 6056–6058.

77 K. Sumida, K. Liang, J. Reboul, I. A. Ibarra, S. Furukawa and P. Falcaro, *Chem. Mater.*, 2017, **29**, 2626–2645.

78 P. Nordeman, L. R. Odell and M. Larhed, *J. Org. Chem.*, 2012, **77**, 11393–11398.

79 S. Ching, J. L. Roark, N. Duan and S. L. Suib, *Chem. Mater.*, 1997, **9**, 750–754.

80 L. I. Simandi and M. Jaky, *J.C.S Perkin II*, 1973, **3**, 1856–1860.

81 S. A. Kulinich, M. Farzaneh and X. W. Du, *Inorg. Mater.*, 2007, **43**, 956–963.

82 J. Pellicer, V. García-Morales, L. Guanter, M. J. Hernández and M. Dolz, *Water J. Phys. Chem. Ref. Data*, 2002, **70**, 817.

83 B. A. Grigoryev, B. V Nemzer, D. S. Kurumov and J. V Sengers, *Int. J. Thermophys.,* 1992, **13**, 2, 453-467

84 W. M. Bloch, A. Burgun, C. J. Coghlan, R. Lee, M. L. Coote, C. J. Doonan and C. J. Sumby, *Nat. Chem.*, 2014, **6**, 906–912.

85 A. Schaate, P. Roy, A. Godt, J. Lippke, F. Waltz, M. Wiebcke and P. Behrens, *Chem. - A Eur. J.*, 2011, **17**, 6643–6651.

86 M. A. Gotthardt, S. Grosjean, T. S. Brunner, J. Kotzel, A. M. Gänzler, S. Wolf, S. Bräse and W. Kleist, *Dalton Trans.*, 2015, **44**, 16802–16809.

Chapter Four: Reactive metal complexes site-isolated in MnMOF

4.1 Introduction

The content of Chapters 2 and 3 explored the photochemistry of manganese (I) carbonyl complexes isolated in a MOF scaffold, showing how the tethering of these complexes within crystalline, porous materials can be used to synthesise and characterise complexes with unusual coordination environments and provide structural detail of reaction intermediates and products. This characterisation of reactive species can provide valuable insight into bond activation mechanisms that are key in catalysis and chemical synthesis. It is known that the active forms of many homogeneous catalysts are formed from ligand dissociation processes producing coordinatively unsaturated species. These species are challenging to characterise *in situ* due to their short lifetimes in solution and have required low-temperature matrix isolation strategies or time-resolved spectroscopic techniques to furnish structural details and information about reactivity.[1–3] Moreover, isolating reactive metal complexes in porous, crystalline scaffolds can allow for the synthesis of biomimetic catalysts which can replicate the selectivity and efficiency of enzymes (Figure 4.1).[4]

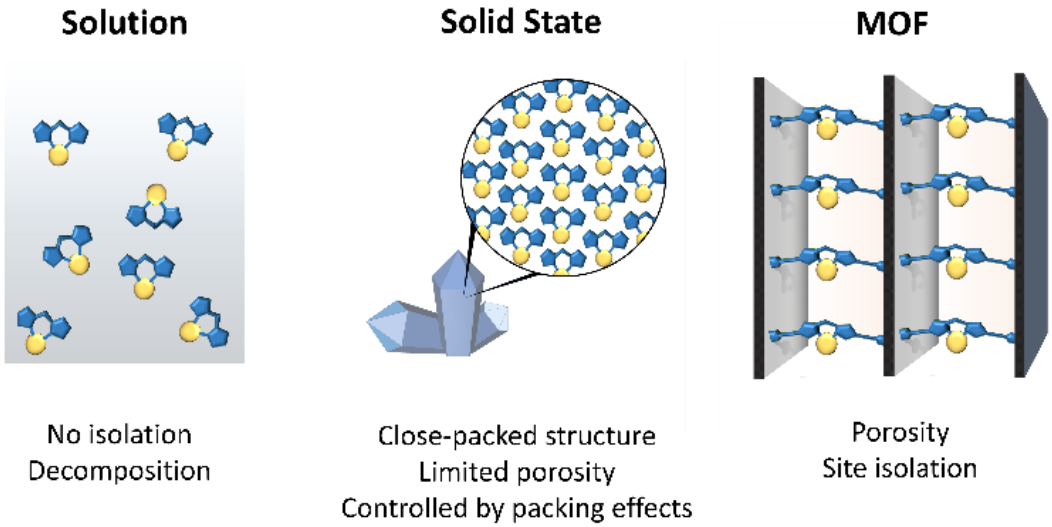

Figure 4.1. Advantages and disadvantages of various strategies for employing metal complexes as catalysts.[4]

Much of the world's production of bulk and fine chemicals relies on the use of metal-based catalysts.[5] Reducing our reliance on precious metal catalysts can be approached from two directions; the first would be to make new catalysts from earth abundant materials, while the second is to make the current catalysts more effective, thus reducing the quantity of precious metal needed. The impetus behind the work in this chapter will be following those two paths, investigating the photochemistry of earth-abundant manganese complexes, with the aim of exploiting their reactivity in the future, and site-isolating mononuclear palladium complexes in the MnMOF support to aid in improving the efficiency of palladium catalysts. The photochemistry of fac-tricarbonyl manganese(I) complexes was explored in Chapters 2 and 3, showing how the complex can undergo decarbonylation to release CO gas. The presence of an uncoordinated bromide anion in the presence of coordinating solvents presented the opportunity to exploit anion exchange to introduce an additional photoactive component, which was chosen to be the azide anion.

4.1.1 Photochemistry of Inorganic Azides and Nitrenes

The diverse and complex photochemistry of the azide (N_3) moiety has been of great interest in the last century, due to its ability to produce a range of highly reactive species through different photolysis pathways.[6,7] Inorganic azides fall into four categories, each with their own photochemistry, as follows; compounds containing free (e.g. NaN_3) or protonated (e.g. HN_3) azide anions (**1**), coordination complexes where the azido ligand(s) is(are) bonded to the central atom (**2**) and coordination complexes containing non-coordinated (3) or coordinated (4) azido ligand(s) (Figure 4.2). Complexes of types 3 and 4 are outside the scope of this study and so subsequent discussion will focus on types 1 and 2. In type 1, ionic azides, the azide unit is linear with $D_{\infty h}$ symmetry and equal N-N bond lengths. In contrast, when bonded to a main group element or transition metal to give a type 2 complex, the azide exhibits a bent *trans* C_S configuration, with a N-N-N bond angle of 172 ± 3° and different bond lengths between the N1-N2 and N2-N3 atoms.[8] This bent configuration is caused by favourable overlap of σ and π* orbitals to give strong negative hyperconjugation, which donates electron density from the filled σ (M-N1) orbital into the unfilled antibonding π* (N2-N3) orbital.[9]

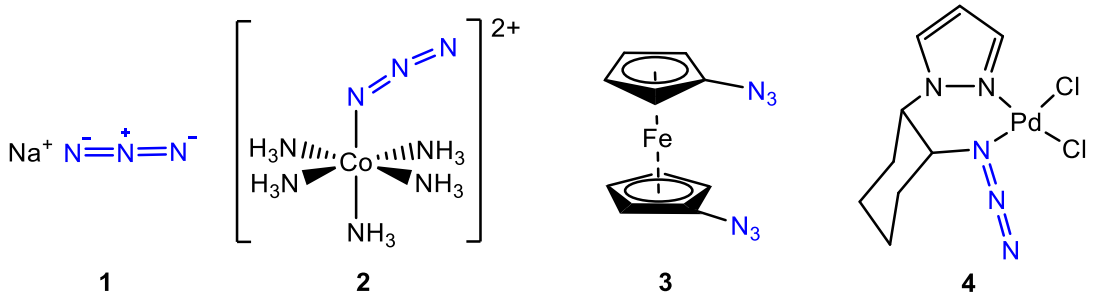

Figure 4.2. Examples of classes of inorganic azides, **1)** ionic compounds containing free or protonated azide anions, **2)** coordination complexes with azido ligand(s) bound to the central metal and coordination complexes containing an organic azide ligand where the azido is **3)** not bound to the metal or **4)** bound to the metal.[10,11]

Compounds containing the free azide anion (type 1) principally follow two reaction pathways when photochemically activated, namely quenching of singlet O_2 and generation of the nitrene anion N^-; however, coordinated azides in general (type 2) have been found to undergo six photoactivated reaction pathways.[12] These are:

i. Formation of a singlet or triplet nitrene following dinitrogen elimination, preserving the oxidation state of the coordinated metal.

ii. Transformation of azido ($-N_3$) to nitrido (=N) complexes correlated with a two electron oxidation of the metal.

iii. Oxidation of the azido anion to its radical (N_3^*) associated with a one electron reduction of the metal.

iv. Photo-ejection of the azido ligand from the coordination sphere (non-redox).

v. Photo-isomerisation.

vi. Reaction with another ligand in the primary coordination sphere.

The azide anion is activated by irradiation by UV light below 270 nm and leads to the population of an intra-ligand or charge transfer to solvent excited states.[12,13] This may be followed by decomposition to release dinitrogen and form a 6 e^- nitrene. With four non-bonding electrons, nitrenes are the nitrogen analogues of carbenes. These highly reactive species can exist in singlet or triplet states, where the electrons are arranged in two lone pairs for the former or across three orbitals, one filled and the others half-filled in the latter case. As such the triplet state shows diradical behaviour, although both forms are unstable and react easily with a range of substrates.[14]

Direct nitrene transfer reactions are one example of this reactivity, allowing the conversion of C-H to C-N bonds, and are a powerful method of introducing synthetically valuable functional groups to inexpensive starting materials.[15–17] Nitrenes act as two electron oxidants and can be generated from azides under thermal, photochemical or oxidative conditions, producing dinitrogen gas as a co-product.[18] Nitrene transfer reactions with organic azides have been explored extensively and have been shown to be useful in a wide range of reactions including asymmetric C-H aminations[19], C=C aziridinations,[20,21] imine formations,[22] and aminochlorinations[23] using a range of transition metal catalysts.[24–26] Therefore the study of inorganic azides and nitrenes may allow for valuable insights into the mechanisms of transition metal catalysed nitrene transfer reactions and present opportunities to access new reactivities.[18,27,28]

4.1.2 Formation of isocyanates from inorganic carbonyl and azide complexes

Organic azides are known to decompose thermally or under UV irradiation to give a nitrene intermediate which can react with carbon monoxide gas to form isocyanates.[10,29] A similar reaction occurs in inorganic complexes (type 2), where a metal carbonyl compound can react with an organic azide to form an isocyanate complex. Isocyanate (NCO) is a useful functional group,[1] often involved as a synthetic intermediate in the formation of heterocycles through cycloaddition reactions, in the reaction of amines to form ureas or in insertions into metal-X (X = C, N or H) bonds to form amidation products.[30,31] They can be formed from metal carbonyl complexes through reaction with azides or hydrazines.[32,33] Metal isocyanate complexes may also be prepared directly by anion exchange.[34]

The formation of an inorganic isocyanate complex was first observed in 1965 in the reaction of tungsten hexacarbonyl with tetraethylammonium azide to produce $[N(C_2H_5)_4][W(CO)_5NCO]$.[35] This compound exhibited carbonyl IR stretching bands at 2067 (w), 1927 (st) and 1868 (m) cm^{-1} and pseudoasymmetric and symmetric NCO stretching bands at 2236 (m) and 1323 (m) cm^{-1}. The authors proposed a mechanism in which the azide undertook a nucleophilic attack on a CO ligand, followed by loss of nitrogen and rearrangement to form a stable isocyanate, in a similar fashion to the Curtius azide

[1] Note that the isocyanate (R-N=C=O) has different properties and behaviour to cyanate (R-O-C≡N) and fulminate (R-C≡N-O), which have different bond lengths, coordination modes and IR absorbances.

rearrangement (Figure 4.3). Later, it was found that not only can metal carbonyl compounds react with organic azides to form isocyanate complexes, but that inorganic azides can react with gaseous carbon monoxide to form the same.[36–38]

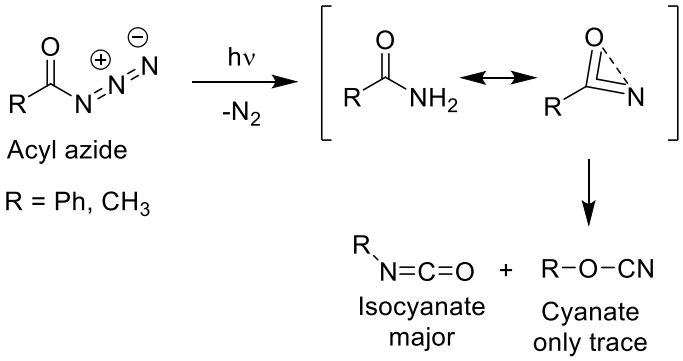

Figure 4.3. Mechanism for the photochemical Curtius rearrangement of an organic acyl azide via a singlet nitrene intermediate to form an isocyanate.[39]

A comprehensive review by Beck and Fehlhammer in 2009 on the reactions of metal carbonyl with the azide ion, and vice versa, showed that most metal carbonyl complexes react with azides to either form isocyanate, dinitrogen or metallacyclic complexes.[40,41] The reaction of metal-azide complexes with carbon monoxide can also produce isocyanate complexes through nitrene intermediates, and proceed through the same intermediate as the metal carbonyl reacting with azide, which is assumed to be a $C(O)N_3$ species coordinated through the carbon atom (Figure 4.4). Solvent was found to play an important role, with reactions carried out in chloroform having a faster reaction rate than those carried out in DCM or acetone. In a rare example of an isocyanate not forming, the UV photolysis of gold (I) azido complexes in the presence of metal carbonyl complexes caused the azide to undergo reductive elimination to form gold (0) – metal-carbonyl clusters.[42] In another unusual case, sterically bulky azides were reacted with $[W(CO)_5THF]$ to form imines or amines through nitrene intermediates. Unfortunately, the post-reaction tungsten complex was not characterised.[43]

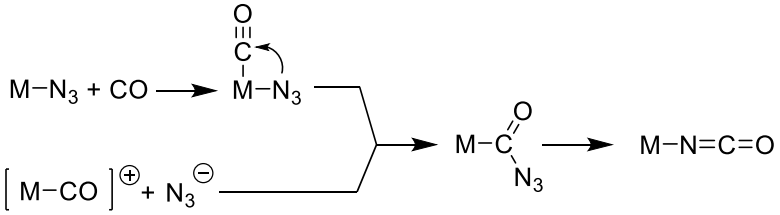

Figure 4.4. Reaction of a metal azide complex with carbon monoxide or vice versa to form a metal isocyanate complex *via* a M-C(O)N$_3$ intermediate.[40]

Transition metal complexes containing both carbonyl and azide ligands are rare in the literature.[44–46] The photochemistry of $[W(CO)_5N_3]^-$ was investigated extensively by Dahlgren and Zink and was shown to follow three pathways (Figure 4.5).[45] When the lithium, sodium and PPN (PPN = μ-nitrido-bis(triphenylphosphorus) cation) salts were photolyzed in a CO-saturated solvent, a mixture of $[W(CO)_5NCO]^-$ and $[W(CO)_6]^-$ were produced; however, when the cation was changed to $AsPh_4^+$, neither of those compounds were observed and a white precipitate with no absorbance in the carbonyl or azide regions of the IR spectrum was produced.

$$W(CO)_5N_3^- \xrightarrow{h\upsilon} [W(CO)_5N_3^-]^* \qquad (1)$$

$$[W(CO)_5N_3^-]^* \xrightarrow{-N_2} [W(CO)_5N^-]^* \xrightarrow{CO} W(CO)_5NCO^- \qquad (2)$$

$$[W(CO)_5N_3^-]^* \xrightarrow{AsPh_4^+} \rightarrow \text{Rapid thermal loss of CO x 5} \qquad (3)$$

$$[W(CO)_5N_3^-]^* \xrightarrow{-CO} [W(CO)_4N_3^-] \xrightarrow{L} W(CO)_4(L)(N_3)^- \qquad (4)$$

Figure 4.5. The photochemical reactions of $[W(CO)_5N_3]^-$ in the presence of different cations and ligands, initially forming an excited state **(1)**, then forming either an isocyanate complex **(2)**, a thermal loss product containing no carbonyl, azide or isocyanate ligands **(3)** or undergoing ligand exchange from the photoactivated loss of CO and coordination of an available ligand **(4)**.[45]

Focussing on the reactions forming isocyanate, it was suggested that isocyanate formation is intermolecular and proceeds through a nitrene intermediate. This process was investigated with the photolysis of $[PPN][W(CO)_5N_3]$ (at 436 nm in a 10^{-2} M PPh_3 solution in chloroform at -6 °C with no added CO) which formed *cis*-$[W(CO)_4(PPh_3)(N{=}PPh_3)]^-$ instead of an isocyanate product. This result was attributed to the bulky ligands preventing the formation of a di-molecular adduct needed to generate NCO.

The results of the study into the photochemistry $[W(CO)_5N_3]^-$ complexes may be summarised as follows. On photolysis an excited state is formed from an $^1A_1 \rightarrow {}^1E$ transition, which is primarily ligand field in character, but contains a large component of ligand to metal charge transfer (Figure 4.6).

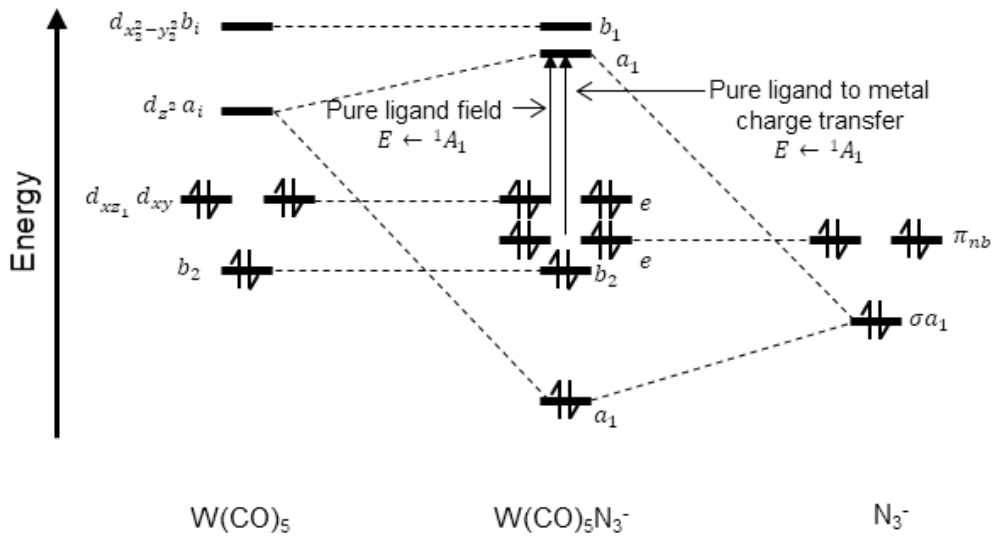

Figure 4.6. One electron molecular orbital diagram for $W(CO)_5N_3$.[45]

The excited state can then react in one of three ways

1. Loss of dinitrogen forming a nitrene, which can then react with available carbon monoxide in solution to form an isocyanate. The nitrene is formed from a state with significant ligand to metal charge transfer character and requires more energy than a pure ligand field transition. The nitrene is then stabilised by backbonding to the metal (Figure 4.5, Equation 2).

2. Reaction with another species ($AsPh_4^+$) by an unknown mechanism, which undergoes further thermal loss steps to produce a final product with no coordinated carbonyl, azide or isocyanate ligands (Figure 4.5, Equation 3).

3. Ligand exchange resulting from the dissociation of a carbonyl ligand to form a coordinatively unsaturated 16 e^- intermediate, then coordination of available ligands to form a more stable 18 e^- species (Figure 4.5, Equation 4). The loss of CO results from the increased σ-antibonding character of the excited state. Although isotopic labelling studies were completed, the relative rates of cis- and trans-CO photodissociation could not be determined due to the rapid rearrangement of the coordinatively unsaturated intermediate (Figure 4.7).

Notably, no azide photolabilisation was observed and the isocyanate formation was stated to be due to intermolecular reactions.

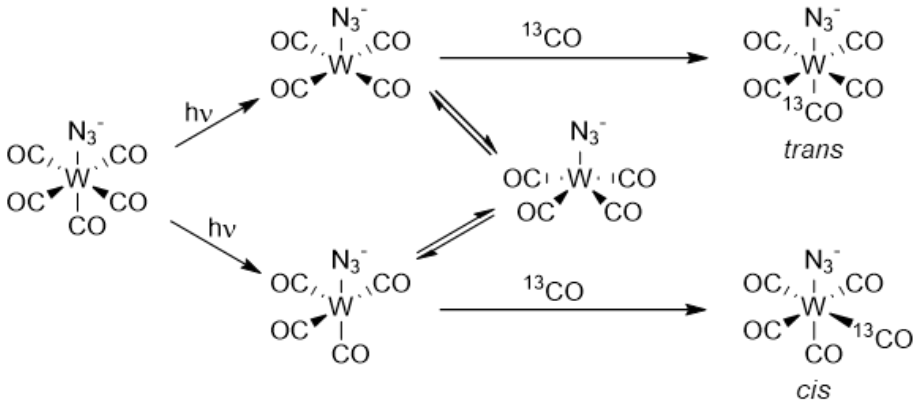

Figure 4.7. Reaction pathway observed from the photolysis of $[W(CO)_5N_3]^-$ in the presence of isotopically labelled ^{13}CO, resulting in the formation of both *cis*- and *trans*-products due to rapid isomerisation via a 5-coordinate intermediate.[45]

Moving to the group 7 metals, the isocyanate forming reaction of *fac*-$[Mn(CO)_3(dppe)(OH_2)]$ (dppe = $Ph_2PCH_2CH_2PPh_2$) was followed by isotopic labelling studies. The axial aqua ligand was quantitatively replaced with the labelled ^{13}CO to give the tetracarbonyl complex (Figure 4.8, complex 1), which was then reacted further with sodium azide to give the isocyanate. Mass spectrometry and IR spectroscopy showed that the isotope label was present in 50% of the isocyanate ligands, with the isocyanate formed at the other axial site in the remainder of cases (Figure 4.8, complexes 2 and 3), while the equatorial carbonyl ligands were not affected.[47]

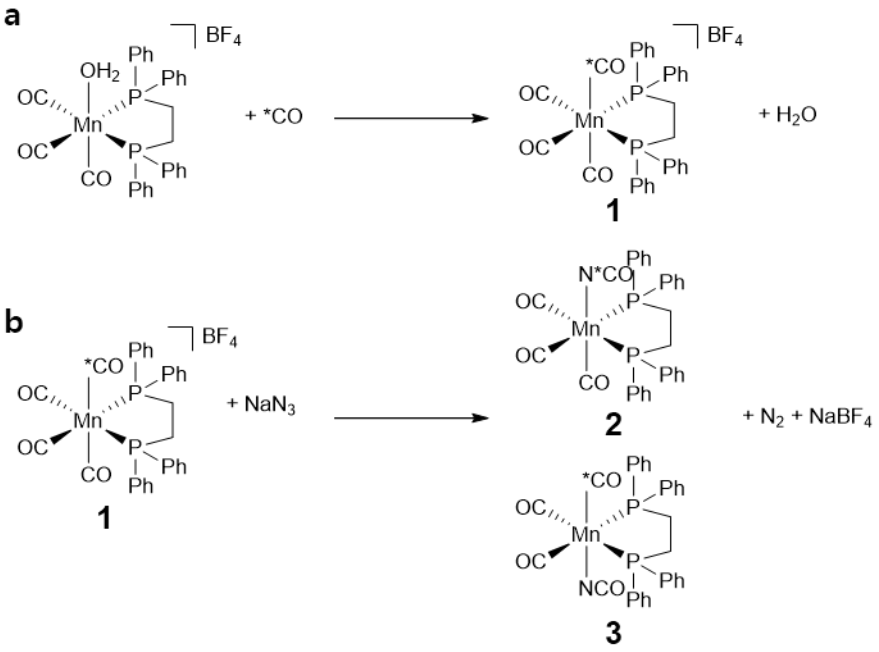

Figure 4.8. Isotopic labelling studies of *fac*-$[Mn(CO)_3(dppe)(OH_2)]$ (dppe = $Ph_2PCH_2CH_2PPh_2$). **a)** Reaction of *fac*-$[Mn(CO)_3(dppe)(OH_2)]$ with ^{13}CO to give the tetracarbonyl complex **(1)** with the isotope label at the axial position. **b)** Reaction of **(1)** with sodium azide to give the isocyanate, from attack at the labelled axial position **(2)** or the position trans to the label **(3)**, resulting in 50:50 ratio of both products.[47]

In general, metal carbonyl complexes have been demonstrated to react with azides and vice versa, producing isocyanates, dinitrogen or metalacyclic products. While investigations into the reactions of metal azidocarbonyl complexes are rare, they have been shown to have intriguing photochemistry, which is highly dependent on not only the primary coordination sphere of the metal, but the non-coordinating cation, solvent, presence of other ligands and wavelength of the incident light. As such, the investigation of such complexes in MOFs, where the constrained pore environment may be tuned, may allow for the study of short lived or unusually coordinated species. As the photochemistry of Mn(I) carbonyl species in MnMOF was explored earlier in this thesis, it is a logical extension to study Mn(I) azidocarbonyl complexes in MnMOF.

4.1.3 Reactions of manganese (I) azidocarbonyl complexes

Manganese is non-toxic, earth abundant and has a wide range of available oxidation states, from -3 to +7. It is of great interest as a catalyst, to replace precious metals or to access new reactivities, but has been underexplored until the last two decades.[48]

No photochemical reactions of manganese (I) azidocarbonyl complexes were found in the literature; however, reactions between Mn(I) azidocarbonyl complexes and other reactants have been explored. One such complex, *fac*-$[Mn(CO)_3(depe)N_3]$ (depe = 1,2-bis(diethylphosphino)ethane) was shown to react with alkynes to produce coordinated triazolate or tetrazolate complexes, which can undergo hydrolysis with aqueous HCl to liberate the heterocyclic ligand and produce a chlorido coordinated species.[34,49] Notably, no isocyanate was observed to be produced from the azide/carbonyl species. A Mn(I) azidocarbonyl complex was made from the reaction of $Mn(CO)_5Br$ with NaN_3 at 20 °C in ethanol/water to give the diamagnetic anion $[Mn_2(CO)_6(N_3)_3]^{3-}$ with bridging azide groups, while reactions at higher temperatures in THF resulted in the formation of dimeric isocyanate products containing mixtures of both azide and isocyanate ligands.[50] The pure azidocarbonyl dinuclear complex was not reacted further.

The use of a bimetallic $[Ru(bpy)_2(bpm)Mn(I)(CO)_3Br](PF_6)_2$, (bpy = 2,2′-bipyridine and bpm = 2,2′-bipyrimidine) complex has been shown to undergo light-induced

electron transfer to catalyse the click reaction between organic azides and alkynes to form 1,2,3-triazoles.[51] This proved to be efficient and more environmentally benign than some previous methods, but the mechanism was not well explored, although it can be assumed to involve a coordinated azide intermediate.

Huxley *et al* used a similar approach to perform a site selective click reaction between a Mn(I) azido complex and a dialkyne by tethering the metal complex in a porous MOF (Figure 4.9).[52] The authors performed an anion exchange on MnMOF[$Mn(CO)_3OH_2$]Br (described in Chapter 2) to produce the azidocarbonyl species, MnMOF[$Mn(CO)_3N_3$]. Unlike some of the previous examples discussed in Section 4.1.2 no isocyanate was detected and the azidocarbonyl complex could be characterised by SCXRD. This species was then reacted with a series of dialkynes with varying chain lengths. This study showed how isolation of a metal complex in a MOF can allow for the isolation and characterisation of reaction intermediates, as well as providing access to selectivities and binding modes unable to be reached with homogeneous analogues, much in the same way as an enzyme binding site.

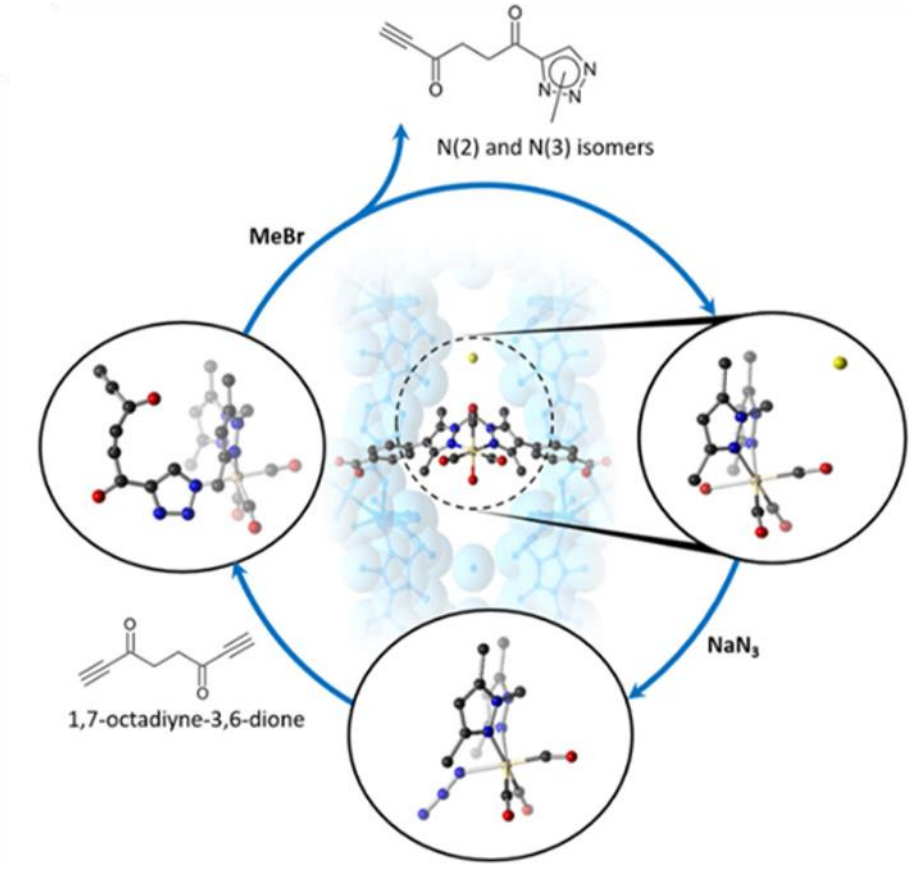

Figure 4.9. Site selective formation of a 1,2,3-triazole from the reaction of a dialkyne and a Mn(I) azidocarbonyl complex tethered to MnMOF. Anion exchange with sodium azide produced the azidocarbonyl complex, which then reacted with the dialkyne to give a coordinated 1,2,3-triazole complex which was liberated by treatment with methyl bromide to regenerate the original species.[52]

As noted in Chapter 1, MOFs have shown to be effective platforms for accessing new reactivities and studying reaction processes.[4] The reactions of azides and metal carbonyl complexes have been extensively explored in homogeneous complexes, but there is a paucity of studies conducted for heterogeneous equivalents, for example within the pores of a MOF. The study by Huxley *et al* showed that exposing MnMOF[$Mn(CO)_3OH_2$]Br to sodium azide resulted in the formation of an azidocarbonyl complex through ligand exchange, with no evidence for a potential isocyanate.[52] However, the photochemistry of this complex and the effects of site isolation within the crystalline framework have not been explored. As discussed in Section 4.1.2, several photochemical mechanisms proposed rely on intermolecular reactions between the metal complexes, which would not be possible when tethered to a MOF scaffold. Thus, a study of the photoreactivity of site-isolated azidocarbonyl manganese complexes may allow for future insights into the mechanisms of manganese-catalysed reactions.[53]

4.1.4 Palladium as a catalyst

While exploring new reactivities of earth-abundant metals is one strategy for improving catalyst usage, enhancing the reactivity of currently used catalysts is another. Palladium catalysts are used in a vast array of reactions, including carbon-carbon bond formations (Heck, Stille, Suzuki, Sonogashira, Tsuji-Trost and Negishi reactions), carbon-heteroatom reactions, and hydrogenations, and have been crucial in opening up the field of C-H activation, a powerful tool for increasing the complexity of organic molecules.[54–56] This is due to the palladium's propensity for forming square planar complexes, with vacant axial coordination sites, and a relatively low activation barrier between oxidation states. The palladium-catalysed coupling reaction between an organometal, RM, and an organohalide, R'X, to give RR' and MX, proceeds through an oxidative addition to reductive elimination catalytic cycle.[57] These have been suggested to involve Pd(0)→Pd(II) or Pd(II)→Pd(IV) complexes, the study of which has been of interest over the last 35 years (Figure 4.10).[57–59] Oxidative organic transformations involving dioxygen as a green and inexpensive oxidant also utilise palladium catalysts in $Pd^{0/II}$ or $Pd^{II/IV}$ oxidation states. Despite their importance, the mechanisms and catalytic cycles behind many palladium catalysed reactions are still unknown.[60,61] Unlike platinum(IV), palladium(IV) complexes stable enough to be characterised are rare. Due

to not having a convenient IR handle and being highly reactive, the number of structurally characterised Pd(IV) complexes in the literature are extremely few.[59]

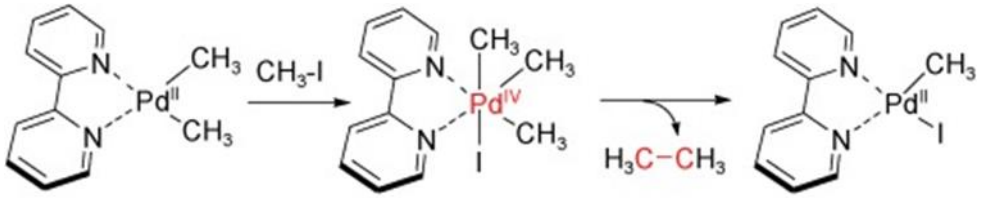

Figure 4.10. Reductive elimination step of a palladium catalysed coupling reaction proceeding through a Pd(IV) intermediate[62]

The first Pd(IV) complex to be structurally characterised by SCXRD was *fac*-[$PdMe_3$(bpy)I] (bpy = 2,2′-bipyridyl), reported by Byers *et al.*[59] This complex was formed by the oxidative addition of iodomethane to [$PdMe_2$(bpy)] at ambient temperature in acetone. X-ray quality crystals were then produced by slow evaporation of the solvent (Figure 4.11). ^{1}H NMR spectroscopy experiments at 10 °C in d_6-acetone showed the Pd(IV) complex was stable for several hours before reductive elimination, producing ethane took place, while at 25 °C the reaction time was shortened to 30-40 min. This reaction also occurred in the solid-state, with reductive elimination occurring at 100-110°C; however, the complex was stable in the solid-state for several days when stored at -20°C. The authors later reported that this reaction takes places through an S_N2 mechanism, in which [Pd(II)Me_2(bpy)] acts as a nucleophile and utilises a cationic intermediate, [Pd(IV)Me_3(bpy)(d_6-acetone)]$^+$ which was detected by ^{1}H NMR spectroscopy at -50°C.[58]

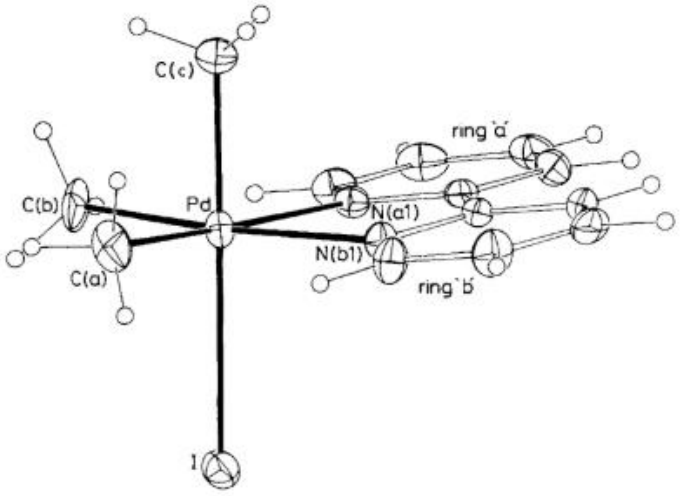

Figure 4.11. SCXRD structure of *fac*-[$PdMe_3$(bpy)I] with all non-hydrogen atoms represented as ellipsoids at 20% probability.[59]

Following these initial studies, a small number of Pd(IV) species have been synthesised with a range of strong oxidants and identified spectroscopically or crystallographically.[63–67] It has, therefore, been suggested that the role of Pd(II)/Pd(IV) species in palladium catalysis is complementary to the Pd(0)/Pd(II) catalytic cycle, allowing for reactions to proceed in the presence of air or water and in influencing selectivity and functional group tolerances.[62,63] As such, the site isolation of palladium catalysed in porous materials may facilitate one catalytic cycle to be favoured over the other, hence allowing for selectivities and mechanisms which are not accessible in solution.

4.1.5 Palladium catalysts in porous materials

Palladium catalysts have been incorporated into MOF scaffolds on many occasions, in most cases as palladium nanoparticles or molecular Pd catalysts loaded into the pores.[68–71] A few cases were also reported which utilised a structural palladium-containing node of a MOF as a catalyst.[72,73] Despite the large number of studies on Pd-containing MOFs, there have been relatively few studies where the palladium is structurally characterised, and fewer still where it is site-isolated and bound to the MOF backbone.

One such case of structural characterisation by Fortea-Pérez *et al* reported well-defined mixed-valence (0/+1) Pd_4 clusters grown in the pores of a Ni-based MOF, as well as mononuclear and di-nuclear Pd complexes formed by varying the pore contents of the host MOF.[74] These Pd_4 clusters were shown to be efficient catalysts for carbene transfer reactions; however, no structural characterisation of reaction intermediates was reported.

Ikemoto *et al* utilised a 'crystalline flask', a Zn-MOF that can be loaded with molecular guests which are then resolvable by SCXRD, to study the mechanism of a palladium-mediated bromination.[75] The guests form infinite stacks in the MOF pores stabilised by π-π interactions but are not bound to the framework itself. Before this study, two reaction intermediates were proposed, either a square planar Pd(II) intermediate or an octahedral Pd(IV) species. Using a time-resolved crystallographic snapshot approach, a square planar intermediate was observed (Figure 4.12). Despite

this success it was noted by the authors that this finding may not extend to the mechanism followed in the solution-state due to the crystalline state preventing the formation of dimers and the possibility that the lifetime of Pd(IV) intermediate may be shorter than the timeframe of a diffraction experiment. Similar experiments with a MOF-bound palladium complex, in a pseudo-solvated pore environment such as that encountered in MnMOF may allow for additional mechanisms and reaction intermediates to be studied.

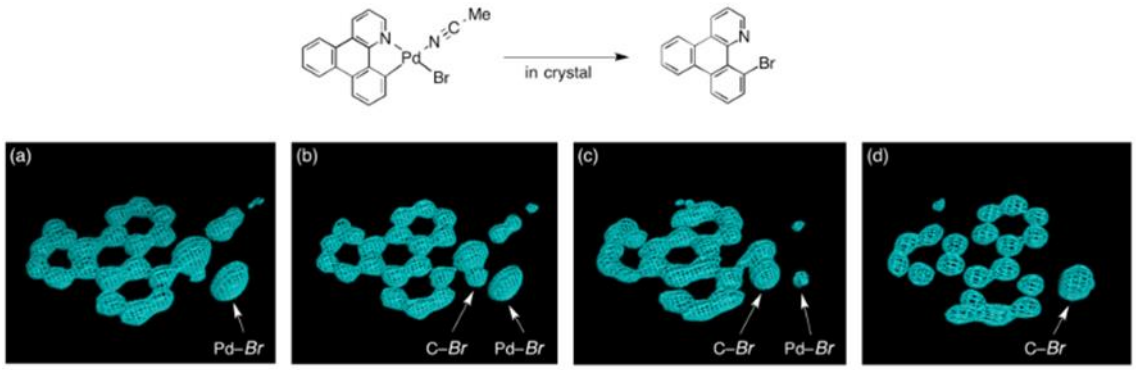

Figure 4.12. Palladium mediated bromination observed by SCXRD snapshots in a MOF 'crystalline flask', exhibiting the formation of a square planar Pd(II) reaction-intermediate. (a-c) Electron density maps (F_0) obtained at 2, 6 and 15 hrs time points and d) the final state.[75]

A molecular Pd(II)(H_2bpydc)Cl_2 (H_2bpydc = 2,2′-bipyridine-5,5′-dicarboxylic acid) complex was immobilised in the MOF UiO-67 ($Zr_6O_4(OH)_4(bpdc)_6$, bpdc = *para*-biphenyldicarboxylate) by a pre-metalation strategy.[76] Thus, the methyl ester of bpydc (Me_2-bpydc) was reacted with [$PdCl_2(CH_3CN)_2$] and then deprotected to form the pre-metalated $PdCl_2$-bound ligand. This was then reacted with zirconium tetrachloride and a large quantity of blank linkers (bpdc) in a 9:1 ratio (bpdc:$PdCl_2$bpydc). This produced the MOF UiO-67 with a 4 mol% loading of palladium, allowing for the reactive metal centres to be separated and dispersed throughout the framework, but preventing structural characterisation of the Pd sites by SCXRD (Figure 4.13). As such, the utility of such an approach is proven, but the mechanism and chemical behaviour of the MOF supported palladium catalyst, in comparison to its molecular analogue, remains elusive.

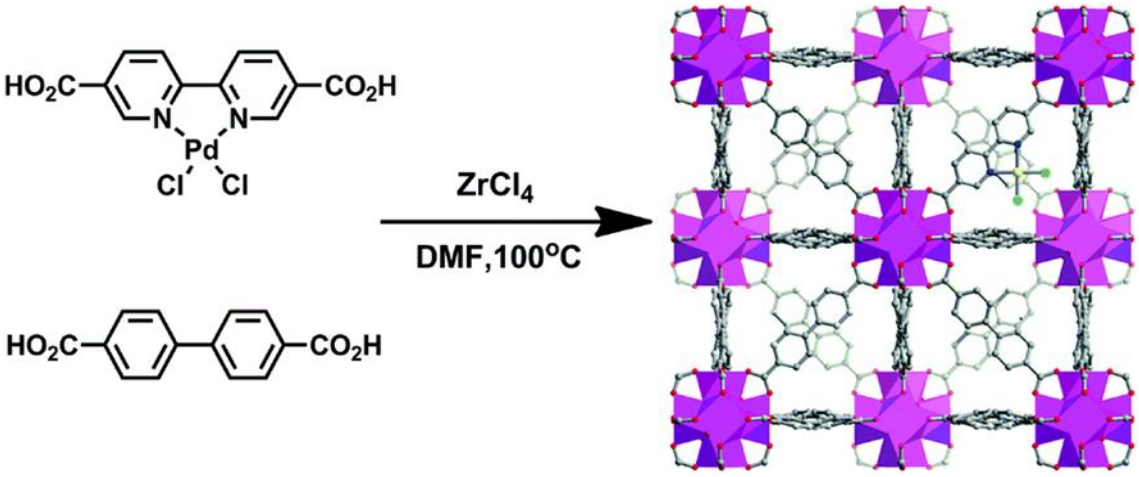

Figure 4.13. Schematic representation of the synthesis of UiO-67[$PdCl_2$] from a mixed ligand, pre-metalation approach. The resulting MOF contains Pd in a 4 mol% loading. (Zr, purple; C, grey; O, red; N, blue; Pd, light yellow; Cl, green)[76]

These examples show that making palladium-catalysed reactions more sustainable has been of great interest due to the rarity and expense of the metal itself, and due to the toxicity of many of the reagents and solvents currently used for palladium-catalysed reactions.[56,77] Site-isolating palladium catalysts in MOFs may allow for some of these challenges to be addressed, by reducing aggregation and deactivation, allowing for recovery and subsequent use of the catalyst and improving selectivity due to a constrained reaction environment in the MOF pore. Despite extensive reports of palladium containing MOFs showing excellent catalytic activities, there has been a notable lack of studies involving site-isolated and crystallographically characterised palladium complexes in MOFs which would allow for reaction mechanisms and intermediates to be identified.

4.2 Aims

Transition metal catalysed reactions are vital to the synthesis of bulk and fine chemicals.[5] The reliance of many of these reactions on precious metals, and a drive to make chemical synthesis more environmentally benign, has resulted in a need to explore new catalysts made from earth abundant materials or to improve the effectiveness of precious metal catalysts. The study of inorganic azides and nitrenes may raise opportunities to access new reactivities and allow for important insights into the mechanisms of transition metal catalysed nitrene transfer reactions.[8,16] One such class of compounds are transition metals coordinated to both carbonyl and azide ligands. While there have been few investigations into the reactivity of these complexes, they have shown interesting photochemical properties.[45] These properties are dependent on not only the primary coordination sphere, but environmental conditions as well. As such, the site isolation of these complexes in MOFs, where the chemical and physical environment can be highly controlled, may allow for the study of these complexes.

The photochemistry of *fac*-tricarbonyl Mn(I) bromide complexes isolated in MnMOF was explored in Chapters 2 and 3, and previous studies have shown that an azidocarbonyl Mn(I) complex can be formed in the same MOF,[52] although the photochemistry of this complex was not reported. As such, this study aims to investigate the photochemistry of this azidocarbonyl Mn(I) complex in MnMOF.

The incorporation of palladium catalysts in MOFs has been shown to improve their performance and access selectivities not available in solution.[68,74,75] The lack of studies into structurally characterised palladium complexes site-isolated in MOFs; however, means that the ability to post-synthetically metalated MnMOF with palladium would be advantageous. Therefore, a secondary aim of this research was to synthesise and characterise site-isolated palladium complexes in MnMOF to enable future explorations of palladium catalysed reactions in MOFs.

Results and Discussion

4.3 Photochemistry of Mn(I) azidocarbonyl complexes

4.3.1 Synthesis and characterisation of [Mn(bdpm)(CO)$_3$N$_3$]

To provide a comparison and to facilitate studies of the photo-reactivity of MnMOF[Mn(CO)$_3$N$_3$], the molecular analogue [Mn(bdpm)(CO)$_3$N$_3$] (bdpm = bis(3,5-dimethyl-1H-pyrazol-1-yl)methane) was synthesised. As reported in Section 2.3.1, the complex [Mn(bdpm)(CO)$_3$Br] was made, before undergoing anion exchange with silver triflate in DCM and then sodium azide in water to exchange the bromide anion for trilfate and then azide (Figure 4.14a).[52] Unfortunately, [Mn(bdpm)(CO)$_3$N$_3$] underwent rapid decomposition when dissolved and exposed to light, and thus an NMR spectrum was unable to be obtained of this complex; however, IR analysis showed anion exchange was successful with the presence of an azide band at 2058 cm^{-1} and shifting of the carbonyl bands (Figure 4.14b, Table 4.1).

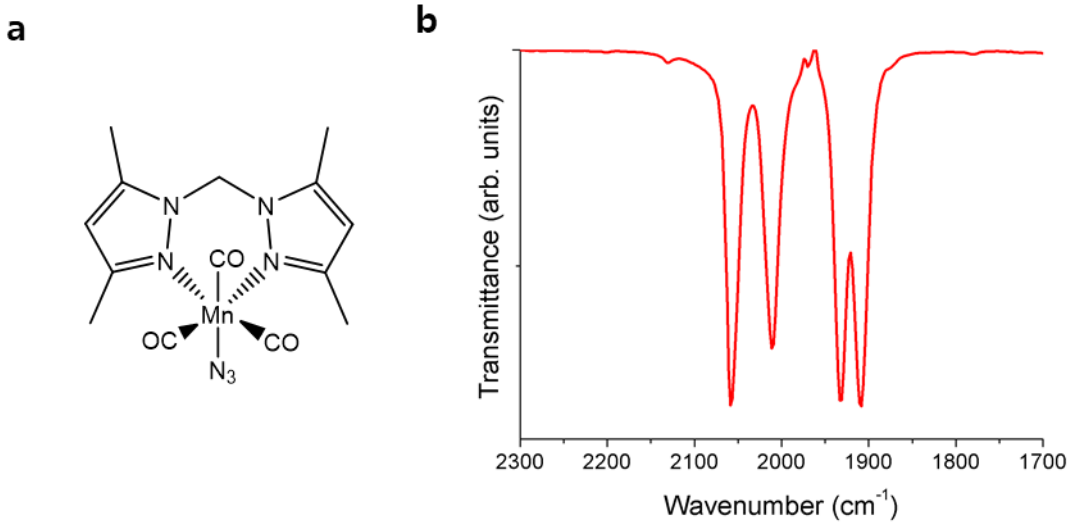

Figure 4.14. Model complex [Mn(bdpm)(CO)$_3$N$_3$], **a)** structure and **b)** IR spectrum dissolved in THF.

Table 4.1. IR peaks and assignments for [Mn(bdpm)(CO)$_3$X] (X = N$_3$ or Br) complexes dissolved in THF

Compound	**CO (A') (cm^{-1})**	**CO (A'') (cm^{-1})**	**CO (A') (cm^{-1})**	**N$_3$ (A') (cm^{-1})**
[Mn(bdpm)(CO)$_3$N$_3$]	1908	1933	2011	2058
[Mn(bdpm)(CO)$_3$Br]	1913	1939	2030	

A single crystal structure of this complex was also obtained, showing the azide ligand bound with an Mn-N_3 bond length of 2.064(2) Å (Figure 4.15, Structure **4.1**). The asymmetric unit contains half the complex, with a mirror plane cutting through the methylene bridge, manganese (I) and axial ligands. The complex co-crystallised with one chloroform molecule per molecule of manganese (I) complex. Like the bromide complex, the azide anion binds to the axial coordination site adjacent to the methylene bridge, which is opposite to where the azide coordinates in the MOF supported complex (Section 4.3.2). Consistent with the literature, the N1-N2-N3 bond angle is 176.8°, with the N1-N2 bond length slightly longer than the N2-N3 bond length (Figure 4.15c). This is caused, as mentioned previously, by the hyperconjugation of the azide causing electron density to be moved from the filled σ (Mn-N1) orbital to the empty antibonding π* (N2-N3) orbital.[8] The azide coordinates to the Mn(I) at an angle (Mn-N1-N2) of 126.5 °, again due to favourable orbital overlap for the σ orbital. The equatorial carbonyl ligands have similar bond lengths (1.805(2) Å) to the bromide analogue, as are the M-C(O) bond lengths. The bond angles around the Mn(I) centre; however, change, bringing the anion closer to the hydrogen atom on the methylene bridge (Br····H 2.259 Å in [$Mn(CO)_3Br$] and N····H 2.203 Å in [$Mn(CO)_3N_3$]) (Figure 4.15).

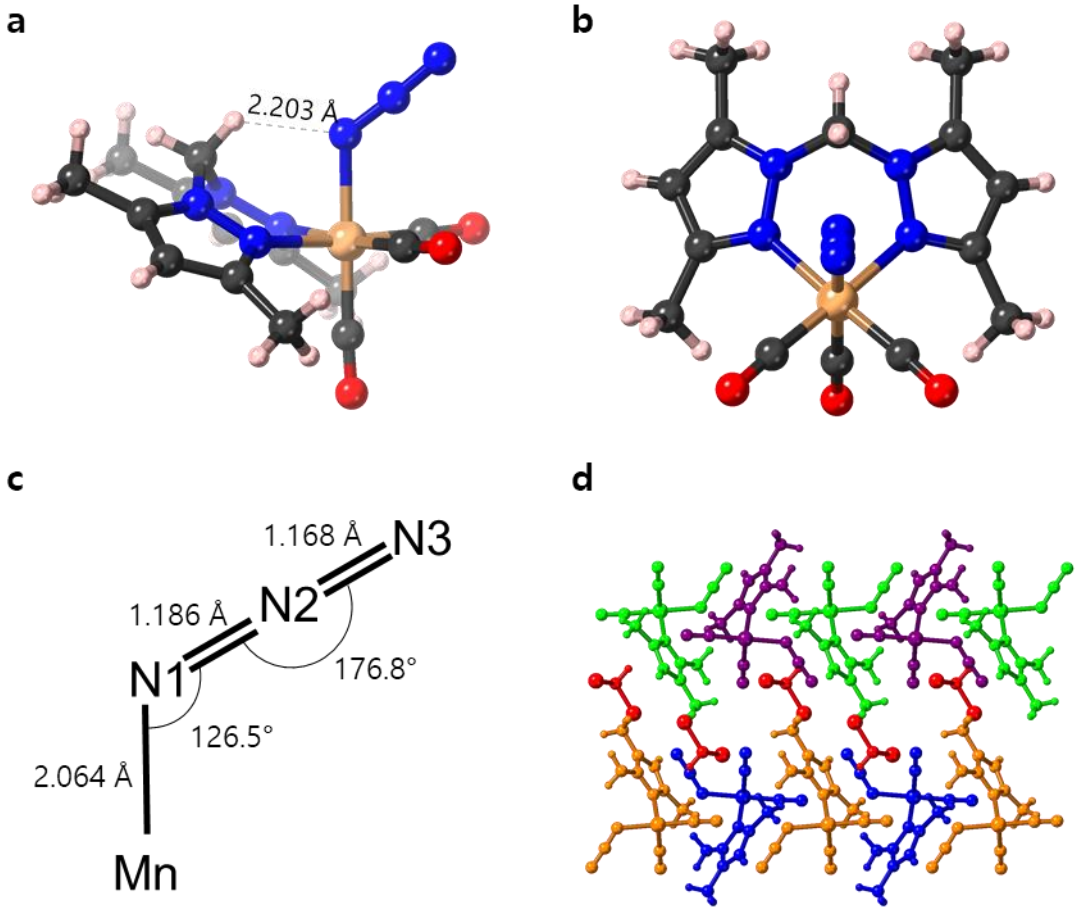

Figure 4.15. Single crystal structure of [Mn(bdpm)(CO)$_3$N$_3$] **a)** side view of complex showing N1-H (CH$_2$) distance of 2.203 Å, **b)** top view of complex, **c)** bond lengths and angles of coordinated azide and **d)** packing viewed down the y-axis showing model complex molecules in green, purple, orange and blue and chloroform molecules in red. (For a and b Mn, beige; N, blue; C, grey; O, red; H, pink).

4.3.2 Photolysis of the model complex [Mn(bdpm)(CO)$_3$N$_3$]

Like the [Mn(bdpm)(CO)$_3$Br] complex, the azido analogue does not show any reaction upon irradiation with visible or UV light in the solid-state. When dissolved in organic solvents (THF and DCM), and exposed to light, the complex very rapidly reacts and loses the CO and azide ligands, as detected by losses of these bands in the IR spectrum. In THF solution, this rapid reaction is accompanied by the formation of two bands at 2097 (broad) and 2130 (sharp) cm^{-1}. After only 30 seconds of irradiation with a UV torch (365 nm), complete loss of the carbonyl and azide bands was observed (Figure 4.16).

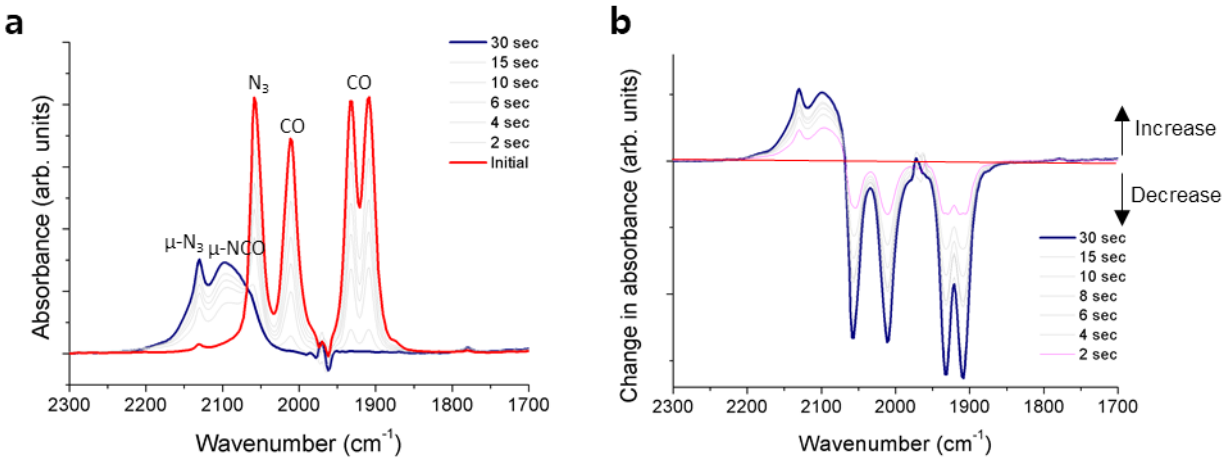

Figure 4.16. Photolysis of model complex, $[Mn(bdpm)(CO)_3N_3]$ dissolved in THF and irradiated with UV light (365 nm) **a)** carbonyl region of IR spectrum, **b)** change in absorbance from parent complex (μ = bridging species).

While the formation of a broad new band between 2100-2300 cm^{-1} is expected upon formation of an isocyanate, the presence of a second band is unexpected (Table 4.2). The peak at 2130 cm^{-1} is also visible in the pre-photolysis complex, albeit with very low intensity. Previous work by Mason *et al*, showed that the reaction of Mn(I) carbonyl compounds with sodium azide could produce mononuclear complexes and also dimers with bridging azides {$[Mn_2(CO)_4(N_3)_3]$, ν_{as} 2070(s) (N_3)} or a combination of bridging azide and isocyanate {$[Mn_2(CO)_4(N_3)_x(NCO)_{3-x}]$, ν_{as} 2079(s) (N_3), ν_{as} 2190(m) (NCO)}.[50] Comparing these dimeric complexes to the mononuclear products of those reactions, $[Mn(CO)_3(PPh_3)_2N_3]$ {ν_{as} 2058(w) (N_3)} and $[Mn(CO)_3(PPh_3)_2NCO]$ {ν_{as} 2238(s) (NCO)}, the NCO peak in the dimer appeared at a lower wavenumber and the azide at a higher wavenumber in comparison to where they were observed in the mononuclear species.

The peaks at 2130 (sharp) and 2095 (broad) cm^{-1} can therefore be assigned as bridging azide and bridging isocyanate species respectively. The presence of bridging azide in the pre-photolysis spectrum may be due to either the formation of a small quantity of dimeric species in solution or some degree of photolysis occurring before the first sample measurement was taken due to ambient light.

Kinetic analysis of the rate of change of the IR peaks shows that the new peaks at 2130 and 2095 cm^{-1} grow at the same rate, while two of the CO peaks (1931 and 1908 cm^{-1}) also decrease at the same rate (Figure 4.17). The rate of decrease of the 2058 cm^{-1} (N_3) and 2011 cm^{-1} (CO) peaks is slightly slower, due to overlap of the broad peak at 2095 cm^{-1}.

Table 4.2. IR peak assignments and changes upon UV photolysis for the model complex, $[Mn(bdpm)(CO)_3N_3]$, dissolved in THF

Peak (cm^{-1})	Change with photolysis	Species
2130	Increasing	N_3 (bridging)
2095	Increasing	NCO(bridging)
2058	Decreasing	N_3
2011	Decreasing	Tricarbonyl
1931	Decreasing	Tricarbonyl
1908	Decreasing	Tricarbonyl

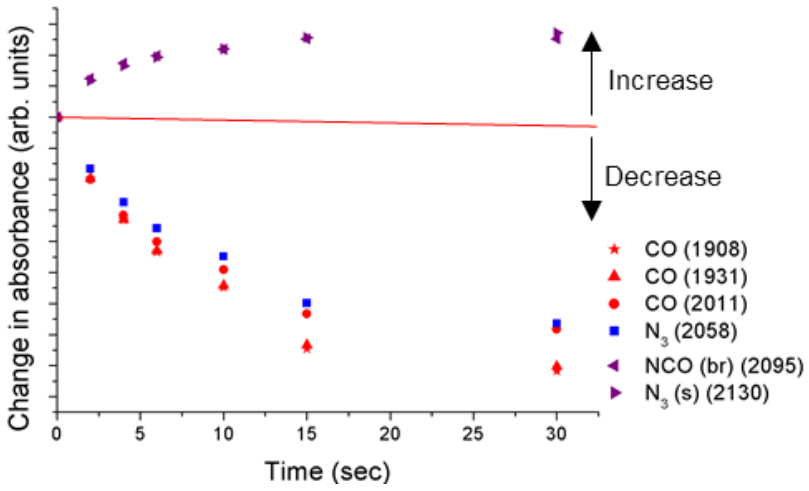

Figure 4.17. Kinetic analysis of the change in peak absorbance during photolysis of $[Mn(bdpm)(CO)_3N_3]$ dissolved in THF and irradiated with UV light.

Therefore, it may be surmised that following irradiation of a THF solution of $[Mn(bdpm)(CO)_3N_3]$ with UV light, the azide undergoes loss of N_2 to form a nitrene, which reacts with a CO ligand to form NCO which binds as a bridging ligand between two manganese complexes. This does not occur for all azide groups, some of which remain and also coordinate as bridging ligands. All remaining CO ligands are photo-ejected from the coordination sphere, leaving vacant binding sites, which are presumably replaced with solvent molecules. The structure of the product dimer(s) is unknown; however, it can be assumed to contain bridging azide and/or isocyanate ligands (binding mode unknown) and no coordinated carbonyl ligands.

The photolysis of the model complex was also performed for the species dissolved in dichloromethane and irradiated with both UV and visible light (Figure 4.18). The same peaks were observed for the reactions in DCM, with slight shifts to higher wavenumbers, but no indication of an alternative reaction mechanism or product (Table 4.3). Again, for both irradiation with UV and visible light, two new peaks were formed at 2136 and 2099 cm^{-1} representative of bridging azide and NCO respectively. As with the samples in THF, the pre-photolysis spectra displayed small peaks corresponding to bridging azide. In the case of the sample irradiated with UV light, a small bridging NCO peak was also evident in the pre-photolysis spectrum. This suggests that these peaks are because of some degree of photolysis occurring before the first spectra were collected, which is unsurprising considering how light sensitive these samples were, and the difficulty in eliminating all sources of ambient light when preparing the samples. Changing the irradiation source from a UV torch (365 nm) to a visible torch saw the time needed to see complete loss of the peaks from parent complex increase from 30 sec to 2 min.

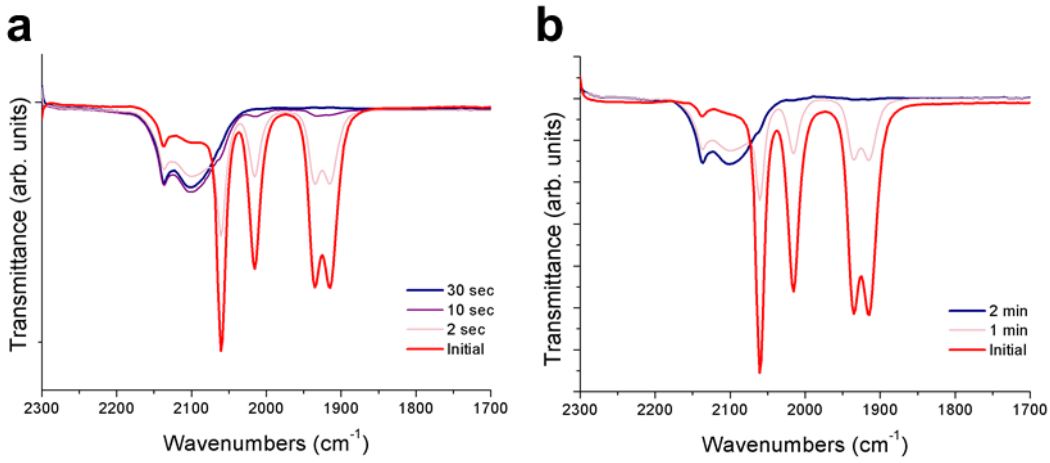

Figure 4.18. Photolysis of model complex, $[Mn(bdpm)(CO)_3N_3]$ dissolved in DCM and irradiated with **a)** UV light (365 nm) **b)** visible light.

Table 4.3. IR peak assignments and changes upon UV photolysis for the model complex [Mn(bdpm)$(CO)_3N_3$]

Dissolved in THF (cm^{-1})	Dissolved in DCM (cm^{-1})	Change with photolysis	Species
2130	2136	Increasing	NCO (bridging)
2095	2099	Increasing	N_3 (bridging)
2058	2060	Decreasing	N_3
2011	2015	Decreasing	Tricarbonyl
1931	1935	Decreasing	Tricarbonyl
1908	1915	Decreasing	Tricarbonyl

The photochemical reaction of the azidocarbonyl molecular complex was found to behave in a similar manner to a combination of the intermolecular reactions reported in the literature between Mn(I) carbonyl complexes and sodium azide and the carbonyl molecular complex reported in Chapter 2.3.2. For the few azidocarbonyl Mn(I) complexes reported in the literature no mention was made of their photochemical behaviour.[34,49,50] As [Mn(bdpm)$(CO)_3N_3$] reacts so quickly when dissolved and in the presence of light, it can be assumed that the previously reported complexes must not undergo the same photo-decarbonylation reactions. Therefore, the behaviour of the model complex is unlike that of any reported in the literature. This is most likely due to the bis-dimethylpyrazolylmethane ligand, which can undergo metal to ligand π-backbonding with Mn(I), lowering the electron density around the metal and labilising the *trans*-carbonyl bonds.

4.3.2 Synthesis and characterisation of MnMOF[$Mn(CO)_3N_3$]

In order to study the photochemical behaviour of *fac*-[$Mn(CO)_3N_3$] site-isolated in a porous support, MnMOF[$Mn(CO)_3$EtOH]Br was synthesised as described in Chapter 2 and washed with methanol before placed with an excess of sodium azide to prepare MnMOF[$Mn(CO)_3N_3$] (Figure 4.19a).[52] This produced a MOF-tethered complex with azide coordinated to Mn(I) at the axial position *anti* to the methylene bridge (the model complex has a *syn* arrangement), as shown by SCXRD (Figure 4.19b, Structure **4.2**). The carbonyl and azide ligands on this complex showed much higher displacement

parameters than the molecular analogue (Appendix 4.5.3) due to the greater freedom within the MOF pore. As such the errors in the bond lengths and angles are greater, but it is evident that there are some differences between the molecular and MOF analogues. The binding angle of the azide ligand is higher in the MOF (147.3(5)° compared to 126.5(2)°) and the N2-N3 bond length is longer (1.25(3) Å to 1.168(3)Å) (Figure 4.19c).

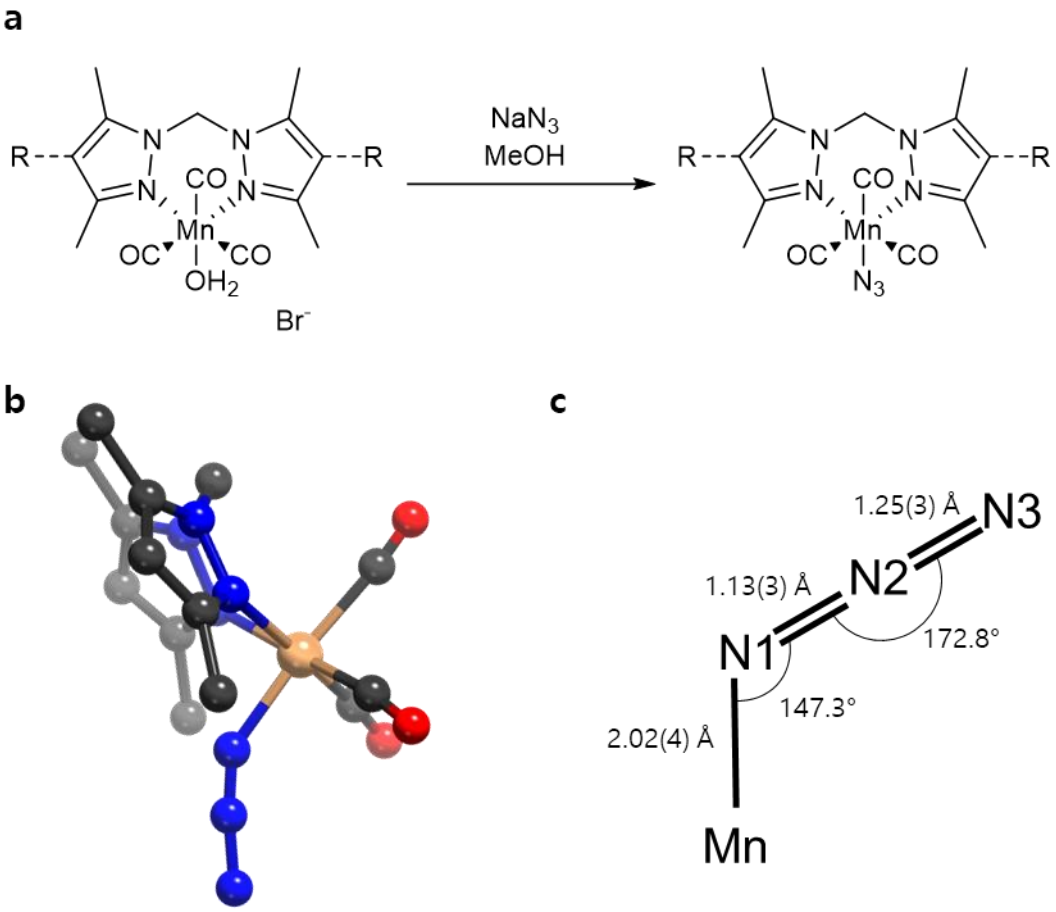

Figure 4.19. a) Anion exchange with sodium azide produces azidocarbonyl complex through a single crystal to single crystal transformation. **b)** Coordination environment of $[Mn(CO)_3N_3]$ coordinated to MnMOF, showing azide coordinated at the axial position *anti* to the methylene bridge, and **c)** bond lengths and angles of the coordinated azide.

A sample of MnMOF$[Mn(CO)_3N_3]$ was washed with dry THF and analysed by ATR-IR spectroscopy under ambient conditions before and after photolysis with UV light (Figure 4.20). The initial complex contains an azide band at 2058 cm^{-1} and three carbonyl bands (Table 4.4). The complex in the MOF (solvated) reacted much more slowly than the molecular model complex (in solution), which showed complete loss of carbonyl bands in 30 sec. In contrast, no change was observed for the CO and azide bands of

the MOF-tethered manganese centre until after 3 min of irradiation. The carbonyl peaks then decrease steadily, while the azide peak decreases, then recovers and broadens, developing shoulders at 2120 and 2084 cm^{-1}. The positions of these peaks are similar to those observed in the molecular species in Section 4.3.2; however, with the formation of dimers prevented by the site isolation of the complexes in the MOF, the peaks cannot be caused by bridging azide or NCO species. Therefore, mononuclear NCO bands are expected to be observed as broad peaks at higher wavenumbers. These type of NCO peaks were observed under matrix isolated conditions and will be discussed in Section 4.3.3, hence the peaks developed after photolysis in Figure 4.20a are assigned as azide species.

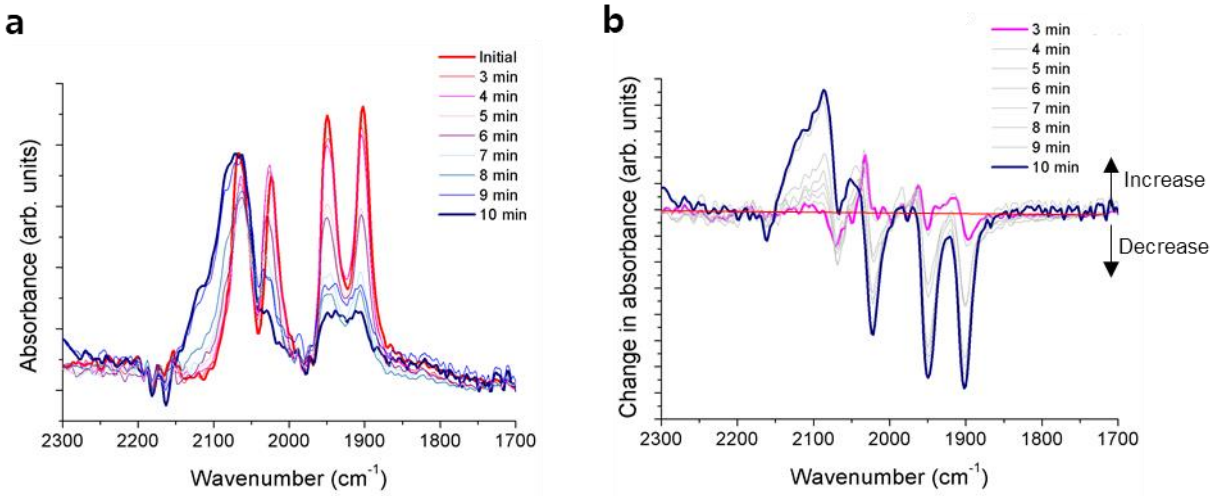

Figure 4.20. Photolysis of MnMOF[$Mn(CO)_3N_3$]·THF irradiated with UV light (365 nm) in ambient atmosphere **a)** carbonyl region of IR spectrum, **b)** change in absorbance from parent complex.

Table 4.4. IR peak assignments and shifts upon UV photolysis for MnMOF[$Mn(CO)_3N_3$]·THF

Peak (cm^{-1})	Change with photolysis	Species
2120	Increasing	N_3
2084	Increasing (shoulder)	N_3
2063	Decreased then recovered	N_3
2023	Decreasing	Tricarbonyl
1950	Decreasing	Tricarbonyl
1902	Decreasing	Tricarbonyl

The kinetics of this reaction are unlike those seen in the model complex or in the bromide analogue discussed in Chapter 2. There is a significant delay before changes appear in the IR spectra and the changes in the azide peaks are not constant over time (Figure 4.21). The loss of the CO peaks occurs as expected, with the decreases in the 2023 cm^{-1} peak being slower than the other due to overlap with the azide peak. The parent azide peak (2063 cm^{-1}) decreases slightly then recovers, while the shoulders to this band increase at a faster rate after 8 min of irradiation.

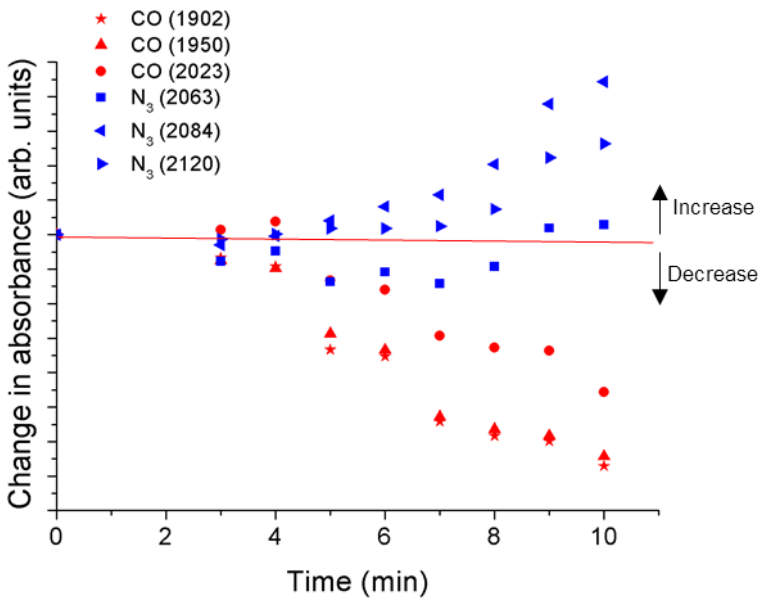

Figure 4.21. Kinetic analysis of the change in peak absorbance during photolysis of MnMOF[$Mn(CO)_3N_3$]·THF, irradiated with UV light.

A possible explanation for this could be due to the parent azide being ejected from the primary coordination sphere, then re-coordinating in either its original position or in one of the positions vacated by a carbonyl ligand. The increase in rate of peak growth after 8 min would then be due to more positions becoming available for coordination due to more complete photolysis of the CO ligands.

4.3.3 Matrix-isolated time-resolved IR studies of MnMOF[$Mn(CO)_3N_3$]·THF

Using the methods described in Chapter 2, photodecarbonylation studies were undertaken with this compound by *in situ* photocrystallography and matrix isolated time-resolved (TR) IR spectroscopy. Matrix isolated TR-IR studies were undertaken with the MOF incorporated into NaCl or KBr disks, placed under vacuum and irradiated at 150, 190 and 296K (room temperature). At 150K, the azide band for the parent complex had split into two equal bands at 2070 and 2060 cm^{-1} (Table 4.5). This is most likely caused by isomerism between the two axial positions. As the compound was photolyzed the three carbonyl bands decreased as expected. A broad dicarbonyl band at 1831 cm^{-1} developed, as well as the free CO gas band at 2130 cm^{-1}. The azide bands decreased in magnitude as well, with the higher wavenumber peak decreasing faster than the peak at 2060 cm^{-1}. The slight shoulder at 2092 cm^{-1} appeared and increased as the sample was irradiated (Figure 4.22).

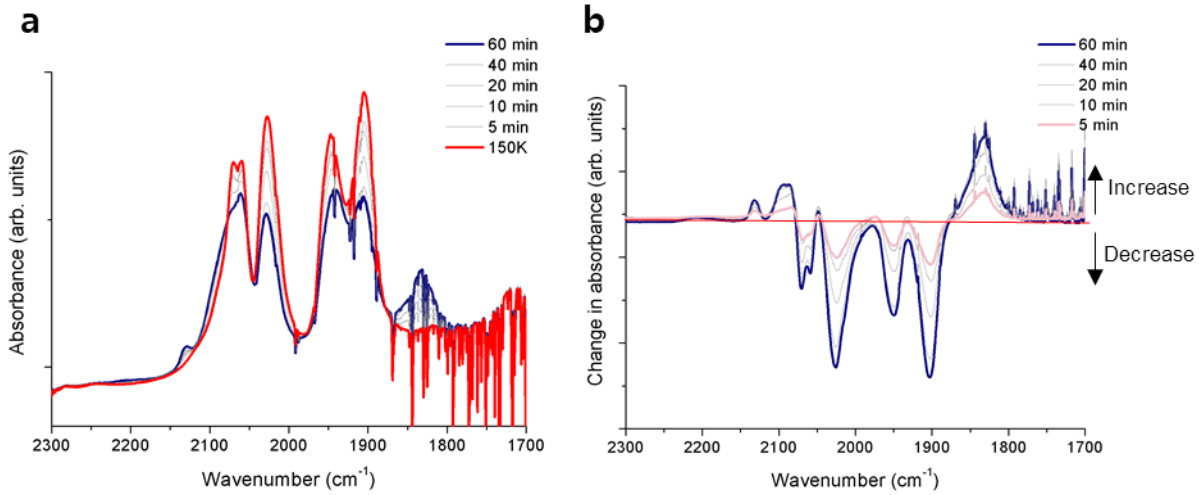

Figure 4.22. a) Carbonyl region of IR spectrum for photolysis in matrix isolated MnMOF[$Mn(CO)_3N_3$] sample dried from THF and incorporated into a KBr disk at 150 K. **b)** Difference spectra showing the change in absorbance from parent complex.

Table 4.5. IR peaks, changes during photolysis and assignments for MnMOF[$Mn(CO)_3N_3$]·THF in a KBr disk at 150K

Peak (cm^{-1})	Change with photolysis	Species
2130	Increasing	Free CO gas
2091	Increasing	Azide (shoulder)
2070	Decreasing	Azide
2060	Decreasing	Azide
2028	Decreasing	Tricarbonyl
1947	Decreasing	Tricarbonyl
1904	Decreasing	Tricarbonyl
1832	Increasing	Dicarbonyl

Kinetic analysis showed that the azide species causing the band at 2091 cm^{-1} is transient, as it reaches a steady state over the timescale of the experiment (Figure 4.23). The formation of the dicarbonyl band at 1832 cm^{-1} is very clear, and although the decrease of the tricarbonyl band at 2028 cm^{-1} is expected to be slower than the other CO bands, due to overlap with the azide, the decrease is less than that seen in the ATR-IR experiment. This is consistent with the presence of the second dicarbonyl band beneath it as observed for MnMOF[$Mn(CO)_3Br$]·THF and discussed in Chapter 2.

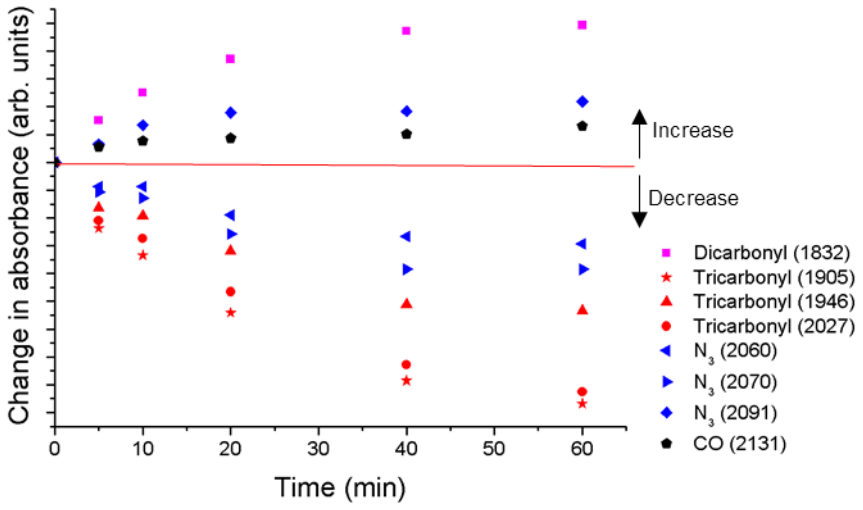

Figure 4.23. Kinetic analysis of the change in peak absorbance during photolysis of MnMOF[$Mn(CO)_3N_3$]·THF in a KBr disk, irradiated with UV light at 150K.

Increasing the temperature to 190 K saw the three carbonyl bands again observed alongside the most prominent azide band at 2070 cm^{-1} with a shoulder at 2063 cm^{-1} (Table 4.6). It can therefore be inferred that the azide isomer producing the peak at 2060 cm^{-1} is the less stable isomer which converts to the form with the band around 2070 cm^{-1} (the *anti*-arrangement) when more thermal energy is available. Photolysis of this sample showed minimal loss of the azide bands, with the band at 2070 cm^{-1} showing a steady decline and the bands at 2062 and 2090 (shoulder) cm^{-1} exhibiting slight increases. These changes are due to photo-induced isomerisations. The most remarkable feature of these measurements are the strength and clarity of the diacarbonyl bands, at 1829 and 1936 cm^{-1}, the latter of which was observed directly for the first time after the tricarbonyl peak at 1949 cm^{-1} decreased to a sufficient extent (Figure 4.24). The kinetics of this band were unable to be analysed due to overlap with the adjacent bands; however, could be clearly seen after only 15 min of irradiation (Figure 4.25). The peak produced by free CO gas trapped in the matrix is less prominent in these spectra compared to those collected at 150K due to the higher temperature allowing the gas to escape from the matrix more easily.

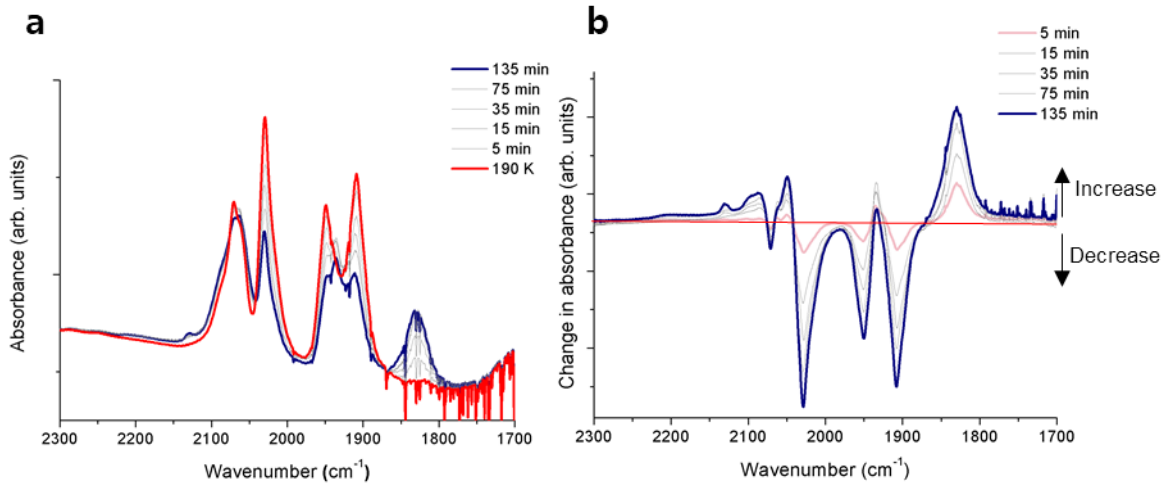

Figure 4.24. a) Time-resolved matrix-isolated IR spectra of MnMOF[$Mn(CO)_3N_3$]·THF in a NaCl disk at 190K with **b)** difference spectra showing changing peak intensities.

Table 4.6. IR peaks, changes during photolysis and assignments for MnMOF[$Mn(CO)_3N_3$]·THF in a NaCl disk at 190K

Peak (cm^{-1})	Change with photolysis	Species
2128	Increasing	Free CO gas
2090	Increasing	Azide (shoulder)
2070	Decreasing	Azide
2062	Increasing	Azide
2029	Decreasing	Tricarbonyl
1949	Decreasing	Tricarbonyl
1936	Increasing	Dicarbonyl
1908	Decreasing	Tricarbonyl
1829	Increasing	Dicarbonyl

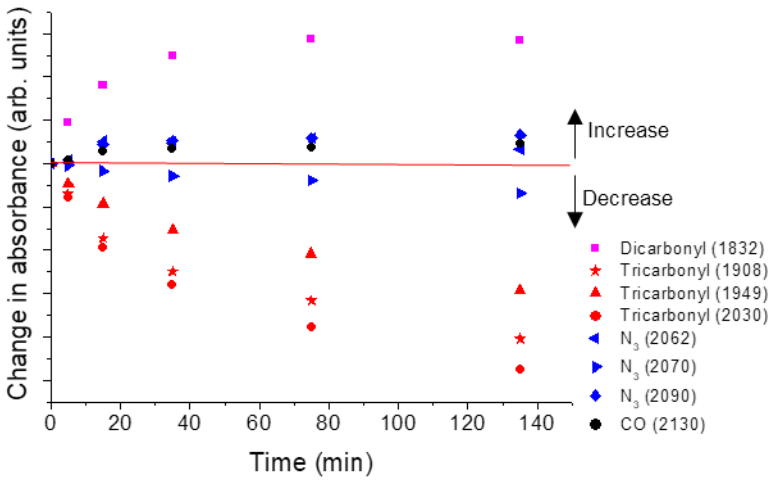

Figure 4.25. Kinetic analysis of the change in peak absorbance during photolysis of MnMOF[$Mn(CO)_3N_3$]·THF in a NaCl disk, irradiated with UV light at 190K.

At 296K the most prominent azide band appeared at 2059 cm^{-1} with a shoulder centred at 2085 cm^{-1} (Table 4.7). Upon irradiation these peaks decreased, along with the three carbonyl bands. No di- or mono-carbonyl bands were observed, but two broad NCO bands at 2187 cm^{-1} and 2205 cm^{-1} developed (Figure 4.26). These peaks are observed at higher wavenumbers than the bridging NCO seen in the model complex, and hence are assigned as mononuclear end-bound isocyanate ligands. The presence of two bands may be consistent with the formation of two structural isomers, or due to splitting of the peak due to two resonance forms. It has been previously reported that the deformation mode of the NCO resonance structures (N^{2-}-C≡O^{+} or N≡C-O^{-}) may be

split in the solid-state by 30-50 cm^{-1}.[78] The frequencies of these NCO bands are consistent with those reported for $[Mn(NCO)(CO)_3(PMe_2Ph)_2]$ (2218(s) cm^{-1})[79] and $[Mn(CO)_3(PPh_3)_2NCO]$ (2238 cm^{-1})[50], with the reported complexes appearing at slightly higher wavenumbers due to the presence of phosphine ligands.

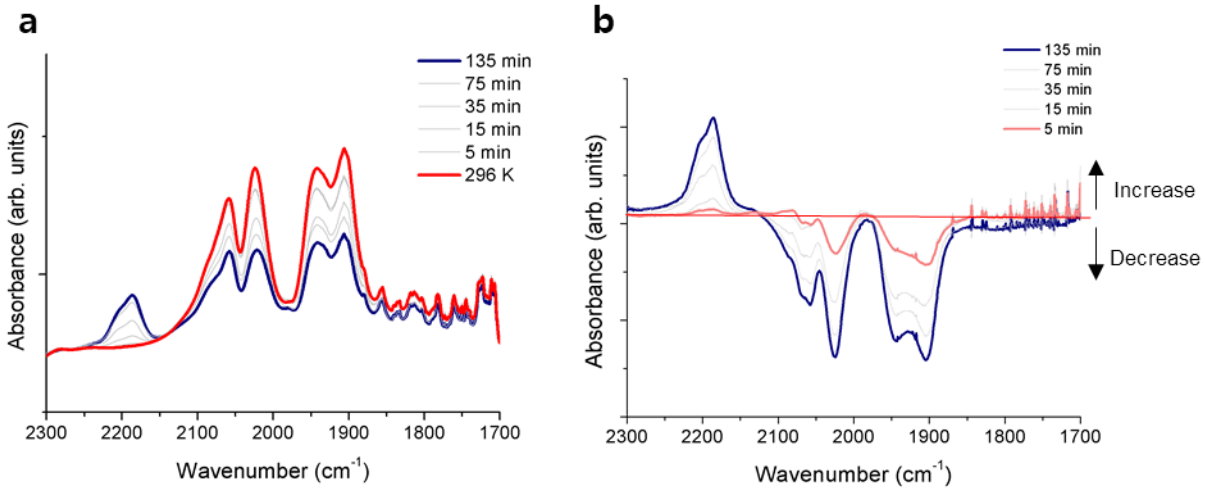

Figure 4.26. a) Time-resolved matrix-isolated IR spectra of $MnMOF[Mn(CO)_3N_3]$·THF in a KBr disk at 296 K (room temperature) with **b)** difference spectra showing changing peak intensities.

Table 4.7. IR peaks, changes during photolysis and assignments for $MnMOF[Mn(CO)_3N_3]$·THF in a KBr disk at 296K.

Peak (cm^{-1})	Change with photolysis	Species
2205	Increasing	NCO (shoulder)
2187	Increasing	NCO
2085	Decreasing	Azide (shoulder)
2059	Decreasing	Azide
2023	Decreasing	Tricarbonyl
1943	Decreasing	Tricarbonyl
1907	Decreasing	Tricarbonyl

The NCO peak at 2187 cm^{-1} grew at a faster rate than the peak at 2210 cm^{-1}, which could be due to one isomer or resonance form being more stable than the other (Figure 4.27). The azide band at 2059 cm^{-1} also decreased at a faster rate than the other azide peak, making it more likely that this isomer was in a more favourable position to react with CO and form NCO.

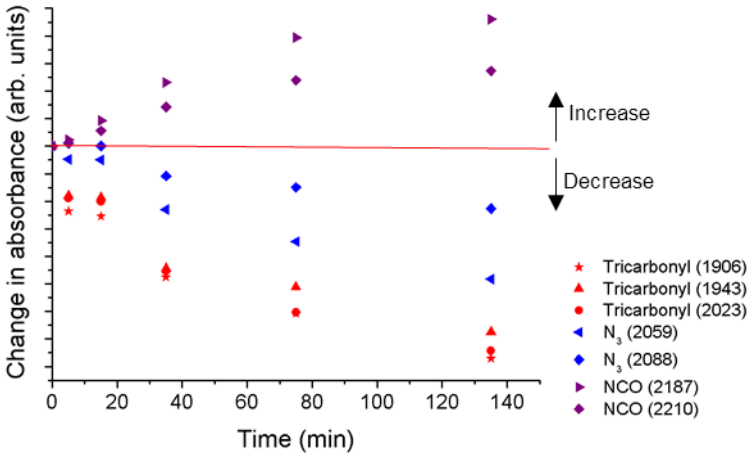

Figure 4.27. Kinetic analysis of the change in peak absorbance during photolysis of MnMOF[$Mn(CO)_3N_3$]·THF in a KBr disk, irradiated with UV light at 296K.

From the TR-IR results it can be concluded that MnMOF[$Mn(CO)_3N_3$]·THF can follow two reaction pathways upon irradiation, depending on the reaction conditions.

1. Loss of CO and expulsion of the azide ligand from the coordination sphere and then recombination in a variety of structural isomers; and,
2. Loss of CO and formation of NCO.

4.4 Photocrystallography of MnMOF[$Mn(CO)_3N_3$]

MnMOF[$Mn(CO)_3N_3$]·THF was then subjected to photocrystallography experiments where single crystals of the MOF were photolyzed at a range of temperatures, while protected under a nitrogen cryostream, and then X-ray diffraction data was collected at 120K. Of note was the finding that when no coordinating solvent was present (e.g., when the MOF was solvated with dry toluene), no changes in the coordination sphere were observed after photolysis, except for a slight elongation of the N2-N3 bond length in the coordinated azide from 1.25(3) Å to 1.35(3) Å (Figure 4.28, Structure **4.3**). This may be due to an azide excited state.[8] This supports literature findings which have shown that photo-ejected carbonyl ligands can recombine with the parent complex when no alternative ligand(s) are present.[80,81]

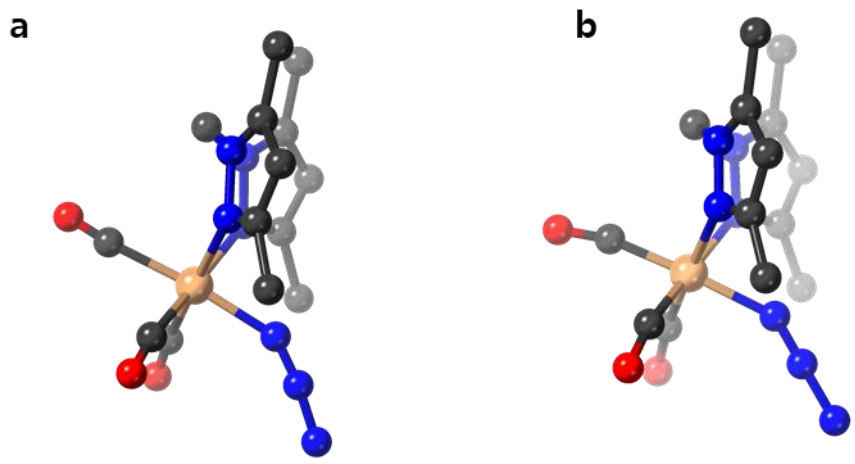

Figure 4.28. Coordination sphere of $[Mn(CO)_3N_3]$ complex in MnMOF **a)** before photolysis in THF and **b)** after photolysis in toluene, noting no change in the coordination environment. (Mn, beige; C, grey; N, blue; O, red, H atoms were omitted for clarity).

4.4.1 Photocrystallography: Photolysis of MnMOF$[Mn(CO)_3N_3]$ at 120K

A single crystal of MnMOF$[Mn(CO)_3N_3]$·THF was mounted in fomblin oil on a loop and flash frozen under a cryostream to 120K. The crystal was then irradiated with visible light for 30 min before the crystal was plunged into liquid nitrogen (77K) and cooled for 1.5 hrs. This additional cooling step was an attempt at producing a more ordered structure and to test whether crystals could be photolyzed then frozen in liquid nitrogen to be sent to a synchrotron for analysis. All the structures presented in sections 4.4; however, were collected on an in-house diffractometer, and so multiple data collections on individual crystals was not possible. The resulting crystal structure (Figure 4.29, Structure **4.4**) showed some disorder in the bis-dimethylpyrazoyl methane ligand binding site of the MOF. The minor component was modelled at a 25% occupancy and is likely a result of the manganese complex becoming partially labilised during photolysis from either one or both pyrazole ligands, which then is free to rotate into the disordered position. As previous EDX results showed minimal leaching after photolysis, it can be assumed that in the bulk phase the manganese is somewhat labile and can form solvated complexes which are disordered in the MOF pores. Therefore, there is an equilibrium between the complex bound to the MOF ligand and the species in the pore. As such, the major component containing the manganese complex and its ligands were modelled with maximum occupancies of 75%.

The azide ligand was clearly visible at the anti-axial coordination site and shows smaller thermal ellipsoids than the pre-photolysis structure collected previously. This may be due to the cooling in liquid nitrogen, or simply due to this crystal being more ordered. The other axial ligand was modelled as CO, while the equatorial positions showed a combination of coordinated CO and THF. The occupancies of the CO and THF were allowed to refine freely with U_{iso} fixed, then fixed at 33% and 66% occupancies (25% and 50% crystallographically, due to the 75% occupancy of the major component containing the Mn complex) respectively before the atoms were modelled anisotropically.

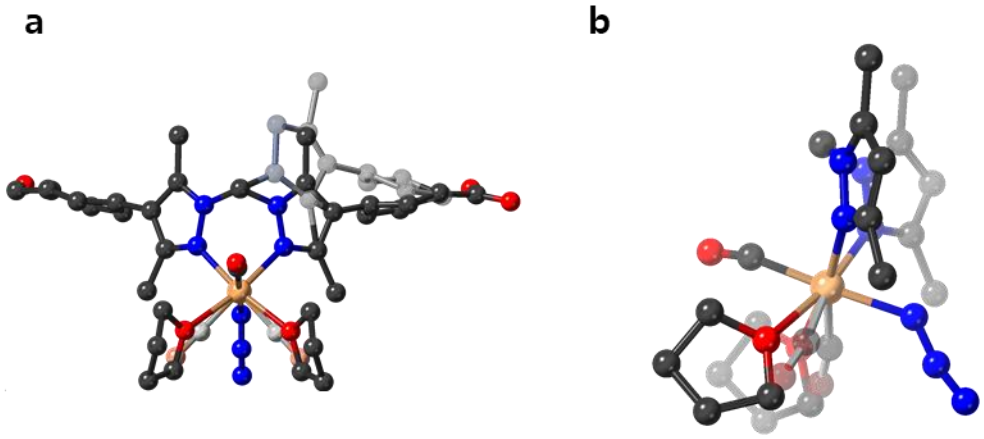

Figure 4.29. SCXRD structure of MnMOF[$Mn(CO)_3N_3$]·THF after irradiation for 30 min at 120K showing **a)** the disordered backbone ligand (modelled at 25% occupancy)* and **b)** Mn(I) coordination environment with overlapping THF and carbonyl ligands at the equatorial site (modelled at 66% and 33% occupancies respectively). *Note that a mirror plane runs through the plane bisecting the Mn atom and methylene bridge, resulting in the ligand being crystallographically disordered on both sides of the bridge. The structure shown is more representative of the chemical occupancy of the ligand. (Mn, beige; C, grey; N, blue; O, red, H atoms were omitted for clarity)

The N2-N3 bond length was unusually short at 1.085(16) Å, compared to 1.25(3) Å in the pre-photolysis structure. This short bond length is analogous to a N≡N triple bond, 1.098 Å in length.[9] This may be indicative of either the excited state which is formed upon photoexcitation and which may lead to the disassociation of N_2 and the formation of a nitrene.[12] This correlates with the findings from the TR-IR data in Section 4.3.3, where photolysis at 150K saw the formation of a dicarbonyl species and the majority of the azide was in one coordination state. Isomeric forms with the azide coordinated at different positions seen in the IR, may be due to solvated Mn(I) complexes in the MOF pore, or disorder in the MOF-bound complex that could not be modelled crystallographically.

4.4.2 Photocrystallography: Photolysis of MnMOF[$Mn(CO)_3N_3$] at 190K

A single crystal of MnMOF[$Mn(CO)_3N_3$]·THF was cooled to 190K under a dinitrogen cryostream and photolyzed for 60 min. The crystal was then cooled to 120K for data collection (Structure **4.5**). Rotational disorder around the methylene bridge was again observed and modelled at 25% occupancy. The coordination environment around the Mn(I) atom is difficult to resolve due to disorder; however, examining the electron density map (F_0) gives some insights (Figure 4.30). Both the axial sites have regions of electron density suggesting three atom ligands. These could be azido or isocyanate ligands (or a mixture), but the binding angles of 173(5) and 171(6)° (Mn-N-C *anti* and *syn* respectively), compared to 148(5)° for the azide in the pre-photolysis structure suggests they are more likely to be isocyanate than azide.[2]

These isocyanate ligands are likely to be overlapping with azido and carbonyl ligands from the parent complex. The ligands at the equatorial positions were also disordered and again the electron density map suggests overlapping carbonyl and THF ligands making modelling extremely challenging. Due to the large number of possible configurations, all the disorder was unable to be modelled, but a reasonable structural model was produced by assigning both axial ligands as isocyanates with the *anti*-NCO (to the methylene bridge) at 2/3 occupancy and the *syn*-NCO at 1/3 occupancy. The nitrogen atom of both ligands was fixed at full occupancy, as the position of this atom is very similar for bound azide, NCO, and axial carbonyl. The bond lengths for the modelled *anti*- and *syn*-NCO ligands were quite different due to the disorder with azide and carbonyl ligands, complicating the refinement (Figure 4.30e). The greatest differences occurred in the C-O bond length {1.02(5) Å (*anti*) and 1.20(2) Å (*syn*)} due to overlap with azide in the *anti*-position and no equivalent third atom at the *syn*-position. Literature bond lengths for transition metal isocyanate ligands are N-C 1.12-1.18 Å and C-O 1.21-1.24 Å.[44,82] The equatorial ligand was modelled as THF at a 66% occupancy. Despite NCO not being observed in the matrix isolated IR at 190K, it is unsurprising that it may be formed in a single crystal irradiated by powerful light, as the exposure is much greater than for a bulk sample pressed into a salt disk and behind several windows.

[2] Bond length and angles of coordinated NCO were cross referenced from $[W(CO)_5NCO]$ complex reported by Jupp *et al.*[82]

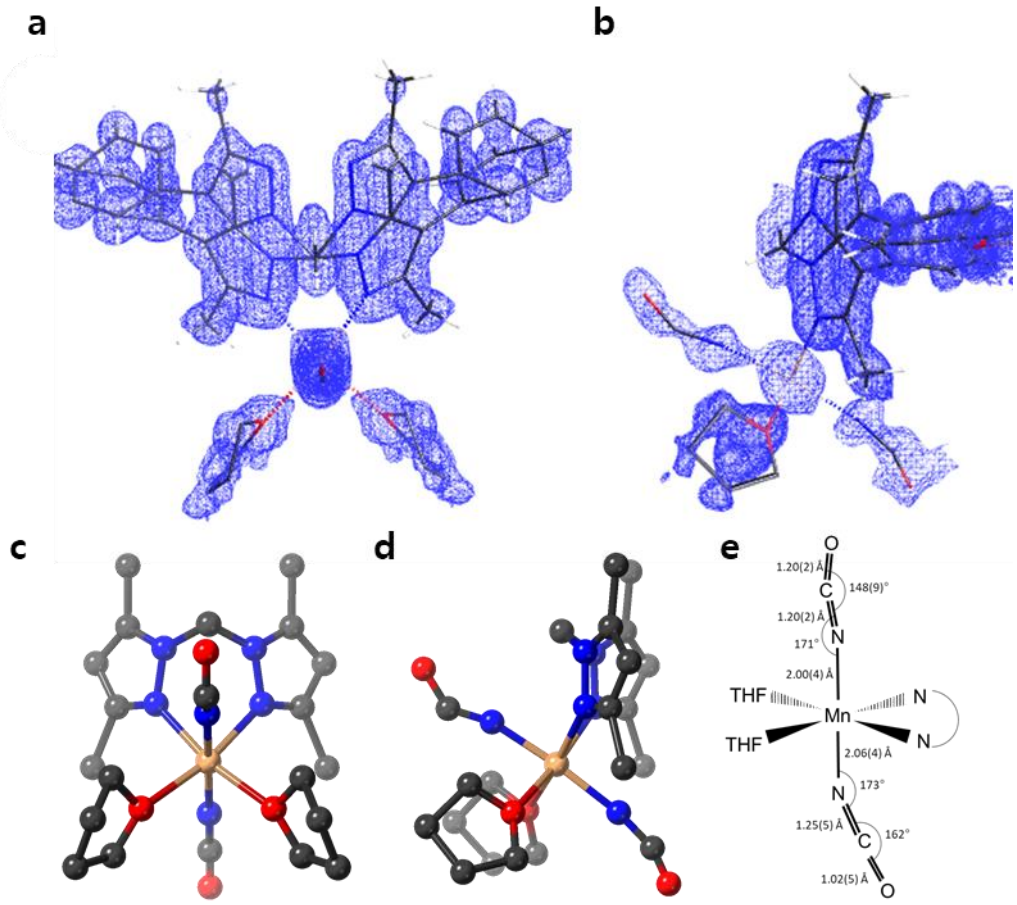

Figure 4.30. MnMOF[$Mn(CO)_3(N)_3$]·THF photolysed for 30 min at 190K showing F_{obs} electron density maps (contoured at 1.2 e/Å^3) displaying **a)** disordered MOF ligand and **b)** Mn(I) coordination sphere and **c)** top and **d)** side views of the Mn(I) coordination sphere modelled with partially occupied NCO and THF ligands. **e)** Bond lengths and angles for the coordinated NCO ligands. (Mn, beige; C, grey; N, blue; O, red, H atoms were omitted for clarity)

4.5 Outcomes of photochemical studies of Mn(I) azidocarbonyl complexes

In summary, photocrystallography studies, in combination with time-resolved infrared spectroscopy, were used to investigate changes in the coordination environment of a Mn(I) azidocarbonyl complex bound to MnMOF. Photolysis in a non-coordinating solvent resulted in no change to the complex (Figure 4.31a), indicating that any formation of coordinatively unsaturated Mn(I) due to the photo-ejection of carbonyl or azido ligands is very short lived and the expelled ligands quickly recombine to re-form the parent complex. Future ultra-fast TR-IR studies would be useful to investigate any short-lived intermediates that form during this process. Photolysis at 120K in THF leads to the formation of a dicarbonyl intermediate, with loss of CO at one

of the equatorial positions and binding of THF. This was seen crystallographically as the superposition of CO and THF ligands on both equatorial binding sites due to the presence of a mirror plane (Figure 4.31b). Finally, photolysis at 190K (single crystal) or 296K (matrix isolated bulk sample) resulted in the formation of an isocyanate (Figure 4.31c). The SCXRD structure was highly disordered; however, the electron density maps and binding angles suggested that NCO could be bound to either axial position, with the *anti*-axial position more occupied than the *syn*-axial position. The formation of NCO indicates that a nitrene intermediate was formed on a time scale not observed crystallographically. Also, the formation of NCO must have occurred in an intramolecular fashion, unlike for molecular species in the literature in which the reaction proceeds by an intermolecular pathway.[45]

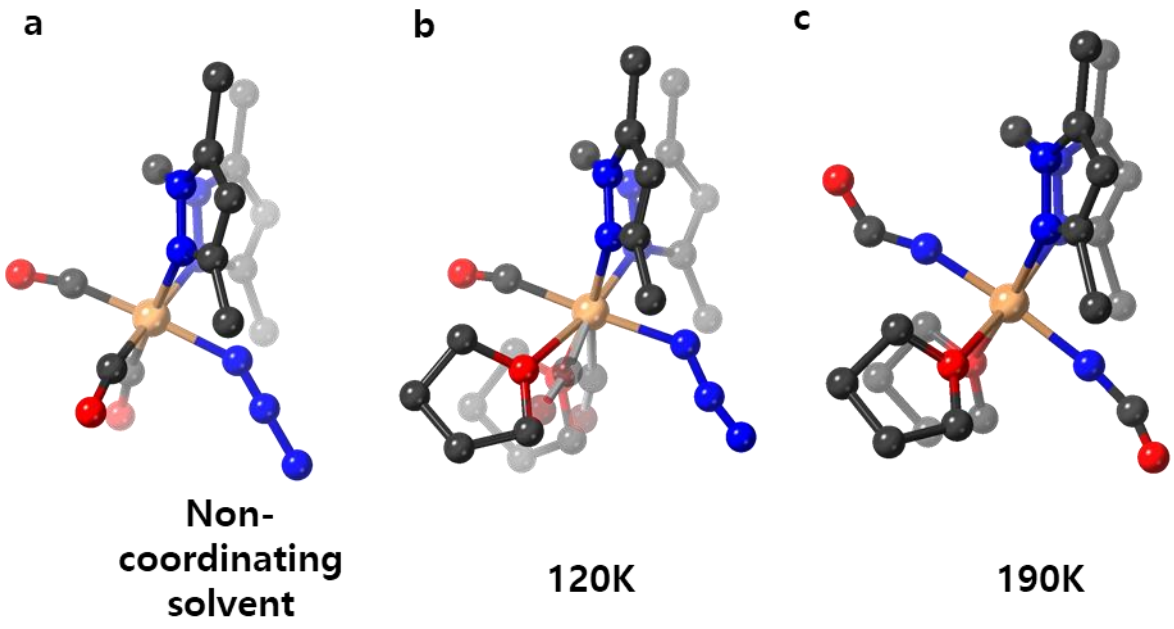

Figure 4.31. Coordination sphere of MnMOF[$Mn(CO)_3N_3$] after photolysis **a)** in a non-coordinating solvent (toluene) showing no change from the pre-photolysis structure, **b)** at 120K in the presence of THF, showing the loss of CO and coordination of THF at the equatorial positions and **c)** at 190K in the presence of THF, showing loss of CO, coordination of THF and formation of NCO. (Mn, beige; C, grey; N, blue; O, red, H atoms were omitted for clarity).

Photochemical studies of Mn(I) azidocarbonyl complexes both bound in MnMOF and in the molecular state were undertaken. Unlike azidocarbonyl complexes of other metals found in the literature (M = Cr, Fe, Re),[8,83] photolysis of the Mn(I) complexes saw reaction of both azido and carbonyl ligands. At low temperatures (120 and 150K) photoinduced decarbonylation was observed, along with ejection and recombination of the azido ligand and coordination of solvent molecules. At higher temperatures (190K and 296K) the azido ligand reacted with CO to form NCO, which in the molecular state

was also accompanied with the formation of a dimer with bridging azido and isocarbonate ligands. At these higher temperatures, the remaining carbonyl ligands were also lost and replaced by coordinated solvent molecules. Due to the same difficulties as discussed in Chapter 2, the final photoproduct of these reactions in MnMOF were not characterised. The main problems encountered were disorder, damage to the crystals and the difficulty in identifying complexes which are spectroscopically silent or hidden by the MOF scaffold.

4.6 Site isolating palladium complexes in MnMOF

4.6.1 Synthesis and characterisation of MnMOF[$PdCl_2$]

As introduced in Section 4.1.4-5, palladium catalysts are used for a wide range of coupling reactions and are thought to utilise Pd(0)/Pd(II) and Pd(II)/Pd(IV) redox cycles. The metalation of MnMOF was initially attempted with $PdCl_2$, $PdCl_2(MeCN)_2$ and $Pd(dba)_2$ (dba = dibenzylideneacetone) in acetonitrile. Acetonitrile was chosen as it is a polar aprotic solvent and hence able to solubilise palladium salts without causing oxidation or reduction of the metal. MnMOF solvated with acetonitrile was successfully metalated overnight at room temperature with palladium chloride to give MnMOF[$PdCl_2$]. Despite this, the crystals were very fragile and lost long range order by visibly shattering within a minute of exposing them to the atmosphere. Attempts were made to improve the stability of the crystals by changing the metalation rates by cooling the sample to 4 °C, warming to 40 °C or placing the palladium salt in a separate vial to diffuse into the MOF crystals (Table 4.8). All these methods caused the single crystals to shatter and become unsuitable for single crystal X-ray diffraction. Crystals taken directly from the metalation solution without washing were found to contain 2.2 equivalents of palladium (by EDX) per metalation site. Metalation with $PdCl_2(MeCN)_2$ resulted in only 67% (± 27) occupancy from EDX measurements, and $Pd(dba)_2$ showed no uptake of palladium, although some was detected on the crystal surfaces. This is likely due to the sterically bulky dba complex being unable to travel through the MOF pores.

Table 4.8. Conditions for metalation of MnMOF with $PdCl_2$ in acetonitrile

Metalation Conditions	Result
Room temperature	Retention of single crystallinity, 223 (±20) % occupancy
4°C	Shattered crystals
40°C	Shattered crystals
Slowed diffusion	Shattered crystals

After washing the MOF with acetonitrile twice, the palladium occupancy dropped to 148% (±6) and after eight washes to 116% (±3) suggesting that the majority of the untethered, pore held, palladium had been washed out. The crystals were left to soak in the solvent for 5 min between washes. As shown in Chapter 2.3.1, five washes with a combined soaking time of 30 min is sufficient for complete solvent exchange from ethanol to toluene in MnMOF, so diffusion of the solvent through the crystal is not a major influence here. A single crystal analysed after eight washes displayed $PdCl_2$ complex bound to the bis-pyrazole site and no observable electron density associated with addition palladium complexes in the pores (Figure 4.32, Structure **4.6**). The complex displays a Pd-Cl bond length of 2.28(1) Å and a Pd-N bond length of 2.04(1) Å, with a Cl-Pd-Cl dihedral angle of 90.3(2)°. The square planar Pd complex was bound to the MOF bispyrazole ligand with a Pd-CH_2 (methylene) distance of 3.005 Å (Figure 4.32b). These values are consistent with analogous molecular complexes.[84]

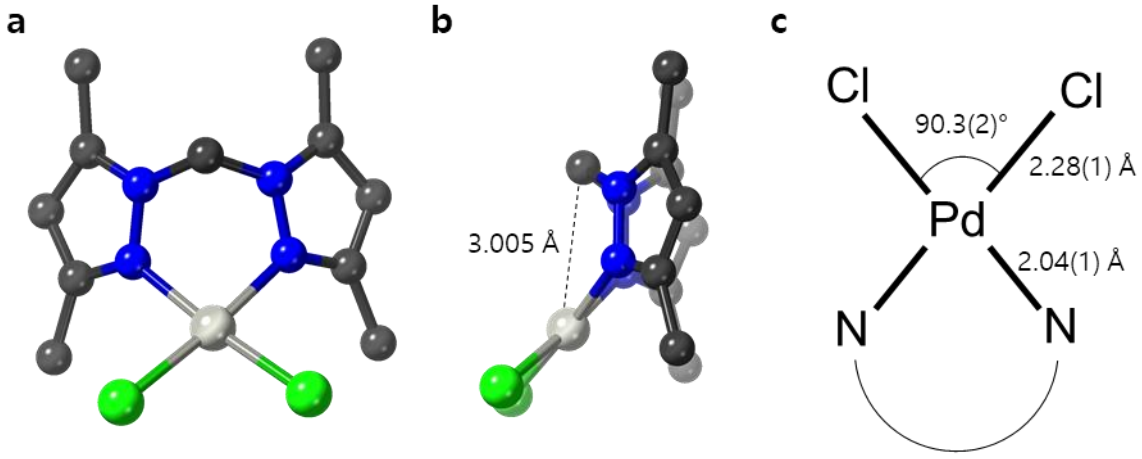

Figure 4.32. Palladium coordination sphere in MnMOF[$PdCl_2$]·MeCN showing **a)** a top view of the complex and **b)** a side view displaying the binding angle to the MOF. **c)** bond lengths and angles for the MnMOF-bound palladium chloride complex. (C, grey; N, blue; Pd, light grey; Cl, green, H are omitted for clarity).

Obtaining only ligand-bound $PdCl_2$ without any palladium chloride species in the pores was difficult due to the ligand bound palladium being quickly labilized in acetonitrile. After achieving close to 100% occupancy of the metalation site after eight consecutive washes leaving the MOF to soak in acetonitrile for 2 hrs resulted in the occupancy dropping to 73% (±7) and after 4 hrs to 54% (±7) (Figure 4.33). This labilization of the palladium did not occur uniformly through the MOF crystals, with the palladium bound close to the crystal surface having lower occupancies per metalation site {63% (±8)} after two hours of soaking in comparison to values of 84% (±11), observed in crushed crystals indicative of the bulk sample. To achieve quantitative metalation without labilization, attempts were made to metalate the MOF with $PdCl_2$ in a range of solvents including diethyl ether, methanol, ethanol and p-xylene; however all were unsuccessful.

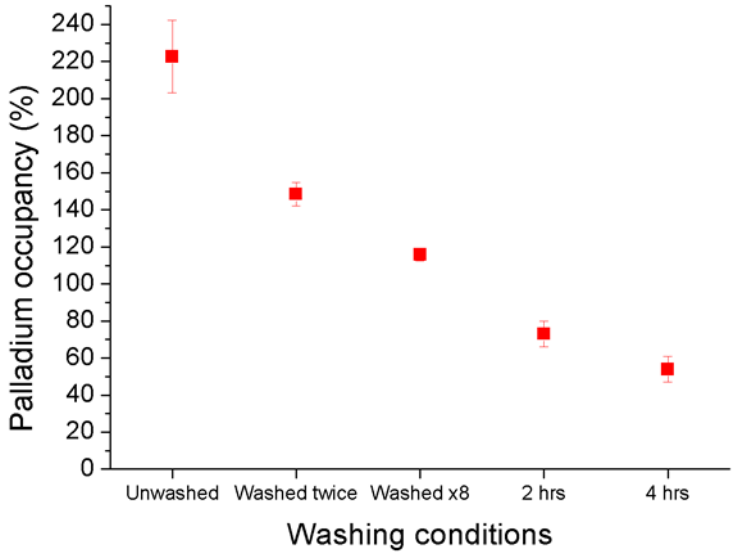

Figure 4.33. Palladium occupancy per metalation site of MnMOF[$PdCl_2$]·MeCN analysed by SEM/EDX after varying washing conditions. (Error bars = SE).

The labilization of palladium from the crystal surface before the interior of the crystal presents an intriguing opportunity to produce core-shell metalated crystals, by first metalating with palladium, washing out the metal bound at the crystal surface, and then metalating with another metal source. This was attempted with cobalt chloride, as its metalation chemistry in MnMOF is well known and it also metalates in acetonitrile.[85] MnMOF was metalated with palladium chloride overnight in acetonitrile, then washed 5 times before one molar equivalent of cobalt chloride was added and the crystals heated overnight at 50°C. The sample was then washed 5 times with acetonitrile, dried and analysed by SEM/EDX. Interestingly, the occupancy of palladium was still 114% (±

2) after this process and cobalt was present at a ratio of 1:9 (Co:Pd). The crystals also changed colour from yellow to green/blue, indicating the presence of cobalt, even though the occupancy observed by EDX was low. While this experiment successfully showed that two metals could be incorporated sequentially into MnMOF, the spatial positions of the cobalt atoms were not determined. SEM mapping is required on whole and cut crystals to determine if true core-shell structures were produced. A single crystal of this sample was analysed by SCXRD and only the metalated palladium chloride could be modelled. This is unsurprising, as the EDX results showed only an 11% (±1) loading of Co; however, it was reassuring that the coordination chemistry of the palladium chloride remained unchanged by the secondary metalation process.

4.6.2 Synthesis and characterisation of MnMOF[$PdBr_2$]

The previously discussed metalation procedure was also used to successfully prepare MnMOF[$PdBr_2$] by metalation with $PdBr_2$. EDX results after washing (x8) showed quantitative metalation of 105% (±5), but due to the fragile nature of the crystals the only SCXRD structure obtained was from an unwashed sample and so extra palladium bromide complexes were observed in the MOF pore (Figure 4.34, Structure **4.7**). The through space distance between the palladium atom and the methylene carbon was shorter than the chlorine analogue, at 2.808 Å compared to 3.005 Å. This may be caused by steric effects from the size of bromide ligands (van der Waals radius =1.83 Å) compared to chloride ligands (van der Waals radius =1.75 Å).[86] The occupancy of the coordinated $PdBr_2$ complex was fixed at 75% and the disordered $PdBr_2$ complexes in the pores fixed at 75% for the Pd atoms and 50% for the Br atoms, resulting in overall 1.5 $PdBr_2$ complexes per asymmetric unit.

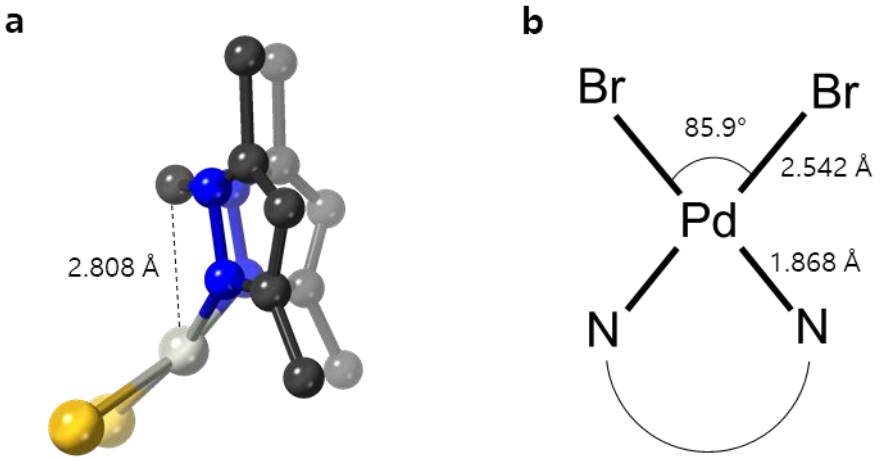

Figure 4.34. a) Palladium coordination sphere of MnMOF[$PdBr_2$]·MeCN and **b)** selected bond length and angles of the coordinated complex.

4.6.3 Reactions of MnMOF[PdX_2] (X = Cl, Br)

Palladium can act as a catalyst through Pd(0)/Pd(II) or Pd(II)/Pd(IV) redox cycles; however, there has been comparatively few studies on the Pd(II)/Pd(IV) cycle, especially in trapping and characterising Pd(IV) intermediates.[87] Byers *et al* synthesised a 6-coordinate Pd(IV) complex through the oxidative addition of iodomethane to [$PdMe_2$(bpy)] (Section 4.1.4).[59] With this in mind, the addition of iodomethane, iodine and bromine to MnMOF[PdX_2] (X = Cl, Br) was attempted. A range of conditions were trialled, including in diethyl ether, dichloromethane and acetonitrile at -20°C, room temperature and 40 °C through direct addition and slow diffusion. Unfortunately, SCXRD studies did not present any 6-coordinate palladium complexes after these reactions, with the post-reaction structures still containing square-planar palladium, albeit with decreased crystal quality. Due to time constraints, further characterisation was not attempted, although NMR and UV-Vis studies would be an interesting extension of this work.

Due to previous work employing alkyl ligands on the Pd(II) precursor instead of halides,[58] attempts were made to metalate MnMOF with Pd(tmeda)Me_2 (tmeda = tetramethylethylene diamine). This was synthesised according to literature procedures from the reaction of [Pd(tmeda)Cl_2] with methyl lithium.[88] Efforts to metalated MnMOF with this complex were unsuccessful with no palladium measured in the MnMOF crystals. In addition, direct addition of methyl lithium to MnMOF[$PdCl_2$] was attempted

to examine if the failure of this metalation was due to the MOF, or to the coordination environment, the synthesis of a model complex was trialled with the previously used ligand bdpm (bis(3,5-dimethyl-1H-pyrazol-1-yl)methane). This was metalated with palladium chloride in dichloromethane then reacted with methyl lithium (Figure 4.35). This did not produce a [Pd(bdpm)Me_2] complex, with only decomposition products observed in the NMR and MS spectra. It can therefore be concluded that the bis-pyrazolyl ligand set is not conducive to stabilising a palladium methyl complex, and that alternative approaches should be tried in the future.

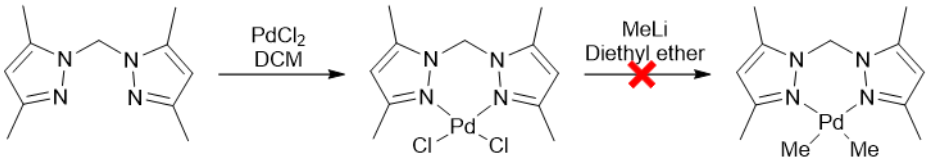

Figure 4.35. Unsuccessful synthetic pathway for [Pd(bdpm)$(Me)_2$].

Despite these unsuccessful reaction attempts, there are many open avenues for further exploration of palladium complexes in MnMOF. Anion exchange with non-coordinating anions may allow for the coordination of weak ligands such as ethylene. The Pd(0)/Pd(II) catalytic cycle could be explored through addition of a reducing agent. The catalytic activity of MnMOF[PdX_2] (X = Cl or Br) could also be investigated for coupling reactions, with the possibility of trapping and structurally characterising reaction intermediates.

4.4 Conclusions and Future Directions

The photochemical behaviour of azidocarbonyl Mn(I) complexes were studied when site-isolated in MnMOF and for an analogous molecular species. It was found that at room temperature both the MOF-bound, and molecular complexes formed isocyanate species. Analysis of IR data suggested that the photolysis of the molecular complex, [Mn(bdpm)$(CO)_3N_3$], produced a dimer with bridging azido and isocyanate ligands. Complete loss of the carbonyl ligands was observed, indicating that the remainder of coordination sites are most likely to be filled by THF solvent molecules, although no structural characterisation was completed of the final reaction product complex. The MOF-bound complex behaved differently, with no observed formation of an isocyanate when photolyzed in air, but with the formation of coordinated isocyanate when matrix isolated. Matrix isolated TR-IR studies showed that at lower temperatures (150K and 190K) no isocyanate was formed from the UV photolysis of MnMOF[$Mn(CO)_3N_3$]·THF; however, loss of carbonyl ligands forming transient dicarbonyl species was observed. Also observed was photo-ejection of the azido ligand and proposed recombination as several structural isomers. These findings were reinforced by photocrystallographic studies, showing initial loss of CO and coordination of THF at equatorial sites and formation of NCO at axial sites.

This study provides new insights into the photochemistry of Mn(I) azidocarbonyl complexes. Firstly, this appears to be the first study of the photochemistry of Mn(I) complexes containing both carbonyl and azido ligands. The photo-induced complete decarbonylation, ejection and recombination of the azide ligand and formation of an isocyanate under different conditions shows the range of reactions and intermediates that can be accessed by this complex. Secondly, the formation of isocyanate in MnMOF must be due to an intramolecular mechanism due to the site isolation of the Mn(I) complexes, which is likely to include a nitrene intermediate. Further elucidation of the mechanism would be of interest through ultrafast TR-IR and nitrene trapping studies. Finally, the lack of reaction in toluene shows the dependence of these reactions on availability of coordinating ligands. This opens up a range of opportunities to study the behaviour of these complexes in the presence of other ligands. Another avenue of opportunity could be in the study of nitrosyl complexes in MnMOF. Nitrosyls are

isoelectric to carbonyls and highly reactive, with applications in catalysis and therapeutics.[89]

The successful metalation of MnMOF with PdX_2 (X=Cl, Br) complexes provides great opportunities for the study of palladium-catalysed reactions in MnMOF; however, inherent difficulties involving metalation and stability must be first overcome. The propensity for palladium complexes to reside in the MOF pores, in addition to coordinating to the ligand binding site, means that they must be washed out in order to study only the site-isolated complex. This is complicated by the lability of the ligand bound complex, hence further optimisation of metalation and washing conditions is required. Retention of long-range order and single crystallinity is difficult with acetonitrile solvated crystals, so additional solvent exchange steps should be investigated to give more stable crystals. Finally, while a palladium methyl complex could not be synthesised in MnMOF using the methods in Section 4.6.3, other avenues should be explored for the installation of reactive ligands. The possibilities for investigations into reaction intermediates and pathways, as well as improving selectivities and efficiencies of reactions are of great potential but were, unfortunately, unable to be undertaken within the timeframe of this project. In addition, further investigations into the formation of bimetallic core-shell metalated MOF crystals may allow for the possibility of cascade reactions requiring two metal catalysts, prevention of deactivation or unwanted selectivities from surface effects and loading and slow release of a metal from a MOF for agrochemical or therapeutic applications.

4.5 Appendix

4.5.1 General Experimental

All chemicals were obtained from commercial sources and used as received unless otherwise stated. Dry solvents were distilled (acetonitrile over calcium hydride, THF over sodium/benzophenone, and ethanol and methanol over magnesium) and degassed with argon before use. The ligand L (L = bis(4-carbonxyphenyl-3,5-dimethylpyrazolyl) methane), MnMOF, MnMOF[$Mn(CO)_3X$] (where X = Br, solvent or N_3)[85] and the model complex azotricarbonyl(bis(3,5-dimethyl-1H-pyrazol-1-yl)methane) manganese (I)[52] were prepared by previously reported methods. MnMOF[$Mn(CO)_3X$] (X = Br, N_3) was stored in the dark and handled with minimal exposure to light.

NMR spectra were recorded on a Varian 500 MHz spectrometer at 23 °C using a 5 mm probe or Brucker DPX400, AV400 or AV(III)400 400 MHz spectrometers with BBFO probes. ^1H NMR spectra recorded in $CDCl_3$ were referenced to the internal standard, Me_4Si (0 ppm) or to the solvent peak. A FEI Quanta 450 high resolution, field emission scanning electron microscope was used to collect images and perform energy-dispersive X-ray spectroscopy (EDX). EDX was collected with an Oxford Ultim X-Max Large Area SDD detector with Oxford Aztec EDX processing software.

Room temperature infrared (IR) spectra were collected on a Bruker Alpha FTIR with an ATR attachment. Matrix isolated IR spectra were collected on a Thermo Nicolet Avatar 360 spectrophotometer with the sample dispersed in dry NaCl or KBr and pressed into a disk (8 mm diameter, 0.5 mm thickness) under 6 tonnes of pressure. The disk was placed into a copper cell with CaF_2 windows, which was sealed and placed inside a vacuum shroud, before cooled to the analysis temperature. Photolysis was performed with a Philips HPK medium pressure 125W mercury arc lamp.

Single crystals were mounted in Fomblin or Paratone-N oil on a MiTeGen micromount. Data for 4.**7** was collected on the i19 beamline at Diamond Light Source at 100K and processed using Xia2 software.[90] Data for 4.**6** was collected at the MX1 beamline at the Australian synchrotron at 170K and process through XPREP software.[91] Data for 4.**1-5** were collected on Oxford SuperNova diffractometers with Atlas S2 detectors using Cu (Kα: 1.54184 Å) radiation at 120K and processed through CrysAlis software. Absorption corrections were applied using empirical methods and the structures were solved by direct methods using SHELXS or SHELXT and refined by full-matrix least-squares by SHELXL,[92] interfaced through Olex2.[93] The SQUEEZE routine of

PLATON was used to subtract the contribution from disordered solvent.[94] Unless stated otherwise, all non-hydrogen atoms were refined anisotropically and hydrogen atoms were included as invariants at geometrically estimated positions. CrystalMakerX was used to produce the figures.[95]

PXRD patterns were collected on a Bruker Advance D8 powder diffractometer (parallel x-ray) equipped with a capillary stage and using Cu Kα radiation (λ = 1.5418 Å), or on a Bruker Endeavour D4 powder diffractometer (parallel x-ray, flat plate loaded) using Co Kα radiation (λ = 1.789 Å).

4.5.2 Synthetic procedures

[Mn(bdpm)(CO)$_3$N$_3$] model complex

[Mn(bdpm)(CO)$_3$Br] (bdpm = bis(3,5-dimethyl-1H-pyrazol-1-yl)methane, 100 mg, 0.24 mmol) was dissolved in dry, degassed dichloromethane (20 mL). Silver triflate (93.8 mg, 0.29 mmol, 1.2 equiv) was then added and the solution stirred at room temperature in the dark for 3 hrs (Scheme 1). The solution was then filtered to remove precipitated silver bromide and sodium azide (45.5 mg, 0.70 mmol, 2.9 equiv.) dissolved in water (10 mL) was added. The mixture was stirred at room temperature overnight in the dark to give a yellow solution. The organic phase was separated and washed with water (5 x 10 mL) then dried over magnesium sulfate. The solvent was removed under reduced pressure to give a yellow solid which was crystallised from chloroform to give Mn(bdpm)(CO)$_3$N$_3$ as large yellow block crystals suitable for SCXRD (6 mg, 6%). IR ν_{max} (cm^{-1}) 1908 (s, CO), 1933 (s, CO), 2011 (s, CO), 2058 (s, N$_3$) . NMR spectra were not obtained due to light sensitivity.

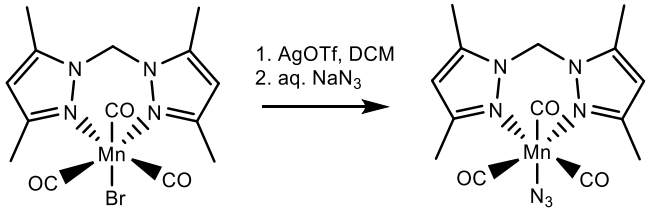

Scheme 1. Synthetic procedure for [Mn(bdpm)(CO)$_3$N$_3$] through reaction with **1.** silver triflate in DCM then **2.** aqueous sodium azide.

MnMOF[$Mn(CO)_3N_3$]

Ligand L (31.6 mg, 0.07 mmol) dissolved in DMF (4 mL) was added to $MnCl_2.4H_2O$ (24.7 mg, 0.12 mmol) dissolved in water (2 mL) in a 20 mL screw cap vial and heated at 100 °C for 2 days. The colourless crystals were then washed with DMF (x5) and ethanol (x5) then metalated with excess $Mn(CO)_5Br$ overnight at 50°C. The metalated sample was washed with ethanol (x5) then methanol (x5) and excess sodium azide added. The sample was left at room temperature for 3 days, then washed with methanol (x5) to produce MnMOF[$Mn(CO)_3N_3$] as yellow crystals {IR ν 1902 (CO), 1950 (CO), 2023 (CO), 2063 (N_3) (cm^{-1})}. Solvent exchanges before reactions were performed with 5 washing steps before the crystals were allowed to soak overnight and exchanged a final time on the day of the reaction.

MnMOF[PdX_2] (X = Cl, Br)

Crystals of MnMOF were solvent exchanged with dry acetonitrile (x5) and an excess of palladium salt ($PdCl_2$ or $PdBr_2$) was added under an inert atmosphere. The sample vial was closed and sealed with parafilm and left at room temperature for 24 hrs. The crystals were then washed with dry acetonitrile as described in Section 4.6 to give bright yellow ($PdCl_2$) or orange ($PdBr_2$) crystals.

The PXRD patterns of these MOFs were recorded and compared to simulated patterns from the SCXRD structures (Figure 4.36). Despite both experimental samples showing sharp crystalline peaks, they did not match well with the simulated patterns. This is not unusual for MnMOF samples, which are flexible and show strong orientation effects; however, some of this change may be due to simple decomposition, as it was observed that when exposed to the air and de-solvated the crystals would shatter and turn grey (Figure 4.37).

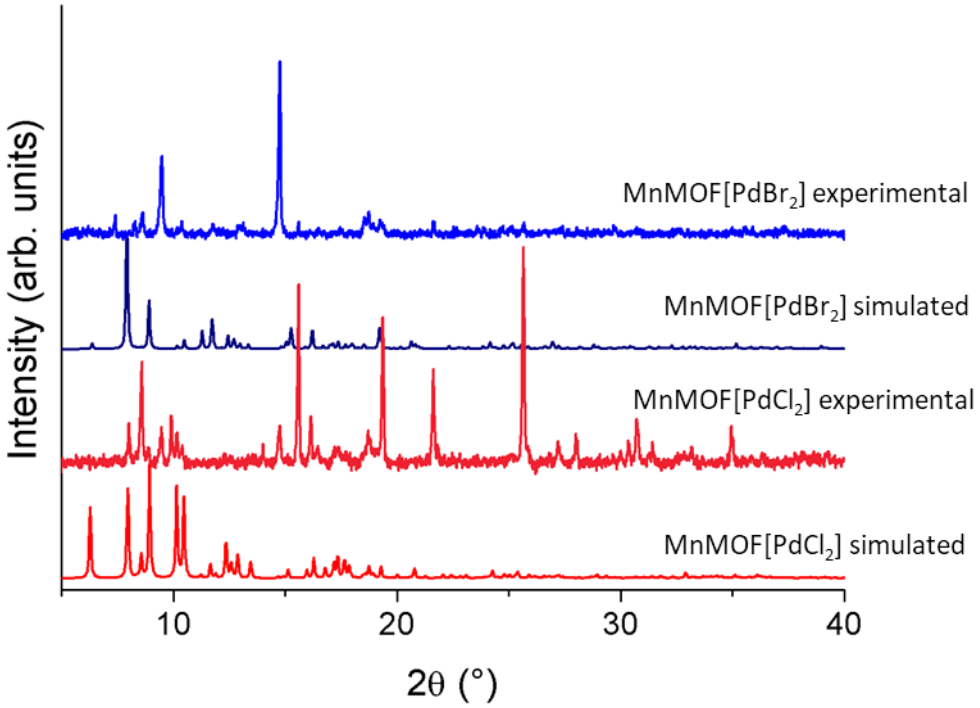

Figure 4.36. PXRD patterns for (top to bottom) MnMOF[$PdBr_2$] (experimental), MnMOF[$PdBr_2$] (simulated), MnMOF[$PdCl_2$] (experimental) and MnMOF[$PdCl_2$] (simulated).

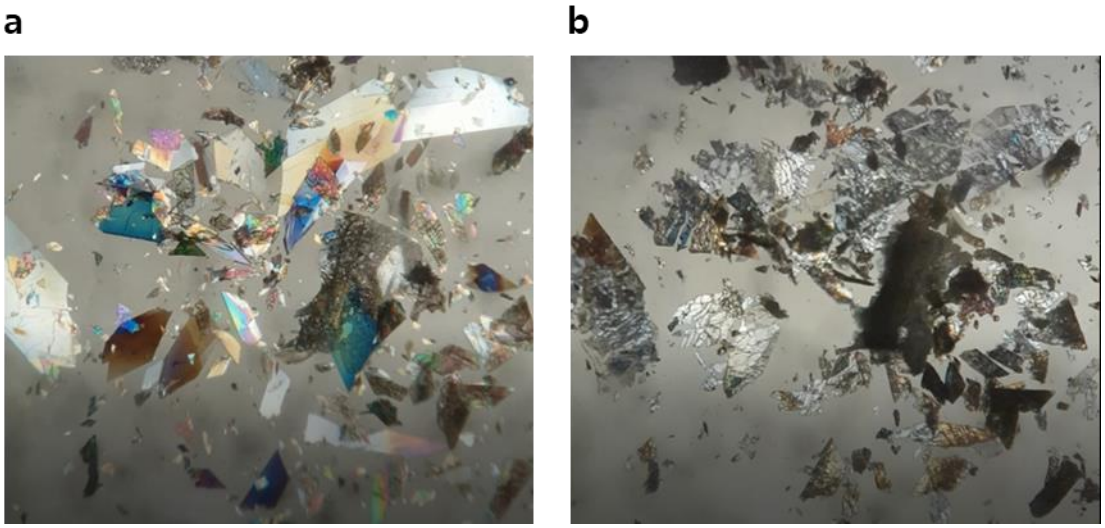

Figure 4.37. MnMOF[$PdCl_2$] crystals in mother liquor viewed through a microscope with plane-polarised light **a)** taken out of the vial in solvent and **b)** 30 sec later.

[Pd(tmeda)(Me)$_2$]

Palladium chloride (500 mg, 2.82 mmol) was added to dry acetonitrile (10 mL) under argon and heated at reflux overnight. The solvent was removed to give the bright yellow solid $Pd(MeCN)_2Cl_2$ (672 mg, 92%).

$Pd(MeCN)_2Cl_2$ (150 mg, 0.58 mmol) was added to dry acetonitrile (5 mL) under argon and stirred with heating until fully dissolved. The solution was then cooled and tetramethylethylene diamine (0.13 mL, 0.87 mmol, 1.5 equiv.) was added dropwise, instantly forming a yellow precipitate. This was isolated by vacuum filtration and washed with diethyl ether to give $Pd(tmeda)Cl_2$ (127 mg, 75%).[88]

$Pd(tmeda)Cl_2$ (100 mg, 0.34 mmol) was added to dry, degassed diethyl ether (5 mL) under inert gas. The solution was cooled to -60 °C before MeLi (1.6M in diethyl ether, 1.2 mL, 0.75 mmol) was added dropwise. The solution was then slowly warmed to 0 °C with stirring before ice water (5 mL) was added. The organic layer was separated and the aqueous layer extracted with dry diethyl ether (x3). The combined organic extracts were dried over $MgSO_4$ and the solvent removed through slow evaporation at 4 °C to give large, off-white single crystals of $Pd(tmeda)Me_2$ (61 mg, 71%, stored in the fridge under nitrogen, NMR data were in accord with reported values).[88,91]

Pd(bdpm)Me$_2$

Bdpm (100 mg, 0.495 mmol) and $PdCl_2$ (132 mg, 0.743 mmol) were added to dry, degassed dichloromethane (5 mL) and stirred at room temperature overnight. The solvent was removed and the remaining orange solid was washed with dry diethyl ether to give [$Pd(bdpm)Cl_2$] {183 mg, 97%, MS (ESI$^+$) m/z 402 ([$Pd(bdpm)Cl_2$]+Na^+)}.[96]

[$Pd(bdpm)Cl_2$] (90 mg, 0.237 mmol) was added to dry, degassed diethyl ether (5 mL) and cooled to -30°C. MeLi (1.6 M in diethyl ether, 0.3 mL, 0.474 mmol) was added dropwise and the reaction mixture was allowed to warm to 0°C. Ice cold water (5 mL) was added and the organic layer separated. The aqueous layer was extracted with diethyl ether (x3) and the combined organic extracts were dried over $MgSO_4$ and the solvent removed to give a pale yellow solid (12 mg, ^{1}H NMR (400 MHz, CDCl3) δ: 8.04 (1H, s) 3.50 (3H q, J = 7 Hz), 2.98 (3H, s), 2.90 (3H, s), 1.23 (5H, t, J = 7Hz), ^{13}C NMR ($CDCl_3$) δ: 36.50, 31.43) ppm MS (ESI$^+$) m/z 227 (1+), 309 (2+), 488 (1+), 635 (1+), 839 (1+) (major peaks), expected 340 [$Pd(bdpm)Me_2$] or 363 [$Pd(bdpm)Me_2$]+Na^+[97]

SEM/EDX

SEM/EDX analysis was done on whole (Figure 4.38a and 4.39a) and crushed (Figure 4.38b and 4.38b) MOF crystals in order to gain a better understanding of the surface and bulk metalation results. EDX spectra were collected over at least 15 regions per sample (Figure 4.38c and 4.39c and d).

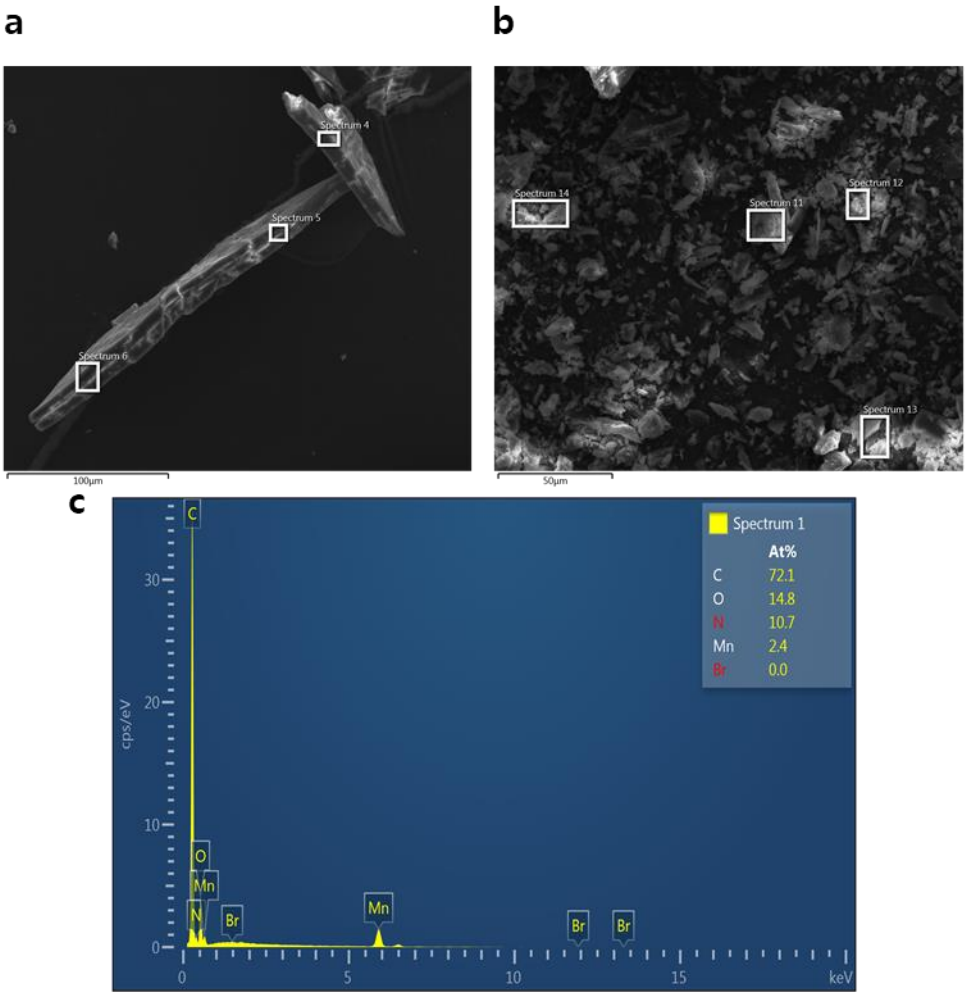

Figure 4.38. Representative SEM images of **a)** whole and **b)** crushed MnMOF[$Mn(CO)_3N_3$] crystals and representative EDX spectra for **c)** MnMOF[$Mn(CO)_3N_3$], showing complete exchange of bromide anions.

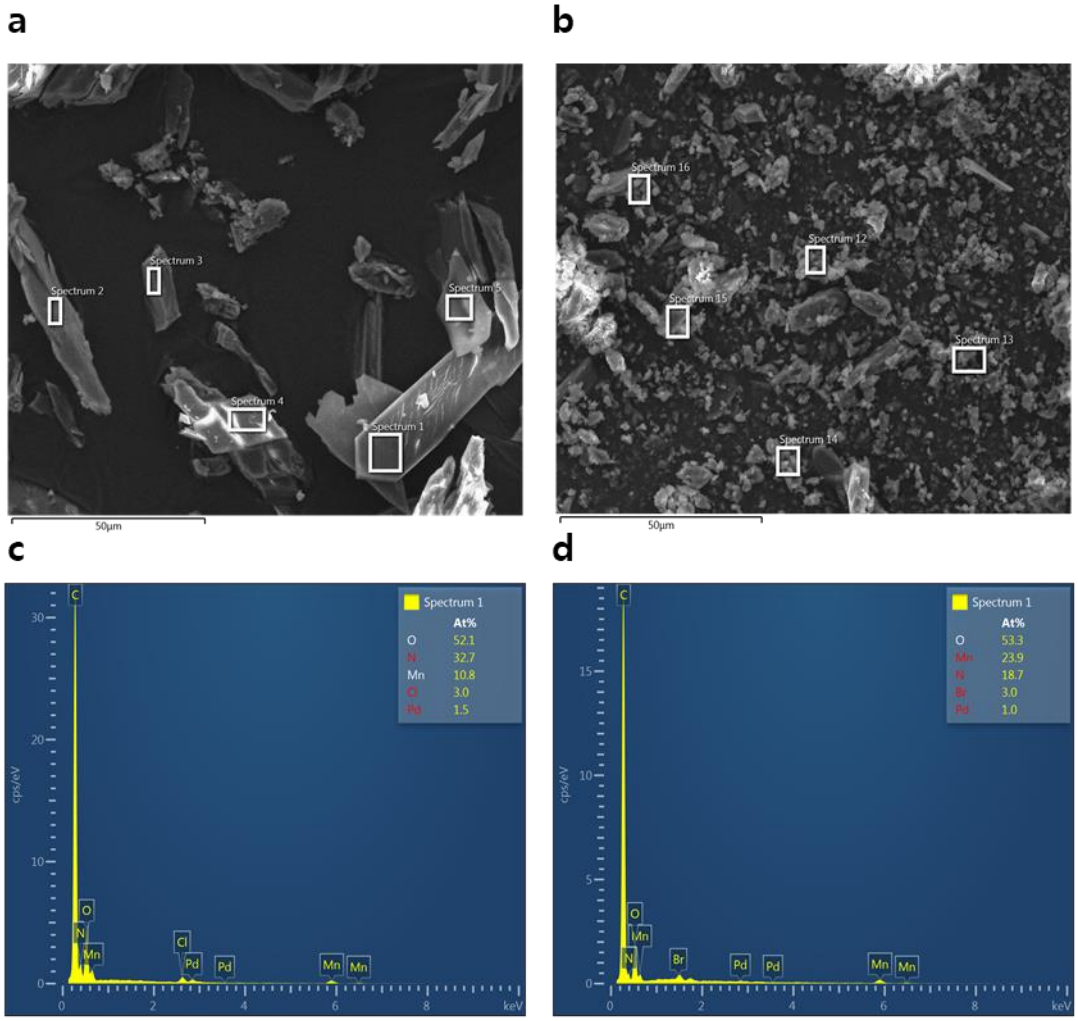

Figure 4.39. Representative SEM images of **a)** whole and **b)** crushed palladium metalated MnMOF crystals and representative EDX spectra for **c)** MnMOF[$PdCl_2$] and **d)** MnMOF[$PdBr_2$].

4.5.3 Additional crystal structure refinement details

Supplementary crystallographic data may be found at https://figshare.com/s/b35758c23efed8465fd8.

MnMOF[$Mn(CO)_3N_3$] (4.2)

To subtract the contribution of the disordered solvent to the F_{obs} values (THF), the SQUEEZE routine of PLATON was applied to the data, which generated a new HKL file. The number of located electrons was 351, which equates to approximately 8 THF molecules per unit cell, and 2 per asymmetric unit. This has been added to the reported formula.

RIGU restraints were used in the refinement of carbonyl and azide ligands and the disordered ligand L phenyl ring (4 restraints in total).

MnMOF[$Mn(CO)_3N_3$]·toluene (4.3) Photolysis at 250K

To subtract the contribution of the disordered solvent to the F_{obs} values (toluene), the SQUEEZE routine of PLATON was applied to the data, which generated a new HKL file. The number of located electrons was 369, which equates to approximately 7 toluene molecules per unit cell, and 1.75 per asymmetric unit. This has been added to the reported formula.

RIGU restraints were used in the refinement of the coordinated azido ligand and the toluene solvent molecule (10 restraints in total). EADP constraints were used on phenyl and pyrazolyl atoms on the non-Mn(I) coordinating ligand due to large ADP min/max ratios (8 constraints)

MnMOF[$Mn(CO)_3N_3$]·THF (4.4)– photolysis at 120K in THF

To subtract the contribution of the disordered solvent to the F_{obs} values (THF), the SQUEEZE routine of PLATON was applied to the data, which generated a new HKL file. The number of located electrons was 174, which equates to approximately 4 THF molecules per unit cell, and 1 per asymmetric unit. This has been added to the reported formula.

DFIX and RIGU restraints were used in the refinement of the overlapping coordinated THF and carbonyl molecules and the disordered ligand L molecule (11 restraints in total).

MnMOF[$Mn(CO)_3N_3$]·THF (4.5)– photolysis at 190K in THF

To subtract the contribution of the disordered solvent to the F_{obs} values (THF), the SQUEEZE routine of PLATON was applied to the data, which generated a new HKL file. The number of located electrons was 214, which equates to approximately 5 THF molecules per unit cell, and 1.25 per asymmetric unit. This has been added to the reported formula.

A series of DFIX, SIMU and RIGU restraints were used in the refinement of the highly disordered coordinated THF and NCO molecules and the disordered ligand L molecule (21 restraints in total). EADP constraints were also used on the carbon atoms of the THF ring (2 constraints).

MnMOF[$PdCl_2$]·MeCN (4.6)

To subtract the contribution of the disordered solvent to the F_{obs} values (MeCN), the SQUEEZE routine of PLATON was applied to the data, which generated a new HKL file. The number of located electrons was 429, which equates to approximately 20 MeCN molecules per unit cell, and 5 per asymmetric unit. This has been added to the reported formula.

RIGU restraints were used in the refinement of the disordered phenyl ring in ligand L (1 restraint in total).

MnMOF[$PdBr_2$]·MeCN (4.7)

To subtract the contribution of the disordered solvent to the F_{obs} values (MeCN), the SQUEEZE routine of PLATON was applied to the data, which generated a new HKL file. The number of located electrons was 197, which equates to approximately 9 MeCN molecules per unit cell, and 2.25 per asymmetric unit. This has been added to the reported formula.

RIGU and DFIX restraints were used in the refinement of the disordered phenyl ring and methylene bridge in ligand L (5 restraints in total). The occupancy of the coordinated $PdBr_2$ complex was fixed at 75% and the disordered $PdBr_2$ complexes in the pores fixed at 75% for the Pd atoms and 50% for the Br atoms, resulting in overall 1.5 $PdBr_2$ complexes per asymmetric unit.

Thermal Ellipsoid plots at 50% probability level

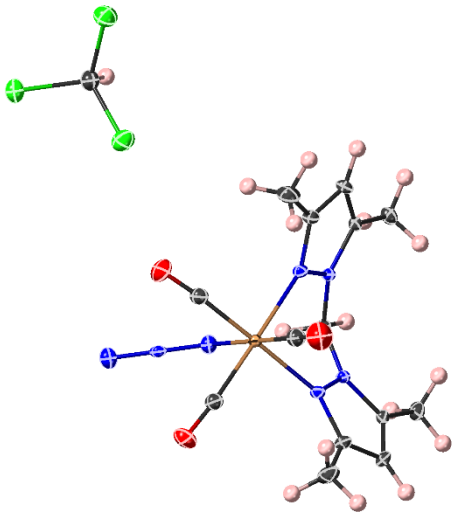

Figure 4.40. Molecule of [Mn(bdpm)(CO)$_3$N$_3$] (**4.1**) with co-crystallised chloroform, with all non-hydrogen atoms represented by ellipsoids at the 50% probability level. (C, grey; Mn, beige; Cl, green; O, red; N, blue; H, pink)

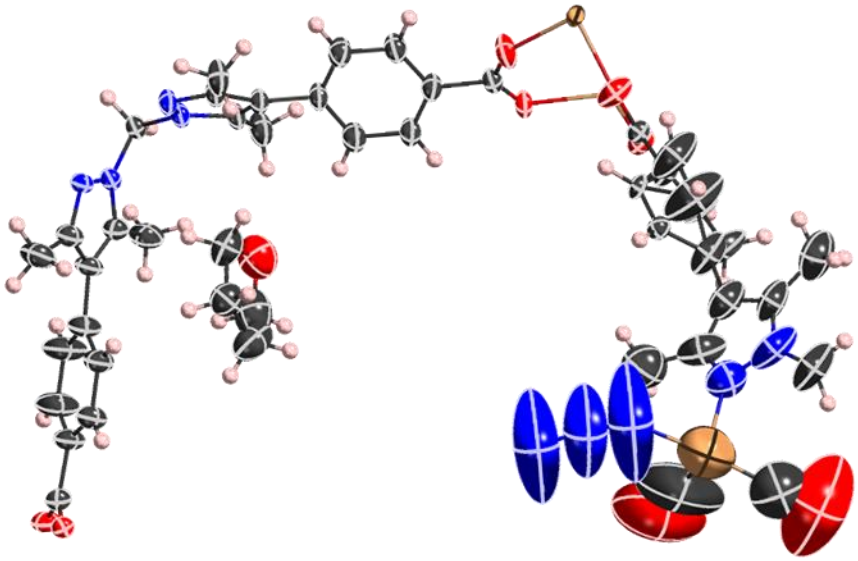

Figure 4.41. Asymmetric unit of MnMOF[Mn(CO)$_3$N$_3$]·THF (**4.2**), with all non-hydrogen atoms represented by ellipsoids at the 50% probability level. (C, grey; Mn, beige; O, red; N, blue; H, pink)

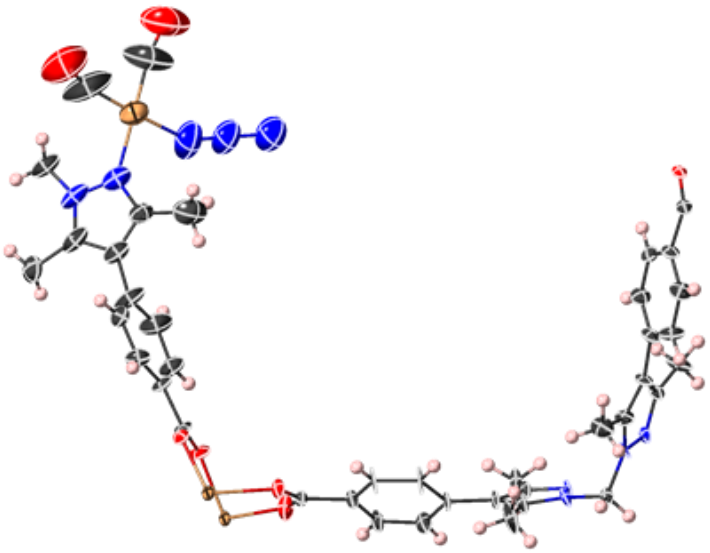

Figure 4.42. Asymmetric unit of MnMOF[$Mn(CO)_3N_3$] (**4.3**) toluene photolyzed for 30 min at 250K, with all non-hydrogen atoms represented by ellipsoids at the 50% probability level. (C, grey; Mn, beige; O, red; N, blue; H, pink)

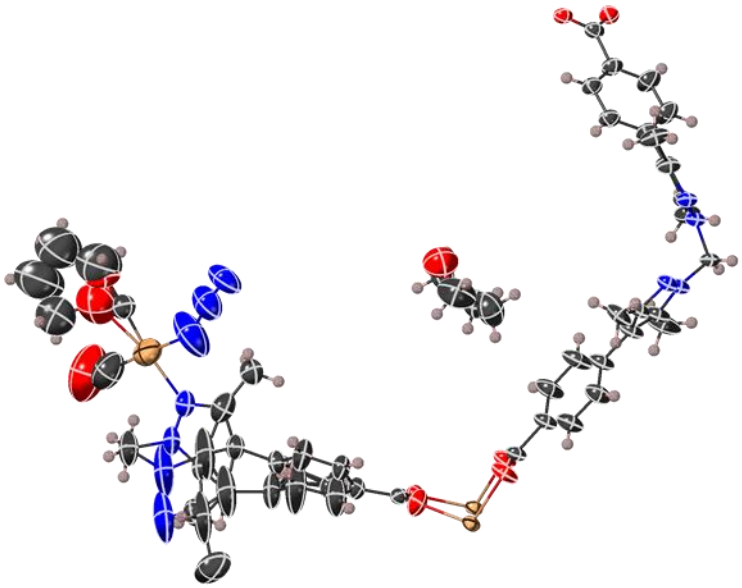

Figure 4.43. Asymmetric unit of MnMOF[$Mn(CO)_3N_3$]·THF (**4.4**) photolyzed for 30 min at 120K, with all non-hydrogen atoms represented by ellipsoids at the 50% probability level. (C, grey; Mn, beige; O, red; N, blue; H, pink)

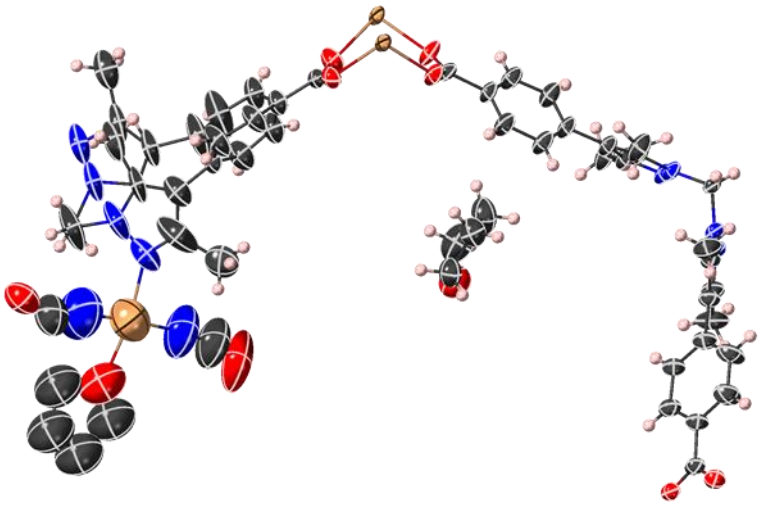

Figure 4.44. Asymmetric unit of MnMOF[$Mn(CO)_3N_3$]·THF (**4.5**) photolyzed for 60 min at 190K, with all non-hydrogen atoms represented by ellipsoids at the 50% probability level. (C, grey; Mn, beige; O, red; N, blue; H, pink)

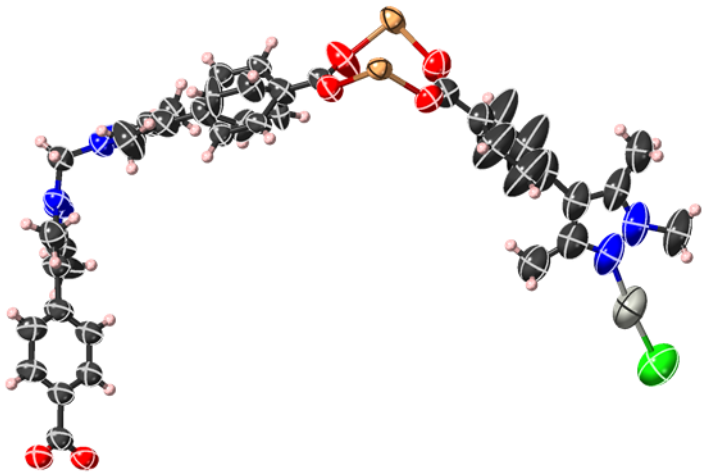

Figure 4.45. Asymmetric unit of MnMOF[$PdCl_2$]·MeCN (**4.6**), with all non-hydrogen atoms represented by ellipsoids at the 50% probability level. (Pd, light grey; Cl, green; C, grey; Mn, beige; O, red; N, blue; H, pink)

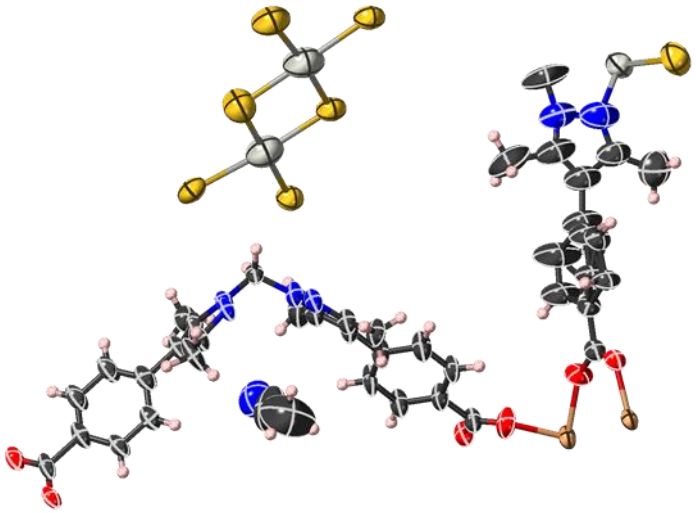

Figure 4.46. Asymmetric unit of MnMOF[$PdBr_2$]·[Pd_2Br_6]·MeCN (**4.7**), with all non-hydrogen atoms represented by ellipsoids at the 50% probability level. (Pd, light grey; Br, yellow; C, grey; Mn, beige; O, red; N, blue; H, pink)

Table 4.9. Crystal data and structure refinement details.

Sample	$[Mn(bdpm)(CO)_3N_3]$ **(4.1)**	MnMOF$[Mn(CO)_3N_3]$·THF **(4.2)**	MnMOF$[Mn(CO)_3N_3]$·tol **(4.3)**	MnMOF$[Mn(CO)_3N_3]$·THF 120K photo **(4.4)**	MnMOF$[Mn(CO)_3N_3]$·THF 190K photo **(4.5)**
Empirical formula	$C_{12}H_{13.6}Cl_{2.4}Mn_{0.8}N_{5.6}O_{2.4}$	$C_{52}H_{56}Mn_3N_9O_{11}$	$C_{58.25}H_{53}Mn_3N_9O_8$	$C_{48}H_{53}N_{8.25}O_{10}Mn_{2.75}$	$C_{48.75}H_{53}N_{7.5}O_{9.5}Mn_{2.75}$
Formula weight	403.72	1147.85	1171.88	1056.53	1047.03
Temperature/K	120(2)	120(2)	120(2)	120(2)	120(2)
Crystal system	orthorhombic	monoclinic	monoclinic	monoclinic	monoclinic
Space group	*Pnma*	$P2_1/m$	$P2_1/m$	$P2_1/m$	$P2_1/m$
a/Å	18.7234(3)	12.3412(4)	12.4070(4)	12.3142(2)	12.3386(3)
b/Å	12.9302(2)	32.5793(19)	32.7198(12)	32.2465(9)	32.4335(13)
c/Å	8.58520(10)	12.9942(4)	12.9895(5)	12.9705(2)	12.9907(3)
α/°	90	90	90	90	90
β/°	90	93.769(3)	94.242(3)	92.826(2)	93.725(2)
γ/°	90	90	90	90	90
Volume/Å³	2078.45(5)	5213.2(4)	5258.7(3)	5144.19(18)	5187.7(3)
Z	5	4	2	3	3
$\rho_{calc}g/cm^3$	1.613	1.506	1.173	1.650	1.643
μ/mm^{-1}	9.007	6.420	4.331	6.583	6.533
F(000)	1024.0	2456.0	1918.0	2631.0	2634.0
Crystal size/mm³	0.287 × 0.163 × 0.11	0.212 × 0.053 × 0.033	0.2 x 0.07 x 0.05	0.551 × 0.166 × 0.050	0.212 × 0.053 × 0.038
Radiation/Å	Cu Kα (λ = 1.54184)	CuKα (λ = 1.54184)	CuKα (λ = 1.54184)	CuKα (λ = 1.54184)	CuKα (λ = 1.54184)
2Θ range for data collection/°	9.448 to 147.164	6.818 to 145.082	6.824 to 148.978	6.824 to 144.63	7.18 to 145.55
Index ranges	-22 ≤ h ≤ 21, -15 ≤ k ≤ 15, -3 ≤ l ≤ 10	-15 ≤ h ≤ 13, -38 ≤ k ≤ 39, -11 ≤ l ≤ 15	-15 ≤ h ≤ 15, -40 ≤ k ≤ 40, -15 ≤ l ≤ 11	-10 ≤ h ≤ 15, -38 ≤ k ≤ 39, -12 ≤ l ≤ 15	-15 ≤ h ≤ 13, -39 ≤ k ≤ 39, -11 ≤ l ≤ 16
Reflections collected	5340	30341	39466	23293	39103
Independent reflections	2143 [R_{int} = 0.0199, R_{sigma} = 0.0195]	10321 [R_{int} = 0.0580, R_{sigma} = 0.0663]	10678 [R_{int} = 0.0809, R_{sigma} = 0.0652]	10083 [R_{int} = 0.0381, R_{sigma} = 0.0465]	10307 [R_{int} = 0.0574, R_{sigma} = 0.0579]
Data/restraints/parameters	2143/0/147	10321/57/587	10678/39/523	10083/68/713	10307/129/663
Goodness-of-fit on F^2	1.061	1.074	1.074	1.049	1.058
Final R indexes [I>=2σ (I)]	R_1 = 0.0279, wR_2 = 0.0743	R_1 = 0.0920, wR_2 = 0.2598	R_1 = 0.1458, wR_2 = 0.3498	R_1 = 0.0695, wR_2 = 0.1925	R_1 = 0.0974, wR_2 = 0.2698
Final R indexes [all data]	R_1 = 0.0289, wR_2 = 0.0751	R_1 = 0.1080, wR_2 = 0.2757	R_1 = 0.1574, wR_2 = 0.3563	R_1 = 0.0775, wR_2 = 0.1989	R_1 = 0.1158, wR_2 = 0.2839
Largest diff. peak/hole / e $Å^{-3}$	0.48/-0.45	0.82/-1.77	1.14/-2.67	0.69/-0.99	1.33/-1.46

Table 4.10. Crystal data and structure refinement details.

Sample	MnMOF[$PdCl_2$]·MeCN **(4.6)**	MnMOF[$PdBr_2$]·MeCN **(4.7)**
Empirical formula	$C_{47}Cl_1Mn_2N_{11}O_6Pd_1H_{46}$	$C_{43.5}H_{40.75}N_{9.25}O_6Br_4Mn_2Pd_{2.5}$
Formula weight	1112.66	1085.27
Temperature/K	173.15	100
Crystal system	monoclinic	monoclinic
Space group	$P2_1/m$	$P2_1/m$
a/Å	12.278(3)	12.3289(3)
b/Å	32.655(7)	32.1669(9)
c/Å	12.900(3)	12.9490(3)
α/°	90	90
β/°	93.28(3)	92.110(2)
γ/°	90	90
Volume/Å³	5163.6(18)	5131.9(2)
Z	8	2
ρ_{calc}*g/cm³*	1.105	0.078
μ/mm⁻¹	0.635	0.146
F(000)	1685.0	110.0
Crystal size/mm³	0.205 × 0.100 × 0.15	0.150 × 0.75 × 0.10
Radiation/Å	MoKα (λ = 0.71073)	ZrKα (λ = 0.6889)
2Θ range for data collection/°	2.494 to 58.464	2.454 to 72.012
Index ranges	-14 ≤ h ≤ 14, -38 ≤ k ≤ 38, -13 ≤ l ≤ 13	-17 ≤ h ≤ 20, -52 ≤ k ≤ 53, -20 ≤ l ≤ 21
Reflections collected	67360	77802
Independent reflections	10027 [R_{int} = 0.0598, R_{sigma} = 0.0370]	23661 [R_{int} = 0.0564, R_{sigma} = 0.2686]
Data/restraints/parameters	10027/3/556	23661/19/577
Goodness-of-fit on F^2	1.188	0.923
Final R indexes [I>=2σ (I)]	R_1 = 0.0996, wR_2 = 0.3159	R_1 = 0.1471, wR_2 = 0.4050
Final R indexes [all data]	R_1 = 0.1347, wR_2 = 0.3403	R_1 = 0.2334, wR_2 = 0.4250
Largest diff. peak/hole / e Å⁻³	1.40/-1.30	1.64/-3.21

Tables of selected bond lengths and angles

Table 4.11. Selected bond lengths and angles.

Parameter	[Mn(bdpm)$(CO)_3N_3$] **(4.1)**	MnMOF[Mn$(CO)_3N_3$] **(4.2)**	MnMOF[Mn$(CO)_3N_3$]·toluene **(4.3)**
Bond lengths	*(Å)*	*(Å)*	*(Å)*
Mn-N1(az)	2.064(2)	2.02(2)	2.02(2)
N1-N2(az)	1.186(3)	1.13(3)	1.14(3)
N2-N3(az)	1.168(3)	1.25(3)	1.35 (3)
Mn-CO(eq)	1.8050(18)	1.91(3)	1.77(2)
Mn-CO(ax)	1.819(2)	2.03(4)	1.82(3)
Mn-N(py)	2.0914(13)	2.14(8)	2.058(11)
Bond angles	*(°)*	*(°)*	*(°)*
Mn-N1-N2(az)	126.52(16)	148(5)	146(2)
N1-N2-N3(az)	176.9(2)	172(6)	179(3)
N(py)-Mn-N(py)	85.126 (7)	82.3 (4)	82.6 (6)
N(py)-Mn-N1(az)	87.073 (5)	89.5 (12)	85.8 (7)

az = azide

eq = equatorial carbonyl with respect to bispyrazolyl ligand

ax = axial carbonyl with respect to bispyrazolyl ligand

py = pyrazole

Table 4.12. Selected bond lengths and angles for MnMOF[$Mn(CO)_3N_3$]·THF after photolysis at 120K (**4.4**).

Parameter	MnMOF[$Mn(CO)_3N_3$]·THF 120K photolysis
Bond lengths	*(Å)*
Mn-N1(az)	2.16(2)
N1-N2(az)	1.21(2)
N2-N3(az)	1.085(16)
Mn-CO(eq)	1.82(3)
Mn-CO(ax)	1.96(2)
Mn-N(py)	2.147(6)
Mn-O(THF)	2.39(2)
C-O(ax)	0.969(16)
C-O(eq)	1.20(3)
Bond angles	*(°)*
Mn-N1-N2	134(2)
N1-N2-N3	166(3)
N(py)-Mn-N(py)	81.3 (3)
N(py)-Mn-N1(az)	84.3 (6)
Mn-C-O(eq)	169(3)
Mn-C-O(ax)	166(3)
az = azide	THF = coordinated tetrahydrofuran
eq = equatorial carbonyl with respect to ligand L	
ax = axial carbonyl with respect to ligand L	
py = pyrazole	

Table 4.13. Selected bond lengths and angles for MnMOF[$Mn(CO)_3N_3$]·THF after photolysis at 190K **(4.4)**

Parameter	MnMOF[$Mn(CO)_3N_3$]·THF 190K photolysis
Bond lengths	*(Å)*
Mn-N1(*anti*-NCO)	2.06(3)
N1-C1(*anti*-NCO)	1.25(5)
C1-O1(*anti*-NCO)	1.02(5)
Mn-N2(*syn*-NCO)	2.00(4)
N2-C2(*syn*-NCO)	1.20(2)
C2-O2(*syn*-NCO)	1.20(2)
Mn-O(THF)	2.26(2)
Mn-N(py)[d]	2.170(13)
Bond angles	*(°)*
Mn-N1-C1(*anti*-NCO)	173(5)
N1-C1-O1(*anti*-NCO)	162(10)
Mn-N2-C2(*syn*-NCO)	171(6)
N2-C2-O2(*syn*-NCO)	148(9)
N(py)-Mn-N(py)	75.8(7)
anti-NCO = isocyanate *anti* to methylene bridge	
syn-NCO = isocyanate *syn* to methylene bridge	
THF = coordinated tetrahydrofuran	
py = pyrazole	

Table 4.14. Selected bond lengths and angles for MnMOF[PdX_2]·MeCN (X = Cl, Br)

Parameter	MnMOF[$PdCl_2$]·MeCN **(4.6)**	MnMOF[$PdBr_2$]·MeCN **(4.7)**
Bond lengths	*(Å)*	
Pd-X	2.279(4)	2.564(3)
Pd-N(py)	2.038(9)	1.907(13)
Bond angles	*(°)*	
X-Pd-X	90.32(19)	85.69(15)
N-Pd-N(py)	84.3(5)	88.9(7)
py = pyrazole		

4.6 References

1 R. H. Crabtree, *Chem. Rev.*, 2016, **116**, 8750–8769.

2 A. S. Weller, F. M. Chadwick and A. I. McKay, in *Advances in Organometallic Chemistry*, Academic Press Inc., 2016, vol. 66, pp. 223–276.

3 S. A. Bartlett, N. A. Besley, A. J. Dent, S. Diaz-Moreno, J. Evans, M. L. Hamilton, M. W. D. Hanson-Heine, R. Horvath, V. Manici, X.-Z. Sun, M. Towrie, L. Wu, X. Zhang and M. W. George, *J. Am. Chem. Soc*, 2019, **141**, 11471–11480.

4 R. J. Young, M. T. Huxley, E. Pardo, N. R. Champness, C. J. Sumby and C. J. Doonan, *Chem. Sci.*, 2020, **11**, 4031–4050.

5 R. A. Sheldon, *J. R. Soc. Interface*, 2016, **13**, 116

6 P. C. Samartzis and A. M. Wodtke, *Phys. Chem. Chem. Phys.,* 2007, **9**, 3054-3066

7 N. Gritsan and M. S. Platz, in *Organic Azides: Syntheses and Applications*, eds. S. Brase and K. Banert, Wiley, 2009.

8 W. P. Fehlhammer and W. Beck, *Zeitschrift fur Anorg. und Allg. Chem.*, 2013, **639**, 1053–1082.

9 W. K. Seok and T. M. Klapötke, *Bull. Korean Chem. Soc.*, 2010, **31**, 781–788.

10 S. Cenini, E. Gallo, A. Caselli, F. Ragaini, S. Fantauzzi and C. Piangiolino, *Coord. Chem. Rev.*, 2006, **250**, 1234–1253.

11 M. Sarakha and M. Bolte, *J. Photochem. Photobiol. A Chem.*, 1996, **97**, 87–92.

12 J. Šima, *Coord. Chem. Rev.*, 2006, **250**, 2325–2334.

13 P. Portius, A. J. H. M. Meijer, M. Towrie, B. F. Crozier and I. Schiager, *Dalton Trans.*, 2014, **43**, 17694–17702.

14 S. Fantauzzi, A. Caselli and E. Gallo, *Dalton Trans.*, 2009, **28**, 5434–5443.

15 B. Darses, R. Rodrigues, L. Neuville, M. Mazurais and P. Dauban, *Chem. Commun.*, 2017, **53**, 493–508.

16 T. G. Driver, *Org. Biomol. Chem.*, 2010, **8,** 3831–3846.

17 P. F. Kuijpers, J. I. van der Vlugt, S. Schneider and B. de Bruin, *Chem. - A Eur. J.*, 2017, **23**, 13819–13829.

18 V. Vreeken, M. A. Siegler, B. de Bruin, J. N. H. Reek, M. Lutz and J. I. van der Vlugt, *Angew. Chem.,* 2015, **127**, 7161-7165.

19 H. Hayashi and T. Uchida, *European J. Org. Chem.*, 2020, **2020**, 909–916.

20 J. Wang, K. Zheng, T. Li and X. Zhan, *Catalysts*, 2020, **10**, 292.

21 T. Uchida and T. Katsuki, *Chem. Rec.*, 2014, **14**, 117–129.

22 Y. Peng, Y. H. Fan, S. Y. Li, B. Li, J. Xue and Q. H. Deng, *Org. Lett.*, 2019, **21**, 8389–8394.

23 T. Bach, B. Schlummer and K. Harms, *Chem. Commun.*, 2000, 287–288.

24 Y.-C. Wang, X.-J. Lai, K. Huang, S. Yadav, G. Qiu, L. Zhang and H. Zhou, *Org. Chem. Front.*, 2021, **8**, 1677.

25 L. Ge, M.-F. Chiou, Y. Li and H. Bao, *Green Synth. Catal.*, 2020, **1**, 86–120.

26 T. Xiong and Q. Zhang, *Chem. Soc. Rev.*, 2016, 45, 3069–3087.

27 K. M. Carsch, I. M. DiMucci, D. A. Iovan, A. Li, S. L. Zheng, C. J. Titus, S. J. Lee, K. D. Irwin, D. Nordlund, K. M. Lancaster and T. A. Betley, *Science*, 2019, **365**, 1138–1143.

28 M. M. Abu-Omar, C. E. Shields, N. Y. Edwards and R. A. Eikey, *Angew. Chem. - Int. Ed.*, 2005, **44**, 6203–6207.

29 R. P. Bennet and W. B. Hardy, *J. Am. Chem. Soc.*, 1968, **90**, 3295–3296.

30 X. Huang, T. Zhuang, P. A. Kates, H. Gao, X. Chen and J. T. Groves, *J. Am. Chem. Soc.*, 2017, **139**, 15407–15413.

31 A. M. Sargeson, *Pure Appl. Chem.*, 1973, **33**, 527–544.

32 R. W. Brink and R. J. Angelici, *Inorg. Chem.*, 1973, **12**, 1062–1067.

33 R. J. Angelici and G. C. Faber, *Inorg. Chem.*, 1971, **10**, 514–517.

34 T. M. Becker, J. A. Krause-Bauer, C. L. Homrighausen and M. Orchin, *Polyhedron*, 1999, **18**, 2563–2571.

35 W. Beck and H. S. Smedal, *Angew. Chem. Int. Ed. English*, 1966, **5**, 253–253.

36 W. Beck and W. P. Fehlhammer, *Angew. Chem. Int. Ed. English*, 1967, **6**, 169–170.

37 J. P. Collman, M. Kubota, and J W Hosking, *J. Am. Chem. Soc.,* 1967, **89**, 18, 4809-4811

38 H. Werner, W. Beck and H. Engelmann, *Inorganica Chim. Acta*, 1969, **3**, 331–334.

39 A. K. Ghosh, A. Sarkar and M. Brindisi, *Org. Biomol. Chem.*, 2018, **16**, 2006–2027.

40 W. Beck and W. P. Fehlhammer, *Zeitschrift für Anorg. und Allg. Chem.*, 2010, **636**, 157–162.

41 R. Murray and D. C. Smith, *Coord. Chem. Rev.*, 1968, **3**, 429–470.

42 J. Strahle, *J. Organomet. Chem.*, 1995, **488**, 15–24.

43 S. T. Massey, B. Mansour and L. Mcelwee-White, *J. Organomet. Chem.*, 1995, **485**, 123–126.

44 A. T. McPhail, P. M. Gross, G. R. Knox, C. G. Robertson and G. A. Sim, *J. Chem. Soc. A Inorganic, Phys. Theor. Chem.*, 1971, 205–214.

45 R. M. Dahlgren and J. I. Zink, *Inorg. Chem.*, 1979, **18**, 597–603.

46 D. Sellmann, W. Weber, G. Liehr and H. P. Beck, *J. Organomet. Chem.*, 1984, **269**, 155–170.

47 T. M. Becker, K. Jayasimhulu and M. Orchin, *J. Organomet. Chem.*, 2000, **610**, 118–121.

48 J. R. Carney, B. R. Dillon and S. P. Thomas, *European J. Org. Chem.*, 2016, **2016**, 3912–3929.

49 G. Qing Li and M. Orchin, *J. Organomet. Chem.*, 1997, **535**, 43–47.

50 R. Mason, G. A. Rusholme, W. Beck, H. Englemann, K. Joos, B. Lindenberg and H. S. Smedal, *Chem. Commun.*, 1971, **364**, 496–497.

51 P. Kumar, C. Joshi, A. K. Srivastava, P. Gupta, R. Boukherroub and S. L. Jain, *ACS Sustain. Chem. Eng.*, 2016, **4**, 69–75.

52 M. T. Huxley, A. Burgun, H. Ghodrati, C. J. Coghlan, A. Lemieux, N. R. Champness, D. M. Huang, C. J. Doonan and C. J. Sumby, *J. Am. Chem. Soc.*, 2018, **140**, 6416–6425.

53 T. Boningari, S. M. Pavani, P. R. Ettireddy, S. S. C. Chuang and P. G. Smirniotis, *Mol. Catal.*, 2018, **451**, 33–42.

54 H. M. L. Davies and D. Morton, *ACS Cent. Sci.*, 2017, **3**, 936–943.

55 K. C. Nicolaou, P. G. Bulger and D. Sarlah, *Angew. Chem. - Int. Ed.*, 2005, **44**, 4442–4489.

56 M. Bihani, T. N. Ansari, J. D. Smith and S. Handa, *Curr. Opin. Green Sustain. Chem.*, 2018, **11**, 45–53.

57 F. Ozawa, M. Fujimori, T. Yamamoto and A. Yamamoto, *Organometallics*, 1986, **5**, 2144–2149.

58 P. K. Byers, A. J. Canty, M. Crespo, R. J. Puddephatt and J. D. Scott, *Organometallics*, 1988, **7**, 1363–1367.

59 P. K. Byers, A. J. Canty, B. W. Skelton and A. H. White, *J. Chem. Soc. Chem. Comm.,* 1986, **1035**, 1722-1724

60 J. W. Schultz, N. P. Rath and L. M. Mirica, *Inorg. Chem.*, 2020, **59**, 11782–11792.

61 A. Biffis, P. Centomo, A. Del Zotto and M. Zecca, *Chem. Rev.*, 2018, **118**, 2249–2295.

62 K. Muñiz, *Angew. Chem. Int. Ed.*, 2009, **48**, 9412–9423.

63 A. J. Canty, *Dalton Trans.*, 2009, 10409–10417.

64 A. J. Canty, H. Jin, A. S. Roberts, B. W. Skelton and A. H. White, *Organometallics*, 1996, **15**, 5713–5722.

65 T. Furuya and T. Ritter, *J. Am. Chem. Soc.*, 2008, **130**, 10060–10061.

66 A. J. Canty, M. C. Denney, B. W. Skelton and A. H. White, *Organometallics*, 2004, **23**, 1122–1131.

67 N. D. Ball and M. S. Sanford, *J. Am. Chem. Soc.*, 2009, **131**, 3796–3797.

68 R. S. Salama, M. A. Mannaa, H. M. Altass, A. A. Ibrahim and A. E. R. S. Khder, *RSC Adv.*, 2021, **11**, 4318–4326.

69 L. Bao, Z. Yu, T. Fei, Z. Yan, J. Li, C. Sun and S. Pang, *Appl. Organomet. Chem.*, 2020, **34**, e5607.

70 Q. Yang, F. Yao, Y. Zhong, F. Chen, X. Shu, J. Sun, L. He, B. Wu, K. Hou, D. Wang and X. Li, *Part. Part. Syst. Charact.*, 2019, **36**, 1800557.

71 S. Opelt, S. Türk, E. Dietzsch, A. Henschel, S. Kaskel and E. Klemm, *Catal. Commun.*, 2008, **9**, 1286–1290.

72 F. X. Llabrés I Xamena, A. Abad, A. Corma and H. Garcia, *J. Catal.*, 2007, **250**, 294–298.

73 S. Parshamoni, R. Nasani, A. Paul and S. Konar, *Inorg. Chem. Front.*, 2021, **8**, 693–699.

74 F. R. Fortea-Pérez, M. Mon, J. Ferrando-Soria, M. Boronat, A. Leyva-Pérez, A. Corma, J. M. Herrera, D. Osadchii, J. Gascon, D. Armentano and E. Pardo, *Nat. Mater.*, 2017, **16**, 760–766.

75 K. Ikemoto, Y. Inokuma, K. Rissanen and M. Fujita, *J. Am. Chem. Soc.*, 2014, **136**, 6892–6895.

76 L. Chen, S. Rangan, J. Li, H. Jiang and Y. Li, *Green Chem.*, 2014, **16**, 3978–3985.

77 P. Devendar, R. Y. Qu, W. M. Kang, B. He and G. F. Yang, *J. Agric. Food Chem.*, 2018, **66**, 8914–8934.

78 J. Nelson and S. M. Nelson, *J. Chem. SOL*, 1966, **8**, 572.

79 J. T. Moelwyn-Hughes, A. W. Garner and A. S. Howard, *J. Chem. Soc., Inorg. Phys. Theor.*, 1971, 2370–2377.

80 T. J. Reade, T. S. Murphy, J. A. Calladine, R. Horvath, I. P. Clark, G. M. Greetham, M. Towrie, W. Lewis, M. W. George and N. R. Champness, *Philos. Trans. R. Soc. A Math. Phys. Eng. Sci.,* 2016, **375**: 20160033

81 A. J. Blake, N. R. Champness, T. L. Easun, D. R. Allan, H. Nowell, M. W. George, J. Jia and X. Z. Sun, *Nat. Chem.*, 2010, **2**, 688–694.

82 A. R. Jupp, M. B. Geeson, J. E. McGrady and J. M. Goicoechea, *Eur. J. Inorg. Chem.*, 2016, **2016**, 639–648.

83 H. Werner, W. Beck and H. Engelmann, *Inorg. Mater.*, 1969, **3**, 331–335.

84 G. Minghetti, M. A. Cinellu, A. L. Bandini, G. Banditelli, F. Demartin and M. Manassero, *J. Organomet. Chem.*, 1986, **315**, 387–399.

85 W. M. Bloch, A. Burgun, C. J. Coghlan, R. Lee, M. L. Coote, C. J. Doonan and C. J. Sumby, *Nat. Chem.*, 2014, **6**, 906–912.

86 M. Mantina, A. C. Chamberlin, R. Valero, C. C. Cramer and D. G. Truhlar, *J Phys Chem A*, 2009, **113**, 5806–5812.

87 Á. Molnár, *Platin. Met. Rev.*, 2014, **58**, 93–98.

88 M. R. Biscoe, B. P. Fors and S. L. Buchwald, *J. Am. Chem. Soc.*, 2008, **130**, 6686–6687.

89 J. Norton, D. J. Valentine and J. P. Collman, *J. Am. Chem. Soc.*, 1969, **91**, 7537–7538.

90 H. Nowell, S. A. Barnett, K. E. Christensen, S. J. Teat, and D. R. Allan, *J. Synchrotron Rad.*, 2012, **19**, 435-441

91 T. M. McPhillips, S. E. McPhillips, H. J. Chiu, A. E. Cohen, A. M. Deacon, P. J. Ellis, E. Garman, A. Gonzalez, N. K. Sauter, R. P. Phizackerley, S. M. Soltis, and P. Kuhn, *J. Synchrotron Rad.*, 2002, **9**, 401-406

92 G. M. Sheldrick, *Acta Crys. A*, 2008, **64**, 1, 112-122

93 O. V. Dolomanov, L. J. Bourhis, R. J. Gildea, J. A. K. Howard and H. Puschmann., *J. Appl. Cryst.*, 2009, **42**, 339- 341.

94 A. L. Spek, *Acta Crystallogr. Sect. C Struct. Chem.*, 2015, **71**, 9–18.

95 CrystalMakerX©, CrystalMaker Software Ltd, Oxford, England, www.crystalmaker.com

96 W. De Graaf, J. Boersma, W. J. J. Smeets, A. L. Spek and G. Van Koten, *Organometallics,* 1989, **8**, 2907-2917.

97 S. Muñoz, J. Pons, J. García-Antón, X. Solans, M. Font-Bardia and J. Ros, *J. Coord. Chem.*, 2009, **62**, 3940–3950.

Chapter Five: Tuning the release of antibacterial silver ions from coordination polymers

5.1 Introduction

5.1.1 Drug Delivery

Treatment of disease through the development of new drugs that increase effectiveness and reduce side effects when compared to existing ones is an ongoing challenge. Non-lethal infections are a major health burden, with over 200,000 people annually, in Australia, developing infections in hospitals and other health care facilities.[1] This is also seen in other regions, with healthcare associated infections each year affecting 4.1 million patients in Europe and 1.7 million patients in the USA, causing 37,000 and 99,000 annual deaths respectively.[2] While most of these can be cured (infections are not among the leading causes of death)[3], the increasing incidence of multiple drug resistant bacteria in hospitals will cause escalating difficulties in treatment in the future. It was reported in 2014, in Australian hospitals and health care facilities, that 13% of all *E. coli* infections were resistant to more than three drug classes and 11-28% of *S. Aureus* infections were methicillin resistant (MRSA), depending on the clinical setting.[4] These rates are rapidly increasing as bacteria evolve resistances to the currently used antibiotics. This has been observed in the UK, where a 32% increase in antibiotic resistant bloodstream infections was reported between 2015 and 2019.[5]

One form of bacterial infections arises from the formation of biofilms on surfaces, including implants inside the body.[6] Biofilms are incredibly difficult to treat and often require combination therapy, even with susceptible strains of bacteria; however, biofilms have higher rates of formation with MRSA than from susceptible strains.[7] Under these conditions implants often need to be removed and replaced as the biofilms cannot be destroyed. It is for these reasons that the development of approaches to treat these diseases, in particular multiple-drug resistant bacterial infections, is of particular importance.

During recent years, advancements in innovative drug delivery systems has broadened the application of drugs from traditional oral, topical or intravenous application to many alternative routes, enabling the use of drugs with historically poor

solubility, physical or chemical stability or absorption.[8] Targeted, controlled drug delivery is necessary to avoid the non-specific release of drugs, minimise side-effects and resistance, and improve their therapeutic efficiency. Porous, inorganic materials, such as zeolites and mesoporous silicas are ideal for this due to their chemical stability, modifiable pores and large surface areas.[9] The use of functional materials for drug delivery has the potential to broaden applicability and enhance the effectiveness of current drugs and open the way for the use of new medicinal compounds.

5.1.2 Drug Delivery Materials

There are many matrices from which a pharmacologically actively compound can be embedded and released. Broadly they can be categorised by the materials they are made from and the mechanism by which the drug is released. Matrix materials include organic carriers such as polymers, micelles, dendrimers, liposomes, hydrogels and activated carbons and inorganic materials such as zeolites and meso-porous silica.[10] These can then be divided into passive or active delivery mechanisms, where passive delivery is controlled by simple diffusion from the carrier to the surrounding media and active delivery occurs as a result of stimulus.[10]

In using a drug delivery matrix, instead of traditional methods of drug delivery, pharmacokinetic control can be achieved to ensure that the active component is present at the therapeutic target in the concentration range over which it has the greatest effectiveness (Figure 5.1). These methods also improve the utility of hydrophobic compounds which normally would not dissolve in biological environments and of compounds which cannot pass through biological membranes to reach their target site. This is crucial, as approximately 40% of current pharmaceuticals have solubility limitations.[11] Using drug carriers can also protect the active compounds from biological degradation before they reach their target and can act as a reservoir for long term release of drugs. As such these materials have the potential to be used in drug containing membranes, coatings, wound fillers, and mobile nanoscale porous vectors.[10]

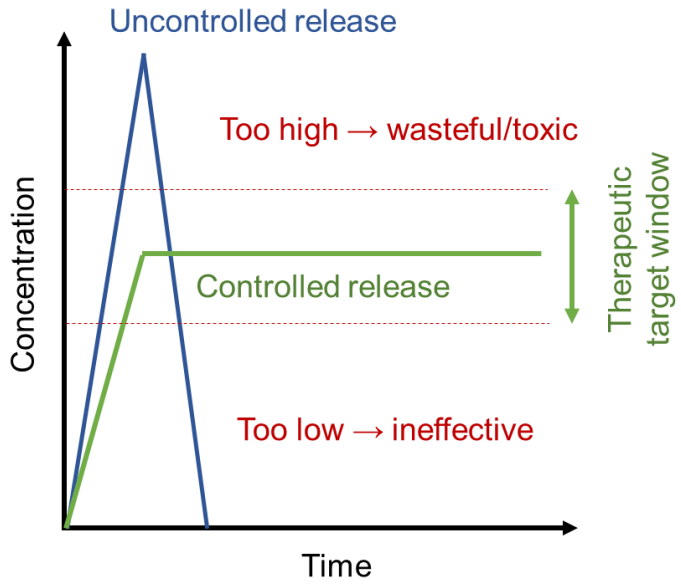

Figure 5.1. Controlled drug delivery ensures that the active compound is present at the biological target in the concentration range where it is most effective.

Among the organic materials considered for drug delivery are hydrogels, three-dimensionally cross-linked networks of hydrophilic polymers, which provide an ideal environment for wound healing due to their high water content. These materials can be loaded with medicinal compounds, for example metal nanoparticles, to give them additional properties such as antibacterial activity.[12] Hydrophilic compounds encapsulated into the hydrogel are released kinetically, while covalently bound drugs are freed through hydrolysis or enzymatic activity. However, tuning the release profile is difficult and their ability to be loaded with hydrophobic drugs is limited.[13] Most organic delivery systems (e.g. hydrogels, micelles and liposomes) show similar results, resulting in high biocompatibilities but low loading capacities and poor tunability.[14]

In comparison, some inorganic porous materials have been shown to have much higher loading capacities. Zeolites, with their large surface area and high adsorption capacity are promising candidates, and have been loaded with antibacterial,[15] anti-inflammatory[16] and anti-cancer[17] compounds; but are limited by poor loading efficiencies and release of the active compound from the pores is dependent on ion exchange. Silver nanoparticles loaded into activated carbon by Zhao *et al* were effective as an antibacterial agent, but silver loadings of only <2 wt.% were achievable.[18] An ideal drug delivery vehicle would combine the strengths of organic and inorganic porous materials to achieve high loading capacities, biocompatibility and release tunability.

5.1.3 MOFs and coordination polymers for drug delivery

MOFs or, more broadly, coordination polymers (CPs), combine the strengths of both organic and inorganic porous materials. These hybrid organic-inorganic materials have high surface areas and modifiable chemical and physical properties, making them ideally suited to drug delivery.[19] Furthermore, as they are formed through a 'building block' approach, their properties can be tuned at the atomic level through modification of the organic ligand, metal node and network topology. The highly tuneable nature of coordination polymers is what makes them of interest for controlled drug delivery, as they can utilise both passive and active release mechanisms. The vast library of metals and ligands available enables opportunities to tailor coordination polymers for the delivery of medicinal compounds to specific targets.

The coordination polymers which may be potentially used for drug delivery applications fall into three general categories:

1. Porous coordination polymers (MOFs) in which the pores can be loaded with a medicinal compound (see Figure 5.2 for a selected example). The drug molecules reside in the pore space and are held through weak intermolecular forces such as H-bonding, π-stacking or hydrophobic interactions. These are the most common systems found in the literature and the release of the active compound can be controlled through the flexibility of the framework (Figure 5.2),[20] post-synthetic modification of the pores,[21] or by utilizing temperature[22] or pH sensitive[23,24] pore opening. These materials have been shown to achieve higher loading capacities than other drug delivery vehicles,[14] and can be constructed from non-toxic building blocks to give low cytotoxicity.[25]

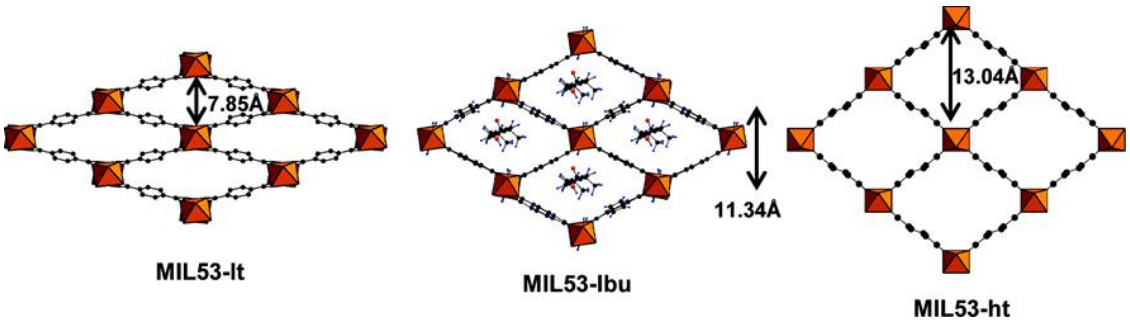

Figure 5.2. Drug storage and release in a MOF demonstrated by the encapsulation of ibuprofen inside the pores of flexible MIL-53.[20]

2. Coordination polymers constructed from metal nodes and/or organic ligands with inherent biological activity. In these cases, the coordination polymer must decompose to release the active components, eventually decomposing the entire framework (Figure 5.3). For this method to be successful both nodes and linkers must be either effective in similar concentration ranges, or one must be biologically inactive or harmless. For the release kinetics to be tuned, the parameters controlling the framework decomposition must be known and modifiable. Examples of materials in this class include silver,[26,27] copper[28] and zinc[29] coordination polymers with antibacterial activity and MOFs containing anti-osteoporosis drugs as the organic linkers.[30]

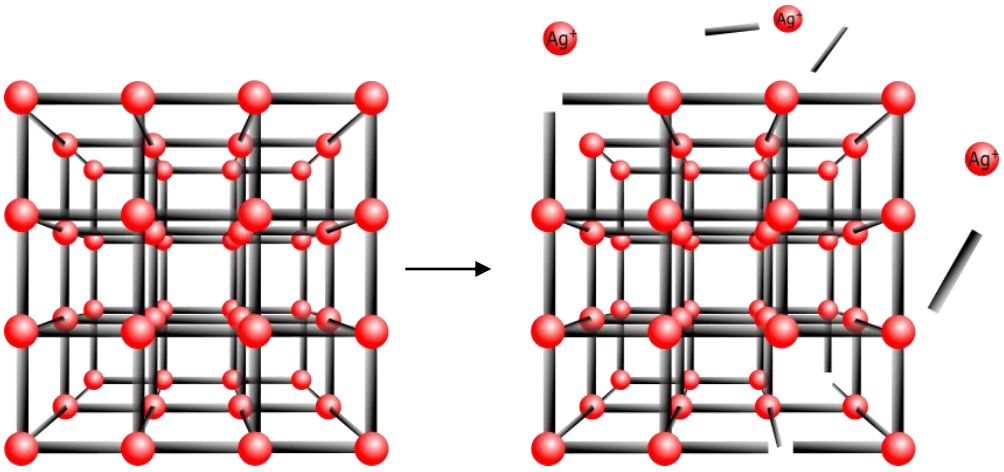

Figure 5.3. A schematic representation of the release of bactericidal silver ions from a coordination polymer susceptible to hydrolysis.

3. MOFs or coordination polymers in which the active compound is chemically bound to the framework, but which can be released without destruction of the overall coordination lattice (see Figure 5.4 for a selected example). The therapeutic agent could be coordinated to the ligand or metal node or only on the crystal surface. In these cases, the framework should be stable under biological conditions and the active compound is released with retention of the original structure. In an ideal case, for topical applications these materials would be able to be emptied then refilled and used again. The release of the active component can be

controlled through modifications of binding site, be it the coordinating ligand or metal centre. This method has only been reported in a few cases, in the most part for the release of small signalling molecules such as NO and CO.[31–33]

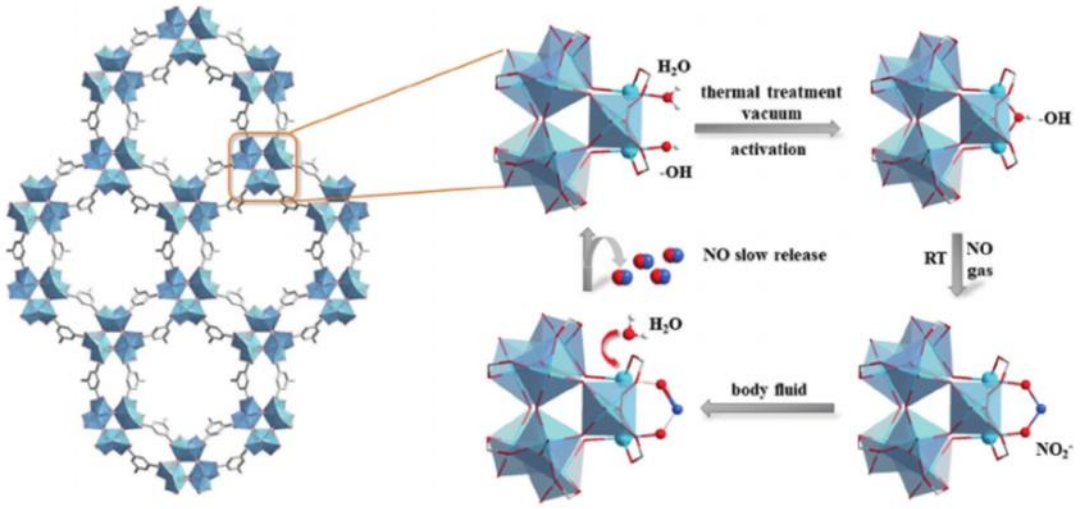

Figure 5.4. Post-synthetic activation of MIP-177 and subsequent NO binding, leading to the controlled release of NO under biological conditions due to hydrolysis and ligand substitution.[31]

For coordination polymers to be viable candidates for clinical use in drug delivery some fundamental questions must be addressed. One consideration for using coordination polymers over other, perhaps cheaper, materials that have been previously discussed, is the potential for their chemical and physical properties to be tuned at the atomic level. While many coordination polymers have been made and their medicinal properties demonstrated, little work has been attempted to tune these properties for a desired outcome. Indeed, little is known about the influence of variables, such as metal-ligand bond strength, porosity, crystal shape and particle size, on release of the active component. However, it is generally agreed that extensive and systematic study is required to understand the parameters governing the release of active compounds from coordination polymers.[34,35] To this end there have been several promising studies that have investigated the effects of topology, pore size and ligands. Cunha *et al* encapsulated caffeine in four common porous metal-organic frameworks, MIL-100 (Fe), MIL-127 (Fe), MIL-53 (Fe) and UiO-66 (Zr).[36] Loadings of up to 50 wt % were achieved and the release kinetics tested in water and the simulated physiological conditions of PBS broth (Figure 5.5). It was concluded from this study that the release of an encapsulated single molecule is controlled primarily by the stability of the framework

to degradation, the mobility of the molecule out of the pores (lower for flexible frameworks) and the strength of the host-guest interactions.

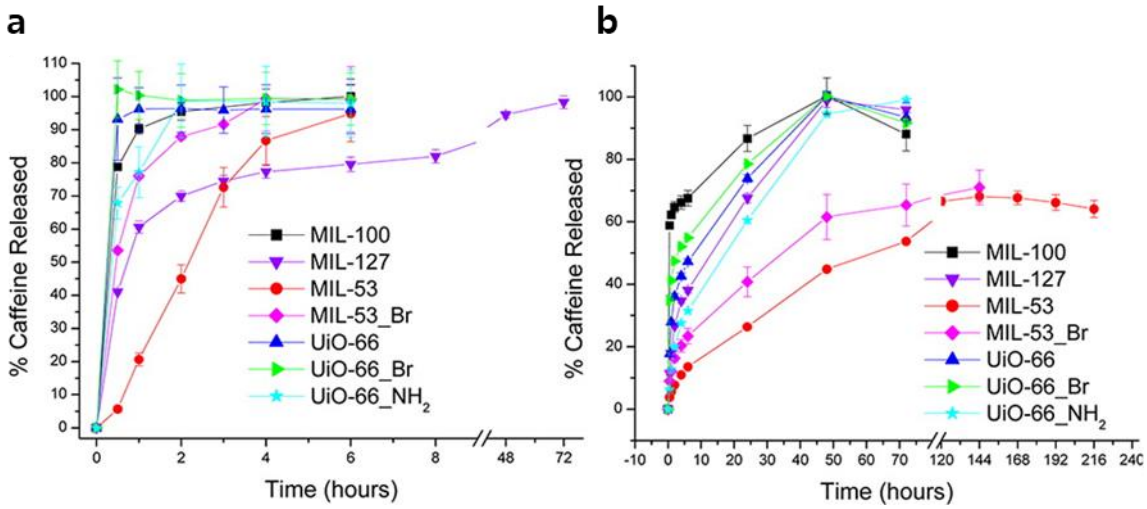

Figure 5.5. Caffeine release profiles from porous MOFs in a) PBS buffer and b) aqueous media at 37 °C.[36]

Teplensky *et al* showed that it is possible to slow the release kinetics of a model drug compound from the zirconium MOF NU-1000.[21] To achieve this, the loaded material was heated to partially collapse the very large pores, hence limiting the diffusion of the compound out of the framework. The scope of this technique is limited, as it only would work for frameworks in which the pore size was the defining parameter to the release kinetics. Moreover, it does not take advantage of the very properties which make coordination polymers so promising, namely being able to synthetically modify the chemical structure.

The loading of multiple drugs into UiO-66 for combinatorial cancer treatment was explored by Lázaro *et al*, in which carboxylate or phosphonate containing drug molecules could act as modulators in the synthesis of the MOF and hence bind to defect sites within the UiO-66 structure (Figure 5.6).[37] This resulted in isostructural MOF frameworks which still maintained accessible pores, which were then filled with another anticancer drug post-synthetically. As such, it was demonstrated that four drugs could be loaded in quantities varying from 1.6 – 27.5% in a single MOF. It was found by using this combination of drugs in a MOF carrier, much higher selectivity towards cancer cells could be achieved. This study demonstrated how defect engineering of the MOF lattice can introduce new sites for drug storage; however, release kinetics were not reported.

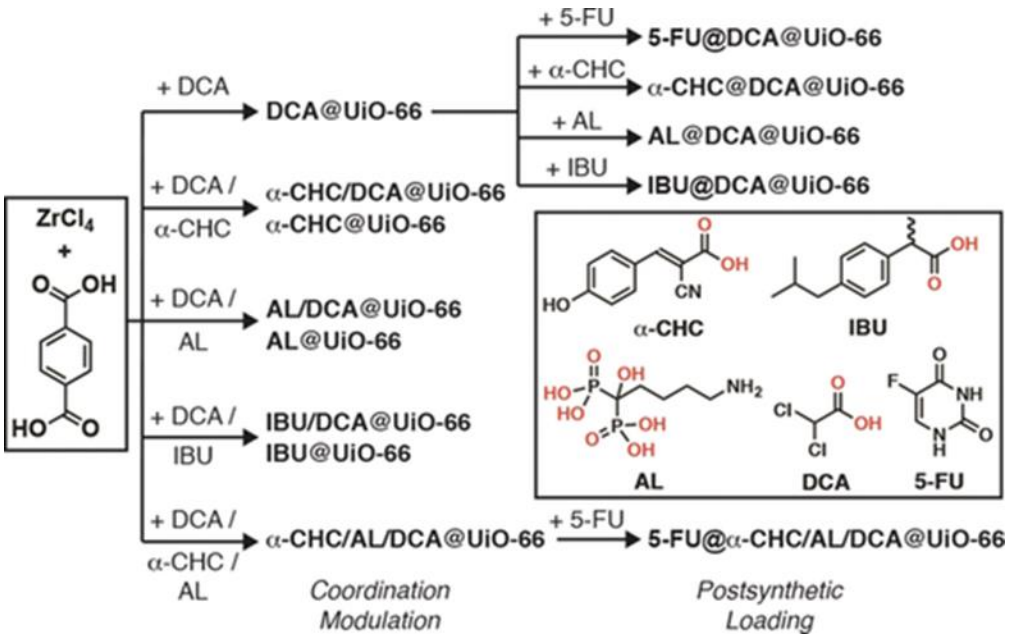

Figure 5.6. Anticancer drug molecules used as multivariate modulators in the synthesis of UiO-66, the pores of which could then be post-synthetically loaded with an additional therapeutic agent.[37]

Of course, when considering MOFs for use as therapeutic agents the potential effects on healthy cells as well as the target cells must be considered. There are several approaches that may be considered to tackle this problem. The first is to construct the MOF from 'safe' components, so that the decomposition of the MOF has no harmful effects. This approach was used by Chen *et al*, in synthesising a MOF from γ-cyclodextrin and potassium ions to be used for the storage and release of curcumin from the pores.[38] The second is to design MOFs which are stable under the therapeutic conditions and so only release the drug and not any degradation products into the body. The final approach is to incorporate the MOFs into a secondary material, such as a polymer, which may act as a barrier for the release of some degradation products.[39]

MOFs and coordination polymers have shown great promise as drug delivery agents, through their inherent components, or when loaded with one or multiple therapeutic agents. There are; however, still many challenges to be overcome before these materials can be used in clinical settings, and there is much scope for the exploration of the medicinal applications of MOFs and coordination polymers.

5.1.4 Silver and Coordination Polymers for Antibacterial Applications

For centuries, it has been known that silver has antibacterial properties, from the use of silver vessels in ancient Persia for keeping wine or water fresh[40] to the drinking of aqueous colloidal dispersions in the 19th century to prevent infections.[41] With the advent of the age of antibiotics in the middle of the 20th century[42] silver compounds were superseded by molecular antibiotics, which for a time seemed to provide the cure for the majority of the world's deadly diseases. Yet even during this period silver nitrate was used in antibacterial eye drops and silver sulfadiazine in a cream to treat burns,[43] even though the exact mechanisms by which silver kills bacteria are still not well understood today. In recent years, it has become evident that the rise in strains of bacteria resistant to multiple drugs will soon render current frontline treatments ineffective, and silver, due to its effectiveness against such resistant bacteria, may find further use.

The form of silver known to be active against bacteria is the Ag(I) cation rather than the neutral metal. The cation can interact with a bacterial cell in several ways to cause cell death; although not all mechanisms occur in all bacterial strains. These multiple mechanisms of action are the main advantage silver has over molecular antibiotics, which have only a single target and hence the development of resistance is relatively easy. In comparison, the development of resistance to silver is inherently difficult as it would require several mutations in the bacterial cell.[44] Some of the main ways in which Ag^+ ions target bacteria are as follows; detaching the cell wall from the cell membrane,[45] binding to DNA,[45] membrane proteins,[46,47] active sites of enzymes[46] and NADH dehydrogenase (Figure 5.7).[48,49]

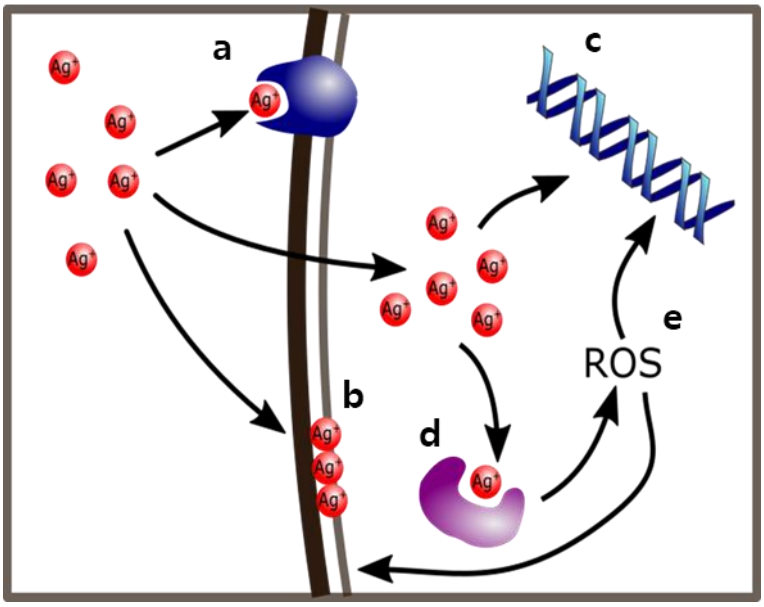

Figure 5.7. Mechanisms through which silver ions can interact with bacterial cells, namely, **a)** binding to membrane proteins and disrupting the proton motive force, **b)** accumulating in the cell membrane and causing it to break away from the cell wall and rupture, **c)** binding to DNA, preventing replication, **d)** binding to enzymes which inhibits activity, **e)** the production of reactive oxygen species (ROS) from binding to NADH dehydrogenase, which can then attack DNA and the cell membrane.

Silver coordination polymers have been shown to have antibacterial effects which are postulated to be from the hydrolysis of the framework to release silver ions into solution.[49] There have been several studies exploring the antibacterial effects of silver coordination polymers; however, in several instances the researchers inexplicably dissolved the coordination polymer before testing,[50–52] thus ignoring any benefit of using a crystalline network, and giving little useful information into how coordination polymers differ from using silver salts. Others have incorporated silver coordination polymers onto or within surfaces to again examine antibacterial properties. Gordon *et al* grew 1D silver coordination polymer chains onto gold surfaces, which proved to be very effective against *S. epidermidis* bacteria. This presents little scope for modification and tuning the antibacterial properties due to the very specific requirements needed to make the 1D coordination polymer and form the attachment to the surface.[53]

Previous work by Rueff *et al* showed that two silver coordination polymers constructed from the same phosphono-benzoic acid ligand and metal salt had different dissolution rates.[54] In this case the framework topology of the silver coordination polymers was determined by the pH used in the hydrothermal synthesis, resulting in either coordination of the metal ions to both the phosphate and carboxylate groups, or only the phosphates. It was found that, as expected, the structures with free

carboxylates dissolved faster than the compounds with silver coordinated carboxylic acids. This does not show whether framework topology inherently controls the dissolution properties of a coordination polymers, as the coordination environment of each metal node was different, even though the chemical components were identical.

Thus, silver salts and silver coordination polymers have been shown to be effective antibacterial agents in a range of studies; however, the mechanism by which silver ions are released from the solid-state material, and the parameters controlling this, such as functionality of the ligand, speciation of the metal precursor, topology, particle size and accessibility of metal centres to solvent, have not been well explored.

5.2 Aims

The following study investigates the effect of topology on the antibacterial properties of four silver coordination polymers. The kinetics of dissolution and hence release of silver ions were analysed for the coordination polymers, both in their as-synthesised forms and embedded into polymer films, thus also exploring consequences of forming coordination polymer-organic polymer composites. The antibacterial activities of the Ag-coordination polymer/polymer composites were analysed by disk diffusion and growth assays to analyse whether silver ion release into water correlates with antibacterial potency.

Statement of Authorship

Title of Paper	Exploring the Use of Structure and Polymer Incorporation to Tune Silver Ion Release and Antibacterial Activity of Silver Coordination Polymers
Publication Status	☑ Published ☐ Accepted for Publication ☐ Submitted for Publication ☐ Unpublished and Unsubmitted w ork w ritten in manuscript style
Publication Details	R. J. Young, S. L. Begg, C. J. Coghlan, C. A. McDevitt and C. J. Sumby, *Eur. J. Inorg. Chem.*, 2018, **2018**, 3512–3518.

Principal Author

Name of Principal Author (Candidate)	Rosemary Young		
Contribution to the Paper	Design, development, and execution of experiments. Analysis and interpretation of data and preparation of the manuscript.		
Overall percentage (%)	70%		
Certification:	This paper reports on original research I conducted during the period of my Higher Degree by Research candidature and is not subject to any obligations or contractual agreements with a third party that would constrain its inclusion in this thesis. I am the primary author of this paper.		
Signature		Date	5/5/21

Co-Author Contributions

By signing the Statement of Authorship, each author certifies that:

i. the candidate's stated contribution to the publication is accurate (as detailed above);

ii. permission is granted for the candidate in include the publication in the thesis; and

iii. the sum of all co-author contributions is equal to 100% less the candidate's stated contribution.

Name of Co-Author	Dr Stephanie Begg		
Contribution to the Paper	Assisted with the conception and execution of the antibacterial studies. Assisted with drafting the manuscript.		
Signature		Date	5/5/21

Name of Co-Author	Dr Cambell Coghlan		
Contribution to the Paper	Assisted with the conception and execution of MOF synthesis, dissolution, and characterisation experiments. Assisted with drafting the manuscript.		
Signature		Date	5/5/21

Name of Co-Author	Prof. Christopher McDevitt		
Contribution to the Paper	Assisted with conception of the project. Assisted with drafting the manuscript.		
Signature		Date	5/5/21

Name of Co-Author	Prof. Christopher Sumby		
Contribution to the Paper	Assisted with the conception of the project, data analysis and preparation of the manuscript.		
Signature		Date	20/05/2021

5.3 Using structure to tune silver ion release and antibacterial activity of silver coordination polymers

Rosemary J. Young,[a] Stephanie L. Begg,[b] Campbell J. Coghlan, [a] Christopher A. McDevitt[b] and Christopher J. Sumby*[a]

Abstract: The use of silver as an antibacterial agent has seen renewed interest as a result of its ability to combat a broad range of bacterial species, including those resistant to multiple classes of antibiotics. Silver coordination polymers (CPs) provide the opportunity to control the release of silver ions, thus avoiding unwanted side effects and toxicity; however, the parameters that tune release remain poorly understood. Here, four silver CPs, namely [Ag_2(**Me_4bpz**)] as both four- and eightfold interpenetrated forms, and [Ag(**dpzm**)(ClO_4)] in its open 3D and close-packed 2D forms, were used to probe the role of structure in the release of silver ions. Release was measured by inductively-coupled plasma mass spectrometry (ICP-MS) and shown to be more marked for the charged networks, [Ag(**dpzm**)(ClO_4)] (complete dissolution). Incorporation of the silver CPs into inert polymer matrices, polyethylene and polycaprolactone, to provide surface coatings was also investigated, and shown to significantly retard silver ion release. The antibacterial activities of all materials as their polymer composites were analysed by disk diffusion and bacterial growth assays. All CPs showed antibacterial activity, with the Gram-positive *Staphylococcus aureus* exhibiting greater sensitivity to silver than the Gram-negative *Escherichia coli*. Metal–ligand bond strength and anion availability were found to influence silver release into aqueous solution but this did not always correlate with the in vitro antibacterial activity.

Introduction

The antibacterial properties of silver have been exploited for centuries,[40,41] but widespread usage was superceded by the development of microbial-derived antibiotics in the 20th century.[42] However, rising rates of multi-drug resistance in human bacterial pathogens and a paucity of new antibiotics has lead to renewed interest in other antibacterial treatments, including silver, with silver salts currently used in topical applications to treat infections.[43,55] The cationic form of silver is known to be antibacterial, displaying multiple mechanisms of action in both species- and concentration-dependent manners.[45–49,56] These multiple mechanisms of action are considered an advantage for silver in comparison to microbial derived antibiotics, which typically only have a single target, and have the potential to limit the development of resistance.[44] Further, silver is one of the most toxic of the microelements to many microorganisms, more so than even mercury and cadmium, while being significantly less toxic to eukaryotic cells.[57]

Although various simple silver salts can be utilised in topical applications,[58] targeted and controlled release of silver is desirable for implant coatings and wound treatment, where long-term activity is required.[44,59] Controlled release from a variety of supporting matrices has been explored, including silver nitrate loaded zeolites[15] and hydrogels,[12,60] and activated carbon containing silver nanoparticles.[18] Temporal control of release by silver coordination polymers (Ag-CPs),[49] a class of crystalline extended solids comprised of metal ions coordinated by organic linkers, has also been investigated. These materials, which are also known as metal-organic frameworks (MOFs), are promising drug delivery vehicles due to their highly tunable composition and structure. Coordination polymers constructed from silver can provide a reservoir of silver ions, which are protected from agglomeration or reaction.[61] The decomposition of Ag-CPs results in the release of small, solvated silver (I) complexes[49] that are potentially active against bacteria. It therefore follows that silver release by means of decomposition can be tuned through the structure by precursor selection, the topology of the coordination polymer and the crystal morphology.

The antibacterial properties of 1D,[53] 2D[50,62] and 3D Ag-CPs[50,54] have been previously explored, and have shown to be very effective in a range of applications, from treating contaminated lake water containing a wide range of bacterial species[63] to preventing implant infection in vivo.[53] There are, however, limited reports correlating activity with chemical composition[61] and/or structure.[52] In part this is due to the established clinical diagnostic methods for testing antibiotic efficacy, including minimum inhibitory concentrations (MICs) and measuring cell counts by optical density (OD), being inadequate for solid state materials such as coordination polymers. As a consequence, it is difficult to readily compare the activities of distinct coordination polymers to develop structure-activity relationships. A number of water soluble Ag-CPs have previously been investigated and have shown antibacterial activity against a range of bacterial species.[64–67] These studies reported different topologies to have altered antibacterial activities; however, as these experiments were done in solution it is problematic to extend these observations to the solid state for the controlled release of silver. Furthermore, solid state Ag-CPs are challenging to incorporate as

[a] R. J. Young, Dr C. J. Coghlan and Prof. C. J. Sumby*
Department of Chemistry and the Centre for Advanced Nanomaterials, School of Physical Sciences
University of Adelaide
Adelaide, South Australia, 5005, Australia
E-mail: christopher.sumby@adelaide.edu.au
[b] Dr S. L. Begg and A/Prof. C.A. McDevitt
Research Centre for Infectious Diseases, School of Biological Sciences
University of Adelaide
Adelaide, South Australia, 5005, Australia
Supporting information for this article is given via a link at the end of the document.

coatings on medical instruments and implants. A previous method to surmount this issue has involved the growth of Ag-CPs directly onto surfaces; however, this technique is limited in scope to specific CPs and their applications.[53] Another approach involved using CPs as a physical barrier to the release of molecular antibacterial agents loaded into titania nanotubes.[68] In such a system the Ag-CP was not the primary antibacterial agent buy the means by which the delivery of the molecular antibacterial agent was controlled. Decreases in the environmental acidity, associated with bacterial infection, resulted in the decomposition of the CP and the subsequent release of the drugs. However a preferred strategy is to embed the Ag-CPs directly into polymer coatings. This is advantageous because it is widely applicable, utilises the inherent antibacterial properties of Ag-CPs and may prevent the development of implant infections and biofilms.[62,69] This work investigates two polymer matrices for the development of antibacterial implant coatings. Polyethylene (PE) is currently used in a wide range of medical implants and is noted for its good biocompatibility.[70] Polycaprolactone (PCL), exhibits the potential to biologically degrade after 3-4 years, making it a viable candidate for biodegradable implants.[71]

Here we report how ligand choice and framework topology, including solvent accessible void volume, contribute to the decomposition of Ag-CPs. We further show a role for polymeric supports like PE and PCL in modulating this activity. We also assess methods for testing antibacterial activity of Ag-CPs incorporated into organic polymer matrices. To examine these aspects four Ag-CPs with similar building blocks were selected as model compounds, namely [Ag_2(**Me_4bpz**)][72] (where **Me_4bpz** = 3,3',5,5'-tetramethyl-4,4'-bipyrazole) as both fourfold (**CP-1**) and eightfold (**CP-2**) interpenetrated forms, and [Ag(**dpzm**)(ClO_4)][73] (where **dpzm** = 2,2'-dipyrazinylmethane) in its open 3D (**CP-3**) and close-packed 2D (**CP-4**) forms (Scheme 1).

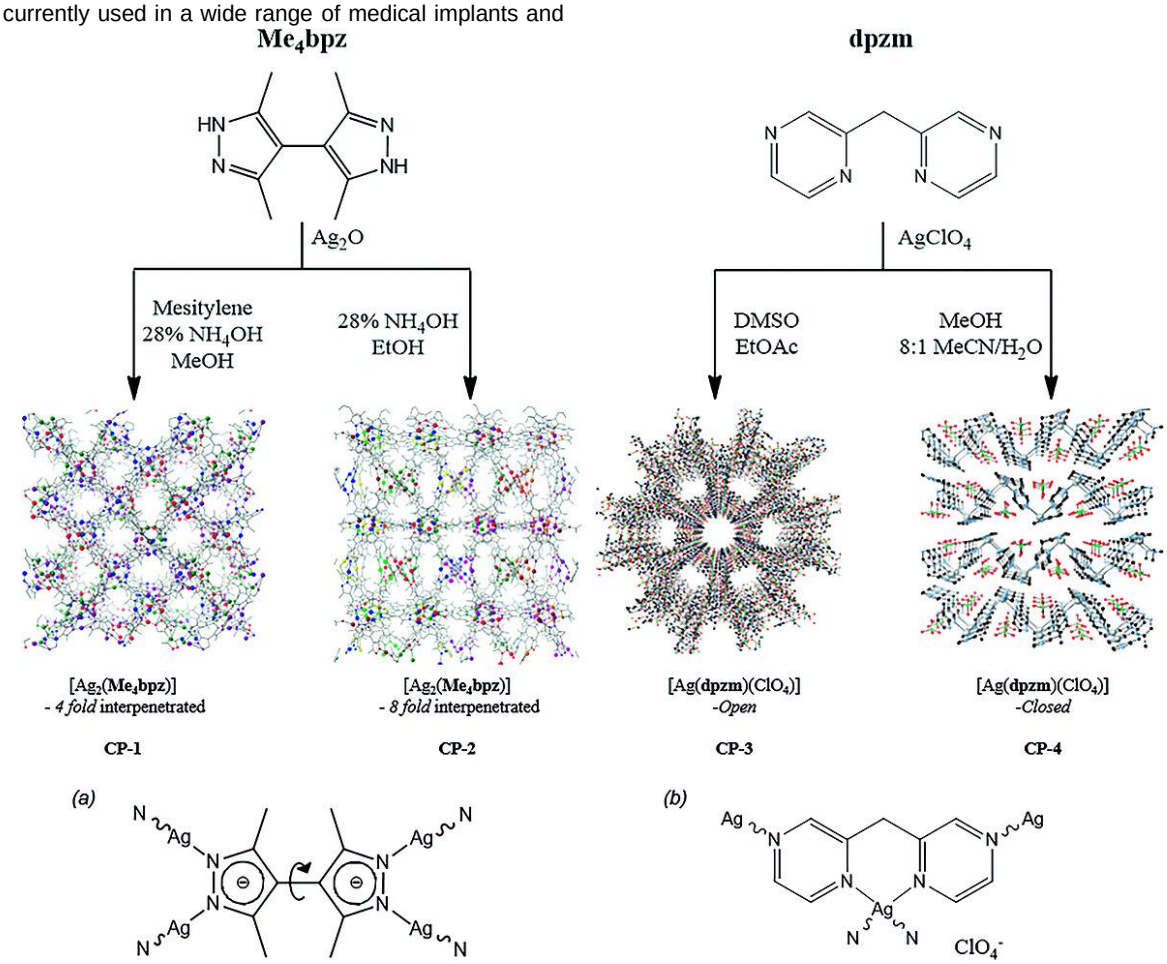

Scheme 1. Conditions of synthesis and structures of [Ag_2(**Me_4bpz**)] - *fourfold* interpenetrated, [Ag_2(**Me_4bpz**)] - *eightfold* interpenetrated, [Ag(**dpzm**)(ClO_4)]-*Open* and [Ag(**dpzm**)(ClO_4)]-*Closed* (**CP-1, -2, -3** and **-4** respectively). a) Coordination environment of **CP-1** and **CP-2**, with structural variation arising from rotation of the pyrazole rings. b) Coordination environment of **CP-3** and **CP-4**. Cambridge Crystallographic Database Centre (CCDC) numbers are given in the Experimental Section.

Results and Discussion

The Ag-CPs were prepared using previously reported synthetic methods as either single crystals or microcrystalline powders,[72–74] and their structures confirmed by PXRD (see Figures 5.11 and 5.12 in the Appendix). The four CPs have closely related chemical compositions with simple heterocyclic ligands; these can be separated into two pairs, each containing an open, potentially porous structure and a more densely packed material constructed from the same ligand and silver source. Each pair contains silver ions with the same coordination environment [Scheme 1 (a) and (b)], but different topology, accessed by established synthetic methods (Scheme 1).[72,73] [Ag_2(**Me$_4$bpz**)]-*4/8-fold* (**CP-1/CP-2**) are charge neutral materials that display high chemical and thermal stability (300°C vs 185/260°C for [Ag(**dpzm**)(ClO_4)]-*open* and -*closed* respectively).[72] [Ag(**dpzm**)(ClO_4)]-*open* and -*closed* (**CP-3**/**CP-4**), are cationic coordination polymers wherein the open 3D form readily converts to a close-packed 2D form in response to heat and pressure.[73]

Dissolution of Ag-CPs

Ag-CP dissolution is necessary for antibacterial activity. This was assessed by measurement of silver concentrations in solution. First, the dissolution behaviour of the four Ag-CPs in water was analysed by inductively-coupled plasma mass spectrometry (ICP-MS). Both [Ag(**dpzm**)(ClO_4)]-*open* and -*closed* dissolved completely within 3 hrs, with the close-packed, 2D form showing more rapid final dissolution (Figure 5.8). After only one hour 75% of the silver in [Ag(**dpzm**)(ClO_4)]-*open* and 80% in [Ag(**dpzm**)(ClO_4)]-*closed* had been released, showing that the dissolution of both forms of [Ag(**dpzm**)(ClO_4)] occurs very quickly after they are immersed in water. Particle size and shape may play a role in these observations, but the release rates and final silver concentrations were broadly similar (87±7% and 108±13% for the open and closed forms, respectively).

The dissolution rates of microcrystalline powders of [Ag_2(**Me$_4$bpz**)]-*4 fold* and [Ag_2(**Me$_4$bpz**)]-*8 fold* were much slower and so dissolution was analysed over 24 hrs. This showed that ~6.5% and ~5% of the silver content in the frameworks, respectively, was released into solution within 24 hrs. There was no appreciable increase in the silver concentration after 8 hrs, suggesting that an equilibrium had been reached. The 4-fold interpenetrated framework decomposed faster and to a greater extent than the 8-fold interpenetrated analogue, suggesting that physical parameters such as particle size or topology influence dissolution, as the materials were chemically identical.

While the extent of interpenetration cannot be explicitly excluded, scanning electron microscopy (SEM) showed that the 8-fold interpenetrated crystals (ranging from 0.5-10 µm) were larger than their 4-fold interpenetrated counterparts (0.5-1 µm) (Figure 5.17). These differences

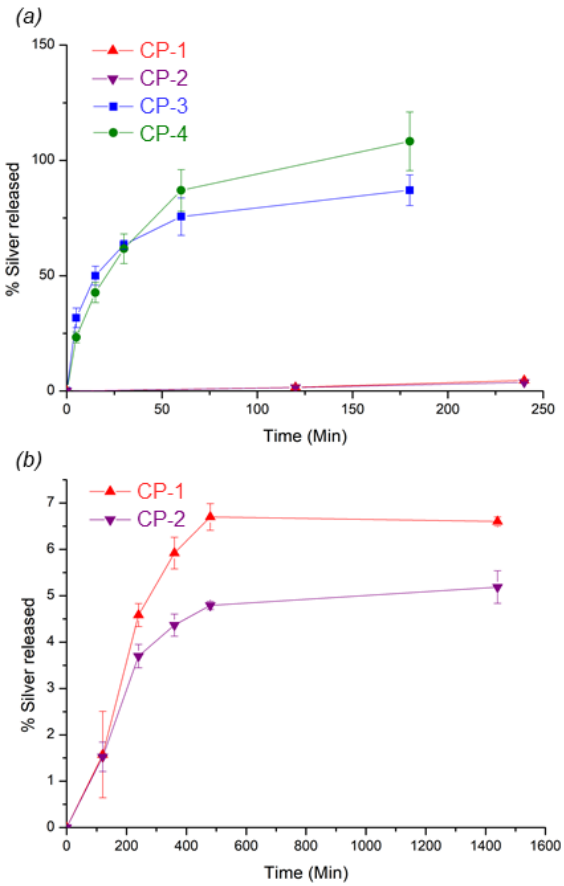

Figure 5.8. Silver release profiles of *(a)* **CP-1**, **-2, -3** and **-4** over 240 min showing complete dissolution of **CP-3** and **CP-4** in 180 min and *(b)* **CP-1** and **CP-2** over 1440 min, showing equilibrium being reached after 480 min.

in crystal size are an artefact of the differing synthesis conditions, with the rapid stirring method used for [Ag_2(**Me$_4$bpz**)]-*4 fold* producing smaller and more uniform crystals than the slow diffusion method used for [Ag_2(**Me$_4$bpz**)]-*8 fold*.

From these results it is evident that the nature of the metal-ligand bond has the most influence on the dissolution. As a soft Lewis acid, the bond strengths between silver and its ligands can be correlated to the pK_a of the organic ligand.[75] Therefore, a decrease in pK_a will accompany a decrease in the stability of the bond to hydrolysis. Thus, pyrazole ligands (pyrazole pK_a ~ 19.8) will form Ag-CPs that are more water stable than pyrazine ligands (pyrazine pK_a ~ 0.6), which coordinate to silver as neutral molecules. For [Ag_2(**Me$_4$bpz**)]-*4 fold* and [Ag_2(**Me$_4$bpz**)]-*8 fold* interpenetrated, the very strong bond between the cationic metal and anionic pyrazole nitrogen donor results in the framework being stable to hydrolysis and as a consequence, releases very little silver into solution. In contrast, the weaker pyrazine nitrogen-silver bonds facilitated complete dissolution. These observations can be correlated with the thermogravimetric analyses (TGA) of the Ag-CPs. [Ag_2(**Me$_4$bpz**)]-*4 fold* and [Ag_2(**Me$_4$bpz**)]-*8 fold* interpenetrated decompose at 300°C and 350°C respectively,[72] while [Ag(**dpzm**)(ClO_4)]-*open* performs a

structural rearrangement at 185°C, converting into [Ag(**dpzm**)(ClO_4)]-*closed* (which decomposes above 260°C).[73] The equilibrium of the hydrolysis of the Ag-CPs is driven not only by the bond strength, but the stability and ease of formation of soluble silver complexes. The pyrazine frameworks contain anions (ClO_4^-), which result in the formation of silver salts in solution, in contrast to the charge neutral pyrazolate CPs, which require the anionic ligand to solubilise. Combined, these results demonstrate the nature of the organic ligand donor to be a significant factor governing dissolution.

Previous studies which measured the decomposition of Ag-CPs into water reported silver release of 0.07-14% over a maximum of five days, depending on the ligand and dimensionality of the structure.[52–54] In all studies equilibrium was reached 6-10 hrs after immersion in water. The study by Rueff *et al* showed that two Ag-CPs with the same ligand, a 3D CP coordinated through phosphorus and oxygen donors and a 2D CP coordinated through only phosphorus, showed differing silver release of 0.07-0.2% and 5.4-5.9% respectively.[54] A 3D carboxylate Ag-CP by Lu *et al* resulted in 2.5% release and Gordon *et al* demonstrated a 1D pyridine Ag-CP had 14% release.[52,53] These studies suggest that Ag-CPs comprised from ligands with a higher pKa and higher dimensionality are more resistant to hydrolysis and thus release fewer silver ions into solution. This is consistent with the results of this study, and shows [Ag(**dpzm**)(ClO_4)]-*open/closed* have the highest release rate of any of the materials studied, even when compared to the 1D pyridine based Ag-CP from Gordon *et al*.[53] This demonstrates that the pKa of the ligand (the conjugate acid in these cases), for which pyridine is higher than pyrazine (pK_a~5.2 compared to ~0.6), is of greater importance than the dimensionality when influencing the hydrolysis of the coordination polymer.

Incorporation into Polymer Matrices

Several strategies exist for depositing Ag-CPs on surfaces. Gordon *et al.* synthesised a CP on orientated Au (III) and Ti (III) monolayers,[53] while Tabacaru *et al.* showed that Ag-CPs could be incorporated into PE matrices.[62] Building on that approach, the four Ag-CPs were embedded into PE and PCL matrices in a matrix-dependent manner; specifically thermal treatment of the microcrystalline Ag-CPs and PE to give PE-based films or dissolution and evaporative casting for PCL-CP composites. Disks were cut from both types of polymer composites and the silver release into water was analysed using the methodology outlined above. It was observed that the incorporation of all Ag-CPs into polymer drastically reduced the silver release over 24 hrs.

Indeed, for all [Ag_2(**Me_4bpz**)] containing composites the release values were too low (<1% of available Ag) to permit valid comparisons to be made (Figure 5.19). Both [Ag(**dpzm**)(ClO_4)]-*open* and -*closed* embedded into PE and PCL showed both a dramatic reduction in silver release compared to the native CPs, but also a marked

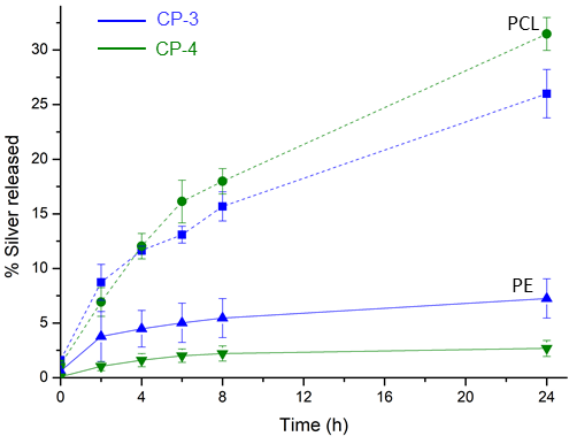

Figure 5.9. Silver release profiles of CP-3 (blue) and CP-4 (green) impregnated into polyethylene (PE, solid line) and polycaprolactone (PCL, dashed line) disks over 24 hours.

difference between the polymer composites (Figure 5.9). The CPs embedded into PCL released approximately five times more silver than those embedded into PE. The trend of the release over time showed than even after 24 hrs, the concentration of silver in solution continued to increase, without the complete release or equilibrium evident for the pure Ag-CPs. The variance in the release rates between the two types of embedded polymers may be a consequence of the water permeability of the polymers, which for water vapour is <0.3 g/m^2/day for PE[76] and 177 g/m^2/day for PCL,[77] for films 1 mm in thickness. The much higher water permeability of PCL allows for increased hydrolysis and diffusion of the silver ions into solution. These results suggest that the water vapour permeability is a good measure for the extent that a polymer matrix will retard the decomposition of Ag-CPs.

Ag-CPs tend to show lower thermal and chemical stability compared to most MOFs. Studies of the [Ag(**dpzm**)(ClO_4)]-PE composites (Figure 5.9) revealed the *open* structure released more Ag compared to the *closed* framework when encapsulated. In particular, this contrasted with both the results from the PCL composites and pure CPs. PXRD data (Figure 5.13) revealed that the heating process necessary to prepare the composite caused a structural rearrangement of the *open* form to the *closed*. Such transformations have been shown for [Ag(**dpzm**)(ClO_4)]-*open*, and take place through single-crystal to micro-crystalline transformations at 185°C.[78] In this work the structural rearrangement occurred during the embedding process which combined thermal (90°C) and mechanical stresses. Thus the following Ag release studies show data for PE composites of only [Ag(**dpzm**)(ClO_4)]-*closed* forms, with a likely explanation for the differences between the two samples being due to crystal size ([Ag(**dpzm**)(ClO_4)]-*open* embedded into PE is denoted as [Ag(**dpzm**)(ClO_4)]-*closed** to indicate that it is the converted material subsequently), therefore resulting in higher particle surface area and so higher silver release.

Antibacterial studies

The antibacterial activities of composites of the four Ag-CPs embedded within PE and PCL were analysed by disk diffusion (Figure 5.3 and Figure 5.20) and bacterial growth assays (Figures 5.21 and 5.22). From the disk diffusion assays it was evident that all four Ag-CPs had antibacterial activity, albeit to varying extents.

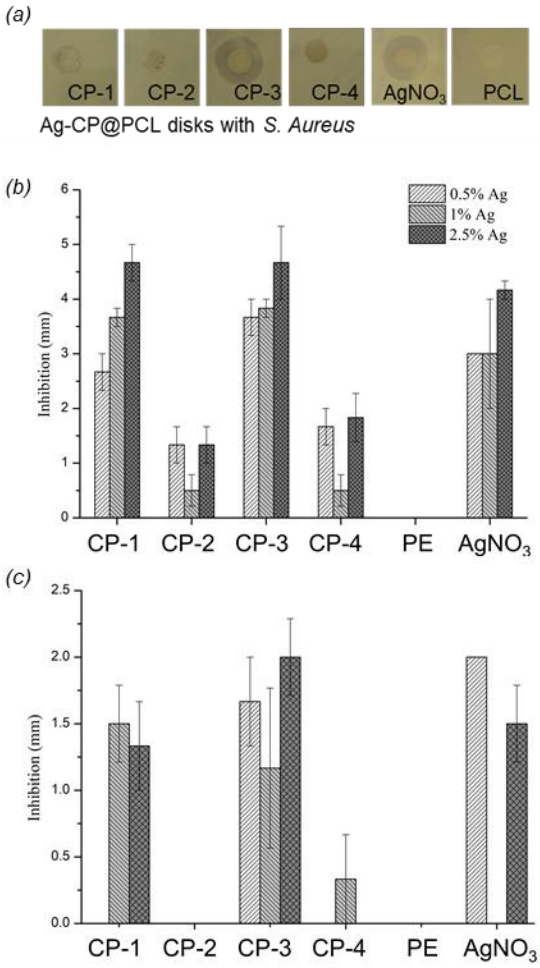

Figure 5.10. ***(a)*** Representative zones of inhibition observed around 5 mm Ag-CP impregnated PCL disks for *S. aureus*. Zones of inhibition measured for PE disks impregnated with silver CPs at different loadings against ***(b)*** *E. coli* and ***(c)*** *S. aureus*. Untreated PE and silver nitrate loaded disks were used as negative and positive controls respectively. The sample labelled **CP-3** is [Ag(dpzm)(ClO_4)]-*open* embedded in PE that has undergone the 3D to 2D transformation to [Ag(dpzm)(ClO_4)]-*closed** (which produces smaller particles).

The Gram-positive human bacterial pathogen *Staphylococcus (S.) aureus* revealed greater sensitivity to silver than the Gram-negative pathogen *Escherichia (E.) coli* upon testing, and contrary to the silver release studies, the Ag-CPs embedded into PE (Figure 5.10) were more effective than those embedded in PCL (Figure 5.20). This may be due to differences between diffusion rates into aqueous media by comparison with the solid agar medium, as well as the presence of salts and amino acids required for bacterial growth. In general [Ag(**dpzm**)(ClO_4)]-*closed** showed the greatest antibacterial activity, comparable in most cases to the silver nitrate control.

Interestingly [Ag_2(**Me_4bpz**)]-*4 fold* (0.5-1 μm particle size) embedded into PE, also showed higher than expected antibacterial activity, with zones of clearance comparable to silver nitrate, while its activity when embedded into PCL was much lower (Figure 5.10 and Figure 5.20). As the PE composites showed the best antibacterial activity, growth assays were conducted for the Ag-CPs embedded into PE, which was reduced to a granular form. Again [Ag(**dpzm**)(ClO_4)]-*closed** showed the greatest activity and was as effective as silver nitrate at eliminating viable cells (Figures 5.21 and 5.22).

These studies show that while Ag release and decomposition into water may provide an indication of the stability of the Ag-CPs and their capacity for Ag release, the release into biological media and interactions with bacterial cells are more complex. [Ag_2(**Me_4bpz**)]- *4-fold/8 fold* released negligible quantities of silver into water, but displayed antibacterial activity in the disk diffusion assays. This may be due to the limited solubility of the anionic ligand in deionised water, which does not contain the anions needed to form silver complexes in solution. The bacterial assay conditions used a broth with large quantities of salts and amino acids required for bacterial growth. Consequently, complex media may make the hydrolysis of these Ag-CPs more favourable. Hence, the *in vitro* and *in vivo* behaviour may be starkly different and further investigations, beyond the scope of this study, are required for elucidation.

Conclusions

Four Ag-CPs were studied to investigate the structural parameters controlling the release of silver ions and hence determine their relative importance in tuning the antibacterial properties of these materials. It was found that the metal-ligand bond strength and anion availability, rather than topological or particle size effects were the factors of most influence, and that frameworks made from anionic azole ligands result in slower decomposition than comparable neutral azine-based ligands. Topology and particle size appear to have a minimal effect on the silver release, compared to coordination environment of the silver ions. Formation of composites of the Ag-CPs with PE and PCL polymer matrices caused a dramatic reduction in the quantity of silver released into water, with the type of polymer and embedding conditions both effecting the release to a substantial extent. All four model silver coordination polymers demonstrated antibacterial activity against *S. aureus* and *E. coli*, with [Ag(dpzm)(ClO_4)]-*closed** (weak bonding, small particle size) showing the best activity. The antibacterial activity of [Ag_2(**Me_4bpz**)]-*open*, which did not show high release of silver ions into water, suggests that the solubility of the counter-anions is important in controlling the equilibrium of the silver release. Therefore, studies investigating the

release of silver from Ag-CPs into biological media with high concentrations of salts are of interest.

Experimental Section

General Experimental: Unless otherwise stated all chemicals were obtained from commercial sources and used as received. When necessary, solvents and reagents were dried following literature procedures and freshly distilled when needed. NMR spectra were recorded on a Varian 500 MHz spectrometer at 23°C using a 5-mm probe. ^{1}H NMR spectra recorded in $CDCl_3$ were referenced to the internal standard, Me_4Si, 0 ppm. A Philips XL30 field emission scanning electron microscope was used to collect images and perform energy-dispersive X-ray spectroscopy (EDX). Powder X-ray diffraction (PXRD) data was collected using a Cu Kα (λ = 1.540562 Å) source on a Bruker D8, Advanced X-ray powder diffractometer (parallel X-ray, capillary loaded) and a Co Kα (λ = 1.78895 Å) Bruker D4, Endeavour X-ray powder diffractometer (parallel X-ray, flat plate loaded).

Coordination polymer synthesis: 3,3',5,5'-Tetramethyl-4,4'-bipyrazole (Me_4bpz)[79–81] and di-2-pyrazinylmethane (dpzm)[74] were synthesized according to literature procedures. [Ag_2(**Me$_4$bpz**)]-*4 fold* and [Ag_2(**Me$_4$bpz**)]-*8 fold* were synthesized according to the procedures reported by Zhang.[72] [Ag(**dpzm**)(ClO_4)]-*open* and [Ag(**dpzm**)(ClO_4)]-*closed* were synthesized by the methods reported by Bloch.[73] PXRD confirmed the synthesis of all four Ag-CPs (Figures 5.11 and 5.12).

Synthesis of PCL Composites: The dried Ag-CPs were reduced to powders by grinding before being suspended in a solution of PCL (500 mg) dissolved in dichloromethane in a 6-cm diameter glass petri dish. The solvent was then allowed to evaporate overnight to leave a thin film ~1 mm in thickness, which was cut into 5 mm diameter disks with silver loadings of 0.5% and 1%.

Synthesis of PE Composites: The dried Ag-CPs were reduced to powders by grinding, before being mixed with granular PE (500 mg). The mixture was placed on a glass surface, which was heated to the melting point of PE (~95 °C), then allowed to cool to form a film ~1 mm thick. As the composite cooled, 6mm disks were cut with silver loadings of 0.5%, 1% and 2.5%.

Dissolution Studies: Samples (Ag-CPs, PCL or PE composites) were placed into Milli-Q water and stirred for 24 hrs. At each time point 200 µL aliquots were removed, diluted with 2% ultra-pure nitric acid (4.8 mL) and filtered through a 0.2 µm filter. Inductively-coupled plasma mass spectroscopy (ICP-MS) was performed on a Solution 7500CS ICPMS spectrometer. All experiments were performed in triplicate and error bars represent the standard error of the mean.

Microbiological Studies: The antibacterial activities of [Ag_2(**Me$_4$bpz**)]-*4 fold*, [Ag_2(**Me$_4$bpz**)]-*8* fold, [Ag(**dpzm**)(ClO_4)]-*open/closed** and [Ag(**dpzm**)(ClO_4)]-*closed* composites in PCL and PE matrices were tested against *Escherichia coli* MG1655, and *Staphylococcus aureus* Newman strain using the following procedures. All assays were performed in triplicate, with error bars representing the standard error of the mean, and positive ($AgNO_3$) and negative controls (PE and PCL) were performed.

Disk Diffusion: Luria-Bertani (LB) broth (20 mL) was inoculated with *S. aureus* or *E. coli* to OD_{600} 0.05 and incubated at 37°C with shaking at 200 rpm for 6 hrs. Bacterial cultures were then diluted to OD_{600} 0.8 with LB broth to ensure even, confluent growth, and 100 µL spread plated onto LB+ 1.5% (w/v) agar plates. The impregnated disks were placed on the plates, and the inhibition zone measured after incubation overnight at 37°C by visual inspection.

Growth Assays: A single colony of either *S. aureus* or *E. coli* was inoculated into 15 mL of broth (Tryptic Soy Broth (TSB) for *S. aureus* and LB broth for *E. coli*) and incubated at 37°C overnight while shaking at 200 rpm. Bacteria were then inoculated into 10 mL of fresh media (LB broth for *E. coli* and TSB for *S. aureus*) starting at OD_{600} 0.2, corresponding to 4 x 10^6 CFU/mL (colony forming units/mL). Ag-CP loaded PE (40 mg, 0.5% loading), which had been reduced to granular form, was added to the bacterial suspensions and the cultures incubated for 8 hr at 37°C while shaking at 200 rpm. At 2 hr intervals 100µL of the culture was removed and a 1 x 10^6 serial dilution into sterile PBS was performed for the initial time point and a 1 x 10^7 serial dilution performed for the subsequent time points. 100 µL aliquots were spread plated onto LB + 1.5% (w/v) agar plates and the CFUs enumerated after incubation overnight at 37 °C by visual inspection.

CCDC 678713 [for **CP-1**], 678715 (for **2**), 855398 (for **3**), and 855401 (for **4**) contain the supplementary crystallographic data for this paper. These data can be obtained free of charge from **The Cambridge Crystallographic Data Centre**.

Acknowledgements

We thank Mr O. Linder-Patton for his assistance with collecting SEM images. We thank the University of Adelaide (Beacon Scholarship) for financial support.

Keywords: silver • structure-activity relationships • antibiotics • metal-organic frameworks • drug delivery

5.4 Conclusions and Future Directions

Four silver-based coordination polymers were synthesised by known procedures and their decomposition in water to release silver ions was studied. It was found that, in this sub-set of materials, the parameter with the most control over the release kinetics was the metal-ligand bond strength, inferred from the pK_a values for ligand conjugate acids, and anion availability, rather than particle size or topology. The release of silver ions was also significantly slowed by the embedding of the coordination polymers into polymer matrices, with the water permeability of the polymer and the embedding conditions both influencing the release. Despite huge variability in decomposition rates, all four coordination polymers showed antibacterial activity, even $[Ag_2(\mathbf{Me_4bpz})]$-*open*, which did not show high levels of decomposition in pure water. This indicates that the availability of counterions and other coordinating species available in biological systems also contributes to the decomposition of the frameworks. Further studies into the decomposition of silver coordination polymers in different biological environments and characterisation of the complexes formed in these settings would be necessary if silver coordination polymers are to be utilised in therapeutic settings. Further antibacterial testing should also be undertaken against a wider range of bacterial species, including multi-drug resistant strains. Toxicity testing of the non-silver components released after CP decomposition should also be completed.

In addition, the synthesis of synergistic antibacterial silver CPs which contain more than one active component, either in the ligand or in the pores, would be of great potential for treating multi-drug resistant bacteria. Furthermore, incorporating MOFs and CPs into polymer films may be of interest for not only therapeutic applications, but for other settings where the slow release of a compound is desirable, such as water treatment or in the food and cosmetic industries.

5.5 Appendix

5.5.1 Properties of Ag-CPs

Table 5.1. Comparison of the physical and chemical properties of the four model silver coordination polymers chosen for this study.

Properties	**$[Ag_2(Me_4bpz)]$- 4/8 fold**	**$[Ag(dpzm)(ClO_4)]$- Open/Closed**
Dimensionality	3D	3D/2D
Ligand	N (pyrazole), anion	N (pyrazine), neutral
Silver coordination environment	2-coordinate	4-coordinate
Thermal stability	300°C[72]	185/260°C[73]
Crystal size (as synthesised)	0.5-1 μm (*4-fold*) and 0.5-20 μm[a] (*8-fold*)	3-6 mm[a]

[a.] Particle size was determined from as-synthesised samples; samples used for polymer incorporation were ground prior to use.

5.5.2 Powder X-ray Diffraction (PXRD) Data for the Ag-CPs

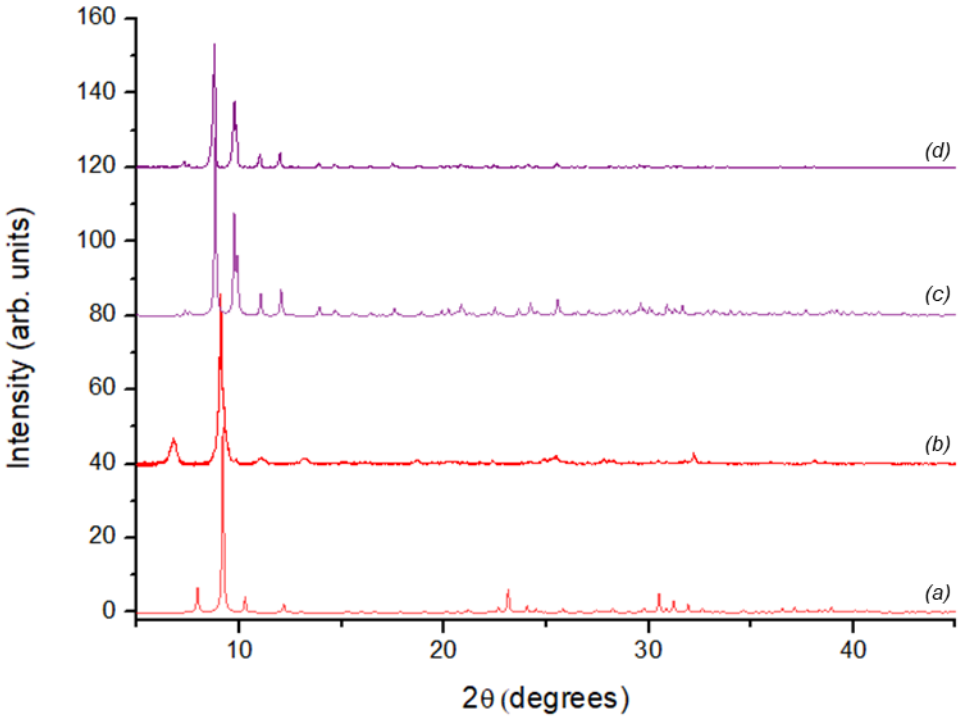

Figure 5.11. Powder pattern overlay of CP-1 and CP-2 (Cu Kα = 1.5418 Å): **a)** CP-1 simulated pattern; **b)** CP-1 as synthesised; **c)** CP-2 simulated pattern; **d)** CP-2 as synthesised. Note that the peaks from CP-1 are broadened and shifted slightly. This is due to structural deformities arising from the rapid method of synthesis using a templating molecule, as opposed to the single crystal synthesis that produced the simulated pattern.

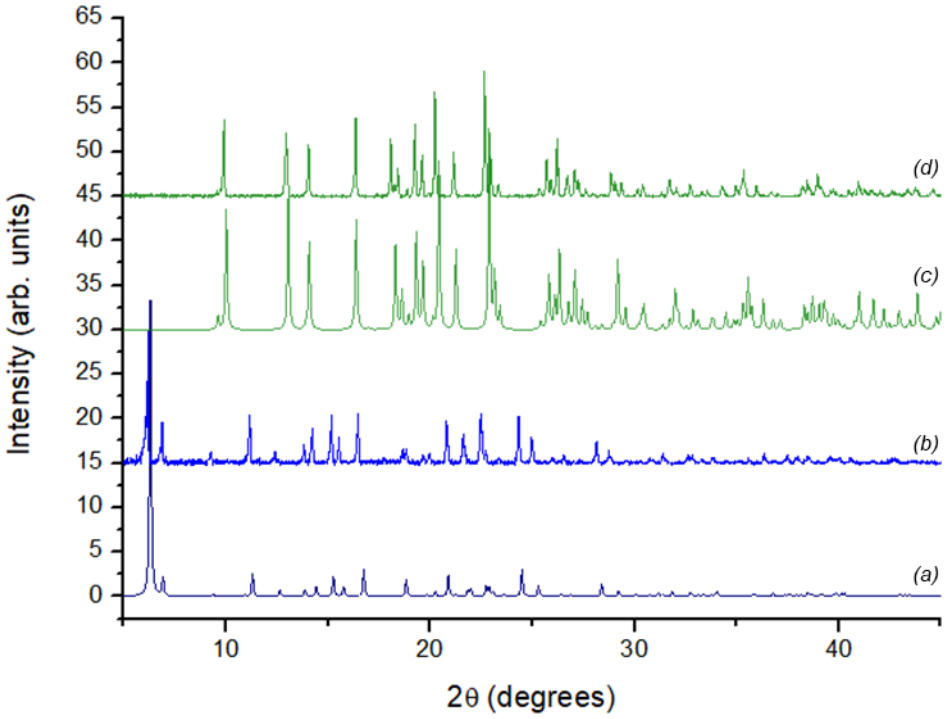

Figure 5.12. Powder pattern overlay of CP-3 and CP-4 (Cu Kα = 1.5418 Å): **a)** CP-3 simulated pattern; **b)** CP-3 as synthesised; **c)** CP-4 simulated pattern; **d)** CP-4 as synthesised. It was very difficult to obtain a good PXRD of CP-3 as vigorous crushing or extended exposure to air triggered the transformation of the sample.

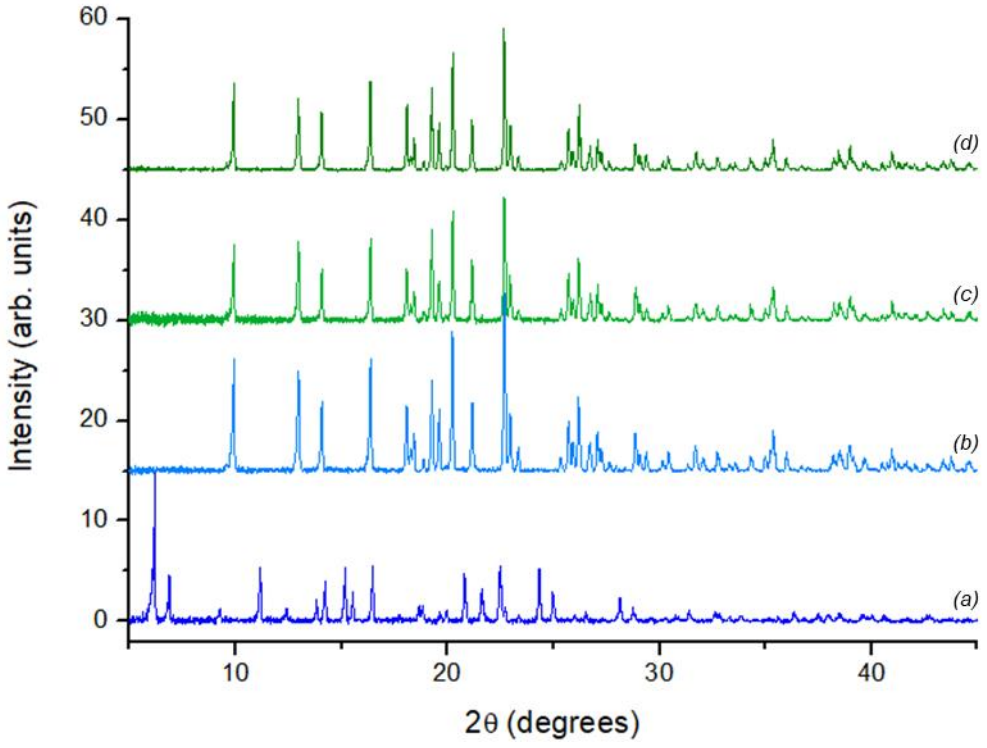

Figure 5.13. Powder pattern overlay of CP-3, CP-4 and both samples heated to 100 °C (Cu Kα = 1.5418 Å) showing complete conversion of the PCP to the close packed CP: **a)** CP-3 as synthesised; **b)** CP-3 heated to 100 °C; **c)** CP-4 heated to 100°C; **d)** CP-4 as synthesised.

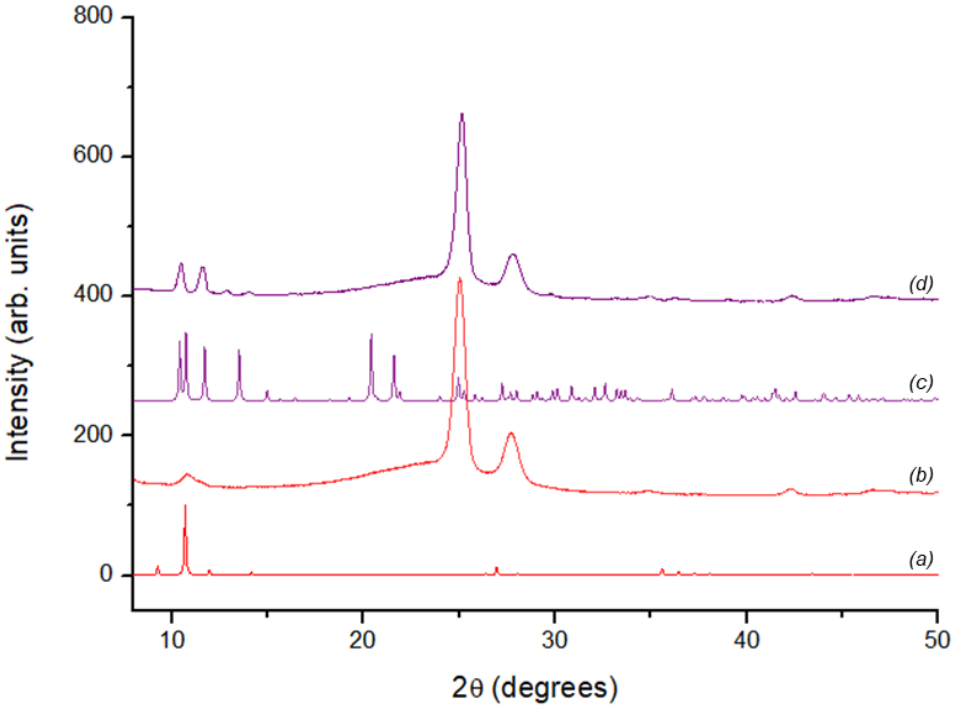

Figure 5.14. Powder pattern overlay of CP-1@ PE and CP-2@PE (Co Kα = 1.789 Å). Large peaks at 2θ = 25 and 28 correspond to the polyethylene; **a)** CP-1 simulated pattern; **b)** CP-1@PE; **c)** CP-2 simulated pattern; **d)** CP-2@PE.

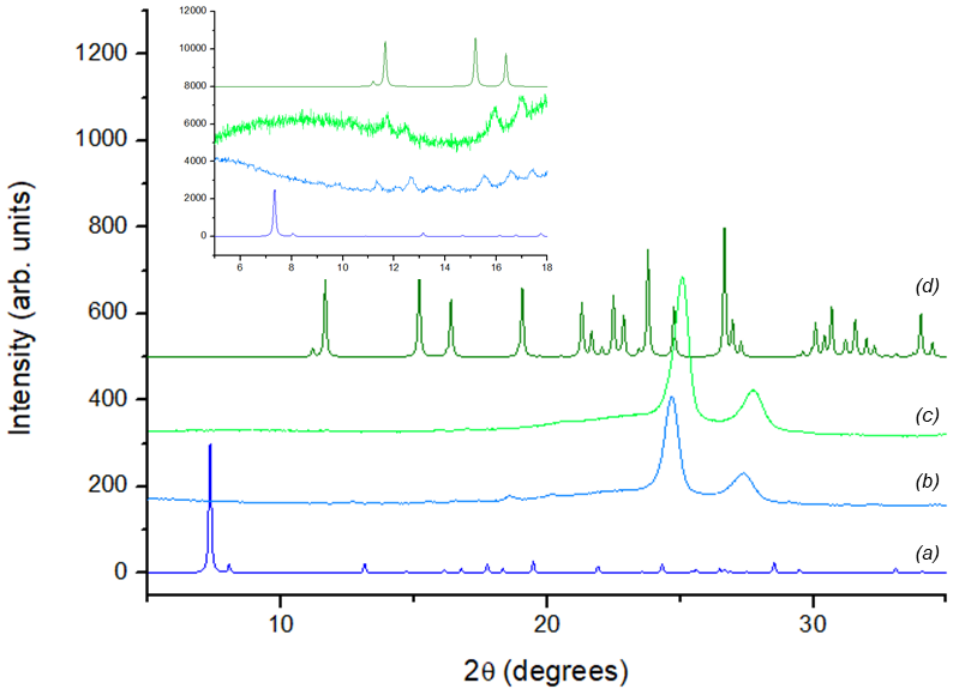

Figure 5.15. Powder pattern overlay of CP-3@PE and CP-4@PE (Co Kα = 1.789 Å). Large peaks at 2θ = 25 and 28 correspond to polyethylene; **a)** CP-3 simulated pattern; **b)** CP-3@PE; **c)** CP-4@PE; **d)** CP-4 simulated pattern. The inset shows the matching CP-4 peaks, although the peaks are shifted due to the material being incorporated into PE.

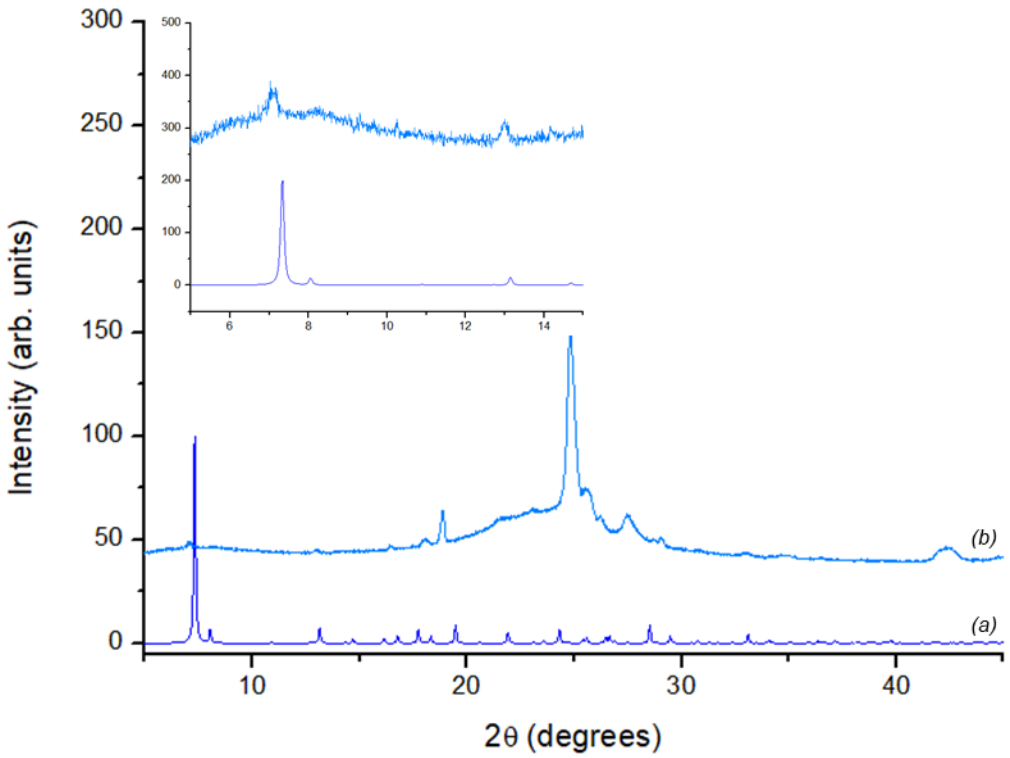

Figure 5.16 Powder pattern overlay of **a)** CP-3 simulated and **b)** CP-3@PCL (Co Kα = 1.789 Å). The peaks at 2θ > 15 correspond to the PCL, while the low angle peaks match the simulated PXRD (inset), although shifted slightly due to incorporation in the polymer. This confirms that CP-3 was successfully embedded into PCL without conversion into CP-4.

5.5.3 Scanning Electron Microscopy (SEM) Images

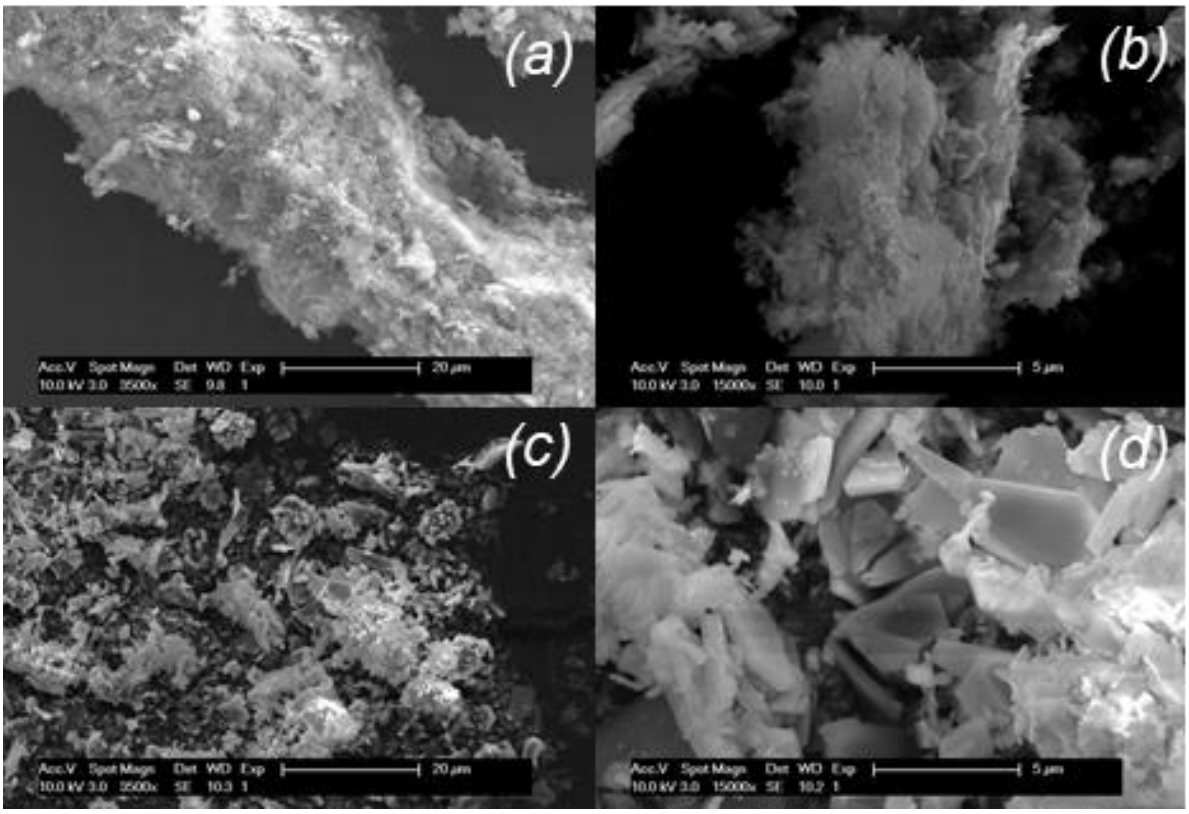

Figure 5.17. Scanning electron microscope images in SE mode of **(a)/(b)** CP-1, with crystallite sizes of <1µm and **(c)/(d)** CP-2 with crystal sizes of 0.5-10 µm.

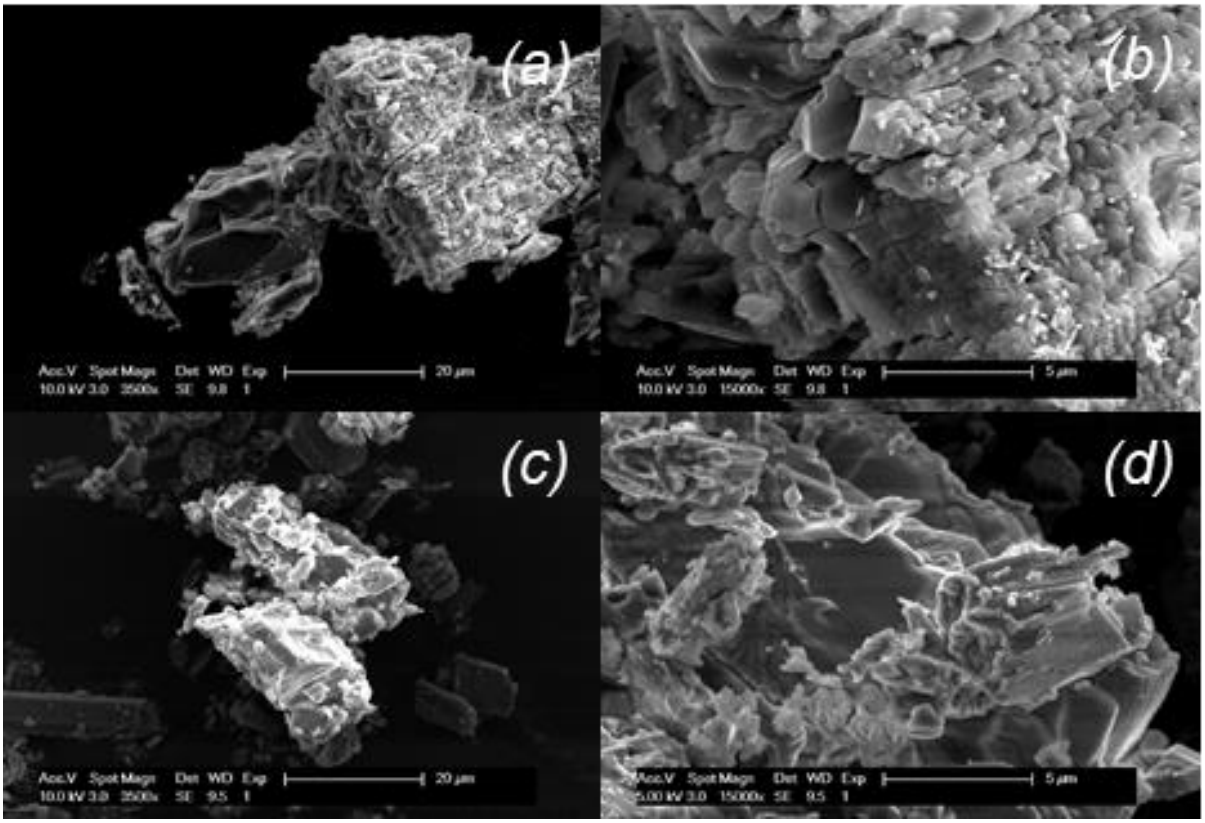

Figure 5.18. Scanning electron microscope images in SE mode of **(a)/(b)** CP-3, with crystallite sizes of 0.5-35 µm and **(c)/(d)** CP-4 with crystal sizes of 0.5-35 µm.

5.5.4 Polymer incorporation: Silver release

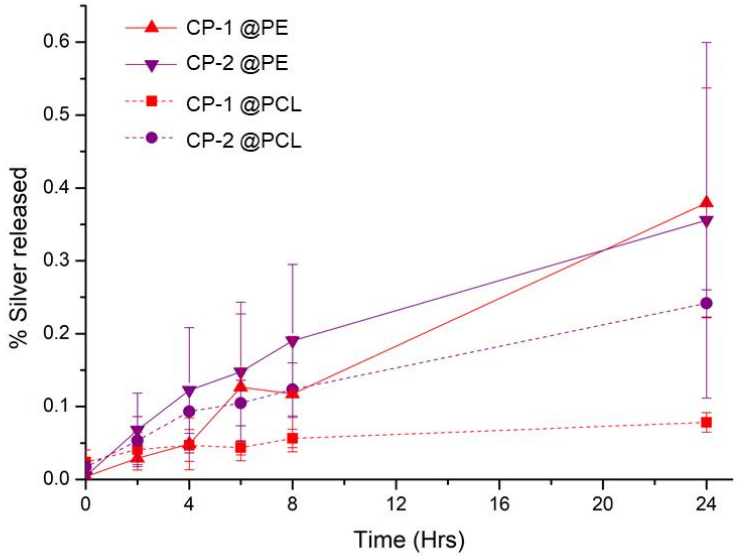

Figure 5.19. Silver release profiles of CP-1 (red) incorporated into PE and PCL and CP-2 (purple) incorporated into PE and PCL over 24 hours, showing a continual release of silver without reaching equilibrium. As the quantities of silver released are so small (<0.6%) comparison between the different CPs is not possible.

5.5.5 Antibacterial assays: PCL disk diffusion

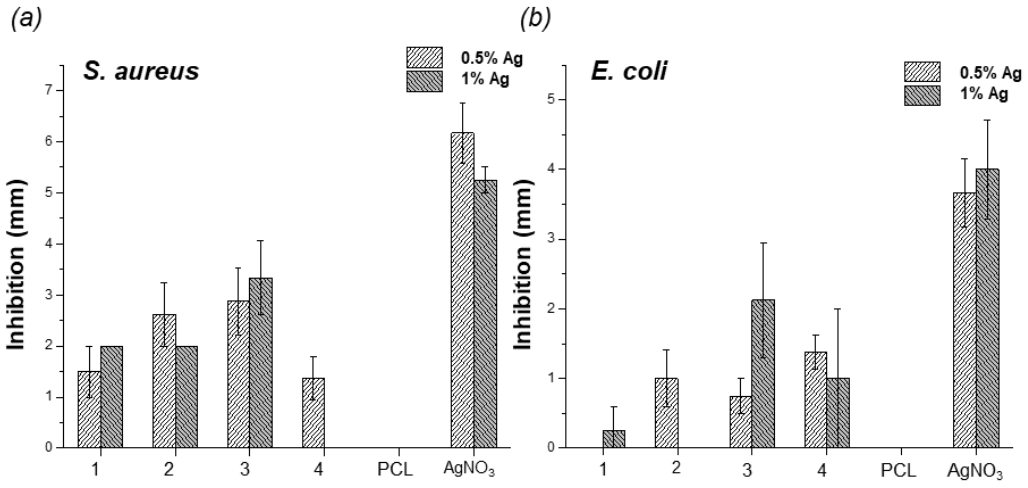

Figure 5.20. Zones of inhibition measured for PCL disks impregnated with silver CPs at 0.5% and 1% loadings against **(a)** S. Aureus and **(b)** E. coli. Untreated PCL and silver nitrate loaded disks were used as negative and positive controls respectively.

5.5.6 Antibacterial assays: PE growth inhibition

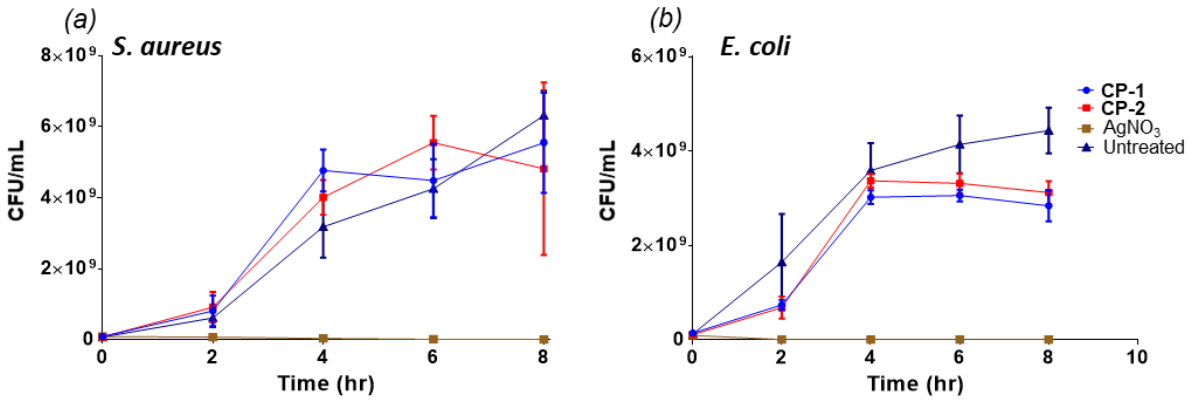

Figure 5.21. Antibacterial activities of CP-1 (blue) and CP-2 (red) against **(a)** S. aureus and **(b)** E. coli. The bacterial growth curve of an untreated culture (dark blue) is shown as a negative control and silver nitrate embedded into PE (brown) as a positive control.

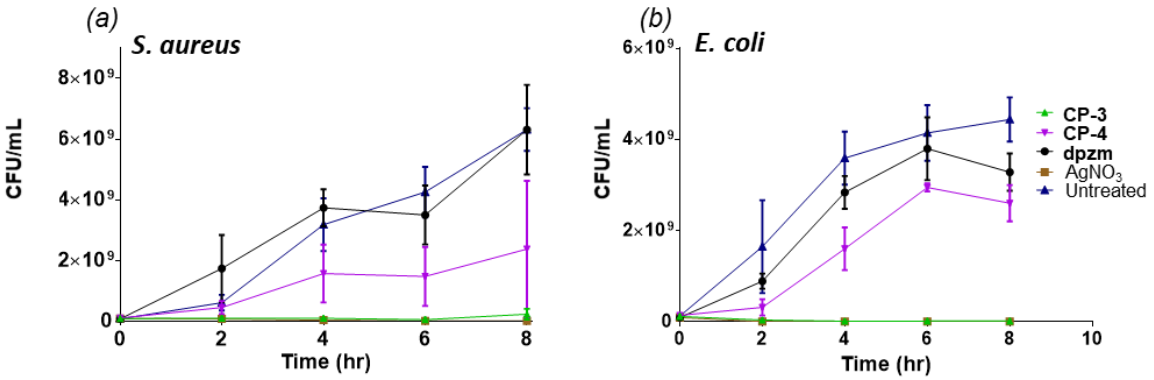

Figure 5.22. Antibacterial activities of CP-3 (green) and CP-4 (purple) against **(a)** S. aureus and **(b)** E. coli. The bacterial growth curve of an untreated culture (dark blue) is shown as a negative control and silver nitrate embedded into PE (brown) as a positive control. The activity of the ligand, dpzm (black), is also shown to be very similar to the negative control

5.6 References

1 M. Cruickshank, J. Ferguson and A. Bull, *Healthc. Infect.*, 2009, **14**, 109–114.

2 M. J. Duncan, P. S. Wheatley, E. M. Coghill, S. M. Vornholt, S. J. Warrender, I. L. Megson and R. E. Morris, *Mater. Adv.*, 2020, **1**, 2509–2519.

3 World Health Organization, The top 10 causes of death, https://www.who.int/news-room/fact-sheets/detail/the-top-10-causes-of-death, (accessed 24 April 2021).

4 J. Turnidge, *Aust. Prescr.*, 2017, **40**, 2–3.

5 Public Health England, *English Surveillance Programme for Antimicrobial Utilisation and Resistance (ESPAUR)*, 2020.

6 P. Y. Chung and Y. S. Toh, *Pathog. Dis.*, 2014, 70, 231–239.

7 A. S. Kwon, G. C. Park, S. Y. Ryu, D. H. Lim, D. Y. Lim, C. H. Choi, Y. Park and Y. Lim, *Int. J. Antimicrob. Agents*, 2008, **32**, 68–72.

8 N. R. Mathias and M. A. Hussain, *J. Pharm. Sci.*, 2010, **99**, 1–20.

9 E. Sayed, R. Haj-Ahmad, K. Ruparelia, M. S. Arshad, M. W. Chang and Z. Ahmad, *AAPS PharmSciTech*, 2017, **18**, 1507–1525.

10 M. Arruebo, *Wiley Interdiscip. Rev. Nanomedicine Nanobiotechnology*, 2012, **4**, 16–30.

11 H. D. Williams, N. L. Trevaskis, S. A. Charman, R. M. Shanker, W. N. Charman, C. W. Pouton and C. J. H. Porter, *Pharmacol. Rev.*, 2013, **65**, 315–499.

12 A. Salomé Veiga, J. P. Schneider, A. S. Veiga and J. P. Schneider, *Antimicrobial hydrogels for the treatment of infection*, John Wiley and Sons Inc., 2013, vol. 100.

13 T. R. Hoare and D. S. Kohane, *Polymer (Guildf).*, 2008, **49**, 1993–2007.

14 P. Horcajada, T. Chalati, C. Serre, B. Gillet, C. Sebrie, T. Baati, J. F. Eubank, D. Heurtaux, P. Clayette, C. Kreuz, J. S. Chang, Y. K. Hwang, V. Marsaud, P. N. Bories, L. Cynober, S. Gil, G. Férey, P. Couvreur and R. Gref, *Nat. Mater.*, 2010, **9**, 172–178.

15 P. Saint-Cricq, Y. Kamimura, K. Itabashi, A. Sugawara-Narutaki, A. Shimojima and T. Okubo, *Eur. J. Inorg. Chem.*, 2012, **2012**, 3398–3402.

16 E. Khodaverdi, H. A. Soleimani, F. Mohammadpour and F. Hadizadeh, *Chem. Biol. Drug Des.*, 2016, **87**, 849–857.

17 B. de Gennaro, L. Catalanotti, P. Cappelletti, A. Langella, M. Mercurio, C. Serri, M. Biondi and L. Mayol, *Colloids Surfaces B Biointerfaces*, 2015, **130**, 101–109.

18 Y. Zhao, Z. Q. Wang, X. Zhao, W. Li and S. X. Liu, *Appl. Surf. Sci.*, 2013, **266**, 67–72.

19 S. T. Gregg, Q. Yuan, R. E. Morris and B. Xiao, *Mater. Today Commun.*, 2017, **12**, 95–105.

20 P. Horcajada, C. Serre, G. Maurin, N. A. Ramsahye, F. Balas, M. Vallet-Regí, M. Sebban, F. Taulelle and G. Férey, *J. Am. Chem. Soc.*, 2008, **130**, 6774–6780.

21 M. H. Teplensky, M. Fantham, C. Poudel, C. Hockings, M. Lu, A. Guna, M. Aragones-Anglada, P. Z. Moghadam, P. Li, O. K. Farha, S. Bernaldo de Quirós Fernández, F. M. Richards, D. I. Jodrell, G. Kaminski Schierle, C. F. Kaminski and D. Fairen-Jimenez, *Chem*, 2019, **5**, 2926–2941.

22 K. Jiang, L. Zhang, Q. Hu, Q. Zhang, W. Lin, Y. Cui, Y. Yang and G. Qian, *Chem. - A Eur. J.*, 2017, **23**, 10215–10221.

23 L. L. Tan, H. Li, Y. C. Qiu, D. X. Chen, X. Wang, R. Y. Pan, Y. Wang, S. X. A. Zhang, B. Wang and Y. W. Yang, *Chem. Sci.*, 2015, **6**, 1640–1644.

24 H. Zheng, Y. Zhang, L. Liu, W. Wan, P. Guo, A. M. Nyström and X. Zou, *J. Am. Chem. Soc.*, 2016, **138**, 962–968.

25 C. Tamames-Tabar, D. Cunha, E. Imbuluzqueta, F. Ragon, C. Serre, M. J. Blanco-Prieto and P. Horcajada, *J. Mater. Chem. B*, 2014, **2**, 262–271.

26 X. X. Lu, Y. H. Luo, C. Lu, X. Chen and H. Zhang, *J. Solid State Chem.*, 2015, **232**, 123–130.

27 J. M. S. Cardoso, A. M. Galvão, S. I. Guerreiro, J. H. Leitão, A. C. Suarez and M. F. N. N. Carvalho, *Dalton Trans.*, 2016, **45**, 7114–7123.

28 K. Wang, Z. Geng, Y. Yin, X. Ma and Z. Wang, *CrystEngComm*, 2011, **13**, 5100–5104.

29 Q. Meng, L. Wang, D. Wang, J. Yang, C. Yue and J. Lu, *Crystals*, 2017, **7**, 112.

30 M. Vassaki, K. E. Papathanasiou, C. Hadjicharalambous, D. Chandrinou, P. Turhanen, D. Choquesillo-Lazarte and K. D. Demadis, *Chem. Commun.*, 2020, **56**, 5166–5169.

31 R. V. Pinto, S. Wang, S. R. Tavares, J. Pires, F. Antunes, A. Vimont, G. Clet, M. Daturi, G. Maurin, C. Serre and M. L. Pinto, *Angew. Chem. - Int. Ed.*, 2020, **59**, 5135–5143.

32 S. Diring, A. Carné-Sánchez, J. Zhang, S. Ikemura, C. Kim, H. Inaba, S. Kitagawa and S. Furukawa, *Chem. Sci.*, 2017, **8**, 2381–2386.

33 C. Kim, S. Diring, S. Furukawa and S. Kitagawa, *Dalton Trans.*, 2015, **44**, 15324.

34 Y. Sun, L. Zheng, Y. Yang, X. Qian, T. Fu, X. Li, Z. Yang, H. Yan, C. Cui and W. Tan, *Nano-Micro Lett.*, 2020, **12**, 1–29.

35 H. D. Lawson, S. P. Walton and C. Chan, *ACS Appl. Mater. Interfaces*, 2021, **13**, 7004–7020.

36 D. Cunha, M. Ben Yahia, S. Hall, S. R. Miller, H. Chevreau, E. Elkaïm, G. Maurin, P. Horcajada and C. Serre, *Chem. Mater.*, 2013, **25**, 2767–2776.

37 I. Abánades Lázaro, C. J. R. Wells and R. S. Forgan, *Angew. Chem. Int. Ed.*, 2020, **59**, 5211–5217.

38 Y. Chen, K. Tai, P. Ma, J. Su, W. Dong, Y. Gao, L. Mao, J. Liu and F. Yuan, *Food Chem.*, 2021, **347**, 128978.

39 K. Peikert, L. J. McCormick, D. Cattaneo, M. J. Duncan, F. Hoffmann, A. H. Khan, M. Bertmer, R. E. Morris and M. Fröba, *Microporous Mesoporous Mater.*, 2015, **216**, 118–126.

40 J. W. Alexander, *History of the Medical Use of Silver*, 2009, vol. 10.

41 S. Chernousova and M. Epple, *Angew. Chem. Int. Ed.*, 2013, **52**, 1636–1653.

42 R. I. Aminov, *Front. Microbiol.*, 2010, **1**, 134.

43 M. Cavicchioli, A. C. Massabni, T. A. Heinrich, C. M. Costa-Neto, E. P. Abrão, B. A. L. Fonseca, E. E. Castellano, P. P. Corbi, W. R. Lustri and C. Q. F. Leite, *J. Inorg. Biochem.*, 2010, **104**, 533–540.

44 S. Eckhardt, P. S. Brunetto, J. Gagnon, M. Priebe, B. Giese and K. M. Fromm, *Chem. Rev.*, 2013, 113, 4708–4754.

45 K. J. Woo, C. K. Hye, W. K. Ki, S. Shin, H. K. So and H. P. Yong, *Appl. Environ. Microbiol.*, 2008, **74**, 2171–2178.

46 R. M. Slawson, M. I. Van Dyke, H. Lee and J. T. Trevors, *Plasmid*, 1992, **27**, 72–79.

47 P. Dibrov, J. Dzioba, K. K. Gosink and C. C. Häse, *Antimicrob. Agents Chemother.*, 2002, **46**, 2668–2670.

48 K. Chamakura, R. Perez-Ballestero, Z. Luo, S. Bashir and J. Liu, *Colloids Surfaces B Biointerfaces*, 2011, **84**, 88–96.

49 K. M. Fromm, *Appl. Organomet. Chem.*, 2013, **27**, 683–687.

50 X. Lu, J. Ye, Y. Sun, R. F. Bogale, L. Zhao, P. Tian and G. Ning, *Dalton Trans.*, 2014, **43**, 10104–10113.

51 S. H. Alisir, S. Demir, B. Sariboga and O. Buyukgungor, *J. Coord. Chem.*, 2015, **68**, 155–168.

52 X. Lu, J. Ye, D. Zhang, R. Xie, R. F. Bogale, Y. Sun, L. Zhao, Q. Zhao and G. Ning, *J. Inorg. Biochem.*, 2014, **138**, 114–121.

53 O. Gordon, T. V. Slenters, P. S. Brunetto, A. E. Villaruz, D. E. Sturdevant, M. Otto, R. Landmann and K. M. Fromm, *Antimicrob. Agents Chemother.*, 2010, **54**, 4208–4218.

54 J. M. Rueff, O. Perez, V. Caignaert, G. Hix, M. Berchel, F. Quentel and P. A. Jaffrès, *Inorg. Chem.*,

2015, **54**, 2152–2159.

55 J. Morones-Ramirez, J. A. Winkler, C. S. Spina and J. J. Collins, *Sci. Transl. Med.*, 2013, **5**, 190

56 Q. L. Feng, J. Wu, G. Q. Chen, F. Z. Cui, T. N. Kim and J. O. Kim, *J. Biomed. Mater. Res.*, 2000, **52**, 662–668.

57 G. Zhao and S. E. Stevens, *BioMetals*, 1998, **11**, 27–32.

58 H. Vermeulen, J. M. Van Hattem, M. N. Storm-Versloot and D. T. Ubbink, *Cochrane Database Syst. Rev.*, 2007.

59 M. J. Muller, M. A. Hollyoak, Z. Moaveni, T. L. H. Brown, D. N. Herndon and J. P. Heggers, *Burns*, 2003, **29**, 834–836.

60 D. E. Fullenkamp, J. G. Rivera, Y. kuan Gong, K. H. A. Lau, L. He, R. Varshney and P. B. Messersmith, *Biomaterials*, 2012, **33**, 3783–3791.

61 G. Wyszogrodzka, B. Marszałek, B. Gil and P. Dorozyński, *Drug Discov. Today*, 2016, **21**, 1009–1018.

62 A. Tăbăcaru, C. Pettinari, F. Marchetti, C. Di Nicola, K. V. Domasevitch, S. Galli, N. Masciocchi, S. Scuri, I. Grappasonni and M. Cocchioni, *Inorg. Chem.*, 2012, **51**, 9775–9788.

63 A. Liu, C. C. Wang, C. zheng Wang, H. fen Fu, W. Peng, Y. L. Cao, H. Y. Chu and A. F. Du, *J. Colloid Interface Sci.*, 2018, **512**, 730–739.

64 S. W. Jaros, P. Smoleński, M. F. C. Guedes Da Silva, M. Florek, J. Król, Z. Staroniewicz, A. J. L. Pombeiro and A. M. Kirillov, *CrystEngComm*, 2013, **15**, 8060–8064.

65 S. W. Jaros, M. F. C. Guedes Da Silva, M. Florek, M. C. Oliveira, P. Smoleński, A. J. L. Pombeiro and A. M. Kirillov, *Cryst. Growth Des.*, 2014, **14**, 5408–5417.

66 S. W. Jaros, M. F. C. Guedes Da Silva, M. Florek, P. Smoleński, A. J. L. Pombeiro and A. M. Kirillov, *Inorg. Chem.*, 2016, **55**, 5886–5894.

67 S. W. Jaros, M. F. C. Guedes Da Silva, J. Król, M. Conceição Oliveira, P. Smoleński, A. J. L. Pombeiro and A. M. Kirillov, *Inorg. Chem.*, 2016, **55**, 1486–1496.

68 T. Wang, X. Liu, Y. Zhu, Z. D. Cui, X. J. Yang, H. Pan, K. W. K. Yeung and S. Wu, *ACS Biomater. Sci. Eng.*, 2017, **3**, 816–825.

69 A. Zirehpour, A. Rahimpour, A. Arabi Shamsabadi, M. G. Sharifian and M. Soroush, *Environ. Sci. Technol.*, 2017, **51**, 5511–5522.

70 A. J. T. Teo, A. Mishra, I. Park, Y. J. Kim, W. T. Park and Y. J. Yoon, *ACS Biomater. Sci. Eng.*, 2016, **2**, 454–472.

71 M. A. Woodruff and D. W. Hutmacher, *Prog. Polym. Sci.*, 2010, **35**, 1217–1256.

72 J. P. Zhang and S. Kitagawa, *J. Am. Chem. Soc.*, 2008, **130**, 907–917.

73 W. M. Bloch and C. J. Sumby, *Chem. Commun.*, 2012, **48**, 2534–2536.

74 W. M. Bloch, S. M. Derwent-Smith, F. Issa, J. C. Morris, L. M. Rendina and C. J. Sumby, *Tetrahedron*, 2011, **67**, 9368–9375.

75 P. Lu, Y. Wu, H. Kang, H. Wei, H. Liu and M. Fang, *J. Mater. Chem. A*, 2014, **2**, 16250–16267.

76 L. K. Massey, *Permeability Properties of Plastics and Elastomers: A Guide to Packaging and Barrier Materials*, Plastics Design Library, 2nd edn., 2003.

77 R. Shogren, *J. Environ. Polym. Degrad.*, 1997, **5**, 91–95.

78 W. M. Bloch and C. J. Sumby, *Eur. J. Inorg. Chem.*, 2015, **2015**, 3723–3729.

79 I. Boldog, E. B. Rusanov, A. N. Chernega, J. Sieler and K. V. Domasevitch, *Polyhedron*, 2001, **20**, 887–897.

80 R. Charles, *Org. Synth.*, 1959, **39**, 61.

81 V. V. Ponomarova, V. V. Komarchuk, I. Boldog, H. Krautscheid and K. V. Domasevitch,

CrystEngComm, 2013, **15**, 8280–8287.

Chapter 6: Conclusions and Future Directions

Metal-organic frameworks allow for reactions to occur in the solid-state which previously had only been accessible in solution or gaseous phases; however, the parameters controlling solid-state reactions are also structurally sensitive. As such, the chemical, topological and morphological influences of reactions occurring in MOFs can be considered. Metal complexes may be tethered to metal-organic frameworks through several methods. Among these, post-synthetic metalation of vacant sites within MOF ligands is an effective means of introducing a site-isolated metal complex to structurally characterise and utilise this complex for further reactions. Another method is to incorporate the metal of interest as the structural node in the framework, either as a dopant, or as the node itself. This latter method is less suited for structural characterisation, as nodes often occupy high symmetry sites, but is a valuable way in which large quantities of metal ions can be site-isolated. The reactivity of site-isolated metals bound to ligands and incorporated into the node of coordination polymers were explored in this thesis.

Chapter 2 was focussed on elucidating the photochemistry of a manganese (I) carbonyl complex tethered to MnMOF. MnMOF was post-synthetically metalated with *fac*-[$Mn(CO)_3Br$] and shown to undergo a series of solvent-induced isomerisations when exposed to solvents of varying coordinating abilities and steric bulk, producing either charge-neutral or charge-separated complexes. Two of these complexes, *fac*-[$Mn(CO)_3X$]Y (X = Br^- or MeCN, Y = THF or Br^-) were chosen to allow study of the behaviour of the metalated MOF under irradiation with visible or UV light. The photolysis reaction proceeded in a stepwise manner, with three CO release steps. The first CO ligand to be lost was from an equatorial coordination position with respect to the bis-pyrazolyl MOF ligand. This observation was made using photocrystallography and is attributed to the π-accepting character of the bis-pyrazolyl ligand. The formation of a transient *cis*-dicarbonyl intermediate was observed in matrix isolated time-resolved infrared spectroscopy at 190K. A second CO ligand was then lost from the other equatorial position, leaving an axially coordinated mono-carbonyl intermediate, observed crystallographically. Although both the charge-neutral and charge-separated species saw the loss of all three carbonyl ligands, the pathway for this step occurred differently. For the charge-neutral species in the presence of THF, loss of the final CO

ligand was associated with disordering of the bromide anion over both axial positions, while in the charge-separated species in acetonitrile, the loss of the last CO ligand saw coordination of the bromide anion at the vacated coordination site. With both these cases, the modelling, and thus interpretation, of the later stage photolysis structures were complicated by reduced occupancies of the manganese (I) ion and hence reductions in the electron densities of the associated ligands. Subsequent exposure of photolyzed MnMOF[$Mn(CO)_3X$]Y to CO gas resulted in the formation of carbonyl bands in the IR spectrum that suggest the formation of a Mn(II) carbonyl species. However, investigations into this oxidation by XPS did not support a changed oxidation state for the material and, additionally, the oxidising agent was not identified. Deeper understanding of the photo-activated decarbonylation reaction may be uncovered through computational and ultra-fast time-resolved infrared spectroscopy studies.

This study showed the formation of a pseudo-solution-state in a solid-state material, where the behaviour of the MOF-bound carbonyl complex was comparable to its molecular analogue, [$Mn(bdpm)(CO)_3Br$] (bdpm = bis(3,5-dimethyl-1H-pyrazol-1-yl)methane), in solution. This has been observed previously in crystalline sponges, where dynamic behaviour allowed in the MOF pore permits solution-state type reactions to occur in the solid-state.[1] The tethering of metal carbonyl complexes to MOFs, where a clear structural and spectroscopic understanding of their CO release processes can be obtained, may allow for future development of CO releasing materials for medical or chemical synthesis applications. Although regeneration of Mn(I) carbonyl complexes could not be demonstrated, the study of other transition metal carbonyl complexes, such as iron or nickel, may give other results.

Exploring potential applications of CO releasing MOFs (CORMats) was the motivation for **Chapter 3**, through testing manganese (I) carbonyl containing MOFs as sources of CO for carbonylation reactions and developing morphological control over MnMOF through structuralisation. Three carbon monoxide releasing MOFs were synthesised from MnMOF (CORMat-1), DUT-5 (CORMat-2) and UiO-67 (CORMat-3), and all were demonstrated to release CO, which was used in a test aminocarbonylation reaction. Different reactor designs were tested, and it was found that several design features are needed for successful *ex-situ* carbonylation reactions to take place, namely, limited headspace for the diffusion of CO, the ability to control the temperatures of the two chambers separately and the capability to remove the MOF after reaction without

need for additional filtration steps. Also advantageous was the facility to limit the exposure of the CORMats to solvents and the means to add reagents separately to the two chambers. These factors were of consideration in the research described herein but the intended application of the CORMats were as CO releasing materials for flow chemistry.

High conversion rates were achieved (>80%) with all three CORMats tested, although different quantities of MOF were required to achieve these rates, and so smaller masses of MOF were able to be used for CORMats with higher CO loadings by weight. As such it was evident that the CO releasing ability of MOFs depends on both the coordination environment of the carbonyl complex, and other structural features such as lattice topology and crystal morphology. Expanding the library of MOFs which may be used as CORMats and further tuning the metalation, morphological and release properties of CORMats1-3 is needed before these materials may be used routine CO sources.

To examine the effects of crystal morphology and to add additional functionalities and processability, attempts were made to structuralise MnMOF from sacrificial manganese oxide supports derived from sol-gels. MOF nucleation and growth was studied through scanning electron microscopy, and was found to be dependent on the structure of the oxide support. MOF growth was only observed on the exterior surfaces of the oxide particles, with the growth rate varying depending on the solvent from which the sol-gel was dried. The MOF crystals grown on the oxide surface eventually grew too large, after which cracks would appear and the structuralised MnMOF would detach from the MnO_x particle in sheets, exposing unreacted manganese oxide. As such, short reaction times were needed to grow structuralised MnMOF while retaining the macrostructural properties of the support. The structuralised MnMOF did not exhibit any significant differences in metalation ability or photochemical behaviour to the conventionally synthesised MnMOF, although further research is needed to investigate the porosity of the manganese oxide precursors and structuralised MOFs. This would be with the ultimate aim to create hierarchically porous materials with micro-, meso- and microporosity and to investigate their effectiveness as chemical storage and delivery vessels. The application of these systems as light activated CO releasing materials for flow chemistry would be of particular interest.

Further exploiting the capacity of MnMOF to site-isolate metal complexes was the focus of **Chapter 4**. The photochemistry of MnMOF[$Mn(CO)_3N_3$] at different temperatures was investigated through matrix isolated time-resolved IR spectroscopy and photocrystallography. The photochemical reaction pathway was found to be dependent on the presence of coordinating solvents and temperature. No loss of CO was observed in toluene solvated crystals, but for THF solvated crystals decarbonylation occurred at temperatures colder than room temperature for bulk samples and colder than 190K for a single crystal. Additionally, isocyanate formation was observed at room temperature for bulk, matrix isolated samples and 190K for a single crystal. Isocyanate formation was not observed under ambient conditions, leading to the implication that the strength of the available coordinating ligands in the environment influences the reaction pathway followed. The [$Mn(bdpm)(CO)_3N_3$] molecular species did not show any change on irradiation; however, in THF or DCM solutions reacted rapidly to from complexes containing bridging isocyanate and azide ligands, with no remaining carbonyl ligands. Unlike the complex examined in Chapter 2, the photochemical behaviour in the MOF did not mimic that which occurred for the molecular species in solution due to the site-isolation of the MOF-bound species preventing the formation of bridging azido or isocyanate species.

The metalation of MnMOF with palladium complexes was achieved through post-synthetic techniques resulting in MnMOF[$PdCl_2$] and MnMOF[$PdBr_2$] compounds. Attempts to post-synthetically metalate the MOF with more reactive palladium compounds bearing alkyl ligands were unsuccessful. It was found that in addition to binding to the bis-pyrazolyl site in the MOF ligand, palladium complexes could be held in the pores, as observed for a number of rhodium(I) complexes, reported in previous work on this MOF.[2,3] This, combined with facile labilisation of the palladium from the ligand binding site, resulted in complications in achieving quantitative metalation without residual palladium in the pores, or displacing the metal the binding site. Despite this, future investigations into the metalation procedure should uncover an optimal method which will allow for consistent, quantitative metalation of MnMOF with palladium complexes. This may be achieved through washing the crystals with different solvents, such as THF, which may remove the pore held complexes without labilising the ligand bound complexes. Already established methods, used in for the anion exchange in the Mn(I) complex, and for the, previously reported, formation of rhodium

ethylene complexes in MnMOF may be applied to access active palladium catalysts (Figure 1), through which reaction mechanisms may be studied..[4]

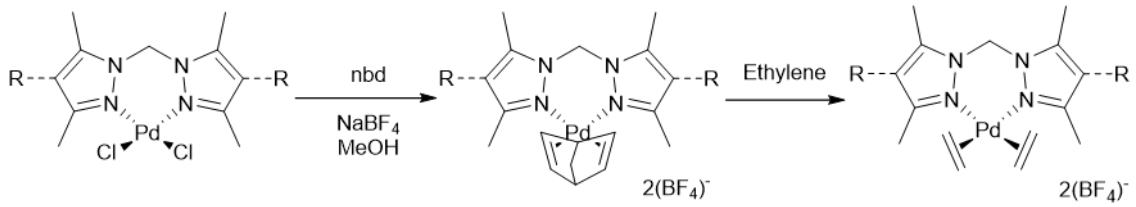

Figure 6.1. Proposed reaction scheme for the formation of an active palladium catalyst in MnMOF through ligand exchange with nbd (nbd = norbornadiene) in the presence of a non-coordinating anion, then exposure to ethylene gas.

Chapter 5 was devoted to investigating the effects of MOF structural properties on their potential application as antibacterial agents. A selection of previously reported silver coordination polymers was chosen to probe the relative significance of framework topology and coordination bond strength on the release of antibacterial silver ions into solution. The dissolution kinetics of these coordination polymers were studied in water, where it was found that frameworks containing weaker coordination bonds between neutral pyrazine donors and silver resulted in significantly faster release rates than coordination polymers formed from stronger pyrazole to silver bonds. This was unsurprising; however, the relative lack of influence of topology was unexpected. The difference in release rates between coordination polymers of some coordination environment but different topologies was an order of magnitude smaller than the difference between release rates of different coordination environments. As such, this should be an important consideration for designing coordination polymers for future applications where sacrificial decomposition is required.

The silver coordination polymers were embedded into organic polymer matrices, and the silver release kinetics into water investigated again. The matrices slowed the release, as expected, with both the water permeability of the polymer and the embedding conditions influencing the release of silver ions, with the silver coordination polymers embedded into polycaprolactone displaying faster release than those in polyethylene.

All four silver coordination polymers displayed antibacterial activity, even those which released negligible quantities of silver ions into water. As such, the antibacterial

activities did not directly correlate to the release kinetics in water. This indicates that the biological environment, particularly the presence of counterions and ligands, can significantly influence the dissolution kinetics of coordination polymers and hence is a topic of interest for further study. Of particular interest is the effect of chloride anions, which are present in high concentrations in biological systems, and which may result in the formation of highly insoluble silver chloride.[5]

This study demonstrated that the antibacterial activity of silver coordination polymers is not simply linked to their chemical or structural properties, but dependant on a combination of factors. The importance of studying these materials in the solid-state and *in vitro* was emphasised, as their behaviour varies depending on their environment. A link between water vapour permeability of organic polymers and their ability to retard the release of embedded silver ions was proposed, but further studies are required to confirm and quantify this correlation. This work only briefly touches on the many further pathways which can be pursued to develop silver coordination polymers as antibacterial agents; they have great potential, especially in treating multi-drug resistant bacteria.

To conclude, this thesis has advanced the understanding of isolating reactive metal complexes in MOFs. Tethered metal complexes were shown to display comparable behaviour to molecular counterparts in solution (Chapter 2), yet to show new behaviour due to the site-isolated nature of the complexes (Chapter 4). Retention of long-range order after reaction was a significant challenge in these studies, with disorder and loss of crystallinity precluding the characterisation of some species. Further optimisation of reaction conditions, including the use of controlled atmosphere crystal mounts for *in-situ* photocrystallography, and judicious choice of reagents can aid in mitigating these obstacles. Potential applications of these materials were proposed and trialled for the storage and delivery of reagents for chemical synthesis (Chapter 3) and of therapeutic agents in antibacterial coatings (Chapter 5), while the fundamental principles surrounding the relative importance of underlying parameters, including coordination environment, topology and crystal morphology, were tested. The efficiency, re-usability and safety of MOFs for these applications remain challenges which need to be overcome before wide-spread application may be realised.

6.1 References

1 W. J. Gee, *Dalton Trans.*, 2017, 46, 15979–15986.

2 A. Burgun, C. J. Coghlan, D. M. Huang, W. Chen, S. Horike, S. Kitagawa, J. F. Alvino, G. F. Metha, C. J. Sumby and C. J. Doonan, *Angew. Chem. Int. Ed.*, 2017, **56**, 8412–8416.

3 W. M. Bloch, A. Burgun, C. J. Coghlan, R. Lee, M. L. Coote, C. J. Doonan and C. J. Sumby, *Nat. Chem.*, 2014, **6**, 906–912.

4 R. A. Peralta, M. T. Huxley, J. D. Evans, T. Fallon, H. Cao, M. He, X. S. Zhao, S. Agnoli, C. J. Sumby and C. J. Doonan, *J. Am. Chem. Soc.*, 2020, **142**, 13533–13543.

5 H. D. Betts, PhD thesis, University of Adelaide, 2020.